Temporal Control of Ion Channel Activation

Thesis by
Oliver Syed Shafaat

In Partial Fulfillment of the Requirements for the
degree of
Doctorate of Philosophy

CALIFORNIA INSTITUTE OF TECHNOLOGY
Pasadena, California

2016
Defended May 6, 2016

DEDICATION

for my family

ACKNOWLEDGEMENTS

It has been an interesting journey here at Caltech. I have not only grown as a scientist, but also as a person, and there are many people who have helped me along the way. While it is not going to be possible to thank everyone that has made an impact, I will try to touch on some memories that I think of fondly (and laugh). When I arrived at Caltech, I had no idea what I wanted to do. Harry and Dennis let me take my project whereever I wanted to go. They both sent me to many conferences, allowing me to further my interests, meet new people, and see new places. I am thankful for finding two professors who me to pursue my, at times eclectic, interests, both in science and in life.

I guess I will start with thanking Professor Harry B. Gray first. Harry was the one who sold me on the big-picture project that has driven my research. Thinking back that first meeting of ours really foreshadowed what my time in the Gray group would be like. Harry has an unending passion for science, and that has provided me with the motivation to carry on more than a few times. I hope that I am one day able to find work I am as passionate about as Harry is science. Beyond being a huge motivator of work, Harry has always encouraged that I have a well-rounded life. From our conversations about Aspen, to the many party-planning sessions, he was always there to talk and check in. Speaking of parties, thank you Harry (and Shirley) for all the free food and booze over the years. There are many memories, experiences and friends that were a result of those parties. I want to thank Harry for introducing me to the Gray Nation, it is sort of surreal to think that I am part of the Gray Nation. I have had a chance to interact with many Gray Nation members both professionally and socially. Harry's deep care for all of his students, even the ones who are now emeritus professors, is unending and I do not think I can thank him enough for that support.

Professor Dennis A. Dougherty provided a different and equally supportive and fun environment to work in. Dennis provided a more grounded perspective in regards to the project progress, and the work I was doing. Dennis always surprised me with his knowledge of some very random topics, which was both frustrating and helpful at the same time. Dennis' deep passion for science, and his enjoyment of life outside of work is something that I strive for. Dennis always listens to anything you have to say, and was there to let me explore on my own various ideas. He only ever said "I told you so" once or twice in regards to the terrible ideas I had. Whenever we talked about life outside science, he made sure I was alright and helped me with the various situations I found myself in from time to time. He never let me bullshit my way out of things, constantly reminding me that it isn't his first time at the rodeo. Dennis always kept me grounded in science and life, and I want to thank him for that.

Working at Caltech, and in particular Harry and Dennis' groups, has provided me with the mentorship of many other fantastic advisors that have taken the time and care to teach me along the way. The first I will mention is Jay Winkler. Jay is, in my mind, the scientist's scientist. He is "The Most Interesting Man in the World (of Science)" to me. I think one of my first memories of Jay is him telling me to run all the damn controls first. That is a lesson that he reminded me of again and again throughout the years. Jay is the most rigorous scientists that I have ever met. Jay goes where the science takes him, it doesn't matter what you hope happens, it matters what happens. That, I think is one of the most important lessons I have learned in graduate school. I also want to thank Jay for being patient and letting me watch as you fixed the various instruments in lab. I would like to think I have learned a little about instrument maintenance and troubleshooting problems, but I am always amazed by the solutions Jay figures out to the issues I inevitably tell him about sheepishly near the exit of his office. Thank you Jay for all the help, and for putting in the effort to teach me about all sort of things, I know it wasn't easy.

I was fortunate to get to know Henry Lester. Henry always provided unique insight into the finer details with regards to ion channel work that progressed my knowledge a lot. While we might have got into a few arguments from time to time about science, it was always in good spirits, and in the name of science. I also need to thank Olaf Andersen and Radda Rusinova. Olaf and Radda were instrumental in helping me functionally reconstitute ELIC. They took me into their lab for two weeks, and motivated me to keep going on the project.

I should also thank my committee Doug Rees and Shu-ou Shan. I had both as teachers during my first year classes and they eased me into the world of biochemistry. They helped provide a sounding board at my yearly meetings, and made sure that I was on the right track. Both Doug and Shu-ou always provided insight that was unique, and I really appreciated that. Something that I wish I would have done better is build a better relationship with my committee. For those first years that are only reading the acknowledgements, meet with your committee more often than required. Just check-in, say hi, and talk a little science. It is always good to get different perspectives on science.

Another wonderful mentor that I was fortunate enough to get to know was the late John Richards. Jack was the voice of reason during Gray group meetings. He was there to encourage you and support you and your results. I wish I had taken advantage of Jack's mentorship more, he was always eager to help. Group meeting have not been the same since he has passed, and I hope he knows that he is truly missed. Bruce Brunschwig was also always in attendance during Gray group meetings, and I always appreciated all of his comments throughout the talks.

I have had the pleasure of working with many wonderful undergraduates, graduate students, and post-docs over the years here at Caltech in the groups of Harry and Dennis. I am sure I will forget someone but I want to try and thank everyone I overlapped with because in some way or another they helped me. I want to thank the following Gray Group Members: Jillian Dempsey, Bryan Stubbert, Qixi Mi, Hema Karunadasa, Smaranda Marinescu, Mike Rose, Paul Oblad, Paul Bracher, Morgan Cable, Josh Palmer, Alec Durrell, Charlotte Whited, Keiko Yokoyama, Matt Biermann, Yan Choi Lam, Carl Blumenfeld, Brad Brennan, Astrid Mueller, Bryan Hunter, Tania Darnton, Mike Lichterman, Sarah Del Ciello, Brendon McNicholas, Josef Schwan, Judy Lattimer, Daniel Konopka, Nicole Bouley-Ford, Heather Williamson, Gretchen Keller, Seiji Yamada, Peter Agbo, Katherine Lee, Sarah Welhin, Brian Sanders, Emmanuelle Despagne-Ayoub, Wes Sattler, Aaron Sattler, Chris Roske, James Blakemore, James McKone, Maraia Ener, Kana Takematsu, and Jeff Warren. From the Dougherty Group I want to thank Jai Shanata, Erin Lamb, Maggie Thompson, Fan Lui, Nyssa Puskar, Sean Kedrowski, Angela Blum, Kay Limapichat, Ethan Van Arnam, Noah Duffy, Kristina Daeffler, Chris Marotta, Ximena Da Silva Tavares, Tim Miles, Clint Regan, Mike Post, Matt Rienzo, Betty Wong, Matt Davis, D. Paul Walton, Catie Blunt, Annet Blom, Bryce Jarman, Richard Mosesso, and Steve Grant. Both the Dougherty and Gray groups have been a wonderful place to work and that is due in large part to the people listed above. Many good conversations, laughs, and drinks were had with everyone listed above; really what more could you want in life?

I want to call out my year-mates in the Dougherty group: Chris Marotta and Tim Miles. We all joined at the same time and it was fun to share in similar experiences of graduate school with them. I am always impressed with Tim, and his ability to make a project work. Chris is an amazing sincere friend to have, and I am glad I was able to help him out in some way by throwing some parties. Mike Post has been a fun person to talk science with and share secret looks across the table at during meetings. I know he will do great things and wish him the best. I also want to thank Paul and Clint for letting me help out on their project, and being patient and understanding of my unique organic chemistry skill set. It has been fun to work together and I am sure the paper will be published one of these days.

The sub-basement of the Beckman Institute is where I have spent most of my time at Caltech. When I first got here the sub-basement crew was strong. Thank you to you all who welcomed me. Gretchen was the first person I really interacted with, and got me situated in the lab. She is the one who I took over party-planning duties for too; I just hope I lived up to her standards. Peter is one of the most diligent scientists I know, and always was there to answer my questions. Peter, I will never forget our food fights or the midnight hallway golf sessions. Kana was there with me until almost the end. She is one of the perkiest people I know, and was very nice to teach me about many of the laser systems we have. I am sure she is kicking butt at her new job. Brian has been in the sub-basement for a little bit now. It has been fun getting to know him and having him around to bounce ideas off of. He is going to do great work on his little endeavor into biology. Roske is the same year as me in the Gray group, and I have enjoyed our more frequent chats as of recent. He is always excited about science, and has new ideas. James Blakemore became my office mate on his first day. Over the years he helped me with everything electrochemistry, and always was good to chat with over a beer. The Sattler brothers provided endless entertainment and critical questions (always about my NMRs). James McKone is someone I always view as having his life together. He was a big proponent of a well balanced life, and I appreciate all of his advice over the years. I know he is going to dominate Pitt in the years to come. Katherine Lee was a pleasure to work with and reminded me to relax and not take things so seriously. She provided entertainment, and a wit, to go along with the science. Thanks for running all those reactions I never wanted to.

When I first got to lab, I knew nothing. I had never worked with a laser before, grown protein, taken a UV-vis spectrum, anything. Maraia was ever-so patient in teaching me how everything worked in lab, and in the world. She trained me on the laser systems, and being responsible for training people now, I can only imagine how painful that was. I remember wandering the streets of Gernoble with Maraia after we had just gotten into town, only to realize that Sundays in France are different than in LA. Thank you for not eating me in that desperate hungry period before we found food. We ate lunch together, shared many beers, celebrated, and consoled one another, and I look forward to doing many more of that in our future. Thank you Maraia for being so kind, caring, and patient with me over the years.

Um...Dude...Professor Jeffrey J. Warren. So Jeff has taught me many things over the years. He was there to help me through running synthetic reactions, fixing various pieces of equipment (as suspect as those fixes were), and helped me learn how to convey science in a general way. Jeff always provides an honest opinion of how things were, and I appreciate that. Outside of lab Jeff has proven to be a wonderful friend that I have shared many adventures across countries with. We have ridden tanks together in Minnesota, shared an intimate gondola ride in France, and I look forward to the future "Dipshit Adventures Starring Jeff and Oliver." Thank you so much for everything, there isn't anything I can do to repay you.

I need to thank Rick Jackson, Catherine May, and Linda Syme for helping me track down advisors, get forms signed, figure out travel, and everything in between. Rick has been particularly awesome to plan parties with and always knows where the stash of booze is hidden. Thank you to the rest of the fabulous staff in CCE and at Caltech, without them this place would be a disaster.

Outside of lab I have made some friends that have provided some memorable times. I want to thank the CP All-Stars for all of the good times, maybe one of these days you will finally win the championship. Peter Bridi and Karen Oren were very close friends my first year and we experienced a lot of LA firsts together. Esteban Hufstedler was my first year roommate, and is my current roommate. He has been wonderful to live with and I don't even remember half of the times we have spent together. Peter, Karen, and Esteban also introduced me to the engineering students at Caltech and I have enjoyed hanging out with the likes of Jason Rabinovitch, among others. Mike Rauls was always around to help with the car, bike, and grab a beer. Mike is one of the nicest and most genuine people I have met and it is always a pleasure to go on an adventure with him. There have been a lot of fun times had with the following people (not limited to): Sam Johnson, Kevin Fiedler, Sarah Slotznick, Jackie Villadsen, Guy Edouard, Jon Rittle, Artemis Ailianou, Lauren Montemayor, Eric Lubeck, Noah Duffy, and Lisa Mauger. Sam MacMillan, thank you for always being there for one more beer in the courtyard, it really wasn't the same when you left. I also want to thank Brad Moore, Alex Fore, Ron Ocampo, Guillaume Blanquart, Peggy Tautz, and the many other mountain bike friends that I have gone on adventures across the west with. I look forward to the many more adventures I get to share with all of those people and the many more I didn't mention.

I need to thank my undergraduate advisor Ka Yee Lee for taking a chance on me. I also need to thank all my family and friends back home where I grew up. It was the wonderful people on Whidbey Island that got me started on the path I am today. I am sure I forgot people in this rambling section of my thesis. It is not that I am not grateful I just had to end it at some point.

Reeve Dunne was my roommate for four years. He got me into mountain biking, and back into snowboarding. Over the years we have had many crazy adventures: countless late night/early morning drives to try and get fresh snow, driving across the western US in search of the elusive perfect mountain run (on the snow or on a bike), and the various parties we have hosted and crashed are things to be remembered (or forgotten). I will never forget the time we rolled into the Snowbird parking lot at 9am, after driving all night from LA, to ride some of the best snow ever. Ask Reeve about what happened while we were changing in the blizzard for a good laugh. Reeve is someone that I know I will continue to have many adventures in for the years to come. I look forward to the future pointless nights drinking beers, driving across the country for 2 feet of pow, and god knows what else, that I will share with Reeve.

I need to thank my family for the endless support that they have provided during my time at Caltech, but more for their support throughout my life. My sister Hannah is awesome, and she is also a chemist. She has helped me with homework over the years, and my research in more recent years. Thank you for always including me, and inviting me to tag along at all the conferences, you helped me meet so many people and taught me so much. It has been awesome to be able to bounce ideas off of you and I am excited to see where the Shafaat group goes; I know it will be amazing places. My mom, Melanie, moved to Bangkok the year I started at Caltech. She is one of the most adventurous people that I know and I aspire to have the courage and heart that she does. My dad, Tariq, has been down in San Diego these years. It has been nice to be able to have him so close these years, even if it just for a weekend visit. Thank you Mom, Dad, and Hannah, for all the endless support over the years I wouldn't be here without you.

Lastly, and most importantly, I need to thank Sunita Darbe. I honestly do not know what to say here. You are the best thing that has happened to me. Thank you for everything, I cannot wait for the years to come. I love you.

ABSTRACT

Ion channels are a large class of integral membrane proteins that allow for the diffusion of ions across a cellular membrane and are found in all forms of life. Pentameric ligand-gated ion channels (pLGICs) comprise a large family of proteins that include the nicotinic acetylcholine receptor (nAChR) and the γ-aminobutyric acid (GABA) receptor. These ion channels are responsible for the fast synaptic transmission that occurs in humans and as a result are of fundamental biological importance. pLGICs bind ligands (neurotransmitters), and upon ligand-binding undergo activation. The activation event causes an ion channel to enter a new physical state that is able to conduct ions. Ion channels allow for the flux of ions across the membrane through a pore that is formed upon ion channel activation. For pLGICs to function properly both ligand-binding and ion channel activation must occur. The ligand-binding event has been studied extensively over the past few decades, and a detailed mechanism of binding has emerged. During activation the ion channel must undergo structural rearrangements that allow the protein to enter a conformation in which ions can flow through. Despite this great and ubiquitous importance, a fundamental understanding of the ion channel activation mechanism and kinetics, as well as concomitant structural arrangements, remains elusive.

This dissertation describes efforts that have been made to temporally control the activation of ligand-gated ion channels. Temporal control of ion channel activation provides a means by which to activate ion channels when desired. The majority of this work examines the use of light to activate ion channels. Several photocages were examined in this thesis; photocages are molecules that release a ligand under irradiation, and, for the work described here, the released ligand then activates the ion channel. First, a new water-soluble photoacid was developed for the activation of proton-sensitive ion channels. Activation of acid-sensing ion channels, ASIC2a and GLIC, was observed only upon irradiation. Next, a variety of Ru^{2+} photocages were also developed for the release of amine ligands. The Ru^{2+} systems interacted in a deleterious manner with a representative subset of biologically essential ion channels. The rapid mixing of ion channels with agonist was also examined. A detection system was built to monitor ion channels activation in the rapid mixing experiments. I have shown that liposomes, and functionally-reconstituted ELIC, are not destroyed during the mixing process. The work presented here provides the means to deliver agonist to ligand-gated ion channels in a controlled fashion.

PREFACE

Dear Reader,

The work I carried out in graduate school started with a very interesting idea: to monitor how ion channels open. The goal is to observe the physical motion of an ion channel under activation; more specifically, I wanted to monitor activation of a pentameric ligand-gated ion channel (pLGICs). pLGICs are a large family of receptors that include the biologically important nicotinic-acetylcholine receptor (among others). Ligand binding results in the activation of the ion channel allowing ions to diffuse across the cell membrane through the channel. The Dougherty group has studied the binding event of pLGIC receptors for decades, but the gating event was less well characterized. I wanted to look at the activation of pLGICs using time-resolved fluorescence energy transfer (TR-FET), a technique that had been developed in the Gray group to monitor conformational changes during protein folding (Figure 0.1). Easy, right? All I had to do was express, label, reconstitute, and trigger ion channel activation and then boom goes the dynamite!!!

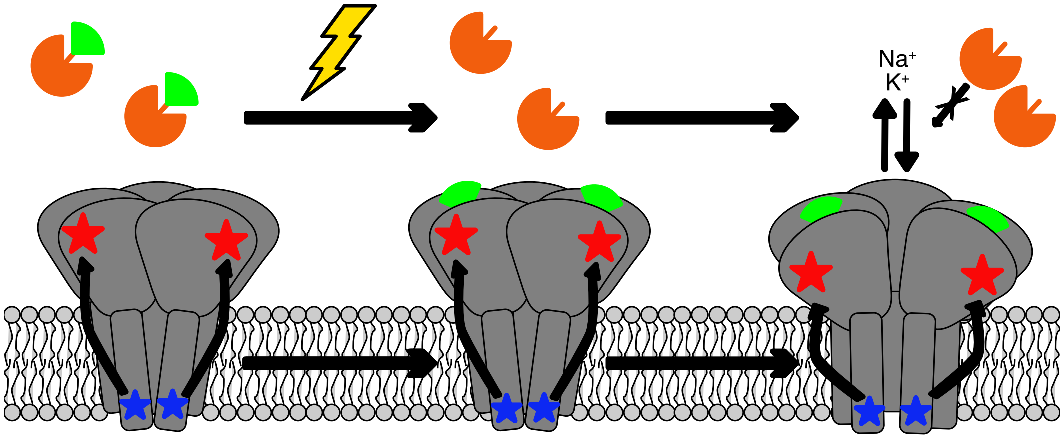

Figure 0.1: A cartoon scheme outlining the motivation for this thesis. pLGICs (gray, bottom) are labeled with a donor (blue star) and acceptor (red star). Without agonist bound, the ion channel is closed. A photocage (orange semicircle) is bound to a protected agonist (green wedge) in solution, and the ion channels are closed. Upon irradiation (lightning bolt) the photocage releases the agonist, the agonist binds the ion channel (bottom middle), and the photoproduct (orange semicircle) remains in solution. After some time, activation occurs (bottom right) resulting in a conformational change in the ion channel. Ion flux can occur and the fluorescence energy transfer between donor and acceptor changes. The conformational change is read out as a change in donor lifetime upon activation, allowing for the distance change to be quantified.

At the start of my research, the project seemed attainable for several reasons. The technology for expression and purification of pLGICs existed. Prokaryotic pLGICs had been recently discovered, which allowed for overexpression of protein in *E.coli*. This resulted in the first high resolution crystal structures of pLGICs, and meant I would be able to obtain enough protein with which to perform experiments. New and more efficient bioorthogonal labeling techniques were being developed meaning I could label the ion channel with the necessary two fluorophores that are needed for TR-FET. I quickly realized that the main hurdle, assuming that I could adapt the other protocols as needed, was the ability to control the activation of the ion channels. TR-FET measurements are ensemble measurements; to get specifics of ion channel gating, one has to know what stage of gating the ion channel is in. No agonist results in a situation where all the channels are closed; if ligand is present in excess, some channels would be open, some would be desensitized, and some might be in any number of hypothesized states that ion channels can exist in. The goal is to watch the movements from closed to open and observe any intermediates in between, which is not possible without precise knowledge of the timepoint at which activation occurs.

This need to control the activation of ion channels drove my research at Caltech and gives the title to my thesis. I knew that none of the most important experiments that were designed to monitor conformational changes could be done if I could not activate ion channels with precise control. I brushed aside the other requirements of the project with the hubris that only exists in a new graduate student. In hindsight, this was a terrible idea, because if I had developed a method of activation, I would still need to express, purify, and functionally reconstitute the ion channels. None of those tasks are trivial, as I would learn later. Regardless, I would ignore those requirements of the project in an attempt to develop methods to trigger activation of ligand-gated ion channels.

In the brain, agonists are delivered into a bulk solution, diffuse to the ion channel, bind, and then activate the channel. For monitoring the activation of ion channels I need to control the delivery of ligand precisely; the delivery also needs to occur faster than the activation process. Ideally delivery of ligand would occur on the single millisecond timescale, ruling out simple addition of ligand to a solution. Mixing of two solutions can take place faster than a millisecond, and will be discussed in Chapter 4. The main focus of this thesis is use of light to trigger ligand delivery. This is in part because both the Gray and Dougherty groups have expertise in photochemistry. Also the color, intensity, length of exposure, and arrival time of light can be precisely controlled. Photochemical cages have also been used previously in biology and chemistry; the idea was to adapt a previous cage for the activation of pLGICs. What could go wrong?

Any photochemical trigger used for ion channel activation must be compatible with the ion channel environment. Ion channels are integral membrane proteins. This requires that any compound used must be water soluble; I am not able to work in acetonitrile, or any other organic solvents. It would also be useful if the compound is stable to dioxygen, but this is not a strict requirement. Working in an inert environment is possible, but O_2 sensitivity limits the generic applicability of any photochemical trigger developed. It would be nice, after all, if any new photocage that is developed can be used for other applications. Activation by visible light is also preferred; UV irradiation can result in damage to proteins (sunburns come to mind) and should be avoided if possible. There are many established photolabile protecting groups that fit these requirements, and adaptation of some will be discussed below.

The compatibility of the photocage with pLGICs must also be examined. For the photocage to be useful it must not perturb the ion channel in any way. Most of my research at Caltech dealt with examining the biocompatability of various photocages. The photocage, in the dark, must not activate the ion channel. The phototriggered release of the ligand must occur with high yield and faster than the timescale of activation. Ion channel activation, monitored by single-channel electrophysiology, appears as a step function with the time resolution of one millisecond. If the yield of ligand release is poor, all the ion channels will not be activated, which will complicate the TR-FET analysis. Likewise, if the ligands are released on the timescale of activation, the ligand-binding event and the ion channel gating event will be convoluted. After the ligand is released, the photocage minus the ligand (the photoproduct), will still exist in solution. The photoproduct must not interact with the ion channel. Perturbation of the ion channel will not provide measurements representative of native ion channel activation. I found, throughout the course of my work that the development of photochemical cages that do not, in any manner, interact with ion channels is extremely difficult. I was able to use many different systems to activate the ion channel, which in some manner also inhibited the ion channel.

The aim of this thesis is to share with you, the reader, the successes and failures of the work that I have done on this project. I will motivate the work in the introduction. The hope is that I will be able to sell the project one tenth as well as Harry Gray did in our first meeting together. I will then outline the status of methods used in my project. I will discuss the various successes I have had with the photoactivation of acid-sensitive ion channels (Chapter 2). In Chapter 3, I follow this up with the discussion of using ruthenium coordination complexes as photocages for the activation of ion channels. I discuss the work that has been done to functionally reconstitute ion channels in Chapter 4. Using the functionally reconstituted channels I will discuss a brute force approach to ligand delivery, ultra-fast mixing, and the prospects of that work (Chapter 5). I believe that I have been able to lay the groundwork upon which this project could move forward, however I caution anyone who is foolish enough to try. The ultimate goal of this project (and beer) is what has driven me throughout my thesis, and I only regret taking on the challenge a little bit. I will watch the field with much anticipation to see the advances made and hopefully someday will be able to see someone succeed.

Sincerely,
Oliver Syed Shafaat

TABLE OF CONTENTS

LIST OF ILLUSTRATIONS

LIST OF TABLES

Chapter 1

INTRODUCTION

1.1 Introduction

Ion channels are membrane proteins found in all forms of life that provide a path for passive diffusion of ions from one side of a cell membrane to the other. Ion channels can be voltage-sensitive, and open with changes in the potential that is applied across the membrane. Ligand-gated ion channels bind a ligand, a naturally occurring neurotransmitter or a recreational drug for example, and after binding of the ligand open. Finally, mechanosensitive ion channels respond to the changes in the mechanical forces of the membrane. After an ion channel is triggered, opening occurs and ions (different ion channels are selective for different ions) flow through.

My primary interest is ligand-gated ion channels. This family of ion channels is involved in fast synaptic transmission between cells, or in other words, intercellular communication. As a result, it is of vital importance to understand how these ion channels function. For a ligand-gated ion channel to function properly, a ligand has to bind (e.g a neurotransmitter for native cellular signaling), and then the ion channel has to open. The ligand-binding event is a a reversible process where the ligand can bind, and dissociate. The ion channel gating event occurs only in a ligand-bound state, and as monitored by electrophysiology, occurs in at least one millisecond. Many groups, including the Dougherty group, have studied the ligand-binding event. Through the use of structure-function studies, the Dougherty group has been able to understand the binding mode of many different ligands to a variety of receptors. The ion channel activation event remains more elusive. After ligand binding, changes have to occur that create a state in which ions can flow through the ion channel. These changes result from physical conformational changes in the protein structure. The ion channel activation event is really an unanswered question. How does the ion channel go from blocking ion flux to allowing ions to flow? The goal of understanding this fundamental, and essential, process in ion channel function is what has motivated this thesis.

1.2 Pentameric Ligand-Gated Ion Channels

The pentameric ligand-gated ion channels (pLGICs) are a large family of ligand-gated ion channels [1, 2]. Members of the pLGIC family include the cation selective nicotinic acetylcholine (nAChR) and 5-hydroxytryptamine (5HT3, or serotonin) receptors, and anionic γ-aminobutyric acid (GABA) and glycine (GlyR) receptors. pLGICs play a crucial role in fast synaptic transmission and proper function requires at least two events to occur: ligand (also called an agonist) binding and ion channel opening [3]. Synaptic signal propagation results from the release of neurotransmitters at the axon of one nerve cell, the neurotransmitters then diffuse across the space between two cells to the dendrite of the next cell. The ion channel then binds a specific neurotransmitter and after binding the ion channel will open and ions will flow through. This event allows for further propagation of the signal. Both ligand binding and ion channel gating must occur for the protein to function properly.

Since pLGICs were first identified, work by many labs on the biochemistry and physiology of these receptors has been carried out. The most studied receptor is the nAChR; a good source of these channels is the electric plaques of *Torpedo californica*. This abundant natural source of nAChRs allowed for the study of these proteins before many of the molecular biology techniques we now take for granted even existed.

A pLGIC is made up of five segments (subunits) that self-assemble into a pentamer. pLGICs can either be homopentameric (five identical subunits) or heteropentameric (two or more different subunits) depending on the specific subtype. Each monomer consists of a large extracellular domain, a transmembrane region, and a cytoplasmic domain (Figure 1.1a). The extracellular domain contains the ligand binding site. The transmembrane domain consists of four helicies, with helix 2 (M2) of each monomer forming the pore. The cytoplasmic domain is highly variable between receptors and is known to effect downstream signaling (Figure 1.1b). pLGICs allow ion flow through the pore only in a ligand-bound state; upon ligand binding, the ion channel opens. The ligand binding event somehow signals the opening of the pore, located tens of angstroms away from the ligand-binding domain and in the transmembrane region.

pLGICs can exist in many different states, three states will be discussed below. The ion channel also can be in a closed state without a bound ligand (also referred to as a resting state); ion flux does not occur in the resting state. Ligand can bind, open the ion channel, and allow ion flow, known as the open state. I use the terms open, activate, and gate interchangeably in this thesis. The ion channel can also be in a ligand-bound non-conducting state, the so-called the desensitized state [1–4]. There are many other states of the ion channel that have been suggested in complicated analyses, but for the sake of this thesis, only the three states above will be considered.

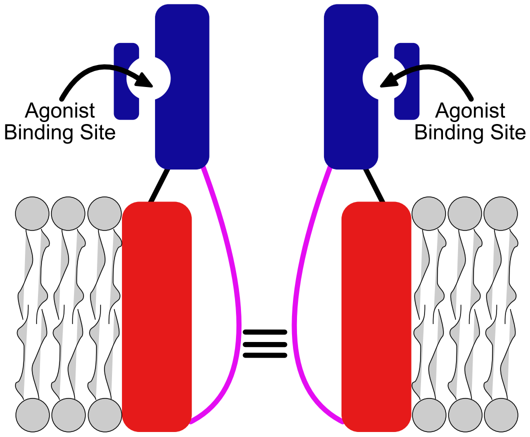

(a)

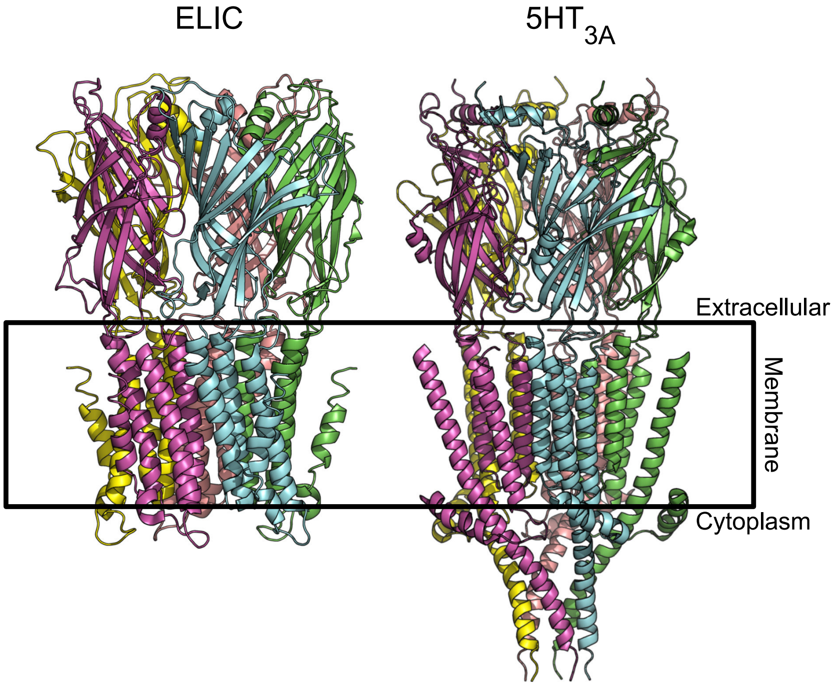

(b)

Figure 1.1: (a) The general architecture of pLGICs, with only two subunits shown for clarity. The extracellular domain (blue) contains the agonist binding pocket, and is connected to transmembrane domain. The transmembrane domain (red) has four helices, with the second helix (magenta line) lining the pore. The ligand-binding site is tens of angstroms away from the gate (horizontal black lines). Upon ligand binding, the gate has to open to allow ions to flow through. (b) The crystal structures of ELIC (left, PDB code 3RQW) and the mouse $5HT_{3A}$ receptor (right, PDB code 4PIR) shown. Each monomer is a shown as a different color. From the crystal structures, the large extracellular domain (above the black box) is seen. The transmembrane region (black box indicating where the membrane would be) consists of four helices per monomer. The serotonin receptor has a cytoplasmic domain (below the box), while ELIC does not.

The ligand binding event has been extensively probed by the Dougherty group and many others over the past 20 years. The Dougherty group has used unnatural amino acid mutagenesis to probe ligand binding (see [5] for a good review on the method). Amino acids are chemically synthesized, allowing for subtle changes in amino acid structure and enabling detailed structure-function studies. The unnatural amino acid is incorporated at the residue of interest using nonsense suppression methodology. In a variety of examples, the group provided detailed binding mechanisms for many drugs and channels. One example provided insight into the differences in binding of nicotine and the native agonist acetylcholine to nAChRs [6, 7]. Structure-function studies showed that a cation-π interaction drives the binding of acetylcholine to the nAChRs [4, 8]. nAChRs are found at the neuromuscular junction and involved in every muscle movement that we (humans) make. nAChRs are also located in the brain, and responsible for the reward properties that accompany smoking a cigarette. The Dougherty group showed that the affinity for nicotine of the muscle-type receptor is different from that of the neuronal subtype [6, 7, 9]. Nicotine does not make a cation-π interaction with the muscle-type receptor, whereas in the primary neuronal nAChR subtype, a strong cation-π interaction between nicotine and nAChRs exists. The muscle-type nAChRs are not activated by nicotine ingested by smoking [9], explaining why paralysis, among other effects, is not observed every time someone smokes tobacco. This is just one example of the extensive work that has been done to examine the properties that drive ligand binding to pLGICs.

Investigation into the gating event of pLGICs has proven more difficult. Using similar methodology as above, cis-trans isomerization of a proline located at the interface of the extracellular domain and the transmembrane domain was shown to be crucial for the gating of the $5HT_{3A}$ receptor [10]. Unfortunately, direct structural information is difficult to obtain because ion channels are membrane proteins and isolation and *in vitro* structural analysis methods (such as crystallography) are very difficult. Very recently high-resolution structural information of pLGICs has emerged [11–16]. Prior to the X-ray structures, Unwin was able to resolve a 4 Å structure of the electric ray nAChR using electron microscopy (EM) [17, 18]. The EM structures initially provided the general topology, and information about the side chains at higher resolution. The EM structures were solved in the absence of ligand; a picture of a single state provides minimal insight into the transition between states. An acetylcholine binding protein (AChBP) had also been isolated and structurally characterized [19, 20]. This protein shares some sequence homology to the extracellular domain of the nAChRs, and importantly binds acetylcholine.

Crystal structures of AChBP confirmed many of the ligand-binding results previously obtained with structure-function studies. Prokaryotic homologs were the first members of the pLGIC family that were crystallized [11–13, 21]. Structures of two different homologs were solved in different proposed states and comparison of these two structures provided the first direct evidence for the conformational changes that occurred during the gating process.

The pLGICs that are the focus of this thesis are the two prokaryotic proteins, Erwinia ligand-gated ion channel (ELIC) and Gleobacter ligand-gated ion channel (GLIC). ELIC and GLIC were predicted to be prokaryotic homologs of pLGICs through a large bioinformatics screen [22], and have about 20% sequence homology with the nAChRs. ELIC and GLIC were both structurally and functionally characterized. The crystal structures of ELIC and GLIC were the first high resolution structures of pLGICs and showed close structural similarities to Unwin's EM structures of nAChR [11–13, 17, 18]. ELIC and GLIC are pentameric, with a large extraceullular domain, and four transmembrane helicies with the M2 helix of each subunit lining the pore. While structural homology is important, functional homology is also needed to be a good model system. Both GLIC and ELIC are monovalent cation selective channels and are blocked in a similar fashion as the eukaryotic homologs (divalent cations and NR_4^+ ions for example) [21, 23]. GLIC is activated by an increase in extracellular proton concentration, making GLIC a proton-gated ion channel. ELIC is activated by small molecule amines, such as cysteamine, propylamine, and GABA. The functional and structural similarities of ELIC and GLIC with the cation-selective members of the pLGICs family, make these ion channels a good model system to study activation of pLGICs.

1.3 Investigation into Ion Channel Gating

The difficulty in elucidating the mechanism of gating of ion channels lies largely in the nature of the proteins themselves; ion channels are membrane proteins. At the onset of my research, the only information about the conformational changes associated with pLGIC gating was a result of the crystal structures of ELIC [11], in the presumed closed state, and GLIC in the presumed open state [12, 13]. Ion channel activation is a dynamic process, and the crystal structures provided snapshots of the potential end points of that process. We want to monitor channels during the gating event using dynamic methods.

Many more high resolution X-ray structures have been solved for members of the pLGIC family since I started this work. Structures of GLIC and ELIC have now been solved under many different conditions: agonist present, antagonist present, potentiators, inhibitors, etc. [23–25]. More recently mammalian serotonin and glycine receptors, as well as nematode GluCl, were crystallized [14–16]. With the surge of structures solved by single-particle cryo-EM, it will not be long until many more members of the pLGIC family are solved. With a relatively large number of pLGIC structures available (recall no structure existed until 2008), comparison of structures provides some of the first insight into the gating mechanism of pLGICs. Each structure is of the channel in a presumed state given the crystallographic conditions. GLIC is a pLGIC that has X-ray structures in many different proposed conformations. Comparison of the same protein provides the safest analysis of ion channel movements between states; the crystal structure of the same ion channel affords direct comparison of the structural changes. Delarue and coworkers were able to solve GLIC at pH 7 [24]. GLIC is a pH-sensitive ion channel that is not activated at pH 7, and the structure is assigned to the closed form. The structure of GLIC in the presumed closed state exhibited some disorder, suggesting that the closed state is dynamic. The closed structure of GLIC is compared with the low pH, open, structure and provides a model for gating in Figure 1.2. The extracellular domain becomes more rigid in the open structure, a twisting and a blooming motion of the extracellular domain occurs during the transition from closed to open. The extracellular domain is coupled to the transmembrane domain through motions in the transmembrane helices. The M2 helix bends away from the pore, causing a widening of the upper region of the pore in the open structure. The functional state of GLIC is not known, but presumed. This is an issue in applying differences observed in X-ray structures to the gating problem. Enzymatic reactions of proteins in crystals have been used to show the functional nature of the protein structure [26]. The mointoring of ion flux through the ion channel would need to occur to examine the functional state of ion channels in a crystal. Regardless, the crystal structures that have been solved provide some of the best experimental insight into a potential gating mechanism.

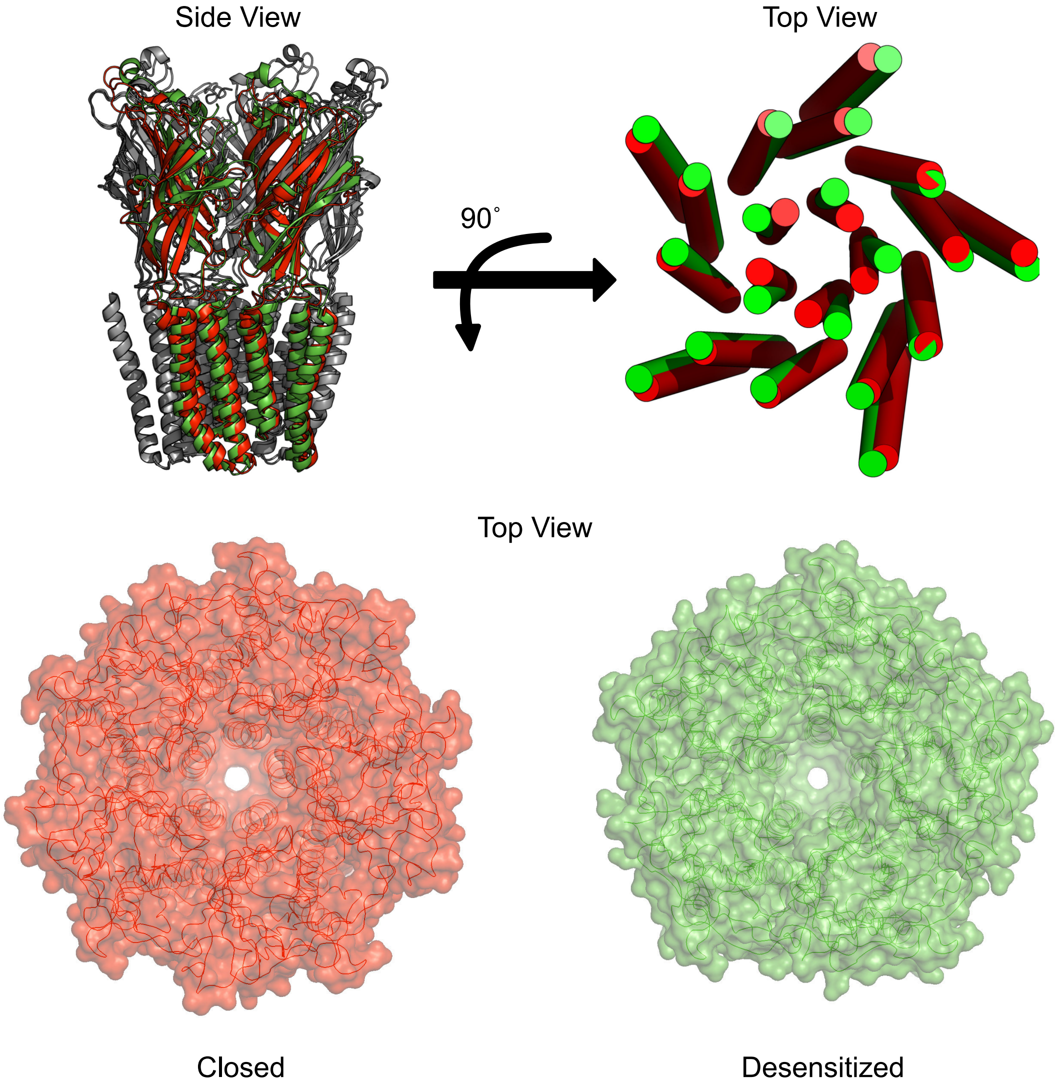

Figure 1.2: The overlaid structures of GLIC in the closed state (red, PDB code 4NPQ) and the desensitized state (green, PDB code 4NPP). Overlaying the closed and open structures of GLIC provides insight into the gating mechanism. The transmembrane helices (top right) show a large motion of the M2 helix that lines the pore. A rotation and slight outward bend of the top of the M2 helix occurs from the closed to desensitized state. The extracellular domain undergoes a rotation, as well as a inward motion. The space-filling models (bottom) highlight the compact extracellular domain in the desensitized state (green) as well as the slight opening of the top of the pore.

Long timescale molecular dynamics (MD) simulations can monitor large-scale conformational changes of ion channels. MD simulations are being used for large scale protein simulations with X-ray structures of ion channels providing the starting point for the simulations. The channels are perturbed *in silico*, and resulting structural changes are monitored. Since ion channels are membrane proteins, simulations require not only the whole 300 kDa protein structure, but the addition of a simulated membrane environment. As a result of the size, MD simulations of ion channels are very computationally expensive. Recently, specialized computers designed for MD simulations have become available enabling long timescale simulations, on the order of 100s of μs to ms to be performed [27]. These computers have been used for the study of large membrane proteins such as ion channels which require long simulation times. Recall that activation of ion channels does not occur on the ns timescale. Work done at the D.E. Shaw Institute used MD simulations to monitor the activation of voltage-sensitive ion channels [28]. *In silico* membrane potential reversal, an event used to open voltage-sensitive ion channels, reveals large movements of the voltage-sensing domain. These MD motions are consistent with the results obtained from experimentally monitoring the voltage-sensing domain under activation. These movements were only observed under conditions of a hyperpolarized membrane environment, an environment where the ion channel is experimentally shown to be open. Little large-scale structural motion is observed on the nanosecond timescale, highlighting the importance of the long MD simulations. Conformational changes associated with ion channel activation were observed. This work was not performed on pLGICs and measurements of pLGICs in the presence of an agonist might provide insight into the movements of the ion channel during activation. Like crystal structures, the MD simulations provide valuable guidance for experiments. In our experiments, we want to observe ion channel activation in a functional, physiologically relevant environment.

Another technique used to investigate ion channel activation is electron paramagnetic resonance (EPR) spectroscopy. Spin-labeling of GLIC M2 pore residues allowed for the comparison of the continuous wave EPR signal in the closed or desensitized state. The EPR line shapes were monitored under a resting and desensitized state of GLIC. Changes in the EPR signal result from different coupling to the different spin-labels in the system. Broadening of the lineshape is assigned to the decrease in distance between spin-labels, and conversely narrowing indicated that the spin-labels move apart. Chakrapani and coworkers showed that in transition from the closed to desensitized state, the top of the pore moves outward, while the bottom of the pore clamps in [29, 30]. In the desensitized state GLIC is non-conducting; closure of the bottom of the pore would prevent ion flux through the channel.

PELDOR (pulsed electron-electron double resonance), or DEER (double electron-electron resonance) are pulsed EPR techniques that also have been used to monitor ion channel activation. Proteins are spin-labeled through site directed mutagenesis, and the dipolar coupling between the two unpaired spin labels is measured. The dipolar coupling between spin-labels enables PELDOR to be used to evaluate of distances between the spin labels from 1 nm to 10 nm [31]. The gating of GLIC has been investigated using PELDOR. Czajkowski and coworkers labeled GLIC at several different positions on the protein and examined the conformational changes that occurred during the transition from closed to desensitized state [32]. Large motions were found at the interface of the extracellular domain and the transmembrane domain, showing that the closed and desensitized state are structurally distinct. The PELDOR measurements provided direct physical measurements of GLIC in the closed and desensitized state. The closed state structure obtained from PELDOR also suggest that ELIC is not a good structural model for the closed state of GLIC. PELDOR measurements were performed on purified, reconstituted GLIC shown to be functionally similar to *in vivo* GLIC. However, PELDOR measurements are performed at 80K, a temperature where the ion channels are not functionally active. This allows PELDOR to provide snap-shots of the gating events of functional ion channels.

Single-molecule FRET (SM-FRET) measurements have been used to monitor ion channel activation. SM-FRET measurements have been made simultaneously with electrophysiology measurements, allowing the SM-FRET signals to be assigned to a known state of the ion channel as reported by electrophysiology. Lu and coworkers applied SM-FRET and electrophysiology to the NMDA receptor, a member of the ionotropic glutamate receeotors [33]. The NMDA receptor is a ligand gated ion channel that belongs to a different family than the pLGICs described above. NMDA receptors were expressed in cells, and labeled with donor and acceptor fluorophores. The activation of the receptor was then monitored by both single-molecule electrophysiology and SM-FRET. Measurements showed a single FRET efficiency associated with the conducting state of the NMDA receptor. However, unique insight into the non-conducting state was also elucidated. Electrically silent states of the NMDA receptor showed at least two distinct SM-FRET conformations. This highlights the ability of FRET to provide information on distinct states that are indistinguishable by electrophysiology. These measurements were used to correlate the electrical and optical signals, and provide information about the conformational organization of the ion channel. The time resolution of SM-FRET is the same as that of the single-channel electrophysiology, on the order of one millisecond. While end states can be observed, information about the transition between the states remains elusive.

Time-resolved energy transfer techniques have been used to monitor the conformational changes associated with ion channel gating. Selvin and coworkers employed luminescence resonance energy transfer (LRET) to study voltage-sensitive ion channels during activation [34–36]. Voltage-sensitive ion channels open under change in the polarization of the membrane, accomplished routinely in electrophysiology. LRET uses a lanthanide donor with a millisecond lifetime, to sensitize the emission of a fluorescent dye acceptor. The LRET donor and acceptor are attached, through site specific labeling to the ion channel. Relative changes in the distance between donor and acceptor are extracted from lifetime measurements of the sensitized emission. Using LRET to monitor the relative change in the distance of various parts of the voltage-sensing domain, Selvin and coworkers observed slight movement in the voltage-sensing domain of 3.2 Å between the closed and activated state. Using a basic geometric analysis, this movement was assigned to a rotation of a helix and a slight vertical (perpendicular to the membrane) displacement. Follow-up work used LRET to test the gating hypothesis of another voltage sensitive ion channel. Selvin and coworkers were able to show that, contrary to the hypothesis, only small movements of the ion channel occurred during activation. Conducting the LRET measurements on ion channels in an *in vivo* environment allows for the ion channel to be in a native environment; a strength of this system is using an environment where the physiology of the ion channel is well characterized. LRET provided information about the conformation of voltage-sensitive ion channels under activation, and I hope to use a similar technique to monitor pLGIC activation.

The method that we want to use is time-resolved fluorescence energy transfer (TR-FET), a method similar to LRET. TR-FET was used previously to monitor large conformational changes that occurred during protein folding. Winkler and coworkers were able to show that during the folding of a small, soluble protein, some regions folded in a two-state fashion, while some regions folded with an additional intermediate state [37–40]. This study monitored the transition from the fully unfolded state to the native state of the protein, where the LRET measurements above examined only either the open or closed conformation. TR-FET measurements will allow monitoring ion channels during the transition process between closed and open states. Because we will study ligand-gated ion channels, this requires precise delivery of the ligand at a known time. Methods to accomplish this will be discussed later and are the focus of this thesis. The TR-FET measurements will be performed on ion channels that are functionally reconstituted in order to probe activation in a near-native system, much like the LRET oocyte measurements. The TR-FET measurements enable us to monitor the ion channel activation of a functional ion channel during the transition from closed to open.

1.4 Photocages: A Method To Deliver Ligands

I want to use TR-FET, an ensemble measurement, to monitor the conformational changes associated with ion channel activation. Measurements in the absence of agonist will provide pictures of the closed state; likewise, measurements made in the presence of agonist will provide a picture of either the open or desensitized state. This work aims to provided insight into the transition from closed to open. To accomplish this, we need to precisely control delivery of agonist in order to control the activation. Photocages are used in this study to deliver ligands upon irradiation of a compound. I want to release small-molecule amines or protons for the activation of ELIC or GLIC, respectively. Many native neurotransmitters (GABA, serotonin, glutamate, etc.) are small molecule primary amines. In addition, compounds that release propylamine for the activation of ELIC have potential to be generically applied for release of other neurotransmitters. To activate GLIC, we release H^+ using a type of photocage commonly referred to as a "photoacid." Photocages are used to activate pLGICs in an effort to control the precise timing of agonist delivery.

To monitor the ability of photocages to activate ion channels whole-cell voltage-clamp electrophysiology will be used. ELIC or GLIC (or any other ion channel of interest) will be expressed in *X. laevis* oocytes. Two electrodes are then injected into the oocyte, and a potential is set (-60 mV vs. ground in my experiments) across the membrane. Changes in the membrane potential are measured and a feedback loop adjusts the current needed to keep the potential at the set value. No perturbation to the system results in a constant current reading seen in Figure 1.3 (black line) under the left magenta buffer box. Application of agonist (Figure 1.3, black box) activates the ion channels, resulting in ion flow into the cell. A current change is needed to keep the potential at the set value and reflected as the downward reflection of the black line in Figure 1.3. This current change indicates that ion channels are activated. Removal of the agonist (Figure 1.3, right magenta box) results in closing of the ion channels, and a return to the baseline current required to hold the potential constant. If the ion channel studied enters the desensitized state, ions no longer flow through the channel when agonist is present. This results in a decrease in the current observed to hold the potential at the set point (Figure 1.3, red line). Any photocage in the dark should not activate the channel (i.e. the photocage should not be an agonist), and application of a photocage will not result in an observed current change (Figure 1.3, orange line). In other words, activation of the ion channels should occur only under irradiation of the photocage. If the photocage is irreversible, each irradiation (Figure 1.3, blue line) should result in release of agonist, and activate some ion channels. The activation is reflected in the change in current seen at the point of each irradiation (lightning bolt). Further irradiation results in release of more agonist, and thus more activation of ion channels. A reversible photocage will activate the ion channel under irradiation (Figure 1.3, green line), but after irradiation stops, the ion channels will close as the photocage undergoes the re-binding of the agonist. In all cases the current required to hold the membrane potential at the set value should be the same before and after manipulation (Figure 1.3, magenta bars). The above mentioned examples are the most straightforward cases of ion channel activation.

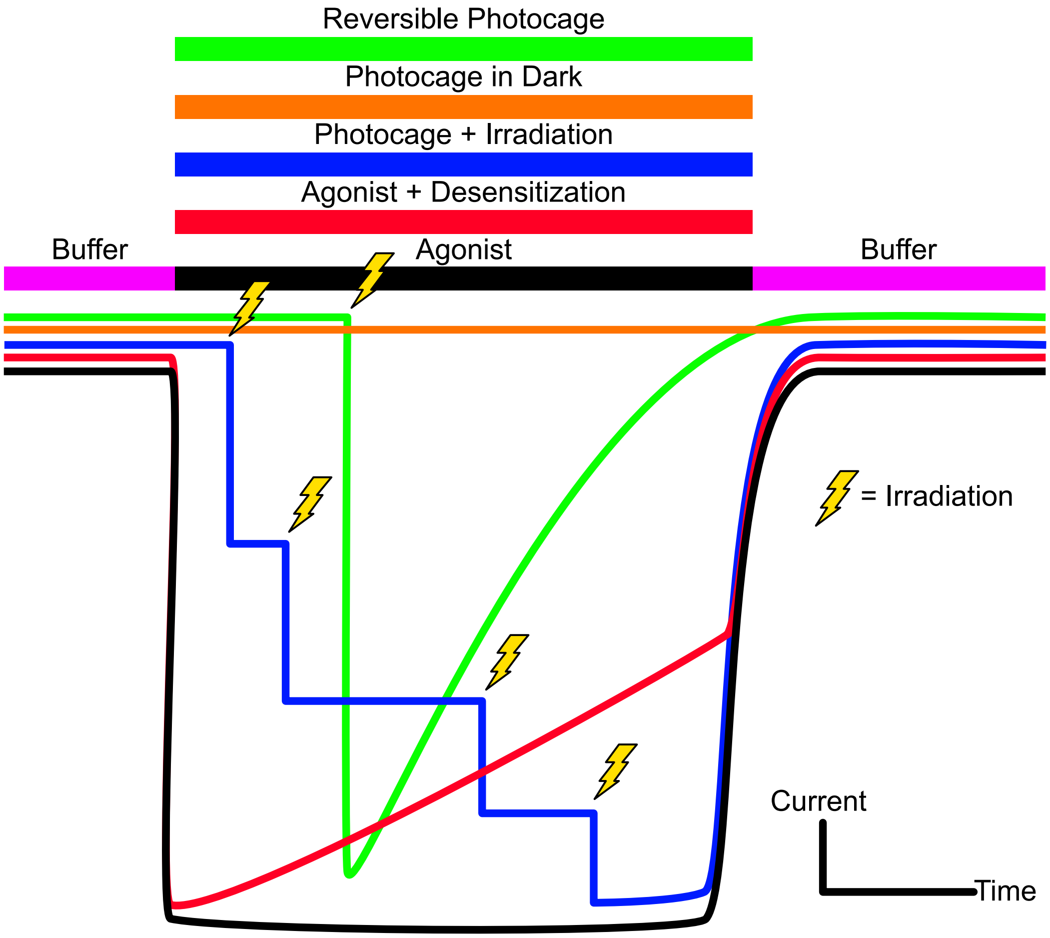

Figure 1.3: The ideal electrophysiology response to ion channel activation under a variety of conditions. Each trace is vertically offset for clarity. Application of agonist alone will result in a large increase (negative in the experimental setup) in current (black line) that remains until the agonist is removed when the buffer is exchanged (denoted by a return to baseline). Ion channels can undergo desensitization (red line). Full activation is observed, however under prolonged exposure to agonist the signal decreases before the buffer is exchanged. Application of the photocage will result in activation of the ion channel under irradiation only (blue line). An irreversible photocage will result in activation at each irradiation event (yellow lightning bolt). More activation will be observed until all the ion channels have been activated. After, the buffer is exchanged and the signal returns to baseline. Photocage applied without irradiation (orange line) will not result in any activation. A reversible photocage will activate ion channels under irradiation only (green line). After irradiation stops, the released agonist will rebind the photoproduct, and result in a decrease in signal observed. In all examples the signal before and after manipulation should be the same, indicating that there is no prolonged effect of the ion channel.

A few general considerations must be applied to any potential photocage (Figure 1.4). To study the activation of ion channels requires that the photocage be soluble in water and stable to air. The photocages must also be triggered by visible light. Irradiation by UV light can cause oxidation of proteins, which could alter the ion channel properties. The light-triggered release of agonist must be faster than ion channel activation. Ligand release and ion channel activation become convoluted if the rate of release is slow. The quantum yield for release of agonist under irradiation must be high; low quantum yields diminish potential for signal to be observed over background. Finally, and in my opinion, the most important requirement for any photocage (or its product) is the absence of any interaction between the photocage and the protein.

Irradiation of the photocage, should release the caged molecule, which will activate the ion channel (Figure 1.3, blue and green line). Any interaction of the photocage, or the molecule that remains after release (photoproduct), with the ion channel results in perturbation of the ion channel out of the native form. To probe for potential interactions, the photocage (or photoproduct) is applied to ion channels in the presence of additional free agonist. Application of photocage with agonist (Figure 1.4, black outlined boxes) should activate the ion channel as just agonist alone (1.4, black line). No interactions between the photocage (or photoproduct) and the ion channel are outlined with the blue and purple lines in Figure 1.4. The current with any agonist present is the same as just the agonist current alone. Perturbation to the ion channel will result in a decrease in the observed current (Figure 1.4, green and orange lines). Any perturbation renders the photocage useless in the study of ion channel activation. In the following section, I discuss the use of two different photocages that are relevant towards the research in this thesis: ruthenium-polypyridyl photocages and photoacids.

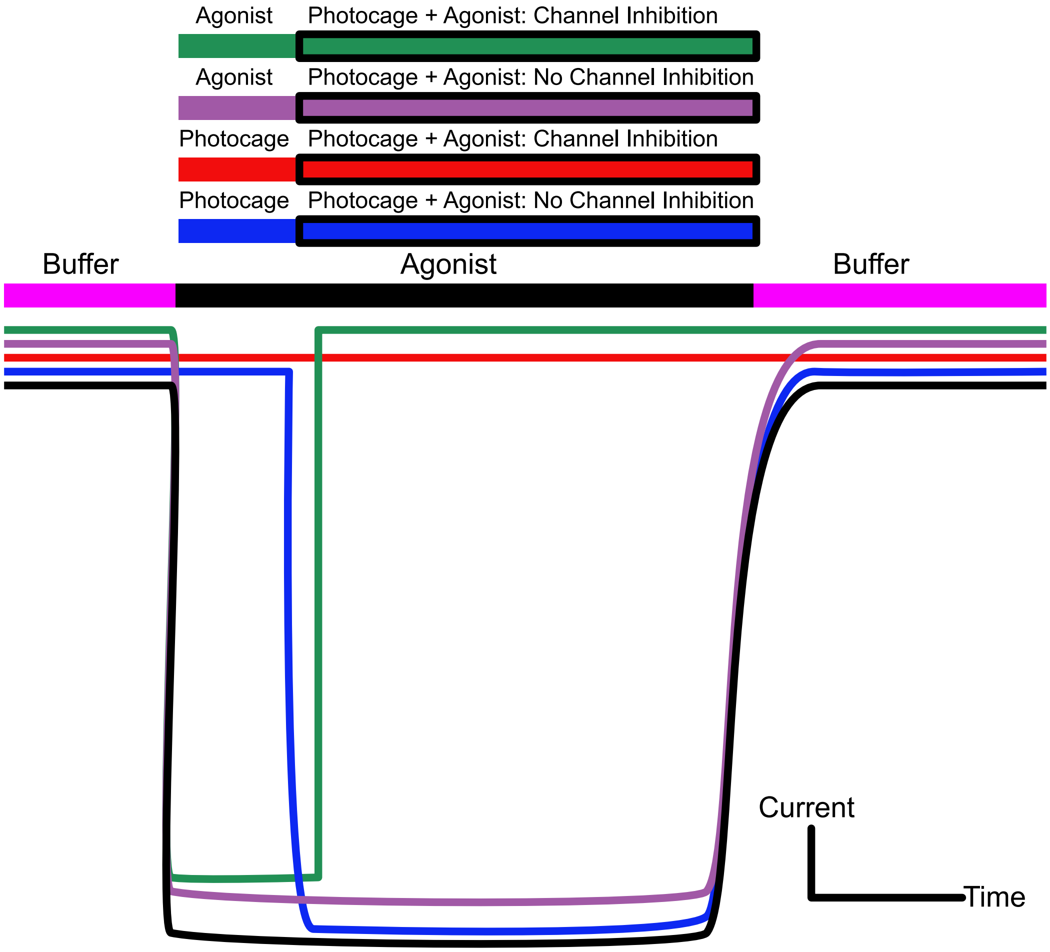

Figure 1.4: The ion channel electrophysiology response to agonist along (black line). Activation is only observed in the presence of agonist, and when the buffer is exchanged (magenta bar), the signal returns to baseline. The photocage, or photoproduct, in solution (blue and orange lines) with the ion channel in the absence of agonist does not result in any signal observed, indicating that the photocage, or photoproduct, does not activate the ion channel alone. Following pre-incubation, application of the photocage, or photoproduct, with agonist will result in a current change (blue line, blue bar with Black outline), to the level of activation without photocage (black line). If any deleterions interaction exists between the photocage and the ion channel, a different signal will be observed upon co-application of agonist and photocage (orange line). To monitor for interactions with open ion channels, the ion channel is activated prior to photcage exposure (purple and green lines) and displays similar currents to the agonist alone application. Application of photocage with agonist following ion channel activation results in the same signal observed (purple line) if no interaction is observed. If the photocage (or photoproduct) somehow interacts with the ion channel a change in current will be observed (green line), shown as inhibition in this example. After the buffer is exchanged, the signal should return to baseline indicating no persistent interactions between the molecules and the ion channel. The photocage, or photoproduct, is not useful if any inhibition of the ion channel occurs (signal less than the agonist alone, black line) in the presence both photocage and agonist (orange and green lines). Each trace is vertically offset for clarity.

1.4.1 Use of Ruthenium Complexes for Photocaging Amines

Ru^{2+}-polypyridyl complexes are known to undergo efficient visible-light photodissociation of amine ligand, and motivated my use of Ru^{2+} as a photocage for the temporal control of ion channel gating [41]. $Ru(bpy)_2(L)_2{}^{n+}$ complexes have been used previously for release of biologically active molecules. Here, I will highlight the work of Etchenique and coworkers who developed systems for the release of neurotransmitters. These compounds are now available commercially, though I recommend preparing them, as the syntheses are straightforward. Etchenique initially released 4-aminopyridine, which was used to block potassium channels [42]. Follow-up work examined the *in vitro* release of a variety of neuroactive molecules such as nicotine, serotonin, and GABA [43–48]. The $Ru(bpy)_2(L)_2{}^{n+}$ systems have small quantums yield for photochemical release, consistent with the work mentioned below. Addition of a PPh_3 ligand, to afford the generic $Ru(bpy)_2(PPh_3)(L)^{n+}$, resulted in a large increase in the photosubstitution quantum yield (0.3 from 0.01). Etchenique and coworkers then demonstrated GABA receptor activation upon irradiation of $Ru(bpy)_2(PPh_3)(GABA)^{+}$. Use with a variety of cells and channels demonstrated the $Ru(bpy)_2(PPh_3)(L)^{n+}$ platform as a generic photocage of amines, with quantum yields around 0.3. Knowledge of the mechanism of photodissociation from Ru(II)-polypyridyl complexes allows for the development of new systems with specific tailored properties such as the efficiency of release or wavelength of light used for photodissociation.

Ru^{2+}-polypyridyl photochemistry is a well studied field [49]; I will only briefly outline some key characteristics that are required to understand the use of Ru^{2+} complexes as photocages. Extensive studies of the photochemical and photophysical properties of Ru^{2+} complexes have been carried out in a variety of solvents [50, 51]. For the purposes of this discussion, the values that are given will be the values that have been collected in water due to their relevance to this study. The prototypical polypyridyl-Ru(II) complex is $Ru(bpy)_3{}^{2+}$. $Ru(bpy)_3{}^{2+}$ is a very stable complex in the resting state, is water soluble, and has strong visible light transitions, which are all requirements for use as a photocage. $Ru(bpy)_3{}^{2+}$ is a low-spin d^6 complex with D_3 symmetry, often thought of as octahedral symmetry for simplicity. The complex has intense absorption features in the UV corresponding to the ligand-centered $\pi \rightarrow \pi^*$ transitions [52]. A broad feature at 453 nm is observed in the visible region of the spectrum [50–52]. This transition is assigned with a metal-to-ligand charge transfer (MLCT). The MLCT transition has a large molar absorptivity of 10^4 $M^{-1}cm^{-1}$ [52, 53]. Excitation of $Ru(bpy)_3{}^{2+}$ results in population of a ^{3}MLCT state that radiatively relaxes to the ground state with a luminescence peak at 600 nm, and a quantum yield of *ca.* 0.3 [52, 54, 55].

The dissociation of a ligand must occur upon irradiation for these complexes to be photocages. Irradiation of the Ru^{2+} complex results in population of the ^{3}MLCT state. The decay from the excited ^{3}MLCT, can occur via a radiative pathway where luminescence is observed (Figure 1.5, dotted arrow). However, for the efficient ligand dissociation to occur, the decay pathway must proceed through a non-radiative mechanism. Thermal population of the ligand-field (LF) excited states is the non-radiative decay mechanism that leads to photodissociation (Figure 1.5, solid arrow), and population of the LF states is known to result in efficient dissociation [51]. Population of the LF states generates antibonding character in the d orbitals. The antibonding character along the d_{z^2} axis results in release of a ligand [56]. The relative energy difference between the MLCT states and the LF states affects the thermal population of the LF states (Figure 1.5, ΔE). The smaller the energy difference, the larger the photodissociation quantum yield (Figure 1.5, left side). If a large energy difference between the MLCT and LF states exists, the complexes are photostable (Figure 1.5, right side). For use as a photocage, a small energy difference between the MLCT and LF states must exist.

Since population of the dissosiative LF states is a non-radiative decay mechanism, thermal population must occur faster than the radiative decay lifetime for Ru^{2+} complexes. In the example of $Ru(bpy)_3{}^{2+}$, radiative decay lifetime is 600 ns, suggesting dissociation must occur faster than 600 ns. All of the above-mentioned ruthenium complexes with efficient photosubstitution yields have low quantum yields of room temperature luminescence. This is evidence that increased photodissociation results in a concurrent diminishing of the radiative relaxation pathway. Dissociation is known to be very efficient after population of the LF states occurs, which allows for the rapid release of ligands [51].

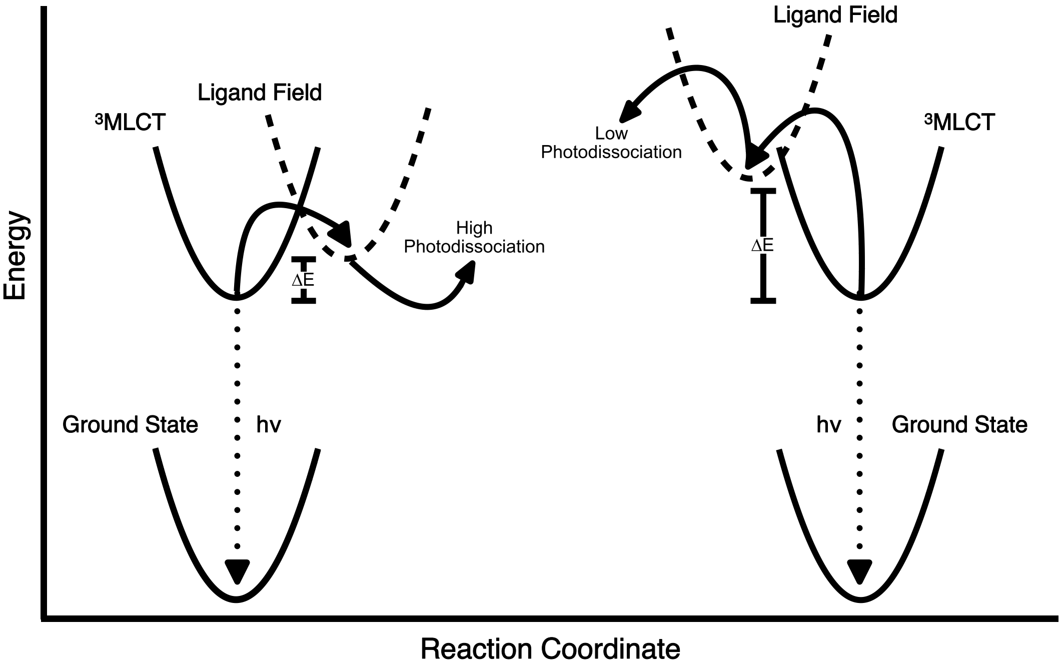

Figure 1.5: A general outline of potential energies of the states involved with ruthenium photodissociation. Low energy differences between the MLCT state and the ligand field states (left) result in effective thermal population of the LF state and high photosubstitution. A large energy difference between the MLCT state and the LF state (right) does not allow for thermal population of the LF state and results in substitutionally inert molecules.

A mechanistic understanding of photosubstitution allows for the synthetic modifications to the system that result in other related compounds to be made. Recent work has shown that Ru^{2+} complexes containing bulky bipyridine ligands can efficiently release amines. Turro and coworkers examined a series of Ru(tpy)(6,6'-X-bpy)$(L)^{n+}$ complexes and observed an increase in photosubstitution occurs when the 6 and 6' position of the bipyridine ligand is stericly bulky [57]. The steric bulk around the metal center distorts the geometry out of pseudo-octahedral symmetry. The distorted geometry lowers the energies of the LF states and enables more efficient thermal population from the MLCT states [58, 59]. Turro and coworkers have shown that the quantum yield for distorted Ru^{2+} cages is increased by 1000 fold. Ultra-fast transient spectroscopy has been used to directly visualize the population of the LF states from the MLCT state. Population of the LF states of the Ru(tpy)(6,6'-X-bpy)$(L)^{n+}$ complexes occurred in 7 ps [60]. The population of the LF states of the distorted Ru^{2+} complexes occurs about 50 times faster than the $Ru(bpy)_2(L)_2{}^{n+}$ system. The Ru(tpy)(6,6'-X-bpy)$(L)^{n+}$ complexes also undergo photodissociation under red-shifted irradiation, compared with the $Ru(bpy)_2(L)_2{}^{n+}$ complexes. Release of a molecule with red light is useful for application in photodynamic therapy.

Above I outlined the photochemistry and photophysics of Ru^{2+}-polypyrdial complexes. These complexes are water soluble, highly stable complexes that are known to undergo photodissociation upon irradiation into the visible MLCT transition. The efficiency of release is strongly dependent on the monodentate ligand properties, with photodissociation quantum yields of 0.3 possible in some systems. Photodissociation occurs as a result of thermal population of the LF states, a non-radiative decay pathway of the excited state. This mode of release results in rapid photodissociation of the ligand. Most importantly, these systems have been used previously in the photoactivation of pLGICs. I seek to use these systems for temporal control ELIC activation. The highly efficient, and rapid release of propylamine will allow for the study of conformational changes associated with ELIC activation.

1.4.2 Photoacids

Photoacids are molecules that release a proton upon irradiation, inducing a local pH change. This requires that the molecule's excited-state pK_a is lower than the ground-state pK_a. To activate acid-sensitive ion channels, irradiation must release protons that are available to bind and activate the ion channel. Protons must be released in sufficient quantity and remain free in solution for a period that allows binding to, and activation of, the ion channel. I will use naphthol and merocyanine photoacids in an effort to activate acid-sensitive ion channels.

Some of the most well studied photoacids are naphthols. Naphtols, upon UV irradiation undergo a $S_0 \rightarrow S_1$ transition, and the excited-state pK_a is substantially lowered, releasing a proton and forming the naphtholate [61]. Water-soluble naphthols are able to induce bulk pH changes in aqueous environments within nanoseconds of irradiation [62]. Naphthols are reversable photoacids and the reprotonation of the naphtholate occurs in *ca.* 1 ms. UV irradiation and the short-lived proton lifetime, however, prevent use of naphthols for photoactivation of ion channels.

Recently, the merocyanine-spiropyran photochromatic reaction (Figure 2.1c) has been used to induce large pH changes upon irradiation. The merocyanine-to-spiropyran reaction results in a large rearrangement; under irradiation, cis-trans isomerization occurs, followed by ring closure [63]. Mechanistic investigations of the merocyanine-spiropyran reaction are mostly done with the deprotonated form, so it is unclear at which step the proton is lost. It is known that upon formation of the ring-closed spiropyran the pH is altered, suggesting that the latest point the proton could be lost is ring closure. These large rearrangements have the potential to result in the slow release of a proton. The proton-release kinetics will be explored in Chapter 2. Liao and coworkers developed a water-soluble merocyanine photoacid that was shown to induce pH changes of 2 units upon visible-light irradiation [64–66]. The lifetime of the pH change was on the order of seconds, about 9 orders of magnitude longer than the naphthol lifetime. The bulk pH of solution was able to be cycled multiple times, highlighting the robust nature of this molecule. The authors were able to induce hydrogel crosslinking and perform esterification reactions under irradiation of the merocyanine photoacid [64]. The merocyanine photoacid meets the *in vitro* requirements for a phototrigger for GLIC, and will be used to photoactivate acid sensitive ion channels.

1.5 Reconstitution

This work aims to study the ion channel opening, and the experimental techniques requires study in an *in vitro* environment. *In vitro* study of ligand-gated ion channels requires that the ion channels be reconstituted, or placed in, an artificial membrane environment. Here, the reconstituted channel must also be amenable to study by pulsed laser methods. Ion channels must function *in vitro* the same way as observed *in vivo* for a relevant mechanistic study. The physiological properties observed in oocytes will serve as the baseline. A variety of ion channels have been reconstituted into many different artificial membrane environments [67]. Prior work on reconstitution has used planar lipid bilayers, vesicles of varying sizes, and detergent as the artificial membrane environment. The membrane environment used for reconstitution dictates the assay(s) that can be used to test for ion channel function. Electrophysiology can be used on planar lipid bilayers and large vesicles. Smaller vesicles and detergent environments are not amenable to electrophysiology; function of ion channels in these environment have been measured through radioactive ion flux, fluorescence quenching (or turn-on) assays, and if the ion channel is ligand-gated through ligand affinity. The above reconstitution environments and assays are described in more detail below. Functional reconstitution of pLGICs requires the binding of an agonist, and ion flux through the pore; any assay that is used must be able to report on both ligand-binding and ion flux.

Reconstitution of ion channels into planer lipid bilayers is common for *in vitro* ion channel studies [32, 68, 69]. Planer lipid bilayers are formed across teflon holes, allowing for lipid composition to be controlled. The ion channels are then added to the bilayers, and assayed using single-channel electrophysiology. GLIC and nAChRs (among others) have been reconstituted and studied *in vitro* using planer lipid bilayers [32, 68]. The single-channel *in vitro* properties are compared to the single-channel recordings of *in vivo* systems, providing a direct measure of perturbation of the reconstituted ion channels. While this is a common and robust method for reconstitution, unfortunately the experimental setup is not amenable to TR-FET measurements.

Ligand-gated ion channels must bind a ligand and then open to allow ions through. To monitor the ligand-binding event, radiolabeled affinity binding studies have been employed. This assay introduces a radiolabeled agonist, or antagonist, and monitors the ligand-binding affinity of the reconstituted ion channel. The reconstituted affinity is then compared to the binding affinity in an *in vivo* membrane environment. Large changes of the reconstituted ion channel binding affinity indicates perturbation of the reconstituted system. The radiolabeled assay highlights discrepancies in the ligand affinity of the reconstituted ion channel; purified GABA receptors were shown to have similar binding affinity of muscimol (an agonist) as observed in *in vivo* systems [70]. However, these assays do not report on the ion channel activation, and subsequent accompanying ion flux. Assaying both the ligand-binding and ion channel gating is crucial. Neither ligand binding or activation can be altered in the reconstituted system if information about the native system is to be gained.

Lipid vesicles are a common membrane environment used for the reconstitution of ion channels. Vesicles of defined composition and size can be formed using robust assays. The vesicles can range from 10s of nm to microns in diameter; molecules such as cholesterol or fluorescently-labeled lipids can be easily added into the lipid membrane composition. The vesicles are then mixed with purified protein to form vesicles with embedded proteins (proteoliposomes). Many methods have been used to verify the function of reconstituted ion channels in vesicles.

If giant unilamellar vesicles (GUVs) are used as the membrane environment, single-channel electrophysiology can be used to monitor the binding and gating of reconstituted ion channels. GUVs are amenable to electrophysiology due to the micrometer dimensions of the vesicles, and purified $5HT_{3A}$ receptors have been reconstituted using this method [14]. The size of the GUVs might result in a large amount of scattered light that is required for future measurements. Little precedent for the reconstitution of ion channels into GUVs led to this membrane environment not being explored.

Smaller vesicles, such as large unilamellar vesicles (LUVs, 100 nm in diameter), require different assays; the small size prohibits the use of electrophysiology. LUV proteoliposomes have been injected into oocytes and the function of the ion channels was examined using electrophysiology (*vida supra*), and has been used to examine reconstituted GLIC function [32]. Injection of oocytes with proteoliposomes does not assay the function of the ion channel LUV environment, but in the oocyte. To measure function of an ion channel in a LUV, the ion channel function must be assayed in the LUV.

Functional reconstitution into lipid vesicles provides a defined "inside" and "outside", in analogy to a cell. The defined spatial separation allows ion flux to be monitored as change in selective ion concentration of the inside of the vesicles (lumen) or the bulk. To monitor the flux of ions into, or out of, a vesicle two different methods are commonly used: radioisotope ion flux or thallium flux. Radioisotope flux has been used to monitor the ion flux into a variety of reconstituted ion channels such as: K^+ channels, nAChRs, $5HT_{3A}$, and Na^+ channels [71–73]. To monitor the ion flux using radioactive ions $^{86}Rb^+$, or $^{22}Na^+$ (for example), are added to a solution of proteolipsomes. The ion channel is then activated by addition of an agonist. The proteoliposomes are then isolated from any excess radioactive ions, and analyzed for radioactivity. In the example of $5HT_{3A}$, the agonist mCPBG was added, and after an incubation period, the vesicles were separated from the excess radioactive isotope, and the radioactivity assayed using scintillation counting [71]. Experiments with radioactivity can measure ion flux over time, and the modulation of the ion flux as a result of known agonists or blockers. An increased flux of $^{22}Na^+$ into the proteoliposomes was observed in the presence of mCPBG with the ion flux blocked by a known antagonist in the serotonin example above [71]. Measurements of ion flux under conditions can be compared to the current response recorded under similar conditions in electrophysiology of the *in vivo* system. These measurements allow for analysis of the ligand-binding event as well as the ion channel activation event.

Thallium (Tl^+) flux through cation selective ion channels is another common assay used to monitor the reconstituted ion channel function. Tl^+ has a similar ionic radius as potassium, allowing flux through cation-selective potassium channel. In this assay, a fluorescent dye is encapsulated inside the proteoliposomes. Under activating conditions, the ion channel will open, and thallium will diffuse through the ion channel (Figure 1.6). Thallium inside the vesicle quenches the fluorescence of the dye; monitoring the fluorescence over time provides a readout of ion flux through the ion channel. Thallium flux has been used to monitor the activation of reconstituted nAChRs and other ligand-gated ion channels [74, 75]. Addition of thallium in the presence of agonist, choline in the case of nAChRs, resulted in rapid quenching of the fluorescence. A choline concentration dependence of quenching was observed and analyzed in a similar fashion to the concentration-dependent current of electrophysiology. The Tl^+ flux measurements also provide information about the ligand-binding events and ion channel activation events.

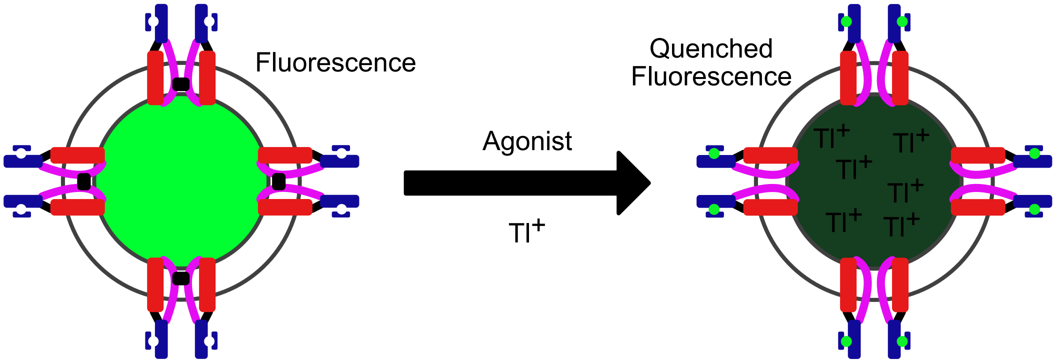

Figure 1.6: Ion channels are reconstituted into proteoliposomes with fluorescent dye (green) encapuslated inside the vesicles. Application of agonist will activate the ion channels, and allow for ions to flow through the pore. If thallium is present, thallium will enter the vesicle and quench the fluorescence of the dye. Non-functional channels will not result in quenching of fluorescent dye, allowing for fluorescence as a readout of the functional state of reconstituted ion channels.

The two different ion-flux assays mentioned (radioisotope flux and thallium flux) above are able to report on both the ligand-binding and ion channel gating properties of the reconstituted ion channels, while being compatible with the constraints of the future experiments. These assays are not ideal, as handling radioactive isotopes, or thallium, can be dangerous. However, monitoring reconstituted ion channel activity by ion flux will be the assay used in this thesis because of the ability to report on both ligand binding and ion channel activation.

1.6 Concluding Remarks

The aim of this chapter is to provide the motivation behind the research conducted in this thesis and a background to previous work done in this field. The ultimate goal of my thesis is to monitor the conformational changes, the physical motions, that ligand-gated ion channels undergo during the activation process. I aim to monitor the activation of pentameric ligand-gated ion channels, which are responsible for fast synaptic transmission in the nervous system. For pLGICs to function properly, at a minimum, the ligand must bind, and the ion channel must open to allow ion flux through the pore. The ligand-binding event has been studied in the Dougherty group for the past 20 years, but information about activation remains elusive. How ion channel activation occurs is largely an unanswered question. To monitor the activation, I want to use time-resolved fluorescence energy transfer, an ensemble measurement that allows for precise distance changes to be measured. To measure the conformational changes associated with ion channel activation, I need to develop methods for temporal control of the activation. I will discuss in detail my efforts toward this end in the remainder of the thesis. Enjoy!

References

(1) Connolly, C. N.; Wafford, K. A. *Biochemical Society Transactions* **2004**, *32*, 529–534.

(2) Sine, S. M.; Engel, A. G. *Nature* **2006**, *440*, 448–455.

(3) Lester, H. A.; Dibas, M. I.; Dahan, D. S.; Leite, J. F.; Dougherty, D. A. *Trends in Neurosciences* **2004**, *27*, 329–336.

(4) Dougherty, D. A. *Chemical Reviews* **2008**, *108*, 1642–1653.

(5) Dougherty, D. A.; Van Arnam, E. B. *ChemBioChem* **2014**, *15*, 1710–1720.

(6) Zhong, W.; Gallivan, J. P.; Zhang, Y.; Li, L.; Lester, H. A.; Dougherty, D. A. *Proceedings of the National Academy of Sciences* **1998**, *95*, 12088–12093.

(7) Beene, D. L.; Brandt, G. S.; Zhong, W.; Zacharias, N. M.; Lester, H. A.; Dougherty, D. A. *Biochemistry* **2002**, *41*, 10262–10269.

(8) Dougherty, D. A. *Accounts of Chemical Research* **2013**, *46*, 885–893.

(9) Xiu, X.; Puskar, N. L.; Shanata, J. A. P.; Lester, H. A.; Dougherty, D. A. *Nature* **2009**, *458*, 534–537.

(10) Lummis, S. C. R.; Beene, D. L.; Lee, L. W.; Lester, H. A.; Broadhurst, R. W.; Dougherty, D. A. *Nature* **2005**, *438*, 248–252.

(11) Hilf, R. J. C.; Dutzler, R. *Nature* **2008**, *452*, 375–379.

(12) Hilf, R. J. C.; Dutzler, R. *Nature* **2008**, *457*, 115–118.

(13) Bocquet, N.; Nury, H.; Baaden, M.; Le Poupon, C.; Changeux, J.-P.; Delarue, M.; Corringer, P.-J. *Nature* **2009**, *457*, 111–114.

(14) Hassaine, G.; Deluz, C.; Grasso, L.; Wyss, R.; Tol, M. B.; Hovius, R.; Graff, A.; Stahlberg, H.; Tomizaki, T.; Desmyter, A.; Moreau, C.; Li, X.-D.; Poitevin, F.; Vogel, H.; Nury, H. *Nature* **2014**, *512*, 276–281.

(15) Huang, X.; Chen, H.; Michelsen, K.; Schneider, S.; Shaffer, P. L. *Nature* **2015**, *526*, 277–280.

(16) Althoff, T.; Hibbs, R. E.; Banerjee, S.; Gouaux, E. *Nature* **2014**, *512*, 333–337.

(17) Unwin, N. *Journal of Molecular Biology* **2005**, *346*, 967–989.

(18) Unwin, N.; Fujiyoshi, Y. *Journal of Molecular Biology* **2012**, *422*, 617–634.

(19) Katju Brejc, A.; van Dijk, W. J.; Klaassen, R. V.; Schuurmans, M.; van der Oost, J.; Smit, A. B.; Sixma, T. K. *Nature* **2001**, *411*, 269–276.

(20) Sixma, T. K.; Smit, A. B. *Annual Review of Biophysics and Biomolecular Structure* **2003**, *32*, 311–334.

(21) Bocquet, N.; Prado de Carvalho, L.; Cartaud, J.; Neyton, J.; Le Poupon, C.; Taly, A.; Grutter, T.; Changeux, J.-P.; Corringer, P.-J. *Nature* **2007**, *445*, 116–119.

(22) Tasneem, A.; Iyer, L. M.; Jakobsson, E.; Aravind, L. *Genome Biology* **2004**, *6*, R4.

(23) Spurny, R.; Billen, B.; Howard, R. J.; Brams, M.; Debaveye, S.; Price, K. L.; Weston, D. A.; Strelkov, S. V.; Tytgat, J.; Bertrand, S.; Bertrand, D.; Lummis, S. C. R.; Ulens, C. *Journal of Biological Chemistry* **2013**, *288*, 8355–8364.

(24) Sauguet, L.; Shahsavar, A.; Poitevin, F.; Huon, C.; Menny, A.; Nemecz, A.; Haouz, A.; Changeux, J.-P.; Corringer, P.-J.; Delarue, M. *Proceedings of the National Academy of Sciences* **2014**, *111*, 966–971.

(25) Spurny, R. et al. *Proceedings of the National Academy of Sciences* **2012**, DOI: `10.1073/pnas.1208208109`.

(26) Mozzarelli, A.; Rossi, G. L. *Annual Review of Biophysics and Biomolecular Structure* **1996**, *25*, 343–365.

(27) Shaw, D. E. et al. *SIGARCH Comput. Archit. News* **2007**, *35*, 1–12.

(28) Jensen, M. O.; Jogini, V.; Borhani, D. W.; Leffler, A. E.; Dror, R. O.; Shaw, D. E. *Science* **2012**, *336*, 229–233.

(29) Velisetty, P.; Chalamalasetti, S. V.; Chakrapani, S. *Journal of Biological Chemistry* **2012**, *287*, 36864–36872.

(30) Velisetty, P.; Chakrapani, S. *Journal of Biological Chemistry* **2012**, *287*, 18467–18477.

(31) Jeschke, G. *Annual Review of Physical Chemistry* **2012**, *63*, 419–446.

(32) Dellisanti, C. D.; Ghosh, B.; Hanson, S. M.; Raspanti, J. M.; Grant, V. A.; Diarra, G. M.; Schuh, A. M.; Satyshur, K.; Klug, C. S.; Czajkowski, C. *PLOS Biol* **2013**, *11*, e1001714.

(33) Sasmal, D. K.; Lu, H. P. *Journal of the American Chemical Society* **2014**, *136*, 12998–13005.

(34) Posson, D. J.; Ge, P.; Miller, C.; Bezanilla, F.; Selvin, P. R. *Nature* **2005**, *436*, 848–851.

(35) Posson, D. J.; Selvin, P. R. *Neuron* **2008**, *59*, 98–109.

(36) Cha, A.; Snyder, G. E.; Selvin, P. R.; Bezanilla, F. *Nature* **1999**, *402*, 809–813.

(37) Pascher, T.; Chesick, J. P.; Winkler, J. R.; Gray, H. B. *Science* **1996**, *271*, 1558–1560.

(38) Kimura, T.; Lee, J. C.; Gray, H. B.; Winkler, J. R. *Proceedings of the National Academy of Sciences* **2009**, *106*, 7834–7839.

(39) Kimura, T.; Lee, J. C.; Gray, H. B.; Winkler, J. R. *Proceedings of the National Academy of Sciences* **2007**, *104*, 117–122.

(40) Yamada, S.; Ford, N. D. B.; Keller, G. E.; Ford, W. C.; Gray, H. B.; Winkler, J. R. *Proceedings of the National Academy of Sciences* **2013**, *110*, 1606–1610.

(41) Pinnick, D. V.; Durham, B. *Inorganic Chemistry* **1984**, *23*, 1440–1445.

(42) Zayat, L.; Calero, C.; Alborés, P.; Baraldo, L.; Etchenique, R. *Journal of the American Chemical Society* **2003**, *125*, 882–883.

(43) Zayat, L.; Salierno, M.; Etchenique, R. *Inorganic Chemistry* **2006**, *45*, 1728–1731.

(44) Zayat, L.; Noval, M. G.; Campi, J.; Calero, C. I.; Calvo, D. J.; Etchenique, R. *ChemBioChem* **2007**, *8*, 2035–2038.

(45) Rial Verde, E.; Zayat, L.; Etchenique, R.; Yuste, R.; Verde, E. M. R.; Zayat, L.; Etchenique, R.; Yuste, R. *Frontiers in Neural Circuits* **2008**, *2*, 2.

(46) Filevich, O.; Salierno, M.; Etchenique, R. *Journal of Inorganic Biochemistry* **2010**, *104*, 1248–1251.

(47) Salierno, M.; Fameli, C.; Etchenique, R. *European Journal of Inorganic Chemistry* **2008**, *2008*, 1125–1128.

(48) Salierno, M.; Marceca, E.; Peterka, D. S.; Yuste, R.; Etchenique, R. *Journal of Inorganic Biochemistry* **2010**, *104*, 418–422.

(49) Kalyanasundaram, K. *Coordination Chemistry Reviews* **1982**, *46*, 159–244.

(50) Caspar, J. V.; Meyer, T. J. *Journal of the American Chemical Society* **1983**, *105*, 5583–5590.

(51) Durham, B.; Caspar, J. V.; Nagle, J. K.; Meyer, T. J. *Journal of the American Chemical Society* **1982**, *104*, 4803–4810.

(52) Nakamaru, K. *Bulletin of the Chemical Society of Japan* **1982**, *55*, 2697–2705.

(53) Creutz, C.; Chou, M.; Netzel, T. L.; Okumura, M.; Sutin, N. *Journal of the American Chemical Society* **1980**, *102*, 1309–1319.

(54) Houten, J. V.; Watts, R. J. *Journal of the American Chemical Society* **1976**, *98*, 4853–4858.

(55) Hager, G. D.; Crosby, G. A. *Journal of the American Chemical Society* **1975**, *97*, 7031–7037.

(56) Miskowski, V. M.; Gray, H. B.; Wilson, R. B.; Solomon, E. I. *Inorganic Chemistry* **1979**, *18*, 1410–1412.

(57) Knoll, J. D.; Albani, B. A.; Durr, C. B.; Turro, C. *The Journal of Physical Chemistry A* **2014**, *118*, 10603–10610.

(58) Göttle, A. J.; Alary, F.; Boggio-Pasqua, M.; Dixon, I. M.; Heully, J.-L.; Bahreman, A.; Askes, S. H. C.; Bonnet, S. *Inorganic Chemistry* **2016**, DOI: `ArticleASAP`.

(59) Bahreman, A.; Limburg, B.; Siegler, M. A.; Bouwman, E.; Bonnet, S. *Inorganic Chemistry* **2013**, *52*, 9456–9469.

(60) Knoll, J. D.; Albani, B. A.; Turro, C. *Chemical Communications* **2015**, *51*, 8777–8780.

(61) Solntsev, K. M.; Huppert, D.; Agmon, N.; Tolbert, L. M. *The Journal of Physical Chemistry A* **2000**, *104*, 4658–4669.

(62) Gutman, M.; Huppert, D. *Journal of Biochemical and Biophysical Methods* **1979**, *1*, 9–19.

(63) Chibisov, A. K.; Görner, H. *The Journal of Physical Chemistry A* **1997**, *101*, 4305–4312.

(64) Shi, Z.; Peng, P.; Strohecker, D.; Liao, Y. *Journal of the American Chemical Society* **2011**, *133*, 14699–14703.

(65) Abeyrathna, N.; Liao, Y. *Journal of the American Chemical Society* **2015**, *137*, 11282–11284.

(66) Johns, V. K.; Wang, Z.; Li, X.; Liao, Y. *The Journal of Physical Chemistry A* **2013**, *117*, 13101–13104.

(67) Miller, C., *Ion Channel Reconstitution*; Springer Science & Business Media: 1986.

(68) Nelson, N.; Anholt, R.; Lindstrom, J.; Montal, M. *Proceedings of the National Academy of Sciences* **1980**, *77*, 3057–3061.

(69) Rosenberg, R. L.; Tomiko, S. A.; Agnew, W. S. *Proceedings of the National Academy of Sciences* **1984**, *81*, 5594–5598.

(70) Dostalova, Z.; Zhou, X.; Liu, A.; Zhang, X.; Zhang, Y.; Desai, R.; Forman, S. A.; Miller, K. W. *Protein Science* **2014**, *23*, 157–166.

(71) Lummis, S. C.; Martin, I. L. *Molecular Pharmacology* **1992**, *41*, 18–23.

(72) Weigele, J. B.; Barchi, R. L. *Proceedings of the National Academy of Sciences* **1982**, *79*, 3651–3655.

(73) Heginbotham, L.; Kolmakova-Partensky, L.; Miller, C. *The Journal of General Physiology* **1998**, *111*, 741–749.

(74) Moore, H. P.; Raftery, M. A. *Proceedings of the National Academy of Sciences* **1980**, *77*, 4509–4513.

(75) Rusinova, R.; Kim, D. M.; Nimigean, C. M.; Andersen, O. S. *Biophysical Journal* **2014**, *106*, 1070–1078.

Chapter 2

ACTIVATION OF ACID-SENSITIVE ION CHANNELS USING PHOTOACIDS

2.1 Introduction

The use of photoacids provides a promising experimental tool for the temporal control of acid-sensitive ion channels, because when and where light is delivered is easily controlled. Given the nature of the system being studied, any photoacid that is employed must be compatible with biological systems. The requirements are as follows: 1 - water soluble, 2 - air stable, 3 - visible-light triggered, 4 - long-lived proton release, and 5 - no perturbation of the system studied beyond proton delivery. Photoacid use in the induction of pH change for the investigation of biological and chemical systems is not a new idea. Traditional photoacids, such as 2-naphthol, suffer from limitations in water solubility, H^+ release lifetime and generally require UV light to trigger the proton release [1, 2]. Use of a nitrobenzyl-protected sulfate group allows for the rapid release of protons in water under near-blue irradiation [3]. Nitrobenzyl protecting groups are common photocages, and the photochemical reaction affords permanent displacement of the cargo, a proton in this case. Recently a new photoacid was synthesized using a merocyanine scaffold [4, 5]. This system is triggered by visible light, unlike the aforementioned systems, and causes a long-lived (seconds) and reversible pH change in water. To the best of my knowledge, photoactivation of acid-sensitive ion channels has not been reported. In this chapter, I will describe the synthesis, characterization, and ability to activate acid-sensitive ion channels using the above systems.

2.2 Methods and Materials

2.2.1 General Procedures

Samples of the photoacids for study were all prepared using the following methods. A stock solution was prepared by dissolving a known amount of photoacid (variable amounts given nature of experiment) in minimal 18 MΩ purified water (Barnsted E-Pure). The stock solution was then diluted to the desired concentrations for further experiments. For experiments where a pH change was required, the photoacid was diluted (ca. 100 to 1000 times) into ND96 salts (96 mM NaCl, 2 mM KCl, 1 mM $MgCl_2$) and the pH was adjusted to the desired pH using a pH meter (VWR sympHony, SB70P). pH switching studies were performed with photoacids dissolved in ND96 salts using the pH meter to measure the pH before and after irradiation by a 455 nm LED (Thor Labs, M455L1). UV-visible studies were carried out using a HP 8453 spectrometer, using 1 cm path-length quartz cuvettes. Extinction coefficients were calculated by dissolution of a known amount of photoacid into pure water, followed by dilution at various concentrations into the mixed buffer system at both pH 4.0 and pH 8.0. Electrophysiology experiments were carried out with the OpusXpress (Molecular Devices) using established methods for ASIC2a or GLIC expression and whole-cell voltage clamp protocols [6, 7]. Organic chemicals were obtained as indicated in each section below, and used without further purification. 3, 4, 3-formyl-4-hydroxybenzenesulfonate and 3-(2,3,3-trimethyl-3H-indol-1-ium-1-yl)propane-1-sulfonate were synthesized according to literature methods [4, 5, 8]. All data processing was performed using MATLAB R2013b (Mathworks, Inc.).

2.2.2 Synthesis of 3H-Indolium, 2-[(1)-2-(2-hydroxyphenyl)ethenyl]-3,3-dimethyl-1-(3-sulfopropyl) (Merocyanine Photoacid, MEH)

MEH was synthesized as previously described [4]. Briefly, 1,3-propane sultone (Aldrich) was added to 2,3,3-trimethylindolenine and stirred at 90°C for 4 hours under argon. The purple solid was collected by filtration and washed with ether and dried under vacuum. This product was then added to 2-hydrozybenzaldehyde in ethanol. The mixture was refluxed overnight, and the orange product was collected by filtration and washed with ether and finally ethanol. Characterization by ^{1}H NMR, mass spectrometry, and UV/Vis spectroscopy agree with published data [4].

2.2.3 (E)-3-(2-(2-(1H-indazol-7-yl)vinyl)benzo[d]thiazol-3-ium-3-yl)propane-1-sulfonate (Indazol-MEH)

Indazol-MEH was synthesized as previously described [5]. Briefly, 1,3-propane sultone (Aldrich) was added to 2-methyl-1-(3-sulfonatepropyl)-benzothiazoium and stirred at 90 degrees C for 5 hours under argon. The yellow solid was collected by filtration and washed with ether and dried under vacuum. This product was then added to 1-H-indazole-7-carbaldehyde in ethanol, with 5 mg NH_4OAc and was refluxed for 2 hours. An orange product was collected by filtration and washed with ether and finally ethanol. Characterization by ^{1}H NMR, mass spectrometry, and UV/Vis spectroscopy agree with published data [5].

2.2.4 Synthesis of (E)-3-(2-(3,3-dimethyl-1-(3-sulfonatopropyl)-3H-indol-1-ium-2-yl)vinyl)-4-hydroxybenzenesulfonate (Sulfonated-Merocyanine, MEHSO3)

MEHSO3 was prepared by a modification of literature procedures [4]. Briefly, 3-formyl-4-hydroxybenzenesulfonate (419 mg, 2.02 mmol) and 3-(2,3,3-trimethyl-3H-indol-1-ium-1-yl)propane-1-sulfonate (501 mg, 1.84 mmol) were combined in dry ethanol (5 mL). The resulting dark purple solution was stirred vigorously and refluxed overnight under argon. The reaction was then filtered to yield an orange solid, which was then washed with excess cold ethanol, and dried overnight, to give MEHSO3. ^{1}H NMR (300 MHz,$(CD_3)_2SO$) 11.45 (s, 1H), 8.53 (d, J = 16.3 Hz, 1H), 8.28 (d, J = 2.1 Hz, 1H), 8.12-8.02 (m, 1H), 7.98-7.81 (m, 2H), 7.75-7.54 (m, 3H), 6.98 (d, J = 8.6 Hz, 1H), 4.76 (t, J = 7.8 Hz, 2H), 2.63 (t, J = 6.8 Hz, 2H), 2.17 (m, J = 7.6 Hz, 2H), 1.79 (s, 6H). ESI-MS (Negative Mode) Calculated for $C_{21}H_{22}NO_7S_2^-$ 464.1, found 464.2.

2.2.5 Synthesis of 1-(2-Nitrophenyl)Ethyl Sulfate (Caged Sulfate)

The caged sulfate was synthesized as previously described [3]. Briefly, sodium borohydride was added to 2-nitroacetophenone (Matrix Scientific) in methanol:dioxane (3:2 by volume). The reaction was stirred for 3 hours, then quenched with water. 1-(2-nitrophenyl)ethanol was extracted into chloroform, and dried under vacuum to yield a yellow oil. Sulfur trioxide-triethylamine was added to the isolated 1-(2-nitrophenyl)ethanol in DMF and stirred for 1 hour. Water was added to quench the reaction and the solvent removed under vacuum yielding a yellow oil. Ion exchange chromatography was performed using a DEAE cellulose column (GE Healthcare). The oil was dissolved into pH 7 water and loaded onto the column, and rinsed with 5 column volumes of water. Pure compound was eluted with 0.1 M NaOH, and dried under vacuum to yield a yellow oil. The ^{1}H NMR and mass spectrometry of the eluted product agrees with published data [3].

2.2.6 Synthesis of 5-sulfonic-6-bromo-2-naphthol

Sulfonation of 6-bromo-2-naphthol was carried out using a literature preparation modified from that for 2-naphthol [9]. 6-bromo-2-naphthol (Sigma-Aldrich) was dissolved in concentrated sulfuric acid to yield a viscous dark brown solution. The solution was stirred for 45 minutes, followed by quenching with a saturated aqueous NaCl solution. This solution was filtered to give a clear filtrate and a fine pink powder. This powder was then washed with DCM to remove unreacted 6-bromo-2-naphthol and dried under vacuum. Further purification was achieved by slow evaporation of diethyl ether into an acetone/benzene solution containing the naphthol, yielding white crystals, which were characterized using ^{1}H NMR and mass spectrometry. ^{1}H NMR (300 MHz, $(CD_3)_2SO$)) 12.03 (s, 1H), 8.55(d, 1H, J = 9.30), 8.03 (d, 1H, J = 2.23), 7.78 (d, 1H, J = 8.95), 7.57 (dd, 1H, J = 2.22, 9.27), 7.07 (d, 1H, J = 8.94). LC-MS (ESI) Calculated for $C_{10}H_6BrO_4S^-$ 302.1, found 302.9.

2.2.7 UV-Visible Kinetics Studies

MEHSO3 and MEH was dissolved as described above, and diluted such that A_{455} <0.4. The kinetics were followed for two hours, collecting a spectrum every 30 seconds using the kinetics software package for the spectrometer. The first two points were baseline of MEHSO3, followed by 30 seconds of irradiation with a 455 nm LED, and the remaining time in the dark. It is important to note that complete conversion of MEHSO3 to Spiropyran-SO3 occurs in a few seconds; however, for the kinetics traces irradiation for the entire dead-time between spectrum collection was needed for a valid baseline.

2.2.8 Transient Absorption Spectroscopy

Samples of MEHSO3, MEH, or Indazole-MEH were prepared as above, and bromocresol green (BCG) was prepared by dissolution of BCG into ethanol, followed by 1:1000 dilution into ND96 salts at pH 6.0. The concentrations of MEHSO3, MEH, or Indazole-MEH were 10 μM, and the concentration of BCG was 20 μM. These solutions were then placed in a quartz cuvette open to air, and the laser experiments conducted. Excitation using the third harmonic from a Q-switched Nd:YAG laser (Spectra-Physics, Quanta-Ray PRO Series) provided 355 nm pulses, 8 ns FWHM, at 10 Hz. This pulse was then used to pump an optical parametric oscillator (Spectra-Physics Quanta-Ray MOPO-700) to provide 455 nm laser pulses. Single-wavelength transient absorption experiments were conducted with a 10 mW He-Ne Laser passed through the sample colinearly with the excitation pulse. The probe wavelength of 632 nm was selected using a double monochromator with appropriate short-pass and long-pass filters to remove stray light, as well as a neutral density filter to regulate intensity. Light was detected by a photomultiplier tube (Hamamatsu R928), and amplified using a custom built voltage amplifier. Around 15 shots were collected for each wavelength, and the data were logarithmically-compressed, then fit, in MATLAB using custom scripts.

2.2.9 Electrophysiology

In general, electrophysiology experiments were conducted as previously published [6, 7]. Briefly, *Xenopus laevis* oocytes were injected with 5 ng of wt-rASIC2a or 50 ng of wt-GLIC *in vitro* transcribed mRNA. Cells were whole-cell voltage-clamped at -60 mV, and experiments were performed following a 24 hour incubation. Expression was tested using low-pH buffers 96 mM aqueous NaCl, 2 mM KCl, 1 mM $MgCl_2$ + buffer (ND96 salts + MES buffer). To test the ability of MEHSO3 to open ASIC2a or GLIC, 3 rounds of pH 5.5 or 5.0 buffer (ASIC2a or GLIC, respectively) was applied to oocytes. Following the third round, MEHSO3 (*ca.* 500 μM), in ND96 salts, was applied. Solution transfer paused for 180 seconds, during which after a short incubation period (*ca.* 25 seconds) each oocyte was individually irradiated by a 455 nm LED for ten seconds. Following the irradiation, the solution was exchanged and two more pH 5.5 or 5.0 buffer (ASIC2a or GLIC respectively) doses were applied to monitor ASIC2a and GLIC expression. Experiments with **1** dissolved in buffer were performed in a similar manner, with 10 mM or 5 mM MES buffer (ASIC2a or GLIC respectively) present in the salts solution. All data were then processed using MATLAB with custom scripts.

2.2.10 UV-Visible pH Titrations

Assignment of the visible optical bands was determined by pH titration of MEHSO3, and monitoring of the change in the optical spectrum using UV-visible spectroscopy. A stock solution of MEHSO3 was prepared as described above. A mixed buffer solution was then prepared with ND96 salts supplemented with a buffer mixture (2.5 mM MES, 2.5 mM NaOAc, and 5 mM Tris) known to support a pH range of 4.0 - 9.0 [10]. Solutions were prepared from pH 4.0 to 8.9 by 0.1 steps in pH, using HCl or NaOH to adjust the pH. Then MEHSO3 stock was diluted 1:1000 in each of the above pH buffer solutions occurred and the optical spectrum recorded. The data were then processed using MATLAB with custom scripts.

2.3 Results and Discussion

2.3.1 Synthesis and Characterization of Merocyanine Photoacids

The structures, general syntheses, and photoreactivity of merocyanine-derived photoacids are shown in Figure 2.1. MEH and indazole-MEH were previously characterized [4, 5]. The ^{1}H NMR spectra of MESO3 and spiropyran-SO3 are shown in Figure 2.2a. The spectra are in good agreement with published NMR of related compounds [11, 12]. Under irradiation the phenolic proton (11.5 ppm) is no longer present, and the di-methyl resonance splits and moves up field. Interestingly, a shift in the water residual peak (in $(CD_3)_2SO$) is observed. This shift might be indicative of a change in the protonation state of OH_2.

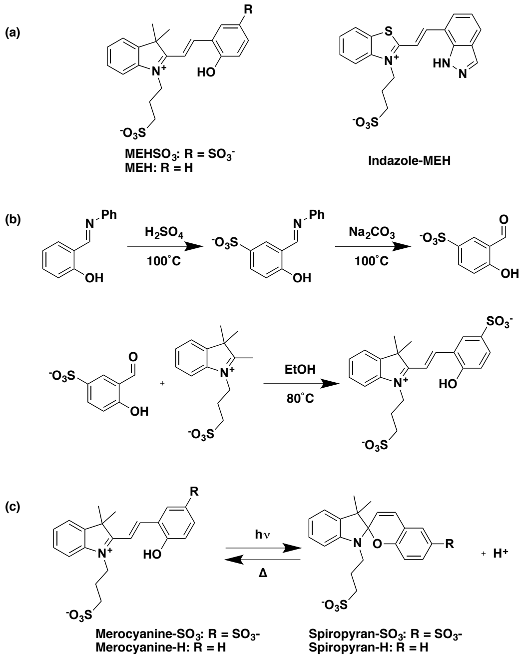

Figure 2.1: (a) Structures of the merocyanine derived photoacids. (b) Three step synthesis of MEHSO3, adaptable for the synthesis of the other two photoacids shown in (a). (c) The photoreaction of merocyanine photoacids

After ^1H NMR characterization of the newly synthesized MEHSO3, I examined the solubility of all the merocyanine photoacids. The indazole-MEH compound was soluble in DMSO to *ca.* 10^{-4} M; indazole-MEH is insoluble in water at this concentration. Both MEH and MEHSO3 display vastly different solubility profiles. Compounds MEH and MEHSO3 have minimal solubility in common organic solvents (chloroform, acetone, dichloromethane, benzene, toluene, ethyl acetate, hexanes, diethyl ether, THF, isopropyl alcohol, and acetonitrile). However, MEH and MEHSO3 are soluble in methanol, ethanol, DMSO, DMF and water. These compounds precipitate out of ethanol during synthesis, indicating limited solubility in ethanol. The purification of MEHSO3 from the starting materials proved difficult; the reactants and the product display similar solubility properties. The product mixture was washed with cold ethanol to remove excess starting materials. This removed both the starting materials and the MEHSO3 product, lowering the yield of the reaction. Use of anion exchange chromatography might provide an alternative purification method.

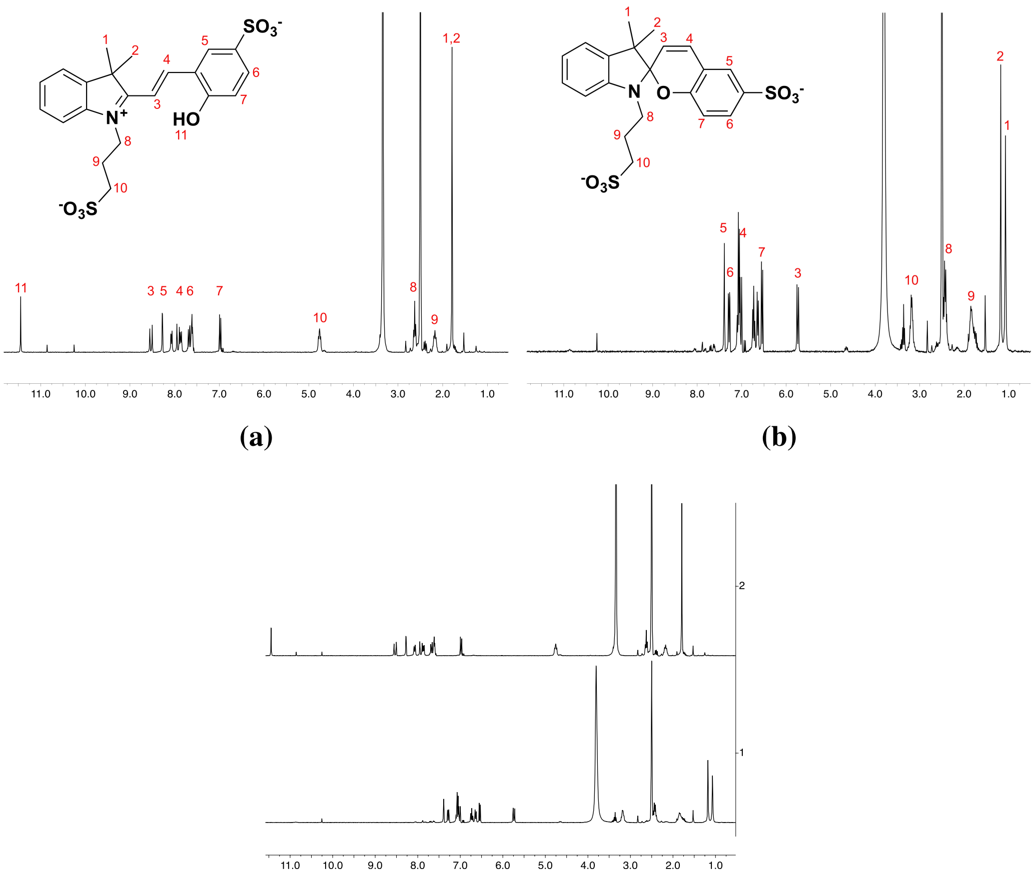

(a)

(b)

(c)

Figure 2.2: The ^{1}H NMR of MEHSO3 (a), and spiropyran-SO3 (b), stacked (c) in $(CD_3)_2SO$.

Biological control over local and global proton concentration (pH) is critical to cellular viability. Enzymatic function [10, 13], protein structure [14], and lysosomal function [15, 16] are a few examples highlighting the importance of pH for proper cellular function. To this end, it is of value to develop photochemical proton control systems for use in kinetic investigations of these systems. A common method to increase the water solubility of organic compounds is to add ionizable groups, such as sulfonate, to the compound. Given the limited solubility of MEH (600 μM), it was anticipated that sulfonation would increase the solubility of this compound. In fact, sulfonation increased the solubility about 140 fold to at least 85 mM in water. The solubility of MEHSO3 relates to the hydrophillic properties of this compound. Often in biology hydrophobic regions of proteins are found. The solubility of MEHSO3 should help limit the interactions with any hydrophobic area, not perturbing the system beyond the release of a proton.

The merocyanine photoacids are yellow solids; in solution the absorbance profiles of the merocyanine photoacids are pH dependent. MEHSO3 has a peak in the visible region of the spectrum at 416 nm, with a shoulder centered around 519 nm consistent with the published values of MEH and indazole-MEH [4, 5]. Previous work assigned the 416 nm band is to the protonated-phenolic moiety of the open merocyanine compound [4]. The 519 nm band is assigned to the deprotonated form. In order to confirm this assignment, stock solutions of MEHSO3 were prepared in water and diluted into a buffered solution (pH 4.0 to pH 8.9 by 0.1 pH increments [10]) and the optical spectrum recorded.

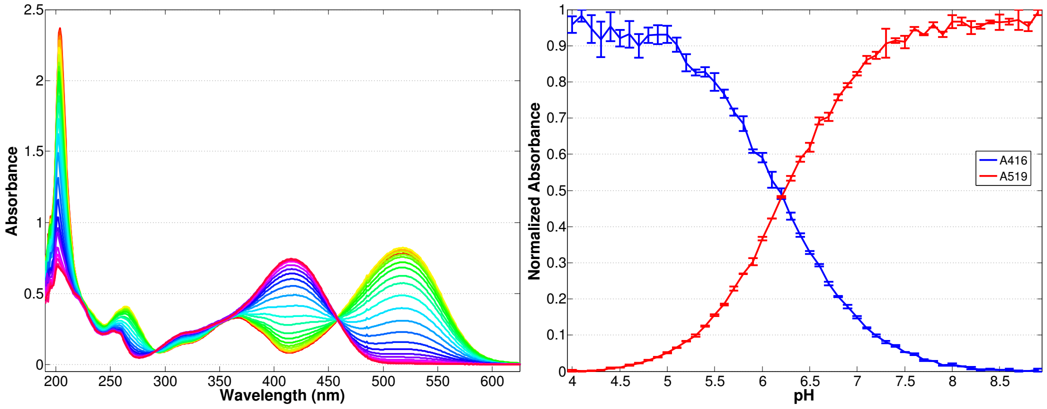

(a) **(b)**

Figure 2.3: (a) Raw UV-visible optical spectrum of pH titration of MEHSO3 from pH 4.0 (red) to pH 8.8 (yellow) by 0.2 pH units. Clean isosbestic behaviour is observed, with an isosbestic point at 458 nm in the visible region. (b) Plotted normalized absorption at 416 nm (blue) and 519 nm (red) of MEHSO3 at indicated pH. When the protonated (416 nm) peak and deprotonated (519 nm) peak are normalized and plotted, the intersection pH indicated the ground-state pK_a of the compound, *ca.* 6.2

The pH titration yields clean conversion between two species (Figure 2.3). From the titrations, the 416 nm band is assigned to the protonated merocyanine, and the 519 nm band to the deprotonated merocyanine, consistent with literature. The pK_a for MEHSO3 is estimated to be 6.2 (Figure 2.3b, crossing point). This is lower than the published pK_a of MEH (7.8) and much lower than the pK_a of indazole-MEH (13.0) [4, 5]. Unfortunately the pK_a of MEHSO3 is slightly lower than is desired for work at physiological pHs; most of MEHSO3 present at pH 7.4 will be deprotonated. Photochemistry can still occur but with no net pH change induced because no protons are released. The ion channels of interest are activated in bulk by solutions with a pH around 5.0, allowing MEHSO3 to be suitable for the photoactivation purposes.

The extinction coefficients of MEHSO3 were determined (Figure 2.4). MEHSO3 is well behaved at pH 4.0 and pH 8.0, allowing for the extinction coefficient of the completely protonated (pH 4.0, 416 nm band), completely deprotonated (pH 8.0, 519 nm band), and an isosbestic point (458 nm) (Figure 2.4). MEHSO3 has a large extinction coefficient at visible wavelengths, consistent with the published values for MEH and indazole-MEH [4, 5]. The pH 4.0 and pH 8.0 extinction coefficients at 458 nm are in good agreement with each other, which is an important self consistency check. The extinction coefficient at the isosbestic point (ϵ_{458}) can be used to calculate the total concentration of MEHSO3 in solution. The high extinction coefficient at 416 nm dominates the spectrum and results in the bright yellow colour in acidic solutions. Deprotonated MEHSO3 has an intense band at 519 nm, and a weaker band at 416 nm, resulting in the observed purple color. The pH of the solution, using the pK_a and the extinction coefficients, can be calculated.

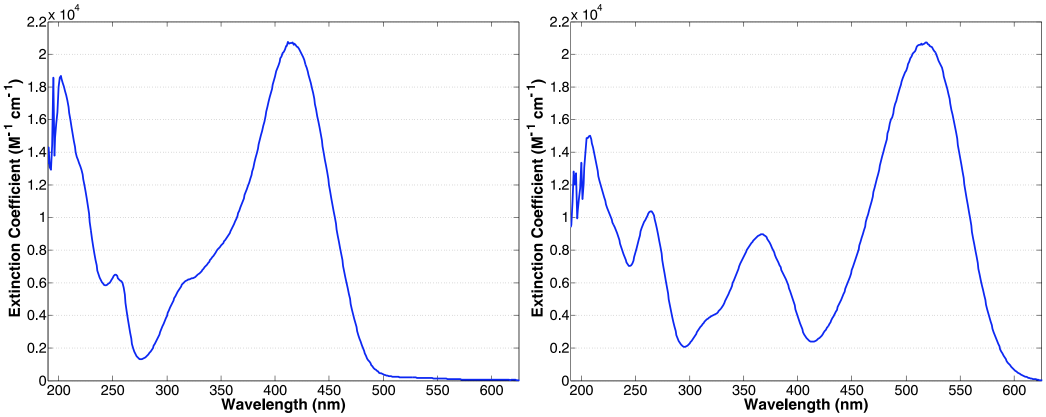

(a) **(b)**

Figure 2.4: (a) UV-visible optical spectrum of the extinction coefficients of MEHSO3 at pH 4.0. ϵ_{416} = 20500 M^{-1}cm^{-1}, ϵ_{458} = 8800 M^{-1}cm^{-1}, and ϵ_{519} < 100 M^{-1}cm^{-1}. (b) UV-visible optical spectrum of the extinction coefficients of MEHSO3 at pH 8.0. ϵ_{416} = 2400 M^{-1}cm^{-1}, ϵ_{458} = 8500 M^{-1}cm^{-1}, and ϵ_{519} = 20500 M^{-1}cm^{-1}.

This compound must undergo a photochemical reaction (Figure 2.1c) to release a proton and serve as a photoacid. This photochemical conversion from MEHSO3 to spiropyran-SO3 and back was examined using UV-visible spectroscopy. MEHSO3 was dissolved in (ND96 salts) to a final concentration of 20 μM; the pH was adjusted to *ca.*6.0 using NaOH. The resulting orange solution exhibits absorption maxima at 416 and 519 nm (Figure 2.5, black trace). Upon irradiation with a 455 nm LED, these visible bands are lost and new bands at 204, 226, and 276 nm developed over the course of seconds (Figure 2.5, red trace). These bands are assigned to the ring-closed, deprotonated spiropyran-SO3. The room temperature thermal opening of spiropyran-SO3 to MEHSO3 was monitored by UV-visible spectroscopy (Figure 2.5). Clean isosbestic points are present at 197, 260, and 301 nm, and complete

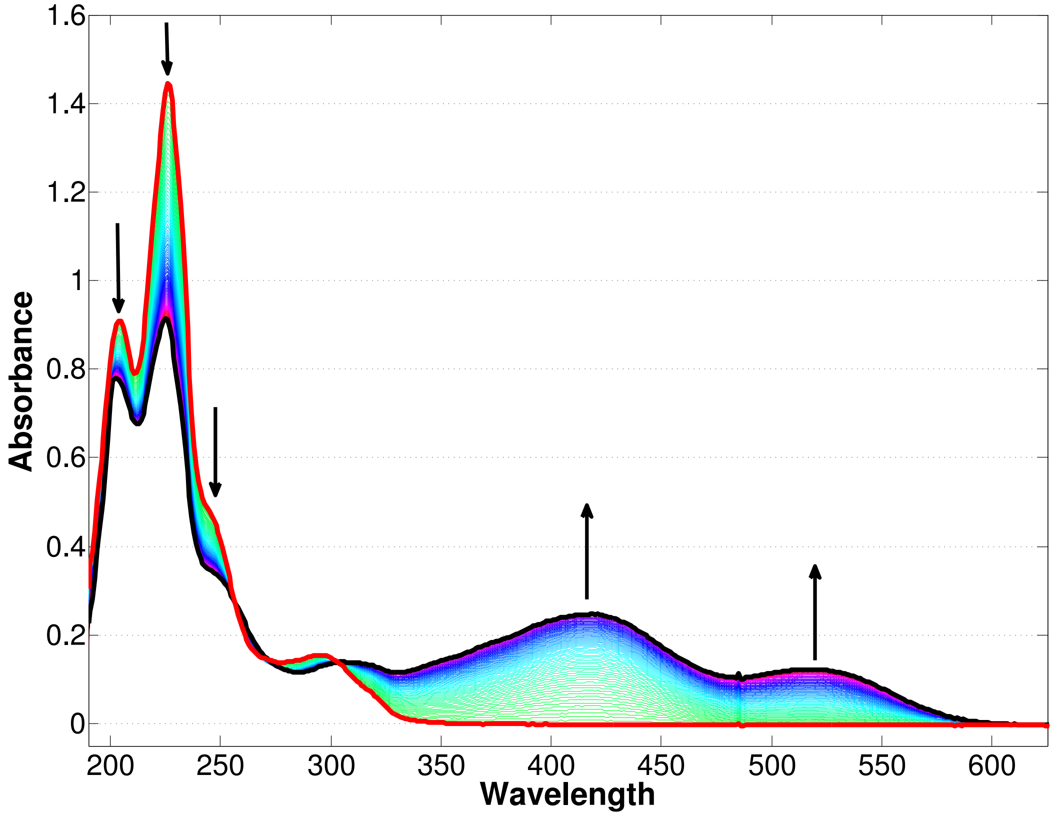

Figure 2.5: Electronic absorption spectra of MEHSO3 (black trace) in the dark, and Spiropyran-SO3 (red trace) after irradiation. Arrows indicate changes observed proceeding from Spiropyran-SO3 to MEHSO3 (in the dark) over the course of 75 min.

conversion back to MEHSO3 occurs over one hour. Shown in Figure 2.6 are absorbance traces at 416 nm and 519 nm during the thermal conversion of the spiropyran-SO3 to MEHSO3 at pH 6.0 and pH 8.0. The lifetime of MEHSO3 is on the order of minutes (Figure 2.6), a period that will allow for the study of ion channel activation.

Irradiation outside of the major absorption bands of MEHSO3 (e.g 632.8 nm, HeNe laser) produced only minimal conversion at pH 6.0 after 140 min, and no conversion after 60 min at pH 8.0 (Figure 2.7). The initial conversion under HeNe irradiation at pH 6.0 is perplexing, as MEHSO3 has no absorbance at 632.8 nm. It could be possible that upon dissolution of MEHSO3 there is some induction period in which the compound might be equilibrating, and that the initial UV-visible spectrum is not representative of the final equilibrium state of the solution. I find this explanation unsatisfying, and cannot reconcile why pH 6.0 would behave differently than pH 8.0; the involvement of a proton is the only likely explanation. Regardless, complete

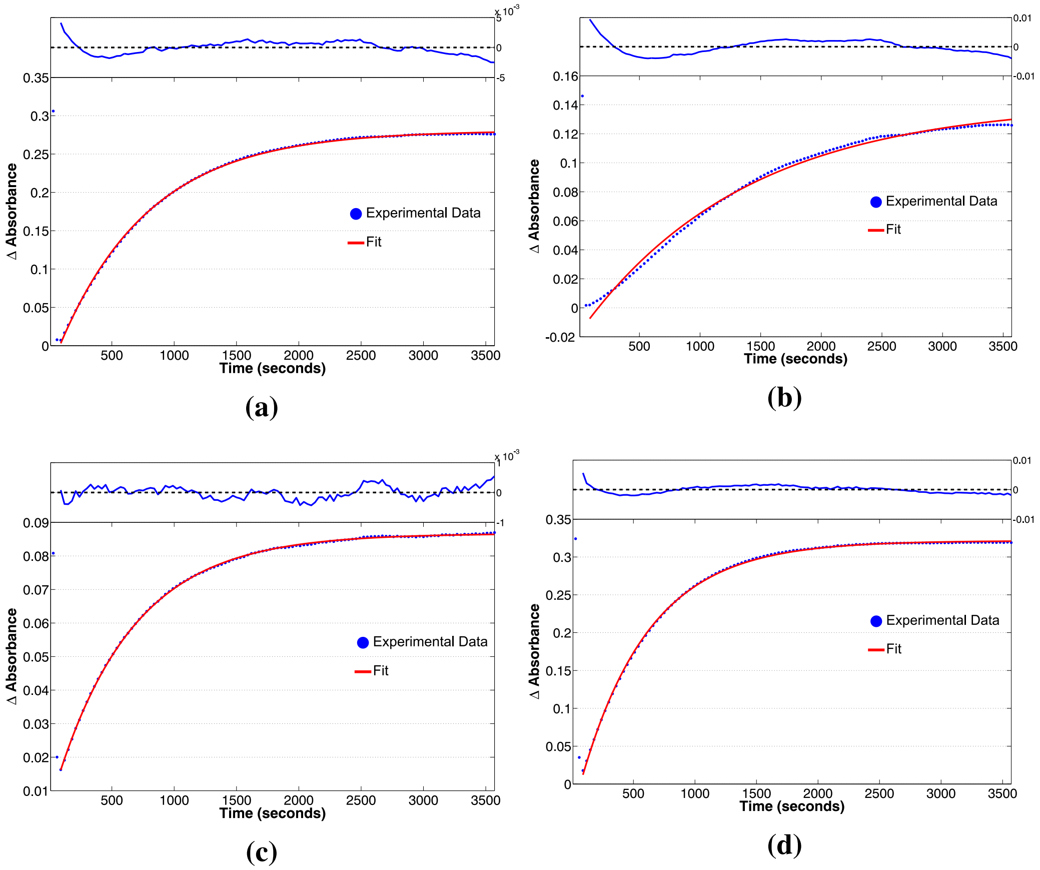

(a) **(b)**

(c) **(d)**

Figure 2.6: The conversion of Spiropyran-SO3 to MEHSO3 observed at 416 nm (a, c) and 519 nm (b, d) at pH 6.0 (a, b) and pH 8.0 (c, d). Each value is plotted versus time and fit to a single exponential equation ($f(t) = A * exp^{-t/\tau} + c$). The lifetime ($\tau$, in seconds) are: (a) 726, (b) 1361, (c) 623, (d) 556.

conversion of MEHSO3 to spiropyran-SO3 under 455 nm irradiation is observed in a few seconds. Irradiation with a HeNe for an hour or more does not result in substantial conversion. This shows irradiation into the optical bands is required for the photochemical proton release to occur.

To examine the ability of MEHSO3, MEH, and indazole-MEH to induce long-lived bulk pH changes in water the compounds were dissolved and the pH monitored under 455 nm irradiation. I will briefly mention the behaviour MEH and indazole-MEH as those two compounds are reported elsewhere [4, 5]. MEH is able to induce bulk pH change of 1.5 units (initial pH *ca.* 6.0), persisting for minutes at saturating concentrations. I was unable to obtain a bulk pH change upon irradiation of saturated indazole-MEH solutions (initial pH *ca.* 6.0) due to the insolubility in water. The pH of solutions of MEHSO3 (ca. 1 mM) in ND96 salts was also monitored. The starting pH was 6.0, and upon irradiation the pH of the solution

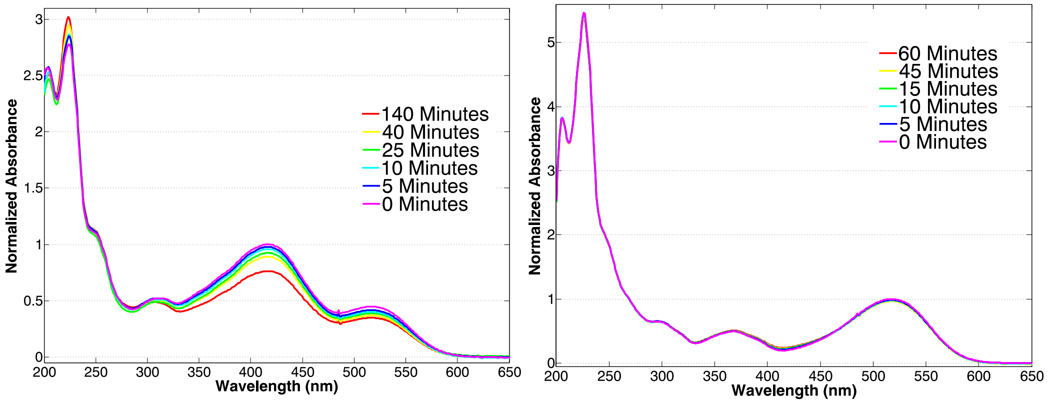

(a) **(b)**

Figure 2.7: UV-Visible spectrum of MEHSO3 upon irradiation using a HeNe laser at pH 6.0 (a) and pH 8.0 (b). The spectra are normalized to the initial starting absorbance at 416 nm (a) or 519 nm (b). Minimal conversion upon irradiation is observed in (a); complete conversion of the spectrum occurs within a few seconds upon 455 nm irradiation. No conversion is observed for (b), again noting complete conversion is observed under 455 nm irradiation conditions in a matter of seconds.

dropped and stabilized at ca. 3.6 over the course of 2 min, at which time the solution had become colorless. Irradiation into the electronic absorption bands was required for the photochemical process to occur; no pH change was observed after 2 h of 632.8 nm irradiation. When 455 nm irradiation was stopped, the solution slowly (60 min) returned to the initial pH and colour. The solution was cycled further resulting in the same net pH changes during and after irradiation. At an initial pH of 6.0, a little over half of the MEHSO3 molecules in solution are protonated. Irradiation would release around 500 μM protons into solution, resulting in a pH of 3.3. A pH of 3.6 achieved under the pH cycling conditions demonstrates that nearly all of the protons available from MEHSO3 are released under irradiation and result in the decreased pH. The bulk pH change can be modulated by the starting pH, as well as the concentration of photoacid in solution; MEHSO3 is soluble to at least 85 mM in water. Notably, at high concentrations of MEHSO3, the rate of formation of spiropyran-SO3 is limited by the irradiation intensity.

I sought to investigate the rate of proton delivery by the photoacids. Proton release must occur much faster than the process being studied (*ca.* one millisecond for ion channels). To monitor the proton release kinetics protonation of a pH sensitive dye, bromocresol green (BCG, pK_a 4.9), was monitored using time-resolved nanosecond transient absorption spectroscopy (Figure 2.8) [2, 17]. MEHSO3 was dissolved in ND96 salts (pH ca. 6.0) and BCG was added. The UV-visible spectrum of the two component system (Figure 2.8a, red line) appears as the sum of the individual spectra. This indicates no ground-state interactions exist between MEHSO3 and BCG.

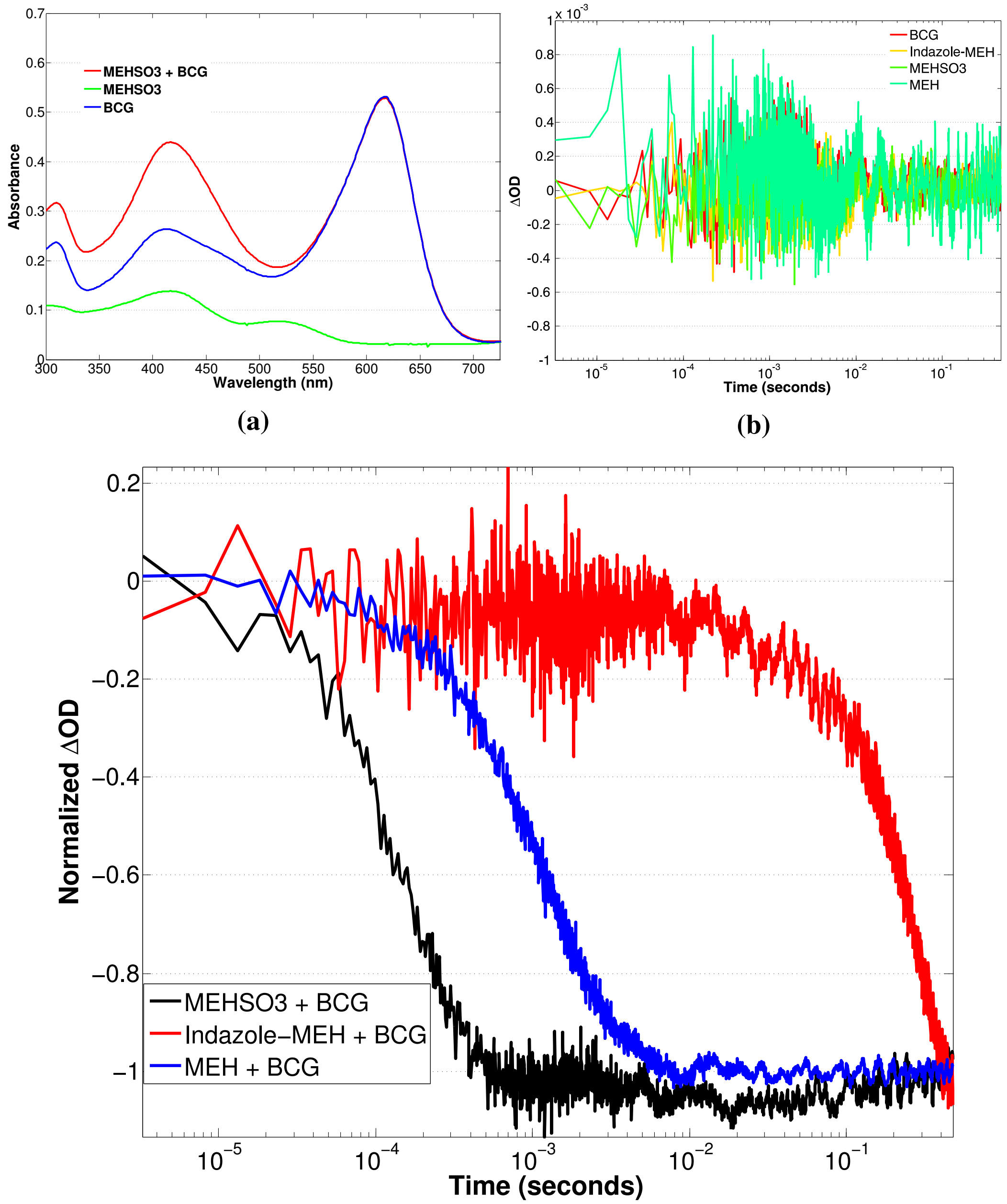

(a)

(b)

(c)

Figure 2.8: (a) UV-visible spectra of MEHSO3, Bromocresol Green (BCG), and MEHSO3 + BCG before nanosecond transient absorption experiments. This is a representative sample, as the other photoacid samples appeared similar. (b) The transient absorption signal at 632.8 nm of all the individual components of the reaction, upon excitation with 455 nm light. (c) The transient absorption signal at 632.8 nm of the merocyanine photoacids combine with BCG, upon excitation with 455 nm light.

Deprotonated BCG has an intense absorbance peak centered at 616 nm, which decreases upon protonation [18]. To observe the rate of proton release, MEHSO3 was photoactivated with 455 nm laser light. Protonation of BCG was observed at 632.8 nm, where there is no interference of any merocyanine photoacid band. Upon excitation of any of the merocyanine photoacids, or BCG alone, no transient signal at 632.8 nm was observed (Figure 2.8b).

A solution of MEHSO3 with BCG was excited with a 455 nm pulse. Rapid bleaching at 632.8 nm was observed. The decrease at 632.8 nm (Figure 2.8c, black line) is consistent with protonation of BCG. The protonation of BCG by MEHSO3 was complete in 1 ms. The transient bleach fit well to a single exponential and results in a time constant of ca. 100 microseconds. The protonation kinetics of BCG were examined using two other previously established merocyanine photoacids (MEH and indazole-MEH) [4, 5]. The concentrations of all the merocyanine photoacids and BCG were the same, allowing for the observed protonation rates to reflect the intrinsic reactivity differences of each photoacid. Replacing the sulfonate with a proton (MEH), and the phenol with an indazole (indazole-SO3) resulted in a markedly slower protonation of BCG (Figure 2.8c, blue and red lines, respectively) when compared to MEHSO3.

The protonation of BCG serves as a good model for the ion channel binding studies. The pH_{50} values for the ion channels of interest are 5.5 and 3.9. These values are proportional to the equilibrium constant for binding to a proton, and are similar to the pK_a of BCG. Ion channel activation measurements have time resolutions approaching one millisecond suggesting that delivery of the activating ligand needs to occur on shorter timescales. The indazole-MEH photoacid requires more than 500 ms for complete BCG proton delivery and is not a viable candidate ion channel activation. The MEHSO3 and MEH photo-protonation of BCG are complete by 1 ms and 10 ms respectively. This suggests that of the three merocyanine photoacids, MEHSO3 is the most likely to be viable (in terms of proton delivery kinetics) for use in photoactivation of acid-sensitive ion channels. The rate of proton delivery is not the only concern, the yield of proton production is also crucial for any potential photoacid. Qualitative calculations for both MEHSO3 and MEH, using the raw ΔOD measurements and the BCG extinction coefficient obtained from the transient absorption experiments, result in about 100 nM of protonated-BCG formed, which translates to 1 percent generation of protons. The low quantum yield of proton production is an issue if the functional readout is not robust, as it might be in the case of some measurements.

Complete characterization of three different merocyanine photoacids, two previously published (MEH and indazole-MEH) and the newly synthesized MEHSO3 provides insight into the properties of these photoacids. Comparison of the determined properties, with the requirements for photoacids mentioned in the introduction to this chapter, allows for the determination of the photoacid applicability for photoactivation of ion channels. All of the merocyanine photoacids are air stable, and undergo a photochemical reaction with visible light (455 nm LED used in these studies). The indazole-MEH compound lacks solubility in water, does not induce a bulk pH change, and has slow release of a proton. This compound will not be used in the photoactivtion of ion channels. MEH, in contrast, is fairly soluble in water, can induce a bulk pH change that lasts for minutes, and delivers protons on the order of 10 ms. MEHSO3 is very soluble, induces a bulk pH change, and has rapid (1 ms) delivery of protons to an external base. I will address the issue of biological compatibility in the next section. MEH and MEHSO3 will be used to investigate the ability of these compounds to photoactivate acid-sensitive ion channels.

2.3.2 Activation of ASIC2a and GLIC by the Sulfonated-Merocyanine Photoacid

In this section I discuss the use of MEHSO3 in the photoactivation of acid-sensing ion channel isoform 2a (ASIC2a) and Gloeobacter ligand-gated ion channel (GLIC). ASIC2a and GLIC respond to bulk pH changes, and the (pH_{50}) values for each are 3.9 and 5.5 respectively [6, 7]. The low sensitivity ion channels will allow for MEHSO3 solutions to be prepared at a starting pH where MEHSO3 is protonated, and the ion channels are not activated. I express ASIC2a and GLIC in *X. laevis* oocytes by injection of *in vitro* transcribed mRNA. I will examine the ability of the photoacid to activate the ion channels, as well as potential undesired interactions of MEHSO3 with the channels.

ASIC2a (*Rattus norvegicus*) DNA was a gift of Professor Stefan Gründer. ASIC2a mRNA was injected into oocytes with the expression levels and functional characterization tested by exposure to low pH buffers. As seen in Figure 2.9, ASIC2a expression was observed after 24 hours of incubation; the observed dose-response to proton concentration agrees well with published data [6]. Desensitization at low pH values is observed and consistent with published results [6, 19]. Desensitization occurs at pH values where all the channels are open (the lowest pH); for the

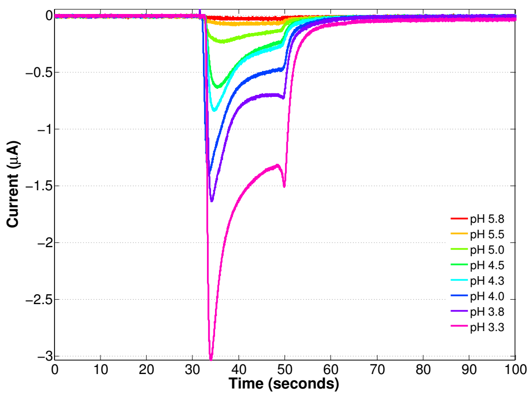

Figure 2.9: Activation of ASIC2a by application of low pH buffers

photoactivation and biocompatibility studies discussed here, pH 5.5 will serve as a reference response. This pH value allows for the monitoring of the ASIC2a channel response, without the added complication of desensitization.

First, the dark response of ASIC2a to MEHSO3 was examined. A photocaged compound must not be active until irradiated. MEHSO3 was applied to ASIC2a expressing oocytes and the current monitored in the dark. No current response was observed in the absence irradiation (Figure 2.10a). The irradiation requirement demonstrates the ability of temporal and spatial activation of ASIC2a with MEHSO3. Oocytes not expressing ASIC2a did not show response upon application, or irradiation, of MEHSO3 (Figure 2.10b) showing that native oocyte ion channels are not activated.

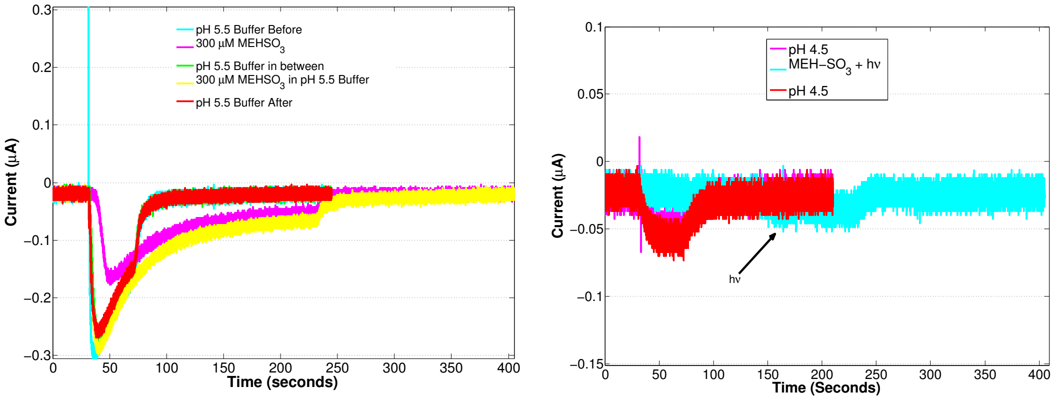

(a) **(b)**

Figure 2.10: (a) Exposure to MEHSO3 (480 μM) without irradiation (cyan trace) does not show activation of GLIC-expressing oocytes. A minimal current change is observed upon application (*ca.* 50 seconds), seen across all samples. (b) Naive oocytes exposed to MEHSO3, and irradiated. Upon irradiation no current change is observed, indicative that native oocyte channels are not activated by 500 μM of MEHSO3.

To demonstrate photoactivation (Figure 2.11a), MEHSO3, dissolved in the ND96 salts, was pH adjusted to *ca.* 5.8, and applied to oocytes expressing ASIC2a. Application of MEHSO3 in the dark resulted in a small current change due to the small basal response of ASIC2a to pH 5.8 solutions. After an incubation time of *ca.* 25 s, a 455 nm LED was then used to irradiate a single oocyte. Irradiation occurred for 10 s, which resulted in rapid current response (Figure 2.11a, black line). This current change is consistent with the activation of ASIC2a resulting from the binding of protons released by irradiated MEHSO3 (Figure 2.1c). After the LED was turned off, current from ASIC2a returned to near-baseline. The oocyte solution was then exchanged and further electrophysiological manipulation occurred. Before and after exposure to MEHSO3, pH 5.5 current response of ASIC2a-expressing oocytes was measured (Figure 2.11a, red and blue lines, respectively). The pH 5.5 current did not change after exposure to MEHSO3 showing that the photoacid does not have any prolonged effect on the channel.

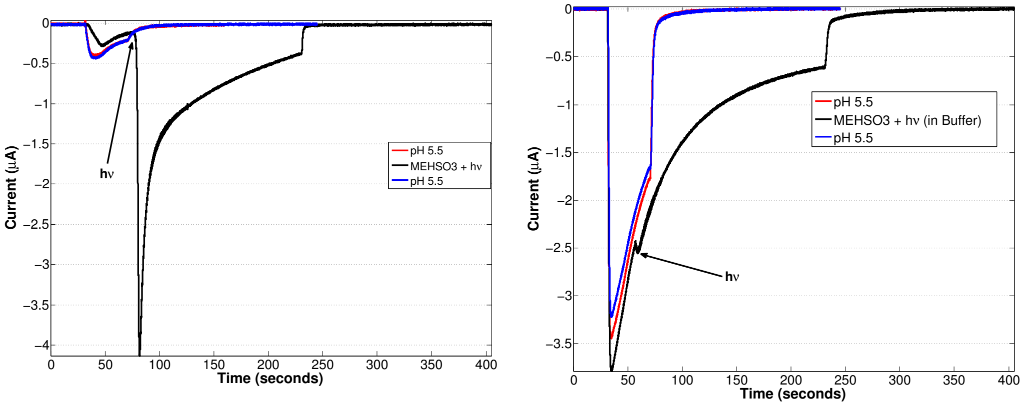

(a)

(b)

Figure 2.11: (a) Activation of ASIC2a upon irradiation (black line, irradiation occurring at position indicated by arrow) for 10 s of MEHSO3 (480 μM) with a 455 nm LED (700 mW peak power) compared to a 30 sec application of a pH 5.5 buffered solution before and after (red and blue lines respectively) application of MEHSO3.(b) ASIC2a activation in the presence of MEHSO3 (280 μM) dissolved in pH 5.5 buffer and irradiated (black line), compared with ASIC2a activation to pH 5.5 buffered solution alone (red and blue lines). The pH 5.5 solutions were exchanged for pH 7.0 buffers after 30 sec, while the sample containing MEHSO3 was exchanged after 200 sec, with a 10 sec photolysis occurring after 25 sec, as indicated by the arrow.

When considering the use of photoactive molecules in a biological context, it is crucial to evaluate the effect of both the “pro-drug” (pre-photolysis) and the “post-drug” (post-photolysis products) on the system of interest. In the present system, that means that both MEHSO3 and spiropyran-SO3 cannot interact with the ion channel. To address this concern, MEHSO3 was dissolved in pH 5.5 MES buffer and applied to ASIC2a-expressing oocytes (Figure 2.11b). The currents observed with MEHSO3 in buffer (Figure 2.11b, black line) are consistent with the pH 5.5 response of ASIC2a before application of MEHSO3 (Figure 2.11b, red line). This result indicates that MEHSO3 (pro-drug) does not affect ASIC2a channels. Upon irradiation of this oocyte, no change in current was observed (Figure 2.11b, black line). Irradiation under these conditions will form spiropyran-SO3 (post-drug) however, a bulk pH change is not induced due to the presence of buffer. Formation of the spiropyran-SO3, without a pH change, allows the interaction between ASIC2a and spiropyran-SO3 to be observed directly. No change in current was observed upon irradiation in buffered solution. Neither MEHSO3 nor spiropyran-SO3 interact with ASIC2a beyond H^+ delivery.

I also demonstrated the photoactivation of GLIC, an acid-sensitive member of the pentameric ligand-gated ion channel family. The specific function of GLIC in the native ogranism *Gloeobacter violaceus* is not known. However, GLIC was one of the first pentameric ligand-gated ion channels crystallized, exhibits typical ion flux characteristics of the cation-selective members of this family, and as a result has served as a good model system for the study of pentameric ligand-gated ion channels. MEHSO3 activates GLIC only upon irradiation (Figure 2.12a) and no deleterious interactions were observed between GLIC and either MEHSO3 or spiropyran-SO3 (Figure 2.12b).

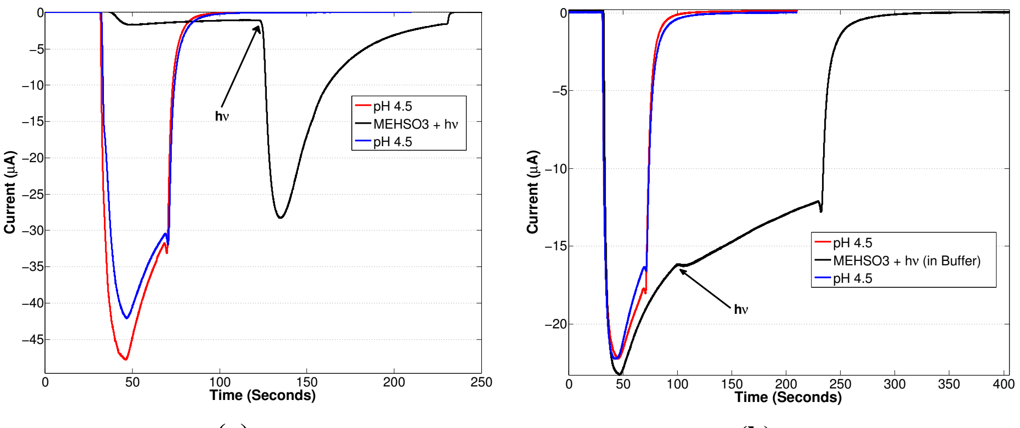

(a) **(b)**

Figure 2.12: As observed with ASIC2a (Figure 2.11), photoactivation of GLIC is also observed, and no inhibition by spiropyran-SO3 is observed. (A) Activation of GLIC is triggered by the release of protons by MEHSO3 under irradiation using a 455 nm LED. (B) No inhibition of acid-induced activation of GLIC by MEHSO3 (before irradiation, black trace) or spiropyran-SO3 (under irradiation).

I have demonstrated the use of MEHSO3 as a photoactivation method of ASIC2a and GLIC. *In vitro* characterization of MEHSO3 showed a rapid, bulk pH change occurs under irradiation; the biocompatibility of MEHSO3 was addressed in this section. Application of MEHSO3 in unbuffered solution results in activation of acid-sensitive ion channels only upon irradiation. Further biocompatibility experiments with MEHSO3 addressed the interactions of MEHSO3 or spiropyran-SO3 with the activated or closed channel. Interaction of MEHSO3 with the open channel will alter the observed pH signal, while interaction of MEHSO3 with the closed channel can alter the channel activation properties after exposure to MEHSO3. With both ASIC2a and GLIC, minimal change in signal is observed when activated channels are exposed to MEHSO3 or spiropyran-SO3. Any perturbation to the system beyond activation is undesirable and would render MEHSO3 useless for the photoactivation of the ion channels. The irradiation of MEHSO3 in buffered solutions results in a small change in both ASIC2a and GLIC signals; these changes are proportional to [MEHSO3]. MES (pK_a = 6.1) is the buffer used in these experiments, and pH 5.0 is approaching the edge of the effective buffering range. As a result this buffer is less effective when large amounts of protons are introduced into the system. Irradiation of 500 μM MEHSO3 in the buffered solutions (*in vitro*) does cause a moderate decrease in the pH of the solution. The decrease in pH could cause the modest current change observed in the buffered experiments. One potential method to address this is to go to higher ionic strength buffers, or switch buffers that have a pK_a closer to the operating pH. Regardless, it is clear that MEHSO3 can be used to photoactivate ASIC2a and GLIC ion channels. This establishes that MEHSO3 is a generic photoacid, capable of activating a range of channels and, by extension, other acid-sensitive proteins.

2.3.3 Activation of GLIC and ASIC2a by MEH

MEH was also found to have *in vitro* properties that could be translated to the activation of GLIC and ASIC2a. The MEH biocompatibility was tested using methods similar to those used in the MEHSO3 evaluation. Oocytes were exposed to saturated MEH solution (adjusted to pH 5.8). After application, a small response to the MEH solution was observed, consistent with GLIC and ASIC2a response to the slightly acidic pH 5.8 solution. Following an equilibration period in which no further change in current was observed, an individual oocyte was irradiated using a 455 nm LED for ten seconds (Figure 2.13a). Upon irradiation, immediate current response is observed. After irradiation ceases, the current slowly returns to pre-irradiation levels. No response is observed under dark conditions, and uninjected oocytes do not exhibit a response to MEH in the dark or under irradiation. This experiment demonstrates that the bulk pH change under irradiation can trigger GLIC activation. The response of GLIC to irradiated MEH solutions is much less than the response to pH 5.0 buffer. This suggests the final pH of the irradiated sample is higher than 5.0, or that MEH is interacting with the channels. At similar concentrations irradiation of MEHSO3 is able to activate GLIC to a comparable level as the low pH buffers (Figure 2.12a). This suggests that MEH is inhibiting the GLIC signal. The blocking appears to be reversible, as GLIC ion channels before and after exposure to MEH (Figure 2.13a, red and blue traces respectively) respond similarly to the low pH buffers, indicating no prolonged interactions with MEH.

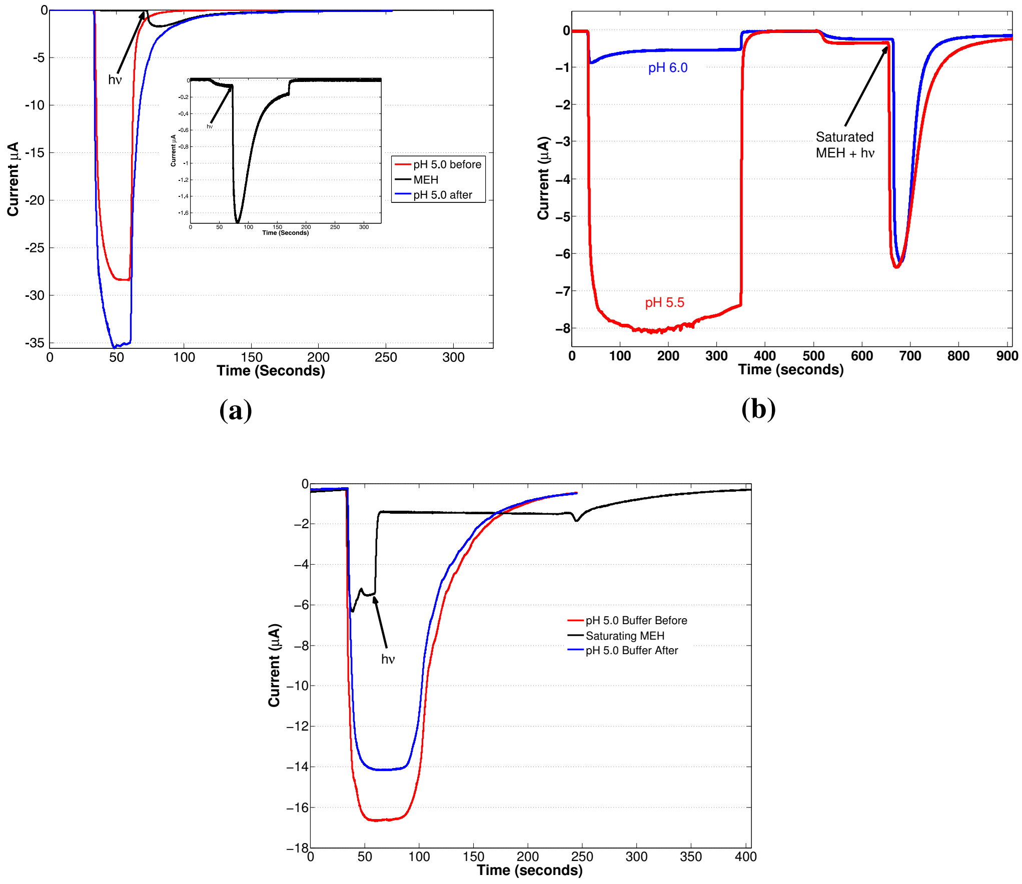

(a) (b)

(c)

Figure 2.13: (a) The activation of GLIC-expressing oocyted upon irradiation of a saturated solution of MEH. (b) Current response of GLIC in the presence of low pH buffers, and under irradiation in a solution of MEH. (c) GLIC response to pH 5.0 buffer (red and blue lines), followed by exposure to low pH buffer with saturated MEH with irradiation occuring as indicated by the arrow (black line).

In the above experiments, a saturating concentration of MEH was used. The solubility of the photoacid has been published [4], but it is unclear the proton concentration produced under irradiation. To examine the final pH of the irradiated solution, oocytes were first exposed to a known pH, and response measured (Figure 2.13b). The buffer was then exchanged for a saturated solution of MEH, and the oocytes irradiated as above. This was repeated for pH 6.0 and pH 5.5 buffers. The current response of the oocyte under irradiation was then compared to the response of the same oocyte to a given pH. The observed signal upon irradiation of the saturated MEH solution is much larger when compared to the pH 6.0 response. The response to pH 5.5 buffer, and the irradiated MEH solution, are similar in magnitude. Current is proportional to the number of GLIC channels activated; these experiments use GLIC response as a biological pH meter. Testing the same oocyte results in little variation of the current response across multiple applications of the same proton concentration. Correspondingly, testing the GLIC response to a known pH, then to irradiated MEH samples allows for the approximation of the pH that the MEH solution reaches under irradiation. To obtain the pH under irradiation using GLIC, the dose-response of GLIC towards protons, and the maximum current for each oocyte is needed. Though useful, this only qualitatively allows for pH achieved under irradiation of saturated MEH to be bracketed between 6.0 and 5.5.

Above, MEH was shown to photoactivate GLIC, investigations into the biocompatibility of MEH and spiropyran-H were needed. Similar to the MEHSO3 experiments, MEH was dissolved in pH 5.0 buffer to saturating concentrations. Irradiation of saturated MEH in buffer does not result in a pH decrease. However, irradiation does result is the photochemical conversion of MEH to spiropyran-H (structure shown in Figure 2.1c). GLIC pH 5.0 activation was examined by exposure to buffer (Figure 2.13c, red and blue lines), before and after exposure to MEH in buffer. Application of saturated MEH in pH 5.0 buffer results in a substantial decrease in GLIC response (Figure 2.13c, black line) compared to the pH 5.0 response in the absence of MEH. This suggests that the merocyanine form of MEH interacts with activated GLIC in a deleterious fashion. Irradiation of MEH in buffer causes further decrease in signal. The decrease in GLIC signal under irradiation shows that spiropyran-H also inhibits GLIC. The mechanism of inactivation caused by MEH is not known. This deleterious interaction is not permanent; after buffer exchange response to pH 5.0 buffer is slightly attenuated when compared to pre-MEH pH 5.0 response (Figure 2.13c, blue and red lines respectively).

The ability for MEH to photoactivate ASIC2a was also investigated. ASIC2a expressing oocytes were exposed to pH 5.5 buffers before and after application of saturated MEH solutions, either buffer free or in a pH 5.5 buffer (Figure 2.14, (a) and (b) respectively). Activation of ASIC2a occurs only under irradiation of the saturated MEH solution (Figure 2.14a, black line), consistent with the above studies with MEH and MEHSO3 on ASIC2a and GLIC. Application of MEH in a pH 5.5 buffer results in a moderate attenuation of the AISC2a response to pH 5.5 buffer. This attenuation suggests MEH interacts with the ASIC2a channel in a manner that inhibits signal. Minimal change in the ASIC2a signal is observed under irradiation of MEH in buffer (Figure 2.14b). Following buffer exchange, application of pH 5.5 buffer results in a smaller response when compared with pre-MEH pH 5.5 signal (Figure 2.14b, blue line). The response of ASIC2a channels to MEH is much different than GLIC. GLIC exhibited substantial inhibition by both the merocyanine and spiropyran form of MEH. Only minimal inhibition of AISC2a is observed. One complication with ASIC2a is the formation of a desensitized state, even at pH 5.5. Competition between entering the desensitized state, and MEH interactions with ASIC2a could explain the different interaction of ASIC2a with MEH. Incomplete recovery of pH 5.5 response after exposure to MEH suggests moderate perturbation of the ASIC2a ion channels exist. In general, less perturbation of the ASIC2a by MEH is observed when compared to the GLIC/MEH interactions; however, a deleterious interaction still exists.

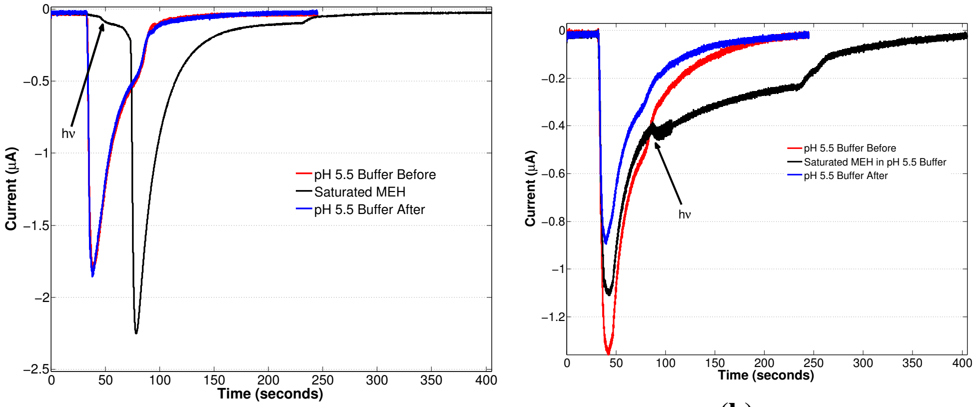

(a) **(b)**

Figure 2.14: (a) The activation of ASIC-expressing oocyted upon irradiation of a saturated solution of MEH. (b) ASIC response to pH 5.5 buffer (red and blue lines), followed by exposure to low pH buffer with saturated MEH with irradiation occurring as indicated by the arrow (black line).

It is not unusual for small molecules with significant hydrophobicity and a cationic center, like MEH, to block ion channels. With GLIC, and to a lesser extent ASIC2a, perturbation of ion channel activity is observed when exposed to MEH. This interaction persists even when the molecules have been thoroughly washed away. The addition of a sulfonate, as in MEHSO3, was designed to increase the hydrophilicity of the photoacid. The addition of an extra sulfonate creates a photoacid that is compatible with GLIC and ASIC2a ion channels.

2.3.4 Caged Sulfate Photoacid Characterization and GLIC Activation

The synthesis of a nitrobenzyl-protected sulfate was previously reported [3]. Abbruzzetti et al. show rapid release (10^7 s^{-1}) of protons occurs; this compound is extremely water soluble due to the sulfate group. UV irradiation is needed to trigger the nitrobenzyl photochemistry that results in the release of a proton (Figure 2.15a). While UV irradiation is not desirable for biological systems, 355 nm irradiation does not excite the protein backbone (220 nm) or aromatic amino acids (280 nm). This compound was synthesized, characterized (Figure 2.15b), and irradiated with a 365 nm LED to produced a decrease in pH. With the caged-sulfate in hand, I examined the ability to photoactivate GLIC, as well as the biocompatibility.

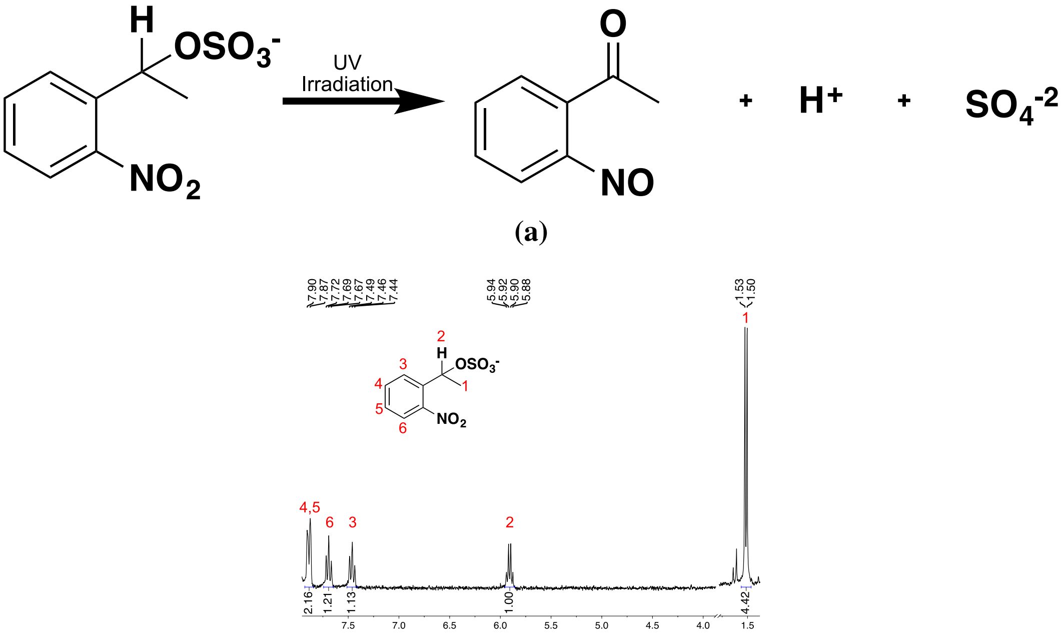

(a)

(b)

Figure 2.15: (a) The photoreaction that occurs upon irradiation of the caged sulfate molecule (left). (b) ^{1}H NMR spectrum of the purified caged sulfate molecule. Caged sulfate was purified from the starting materials using a DAEA cellulose anion exchange column.

A 1 mM solution of caged sulfate was prepared in ND96 salts and the initial pH was adjusted to *ca.* 7.0. Application of the caged sulfate results in minimal GLIC response, consistent with no GLIC response to pH 7.0 solutions. Irradiation of the GLIC-expressing oocyte exposed to caged sulfate results in a rapid change in signal (Figure 2.16a, black trace). A sharp return to baseline currents was observed after irradiation was stopped. The solution was exchanged and the oocytes exposed to the low pH buffers. GLIC response to low pH buffer before and after exposure to the caged sulfate photoacid were similar (Figure 2.16, red and blue traces respectively), suggesting prolonged interactions do not exist between the caged sulfate or the photoproduct and GLIC. The sharp decrease in signal after irradiation is perplexing. GLIC ion channels do not desensitize until extremely low pH exposures [20]. One cause of the decrease in signal could be desensitization resulting from low pH. The sharp decrease could also result from interaction between GLIC and the caged sulfate photoacid. The caged sulfate in these experiments (1 mM) allows for a theoretical maximum release of 1 mM protons, assuming complete conversion under the 5 seconds of irradiation. The result of releasing 1 mM protons is a pH = 3.0. Experience with oocyte electrophysiology suggests that, in general, oocytes do not survive pH 3.0 solutions well. The response to pH 5.0 buffer after caged sulfate irradiation is unaltered compared to the pre-exposure response (Figure 2.16, red and blue lines). Combined with the survival of the oocytes, this would suggest that pH 3.0 is not reached. Complete conversion is unlikely to occur in 5 seconds of irradiation; the quantum yield for the nitrobenzyl photochemistry is not unity [3].

To examine the effect of the pH on GLIC activation/inactivation, the concentration of caged sulfate was decreased. Caged sulfate dissolved at 100 μM was exposed to GLIC. Irradiation for five seconds afforded a rapid increase in current (Figure 2.16c, black trace). Following an equilibration period, irradiation of the same oocyte saw further increase current. This process was repeated multiple times with the same phenomenon being observed. The caged sulfate is an irreversible photoacid resulting in the observed step-function responses to irradiation. The presence of multiple activation steps demonstrates that complete conversion does not occur during 5 seconds of irradiation. At the lower concentrations of caged sulfate, the rapid decrease in signal after irradiation stops is not observed. After multiple irradiation events of a single oocyte, the desensitization-like events start to occur. This could suggest that the pH has reached a level where GLIC desensitizes (pH < 4.0 and 100% conversion). Another consequence of the multiple irradiation events is the formation of more activated GLIC channels, and more photoproduct. To examine the observed decrease upon prolonged irradiation, a 200 μM solution of caged

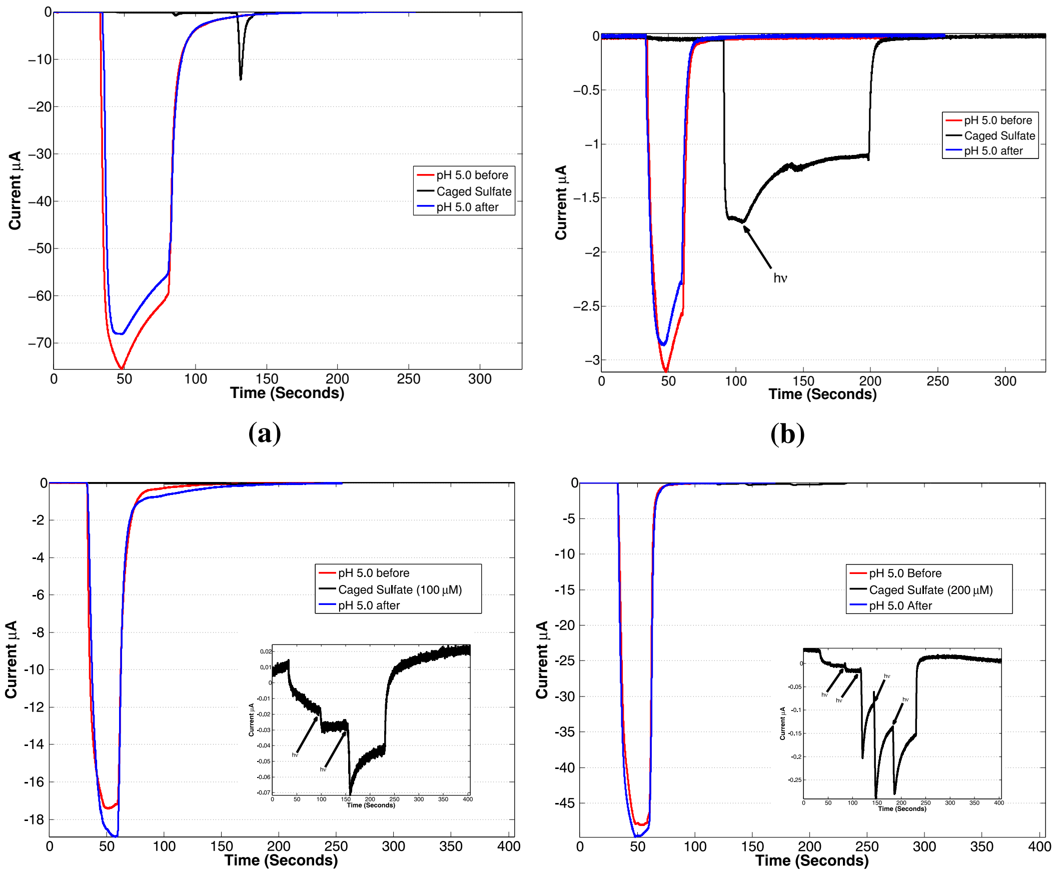

(a) **(b)**

(c) **(d)**

Figure 2.16: (a) The activation of GLIC-expressing oocytes upon irradiation of a 1 mM solution of caged sulfate. (b) Exposure of GLIC to low pH buffers with (62 μM Caged sulfate) in the dark and under irradiation. (c) GLIC activation under irradiation in the presence of 100 μM caged sulfate and (d) 200 μM caged sulfate.

sulfate was tested. The step function response is also present upon irradiation of the 200 μM sample (Figure 2.16d, black trace). However, after the first irradiation the desensitization-like behaviour is present. A higher proton concentration is achieved under prolonged irradiation of the 100 μM sample, as well as a higher photoproduct concentration. Similar proton concentrations are achieved under shorter irradiation periods with 200 μM caged sulfate. These experiments are only able to determine that higher concentrations of protons and/or photoproduct result in the decrease in GLIC signal observed.

To determine interactions between GLIC and the caged sulfate or photoproduct a similar set of experiments were performed as for the merocyanine photoacids. In these experiments GLIC expressing oocytes were exposed to pH 5.0 in the presence and absence of caged sulfate. Exposure to 65 μM caged sulfate dissolved in pH

5.0 buffer results in attenuation of observed current response (Figure 2.16b, black trace) indicating that the caged sulfate interacts with GLIC in a deleterious manner. Upon irradiation of that sample, a further decrease is observed in GLIC current response, suggesting that the photoproduct also interacts with the channel. Buffer exchange returns the pH 5.0 current response to the pre-caged sulfate level, showing the interactions between GLIC and the caged sulfate are reversible.

While the caged sulfate photoacid displays the necessary *in vitro* properties for use in the photoactivation of ion channels, the biological characterization argues otherwise. Upon irradiation the caged sulfate does activate GLIC; however, further investigation revealed that both the pre-irradiation molecule (caged sulfate) and the proton released form (photoproduct) significantly attenuate of the pH-induced current response of GLIC. This attenuation eliminates the use of the caged sulfate photoacid as a viable compound for the photoactivation of GLIC.

2.3.5 Sulfonated Naphthol Synthesis, Characterization, and GLIC Activation

Use of naphthols as photoacids are well studied and derivatized easily to afford water solubility [2, 9]. Naphthols are known to release protons on the order of nanoseconds [21] under UV irradiation. The lifetime of the deprotonated naphtholate is very short (ns), as opposed to minutes or infinite for the other photoacids examined in this chapter. Despite these potential complications, naphthols were investigated as photoacids to trigger the activation of GLIC.

The synthesis of the sulfonated naphthol was achieved readily though the use of concentrated sulfuric acid following a published procedure [9]. From the analysis of the 1-D, and 2D-COSY ^{1}H NMR (Figure 2.17) a single sulfonate group was added at the one position of the ring. Both substitution at the one and the five position results in the coupling observed; however, the 1-position is more activated. To confirm the precise substitution position a crystal structure or more advanced 2-D NMR is needed. This sulfonate group affords solubility in water, crucial for the use in biological studies. Irradiation of a sulfonated naphthol sample dissolved in water did not result in a decrease of the bulk pH.

Despite the lack of measurable bulk pH change, GLIC was expressed in oocytes as above, and activation in the presence of sulfonated naphthol was examined. For the irradiation of the sulfonated naphthol, both a 254 nm Hg-lamp and a 365 nm LED were used. GLIC-expressing oocytes under irradiation using either light source showed no activation (Figure 2.18, black and green lines). Current response to

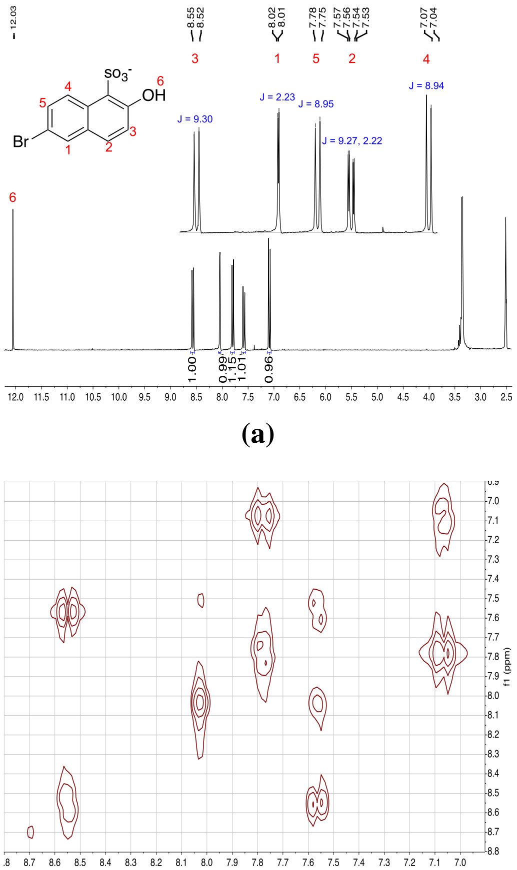

(a)

(b)

Figure 2.17: The 1-D ^{1}H (a) and 2-D ^{1}H (b) NMR of the sulfonated Naphthol.

pH 5.0 buffer was attenuated after exposure and irradiation of naphthol. Because 254 nm is not desirable for biological applications more effort was placed into the irradiation with 365 nm LED. No current change was observed under 5 minutes irradiation with the LED. This demonstrates that the sulfonated naphthol is not viable as a photoacid trigger of GLIC. While the lifetime of naphthols are short, constant irradiation could provide a labile pool of protons. If GLIC was able to bind one of these free protons, and activate, the hope was that the proton would stay bound to GLIC, and extend the naphtholate lifetime. It is not clear whether this assumption was wrong, or the irradiation does not result in the desired photochemistry, but no activation of GLIC is observed. The sulfonated naphthol was not pursued further as a result of the requirement of UV irradiation, and no observed activation of GLIC.

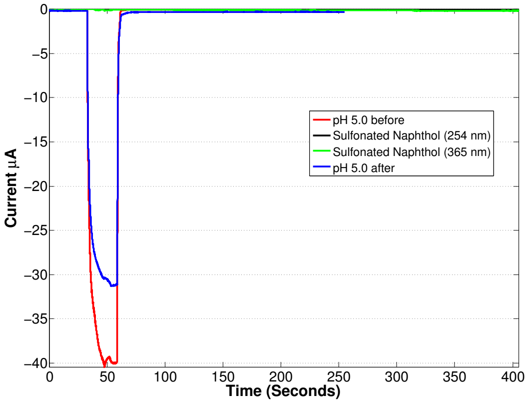

Figure 2.18: Activation of GLIC by application of low pH buffers, and exposure to sulfonated naphthol under irradiation

2.4 Conclusions and Future Outlooks

In this chapter a variety of photoacids was examined for the potential use in the activation of ASIC2a and GLIC acid-sensitive ion channels. The study of biological systems requires any photoacid to be water soluble, air stable, visible light activated, and biocompatable. Each of these properties were examined with merocyanine photoacid derivatives, a nitrobenzyl-protected sulfate, and a naphthol photoacid. The naphthol photoacid was solublized by addition of a sulfonate group through synthetic modification. Unfortunately under UV irradiation, GLIC activation was not observed, eliminating the use of sulfonated naphthol as a potential photoacid trigger for ion channel activation.

The caged sulfate molecule was well characterized in the literature [3], and was easily synthesized. This compound displays rapid, irreversible proton release, and the necessary solubility and stability properties. While UV irradiation is required, 365 nm irradiation is amenable to biological systems. Photoactivation of GLIC was observed under irradiation of the caged sulfate. Unfortunately the caged sulfate molecule did not have the desired biocompatible properties. Both the caged sulfate, and its photoproduct, interact with GLIC in a deleterious manner.

The last class of photoacids investigated were merocyanine-derived photoacids. *In vitro* characterization of the proton release rate of all of the merocyanine photoacids, and full characterization of the newly synthesized MEHSO3 occurred. All the merocyanine photoacids are visible-light triggered unlike the previously mentioned photoacids. Unfortunately, the indazole-MEH is not soluble at concentrations that will elicit a bulk pH change. The very slow release of a proton (> 500 ms), combined with the solubility issues resulted in the indazole-MEH compound not being subjected to biological testing. The remaining merocyanine photoacids differ by a single substitution. The protonation of a pH sensitive dye occurred on the order of 1 ms for MEH and 100 μs for MEHSO3. The difference of a single sulfonate group results in an increase in protonation by an order of magnitude. No dark activation of ion channels was observed for MEH or MEHSO3 and no native oocyte ion channels were activated in the presence or absence of light for both MEH and MEHSO3. The application, and subsequent irradiation, of MEH in the presence of an acid-sensitive ion channel results in activation only upon irradiation, a requirement for the compound to be a phototrigger. However, further studies showed that the MEH, and the photoproduct (spiropyran-H), inhibited the ion channel. This eliminates the possibility of MEH as a viable photoactivation method. Application and irradiation of MEHSO3 also activated acid-sensitive ion channels. In contrast to all the other compounds discussed in this chapter (spoiler alert...the whole thesis), MEHSO3 and the photoproduct (spiropyran-SO3) did not interact with the channel in any detectable manner. The addition of the sulfonate group enhances the water solubility of the molecule, presumably eliminating any potential interaction with the hydrophobic membrane of the oocyte or ion channel. MEHSO3 is the only photoacid examined in this chapter that meets all of the requirements for use in the photoactivation of acid-sensitive ion channels.

MEHSO3 has potential use in other pH sensitive systems, not just the activation of acid-sensitive ion channels. The low pK_a (6.2) of MEHSO3 will hamper the use under physiological conditions. The substitution of phenols is well studied, and I think that with some modest synthetic modifications to the MEHSO3 phenolic ring, the pK_a could approach 7. A pK_a of around 8.5 would result in almost all of the molecule being protonated at physiological pH, and would be ideal. It would be important to examine the new molecule's properties, as any synthetic modification that eliminates the biological compatibility, or solubility is undesired. I also think further analysis of the MEHSO3 protonation of BCG is of interest. Examining the rate of protonation would allow for the determination of the order of this reaction. These exercises are left to a future graduate student. What is attractive about this molecule is the relative inertness to biological conditions, suggesting that MEHSO3 can act as a generic photoacid with potential use in the study of other pH sensitive chemical and biological systems.

References

(1) Clark, J. H.; Shapiro, S. L.; Campillo, A. J.; Winn, K. R. *Journal of the American Chemical Society* **1979**, *101*, 746–748.

(2) Gutman, M.; Huppert, D. *Journal of Biochemical and Biophysical Methods* **1979**, *1*, 9–19.

(3) Abbruzzetti, S.; Sottini, S.; Viappiani, C.; Corrie, J. E. T. *Journal of the American Chemical Society* **2005**, *127*, 9865–9874.

(4) Shi, Z.; Peng, P.; Strohecker, D.; Liao, Y. *Journal of the American Chemical Society* **2011**, *133*, 14699–14703.

(5) Abeyrathna, N.; Liao, Y. *Journal of the American Chemical Society* **2015**, *137*, 11282–11284.

(6) Bartoi, T.; Augustinowski, K.; Polleichtner, G.; Gründer, S.; Ulbrich, M. H. *Proceedings of the National Academy of Sciences* **2014**, *111*, 8281–8286.

(7) Rienzo, M.; Lummis, S. C. R.; Dougherty, D. A. *Chemistry & Biology* **2014**, *21*, 1700–1706.

(8) Driouich, R.; Takayanagi, T.; Oshima, M.; Motomizu, S. *Journal of Chromatography A* **2001**, *934*, 95–103.

(9) Engel, K. H. *Journal of the American Chemical Society* **1930**, *52*, 2835–2844.

(10) Williams, J. W.; Morrison, J. F. *Biochemistry* **1981**, *20*, 6024–6029.

(11) Shiraishi, Y.; Itoh, M.; Hirai, T. *Physical Chemistry Chemical Physics* **2010**, *12*, 13737–13745.

(12) Johns, V. K.; Wang, Z.; Li, X.; Liao, Y. *The Journal of Physical Chemistry A* **2013**, *117*, 13101–13104.

(13) Kohse, S.; Neubauer, A.; Pazidis, A.; Lochbrunner, S.; Kragl, U. *Journal of the American Chemical Society* **2013**, *135*, 9407–9411.

(14) Donten, M. L.; Hassan, S.; Popp, A.; Halter, J.; Hauser, K.; Hamm, P. *The Journal of Physical Chemistry B* **2015**, *119*, 1425–1432.

(15) Luzio, J. P.; Pryor, P. R.; Bright, N. A. *Nature Reviews Molecular Cell Biology* **2007**, *8*, 622–632.

(16) Saftig, P.; Klumperman, J. *Nature Reviews Molecular Cell Biology* **2009**, *10*, 623–635.

(17) Nunes, R. M. D.; Pineiro, M.; Arnaut, L. G. *Journal of the American Chemical Society* **2009**, *131*, 9456–9462.

(18) Lau, K. T.; Shepherd, R.; Diamond, D.; Diamond, D. *Sensors* **2006**, *6*, 848–859.

(19) Sherwood, T. W.; Frey, E. N.; Askwith, C. C. *American Journal of Physiology - Cell Physiology* **2012**, *303*, C699–C710.

(20) Hilf, R. J. C.; Dutzler, R. *Nature* **2008**, *457*, 115–118.

(21) Solntsev, K. M.; Huppert, D.; Agmon, N.; Tolbert, L. M. *The Journal of Physical Chemistry A* **2000**, *104*, 4658–4669.

Chapter 3

CHARACTERIZATION AND USE OF RUTHENIUM COMPLEXES AS PHOTOLABILE PROTECTING GROUPS FOR THE ACTIVATION OF LIGAND-GATED ION CHANNELS

3.1 Introduction

This chapter focuses on the photoactivation of ligand-gated ion channels using ruthenium complexes as cages. The basis for the caged compounds is a polypyridyl-Ru(II) center. Polypyridyl-Ru(II) photochemistry and photophysics have been extensively studied [1–4]. The Ru(II) chromophore has strong absorption bands in the visible region of the spectrum; a visible peak at 453 nm in tris-(bipyridyl)-Ru(II) ($Ru(bpy)_3{}^{2+}$) has an extinction coefficient on the order of 10^4 $M^{-1}cm^{-1}$ [1]. This electronic band is assigned to the metal-to-ligand charge transfer transition (MLCT), where an electron is excited from the ruthenium center onto a primarily ligand-centered orbital [5, 6]. Inter-system crossing, followed by relaxation back to the ground state results in luminescence at 600 nm. The $Ru(bpy)_3{}^{2+}$ excited state is long-lived; the excited state of $Ru(bpy)_3{}^{2+}$ can be quenched by both electron donors and acceptors affording the (formally) Ru(I) or Ru(III) species, respectively [2]. The excited state of Ru(II) is a good (0.8 V) oxidant and reductant, while Ru(I) and Ru(III) are powerful (*ca.* 1.24 V) oxidants and reductants [7]. The favourable photochemical and photophysical properties have seen $Ru(bpy)_3{}^{2+}$ used in a wide variety of applications including: solar energy conversion [8], chemical catalysis [9], biological electron transfer [10], and cellular toxicity [11, 12].

Ru(II) complexes have also been used for photochemical caging studies. The Ru(II) photocage utilizes the transition from the populated MLCT orbitals into ligand-field (LF) centered orbitals (Figure 1.5). Population of the LF orbital results in distortion of octahedral geometry and release of a ligand [3, 13]. Population of the LF states is a competing decay pathway of the excited $Ru(bpy)_3{}^{2+}$. For photodissociation to occur, LF states must be populated before the radiative decay of the excited state. This competition results in rapid photodissociation of the ligand. Substitution of a pyridine ligand of $Ru(bpy)_2(py)_2{}^{2+}$ was shown to have efficiencies of 0.3 in dichloromethane with excess halide present [3]. Interestingly the substitution of Ru(II) complexes in neutral water is significantly attenuated. This highlights the importance of the relative energies of the MLCT and LF states, and the sensitivity to solvents and ligands [14]. Photodissociation of nitriles from $Ru(bpy)_2(L)_2{}^{n+}$, is readily achieved, and has been implemented in a photodynamic therapy application [15, 16]. The photosubstution of amines using the $Ru(bpy)_2$-platform is not as efficient.

Many native neurotransmitters (serotonin, GABA, glutamate, etc.) and common drugs (nicotine, DMT) contain amine functional groups. Etchenique and coworkers recently developed $Ru(bpy)_2$-based photocages for amine ligands [17–22]. Importantly, they demonstrated the release of nicotine, GABA, and glutamate using the photochemical platform of $Ru(bpy)_2(PPh_3)(L)^{n+}$. I sought to use the $Ru(bpy)_2(L)(L')^{n+}$ systems as photochemical triggers of ion channel activation. The Ru(II) systems display visible-light activation, high quantum yield of substitution, rapid release of ligand, and stability in water and air. I focus mostly on the release of propylamine ($PrNH_2$) for the activation of ELIC. I will discuss the use of the Etcheniuqe system, as well as other derivatives of Ru(II)-polypyridyl. I will outline the benefits and shortcomings of these systems for use in ion channel activation.

3.2 Methods and Materials

3.2.1 General Procedures

Chemicals, $Ru(bpy)_2(Cl)_2$, $RuCl_3$, 2,2'-bipyridine (bpy), (4,4'-dicarboxy)-bpy, (6,6'-dimethyl)-bpy, NH2-PEG1K, PPh_3, 2,2':6'2"-terpyridine (tpy), propylamine, GABA, 5-hydroxytryptamine, were purchased Sigma-Aldrich. $Ru(bpy)_2(PPh_3)(L)$, $Ru(bpy)_2(L)_2$, $Ru(tpy)(L)_3$, $Ru(dmb)_2(L)_2$, and Ru(tpy)(dmb)(L) were synthesized as previously described [14, 15, 18, 21, 23–26]. Synthesis of the bpy-PEG ligand occured through standard HATU couplings outlined in Figure 3.11. UV-Visible spectra were obtained using a 1 cm quartz cuvette and a HP-8453 spectrometer. Steady-state luminescence experiments were conducted using a Jobin Yvon Spex Fluorolog-3-11 spectrometer. Samples were excited by a 450 W xenon arc lamp through a monochromator for excitation at 455 nm. Emission was collected using a scanning monochromator, with detection achieved by a Hamamatsu R928P photomultiplier tube in photon counting mode. For 77K measurements, complexes were dissolved in a 1:1 methanol:ethanol solution and flash frozen in liquid nitrogen in a standard NMR tube. The measurements were made with the tube submerged in liquid nitrogen contained in a glass dewar. NMR solvents were purchased from Cambridge Isotope. All ^1H spectra were reported in reference to the solvent peak. Spectra were collected using a Varian Mercury 300 MHz spectrometer. Steady-state irradiation occurred using a Thorlabs 455 nm LED (M455L1) unless otherwise noted. All electrophysiology experiments were carried out as mentioned elsewhere [27–29]. Briefly, oocytes were injected with mRNA coding for the ion channel of interest, incubated for 24 hours, then subjected to whole-cell voltage-clamp electrophysiology using the OpusXpress (Molecular Devices) with a holding voltage of -60 mV, and a sampling rate of 125 Hz. HEK cell studies and FlexStation measurements were made as previously described [30]. All data work up was done in MATLAB R2013b (Mathworks, Inc.).

3.3 Results and Discussion

3.3.1 Use of $Ru(bpy)_2(PPh_3)(Agonist)^{n+}$ in the Photochemical Activation of Ion Channels

In this section I discuss the use of $Ru(bpy)_2(PPh_3)(Agonist)^{n+}$ in the photochemical activation of ELIC and $GABA_A$ receptors. Synthetic modification of the bipyridine and phosphine ligands afforded new derivatives that were used in activation studies. I will examine the biocompatibility of the Ru(II) photocages with a series of representative of ligand-gated ion channels. The section will conclude with the prospects of these systems for use in the photoactivation of ion channels.

The photoactivation of GABA receptors using $Ru(bpy)_2(PPh_3)(GABA)^+$ was explored previously [18]. The photochemical modulation of pH by release of butylamine has also been studied [21]. The $Ru(bpy)_2(PPh_3)(PrNH_2)^{2+}$ ion was synthesized as described above (Figure 3.1a) for use in the photoactivation of ELIC by release of propylamine. Synthesis in the absence of light is crucial; the yield for photodissociation of propylamine is very high and occurs under room light irradiation. A red-shift in the absorbance spectrum (Figure 3.2c), and pH increase, was observed upon irradiation of an aqueous solution of $Ru(bpy)_2(PPh_3)(PrNH_2)^{2+}$. The photodissociation was monitored by NMR and the release of free propylamine upon irradiation was observed (Figure 3.2a and b). The *in vitro* release of propylamine is consistent with published results of related compounds [21].

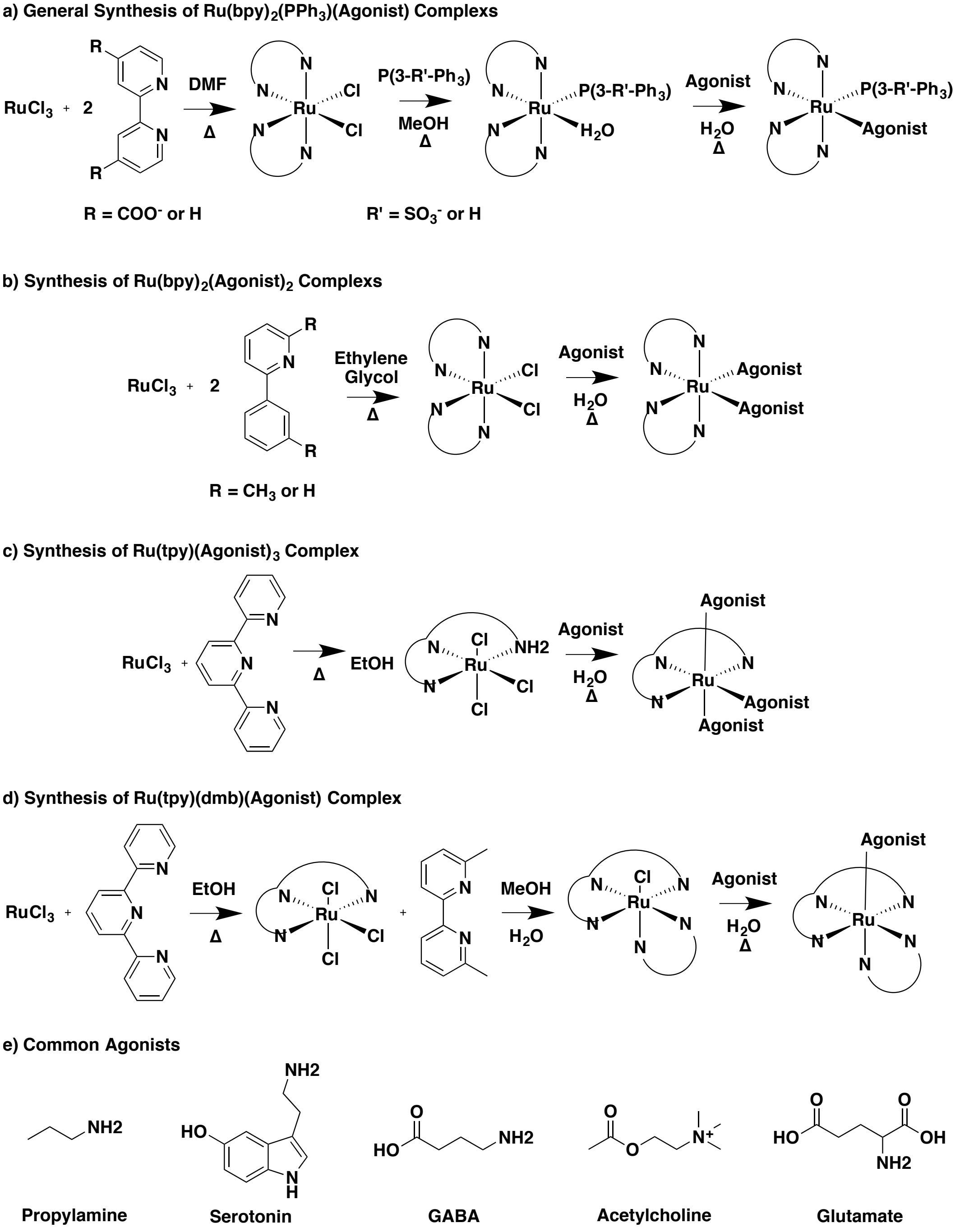

Figure 3.1: A general scheme outlining the synthetic pathways taken for the various ruthenium photocages synthesized in this chapter. The derivatives with a PPh3 ligand were synthesized as in (a). The Ru(dmb)$_2$ complexes were synthesized as in (b). Ru(tpy) protecting groups were synthesized as in (c) and (d) depending on the remaining ligands. The charge on the ruthenium complex is dictated by the charges on the agonist. The oxidation state of ruthenium is 2+ for all photocages. (e) Structures of common agonists that are used in this chapter. All of the agonists are caged by the free amine; acetylcholine is just shown for the sake of posterity.

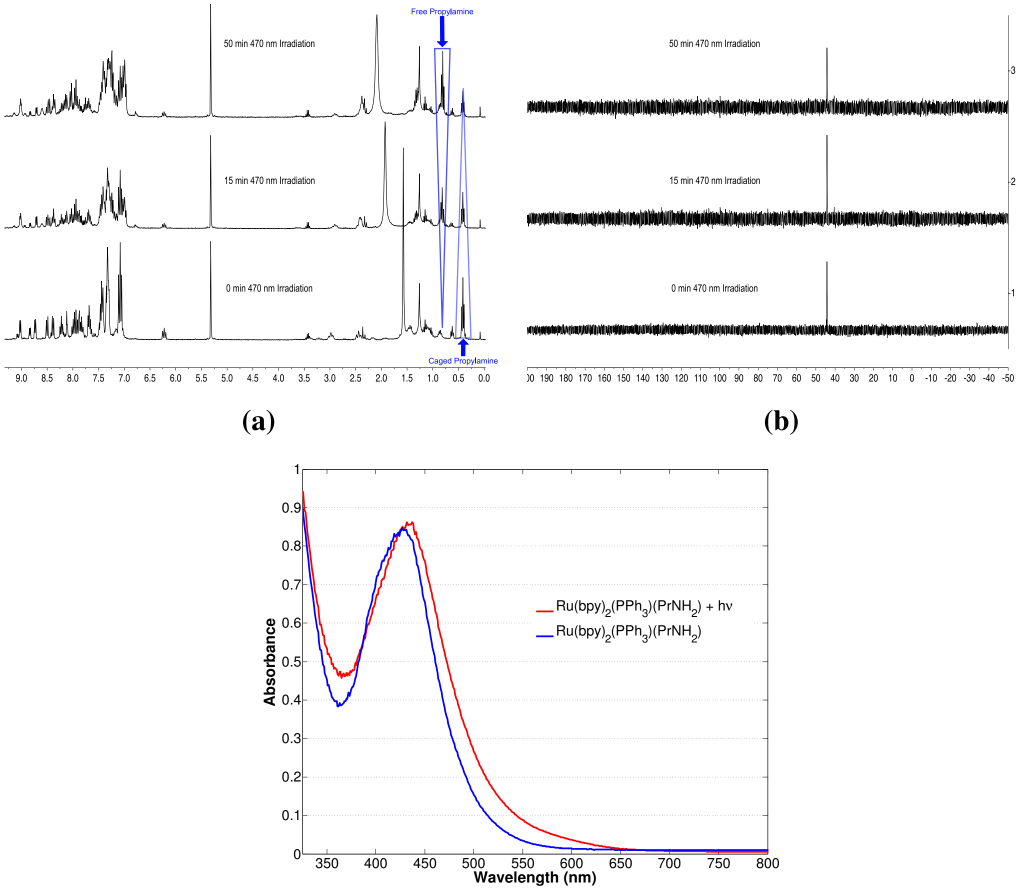

(a) **(b)**

(c)

Figure 3.2: (a) The ^{1}H and (b) ^{31}P NMR spectra of the irradiation of $Ru(bpy)_2(PPh_3)(PrNH_2)^{2+}$ in D_2O. Free propylamine is observed in the 1H NMR, while there is no shift in the 31P peak. (c) The UV-visible spectra of $Ru(bpy)_2(PPh_3)(PrNH_2)^{2+}$ under 10 minutes of irradiation. A red-shift is observed consistent with release of propylamine.

Wild-type ELIC ion channels were expressed in oocytes and the dose-response of ELIC to propylamine confirmed functional expression [28]. $Ru(bpy)_2(PPh_3)(PrNH_2)^{2+}$ was then used in for the photoactivation of ELIC. Propylamine response of ELIC was measured prior to exposure to ruthenium (Figure 3.3a, red line). Propylamine response before Ru provides a reference for ELIC sensitivity that will be used to monitor any functional changes as a result of ruthenium exposure. Application of $Ru(bpy)_2(PPh_3)(PrNH_2)^{2+}$ then occurred; in the dark no current change is observed in response to the ruthenium compound. Any current change observed in the dark might result from minor photolysis of the solution due to adventitious light. Irradiation of the Ru(II)-caged propylamine for five seconds did not result in activation of ELIC (Figure 3.3a, black line). Activation of ELIC upon irradiation would result in more current response, and the black line in Figure 3.3a would read a different value than zero. $Ru(bpy)_2(PPh_3)(PrNH_2)^{2+}$ was added at a concentration of *ca.* 100 μM; under complete conversion the propylamine concentration would be much lower than required for ELIC activation (EC_{50} = 500 μM). This low concentration used would result in a very small signal observed under complete conversion.

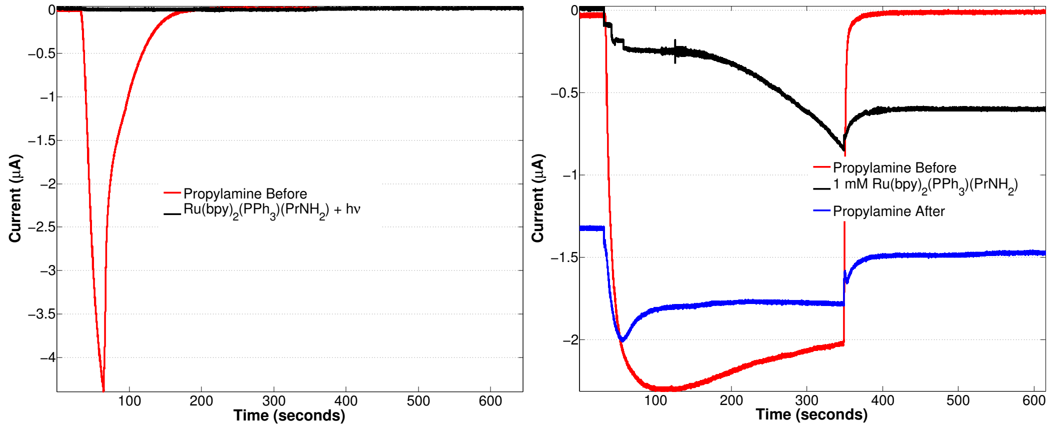

(a) **(b)**

Figure 3.3: (a) ELIC-expressing oocytes response to propylamine before $Ru(bpy)_2(PPh_3)(PrNH_2)^{2+}$ exposure, red line. Application of $Ru(bpy)_2(PPh_3)(PrNH_2)^{2+}$, black line, does not result in activation of ELIC in the dark or under irradiation. (b) Application of 1 mM $Ru(bpy)_2(PPh_3)(PrNH_2)^{2+}$, black line, results in cell death as evident by the loss of the washout current. After complete removal of $Ru(bpy)_2(PPh_3)(PrNH_2)^{2+}$ the propylamine response was diminished, and the holding current was significantly off 0 (blue line), a sign of very unhealthy cells.

Addition of a 1 mM solution of $Ru(bpy)_2(PPh_3)(PrNH_2)^{2+}$, a concentration that would release ample propylamine for ELIC activation, resulted in cell death (Figure 3.3b). Cell death is evident by a change in the current observed after 350 seconds in Figure 3.3b. Before exposure to Ru (Figure 3.3b, red line), when the propylamine is removed from solution at 350 seconds, the current returns to zero. Addition of $Ru(bpy)_2(PPh_3)(PrNH_2)^{2+}$ (Figure 3.3b, black line), followed by removal of the ruthenium (350 seconds) results in a current response well below zero. The change in current after removal of the applied buffer is indicative of cell death. Buffer exchange of the low concentration samples, and subsequent propylamine applications, resulted in similar propylamine response of ELIC before exposure to the Ru photocage. The robust propylamine response after exposure to ruthenium suggests that there is little prolonged interaction between the channel and the complex. Photodissociation of propylamine results in the formation of $Ru(bpy)_2(PPh_3)(H_2O)^{2+}$ as the photoproduct. Propylamine will activate ELIC, but it is unclear what interaction(s) $Ru(bpy)_2(PPh_3)(H_2O)^{2+}$ has with the system. For an effective photocage, all the photoproducts must be inert (see Chapter 2).

To examine potential interactions of $Ru(bpy)_2(PPh_3)(H_2O)^{2+}$ (the photoproduct) with ELIC, ELIC-expressing oocytes were incubated for 30 seconds with 50 μM $Ru(bpy)_2(PPh_3)(H_2O)^{2+}$ followed by co-application of 50 μM $Ru(bpy)_2(PPh_3)(H_2O)^{2+}$ in propylamine (Figure 3.4, black line). The application of $Ru(bpy)_2(PPh_3)(H_2O)^{2+}$ in propylamine resulted in complete attenuation of the ELIC response to propylamine. An extended wash occurred to remove $Ru(bpy)_2(PPh_3)(H_2O)^{2+}$ from solution. Application of propylamine following exposure to ruthenium resulted in almost complete attenuation of ELIC response to propylamine (Figure 3.4, blue line). The complete inhibition of ELIC response to propylamine by application of $Ru(bpy)_2(PPh_3)(H_2O)^{2+}$ shows that a significant irreversible interaction exists between ELIC and the Ru complex. The deleterious interaction between ELIC and the $Ru(bpy)_2(PPh_3)(PrNH_2)^{2+}$ eliminates its use as a photolabile protecting group for the activation of ELIC ion channels.

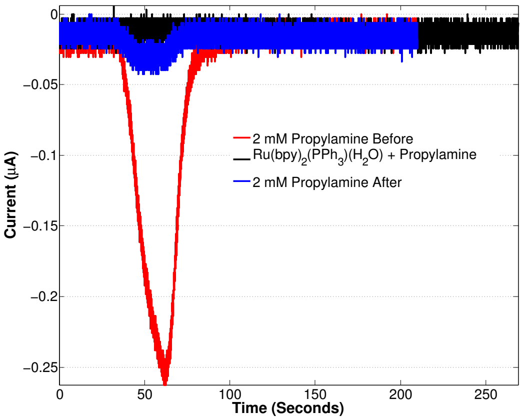

Figure 3.4: Robust propylamine response was observed from ELIC before application of the ruthenium photoproduct, $Ru(bpy)_2(PPh_3)(H_2O)^{2+}$, red line. Upon application of $Ru(bpy)_2(PPh_3)(H_2O)^{2+}$ with propylamine, the ELIC response to propylamine is completely inhibited, black line. After wash out of $Ru(bpy)_2(PPh_3)(PrNH_2)^{2+}$, blue line, ELIC response to propylamine is not recovered.

The $Ru(bpy)_2(PPh_3)(Agonist)^{n+}$ scaffold is incredibly modular and affords the release of many neurotransmitters and biologically active drugs. To examine if the inhibition observed is a result of the need for high concentrations other, more sensitive, ion channels were investigated. The GABA-protected compound was synthesized ($Ru(bpy)_2(PPh_3)(GABA)^{+}$), and photochemical activation of GABA was examined. $GABA_A$ receptors were expressed in oocytes and photoactivation studied. Irradiation of *ca.* 30 μM $Ru(bpy)_2(PPh_3)(GABA)^{+}$ resulted in immediate response, in a step-function shape (Figure 3.5a, black line). After irradiation the current reached a new steady-state. Additional irradiation events resulted in a similar responses. The release of GABA from the ruthenium complex is irreversible; each additional irradiation released more GABA that can activate the channels.

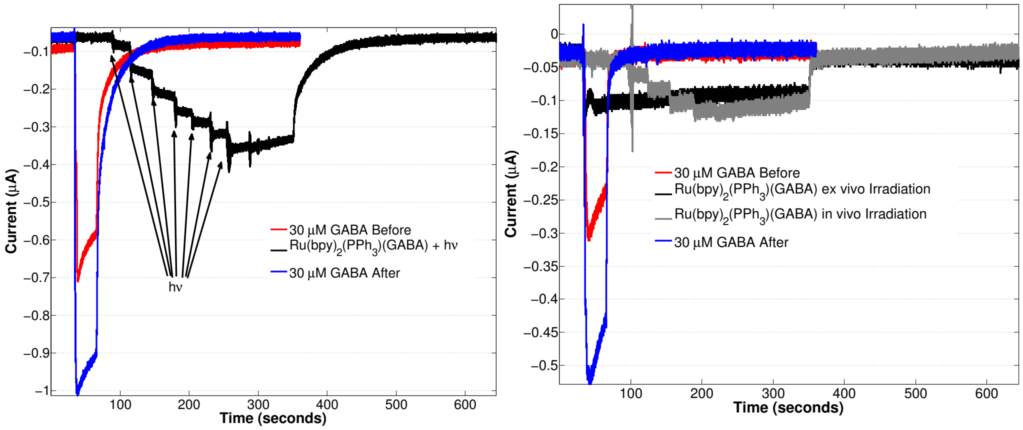

(a) **(b)**

Figure 3.5: (a) GABA$_A$ receptors, upon application of GABA, respond with a robust current change (red line). Application of Ru(bpy)$_2$(PPh$_3$)(GABA)$^+$ results in activation of the GABA$_A$ receptors only upon irradiation, black line. After washout of the ruthenium, the GABA$_A$ response is similar to the pre-ruthenium levels, blue line. (b) The *ex vivo* irradiation of Ru(bpy)$_2$(PPh$_3$)(GABA)$^+$, black line, results in a response of GABA$_A$ receptors that is similar to the *in vivo* irradiation, gray line. Either irradiation method does not elicit current response on the level of just application of GABA alone, red and blue lines.

GABA$_A$ receptor response was larger to 30 μM GABA than the response under irradiation of 30 μM Ru(bpy)$_2$(PPh$_3$)(GABA)$^+$ (Figure 3.5a, red and blue lines). The difference could be due to incomplete photolysis of the Ru photocage. Prolonged irradiation resulted in a steady-state GABA response, where more irradiation did not result in an increase in current, suggesting that a maximum current is reached. Samples of the Ru(bpy)$_2$(PPh$_3$)(GABA)$^+$ complex were irradiated *ex vivo* for 30 minutes, and applied to GABA$_A$ receptors. The GABA$_A$ response to the *ex vivo* application was similar to what is observed under *in vivo* irradiation experiments (Figure 3.5b, black and gray lines). This similar response suggests that *in vivo* irradiation proceeds to completion. GABA$_A$ receptors also undergo desensitization (the decrease in signal observed from 30 to 60 seconds in Figure 3.5 red and blue lines), complicating comparison of the absolute current values. Application of GABA results in desensitization observed within 30 seconds. The Ru photolysis experiments occur over a five minute period. Desensitization under photolysis could cause the observed current discrepancies. A simple explanation is the concentration of Ru(bpy)$_2$(PPh$_3$)(GABA)$^+$ in solution is lower than free GABA. In either case, activation of $GABA_A$ receptors is observed under irradiation, suggesting that the lack of activation of ELIC is likely due to the low affinity of ELIC towards propylamine.

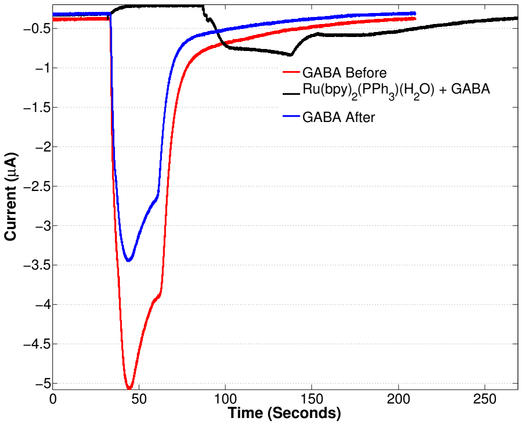

Figure 3.6: $GABA_A$ receptors were exposed to saturating GABA concentrations (red line) followed by application of $Ru(bpy)_2(PPh_3)(H_2O)^{2+}$ with saturating GABA (black line). A complete attenuation of the $GABA_A$ receptor response was observed. After removal of ruthenium, the response towards GABA did not return to pre-ruthenium levels (blue line).

$GABA_A$ receptor activation was then tested with $Ru(bpy)_2(PPh_3)(H_2O)^{2+}$, as with ELIC, to test for possible interactions between the ion channel and the photoproduct. Application of 11 μM GABA to provide a baseline $GABA_A$ response (Figure 3.6, red line). Receptors were then incubated with $Ru(bpy)_2(PPh_3)(H_2O)^{2+}$ for 30 seconds. Co-application of $Ru(bpy)_2(PPh_3)(H_2O)^{2+}$ + 11 μM GABA then occurred and significant attenuation of the $GABA_A$ response was observed (Figure 3.6, black line). This attenuation suggests interactions between $GABA_A$ receptors and the Ru that results in inhibition. Removal of the $Ru(bpy)_2(PPh_3)(H_2O)^{2+}$ and application of 11 μM GABA resulted in a diminished GABA response when compared with the pre-ruthenium currents (Figure 3.6, blue line). The diminished GABA response shows the $GABA_A$-Ru interaction is prolonged, and not reversed by extended periods of wash. The evidence for interaction between the Ru photoproduct and $GABA_A$ receptors cautions against the use of the $Ru(bpy)_2(PPh_3)(GABA)^+$ compound for photoactivation. GABA is released upon irradiation and able to activate channels, but the photoproduct also exists and inhibits the channels as well.

Perturbation by $Ru(bpy)_2(PPh_3)(H_2O)^{2+}$ of ELIC and $GABA_A$ receptors suggest that the effect observed with ELIC is not unique. ELIC is a cation selective channel. One mode of interaction could be the blocking of ELIC by the divalent Ru(II) complexes. Blocking of cation channels by divalent cations is a well known phenomenon; Zn^{2+} and Ca^{2+} are known blockers of ELIC [31]. Blocking exclusively

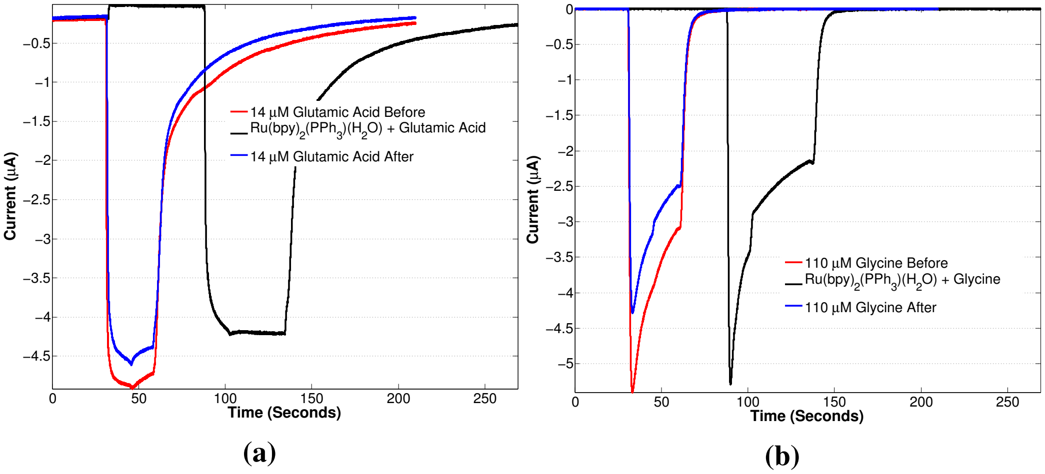

(a) **(b)**

Figure 3.7: Unusually, no inhibition of the agonist response is observed in the presence of $Ru(bpy)_2(PPh_3)(H_2O)^{2+}$, black line, for the AMPA receptor (a) and the Glycine receptor (b). The current response of the AMPA receptor (a) and Glycine receptor (b) to agonist are not altered after exposure to $Ru(bpy)_2(PPh_3)(H_2O)^{2+}$, blue lines.

by electrostatic interactions is unlikely as GABA$_A$ is an anion selective channel. To examine if the $Ru(bpy)_2(PPh_3)(H_2O)^{2+}$ inhibition is general a variety of ligand-gated ion channels were screened in the same manner. The glycine receptor and the AMPA receptor did not display any attenuation of agonist response in the presence of $Ru(bpy)_2(PPh_3)(H_2O)^{2+}$ (Figure 3.7). The glycine receptor is, like GABA$_A$, an anionic selective pentameric-ligand gated ion channel. The different inhibition properties suggests that inhibition is not just due to the ion selectivity. The AMPA receptor is a member of the ionotropic glutamate receptor family, not the petameric ligand-gated ion channel family. This family has vastly different molecular architecture that might be the origin of the difference in response that is observed. Significant inhibition was observed for ELIC, GLIC, GABA$_A$, 5HT$_{3A}$, $\alpha4\beta2$, $\alpha4\beta4$ $\alpha7$ and mouse muscle nAChR receptors by $Ru(bpy)_2(PPh_3)(H_2O)^{2+}$ (Figure 3.8). Regardless, significant and persistent perturbation is observed between the photoproduct and many ion channels. This perturbation limits the $Ru(bpy)_2(PPh_3)(L)^{n+}$ platform for use in photoactivation of ligand-gated ion channels.

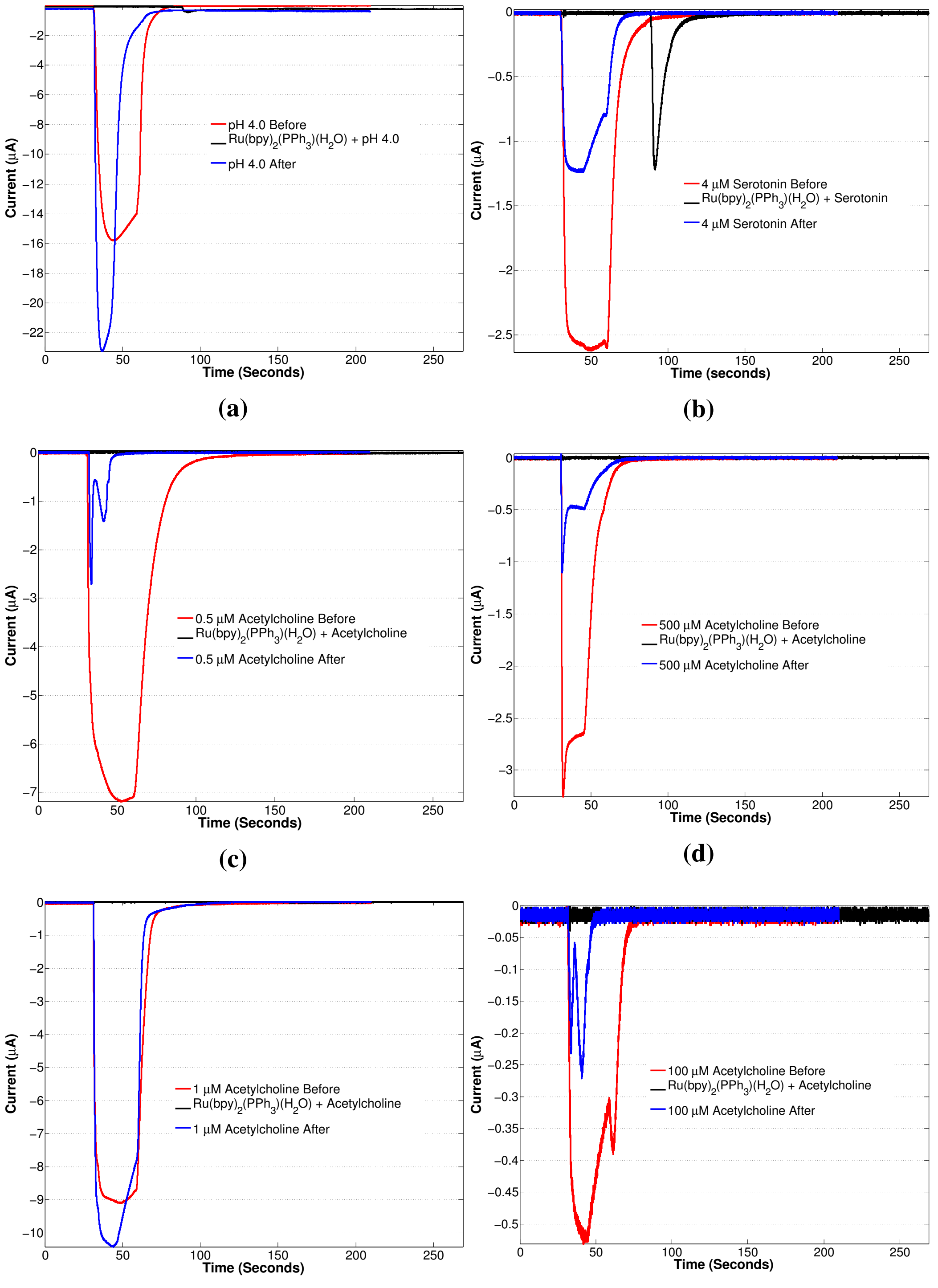

(a) **(b)**

(c) **(d)**

(e) **(f)**

Figure 3.8: Whole-cell voltage-clamp electrophysiology traces of ligand-gated ion channels exposed to Ru complexes. The inhibition of GLIC (a), $5HT_{3A}$ (b), A4B2 nAChR (c), A4B4 nAChR (d), Mouse Muscle nAChR (e), and A7 nAChR by co-application of saturating agoinst in the presence of $Ru(bpy)_2(PPh_3)(H_2O)^{2+}$ (black line). All of the ion channels show altered response to agonist after exposure to ruthenium, blue line.

A dose-response relation between Ru(bpy)$_2$(PPh$_3$)(H$_2$O)$^{2+}$ and the serotonin receptor (5HT$_{3A}$) was then examined. The serotonin receptor has an EC$_{50}$ value of 1.6 μM; the low EC$_{50}$ value suggests that the serotonin receptor does not need high ruthenium concentrations for potential activation. Incubation with Ru(bpy)$_2$(PPh$_3$)(H$_2$O)$^{2+}$ for 30 seconds, followed by co-application with 4 μM serotonin resulted in an inhibition dose-response relationship for the serotonin receptor (Figure 3.9). The IC$_{50}$ value for Ru(bpy)$_2$(PPh$_3$)(H$_2$O)$^{2+}$ is 2.5 μM (Figure 3.9b). This value is high in comparison to known inhibitors of the serotonin receptor that have low nanomolar inhibition [29]. Regardless, Ru(bpy)$_2$(PPh$_3$)(H$_2$O)$^{2+}$ displays clear inhibition properties in a concentration regime that competes with agonist binding. The inhibition at these concentrations limits the use of Ru(bpy)$_2$(PPh$_3$)(serotonin)$^{2+}$ for photoactivation of serotonin receptors. The serotonin receptor dose-response does not provide insight into the inhibition relationships with the remaining ligand-gated ion channels, but clearly demonstrates dose-dependent inhibition of an ion channel by Ru(bpy)$_2$(PPh$_3$)(H$_2$O)$^{2+}$.

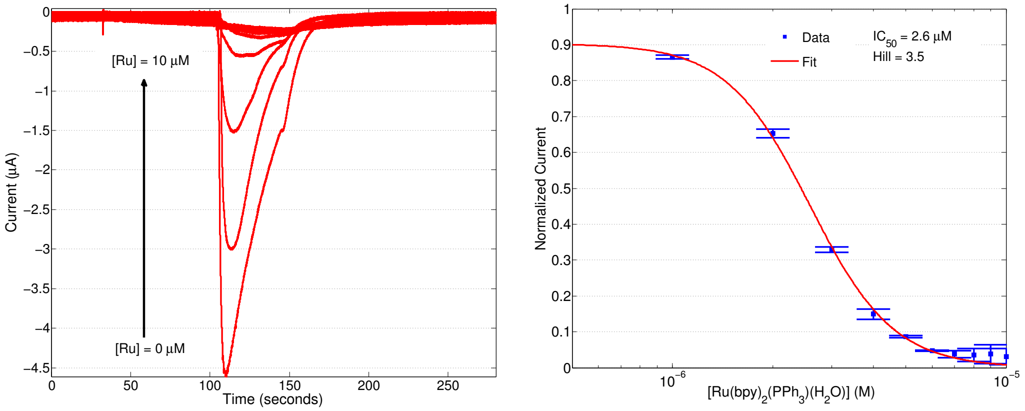

(a) **(b)**

Figure 3.9: A dose-dependent inhibition is observed for 5HT$_{3A}$ receptors upon co-application of Ru(bpy)$_2$(PPh$_3$)(H$_2$O)$^{2+}$ with serotonin. The complete inhibition of serotonin response is observed by 10 μM serotonin, (a). (b) The concentration where 50% of the 5HT$_{3A}$ receptors are inhibited is 2.6 μM , with a hill coefficient of 3.

3.3.2 Synthetic Modification to the Bipyridine and Phosphine Ligands

One potential workaround to the inhibition would be to attach an agonist that activates the receptor at much lower concentrations than the inhibition concentration. However, this is not possible for ELIC since propylamine is one of the most potent agonists, highlighting the insensitivity of ELIC in general. In an effort to remove deleterious interactions, synthetic modifications to the Ru(bpy)$_2$(PPh$_3$)(Agonist)$^{n+}$

scaffold were carried out (Figure (3.1a). The bipyridine ligands were substituted with carboxylic acid groups at the 4 and 4' positions. Also, each phenyl group of the phosphine ligand was substituted with sulfonate groups at the 3 position. The two modified ligands were used to synthesize a the series of Ru(II)-propylamine complexes. At physiological pH both the carboxylic acid and the sulfonate will be deprotonated, resulting in an overall charge of the Ru(II) species of +2, -1, -2, and -5 for $Ru(bpy)_2(PPh_3)(PrNH_2)^{2+}$, $Ru(bpy)_2(PPh_3\text{-}(SO_3^-)_3)(PrNH_2)$, $Ru(bpy\text{-}(COO^-)_2)_2(PPh_3)(PrNH_2)$, and $Ru(bpy\text{-}(COO^-)_2)_2(PPh_3\text{-}(SO_3^-)_3)(PrNH_2)$, respectively. Salt metathesis, used in the purification of $Ru(bpy)_2(PPh_3)(PrNH_2)^{2+}$, did not result in the successful isolation of any of the modified complexes. To purify these complexes, anion-exchange chromatography on a Q-column with an FPLC was used. The modified ruthenium complexes stacked at the top of the column upon loading. Reaction byproducts eluted in the void volume of the column, and the column was washed with excess pH 7.0 water. Either acidic water, or excess NaCl was used to elute of the modified Ru complexes. Each complex was then isolated by evaporation of the water *in vacuo*. Characterization of the photochemistry by NMR and UV-visible spectroscopy showed rapid release of propylamine in all cases

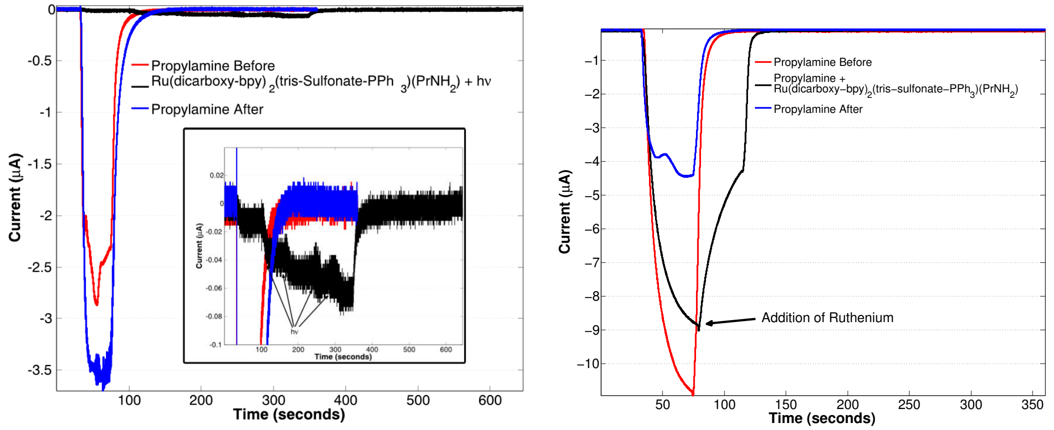

(a) **(b)**

Figure 3.10: (a) The photoactivation of ELIC is observed (black line, inset) by irradiation of the modified ruthenium protecting group, $Ru(4,4'\text{-dicarboxy-bpy})_2(PPh3\text{-}SO_3^-)(PrNH_2)^{5-}$. The activation upon irradiation is very small compared with the response of ELIC to just propylamine, red and blue lines. No inhibition of ELIC is observed after ruthenium exposure (blue line), when compared to before ruthenium (red line). (b) The addition of $Ru(4,4'\text{-dicarboxy-bpy})_2(PPh3\text{-}SO_3^-)(PrNH_2)^{5-}$ to activated ELIC results in attenuation of the propylamine response (black line). After removal of the ruthenium complex, the ELIC response to propylamine alone was significantly inhibited (blue line).

The modified Ru complex (*ca.* 50 μM) was then applied to ELIC-expressing oocytes and activation of ELIC was observed only under irradiation (Figure 3.10a, black line). Only a very small amount of activation was observed under irradiation due to the low concentrations of ruthenium photocage used. The ELIC response to propylamine is similar before and after exposure to the ruthenium complexes. However, upon application of propylamine, and exposure to the modified photocage, attenuation of the propylamine signal is observed (Figure 3.10b, black line). This signal attenuation remained after extended wash periods suggesting perturbation by either the ruthenium photocage, or the photoproduct. It is likely the inhibition also attenuates the observed photoactivation signal. ELIC would be activated by the released propylamine, and simultaneously inhibited by the presence of the ruthenium complex. The synthetic modifications made did not allay the inhibition observed between the ruthenium complexes and ELIC. These complexes were not tested with other channels because of the difficulty in purification.

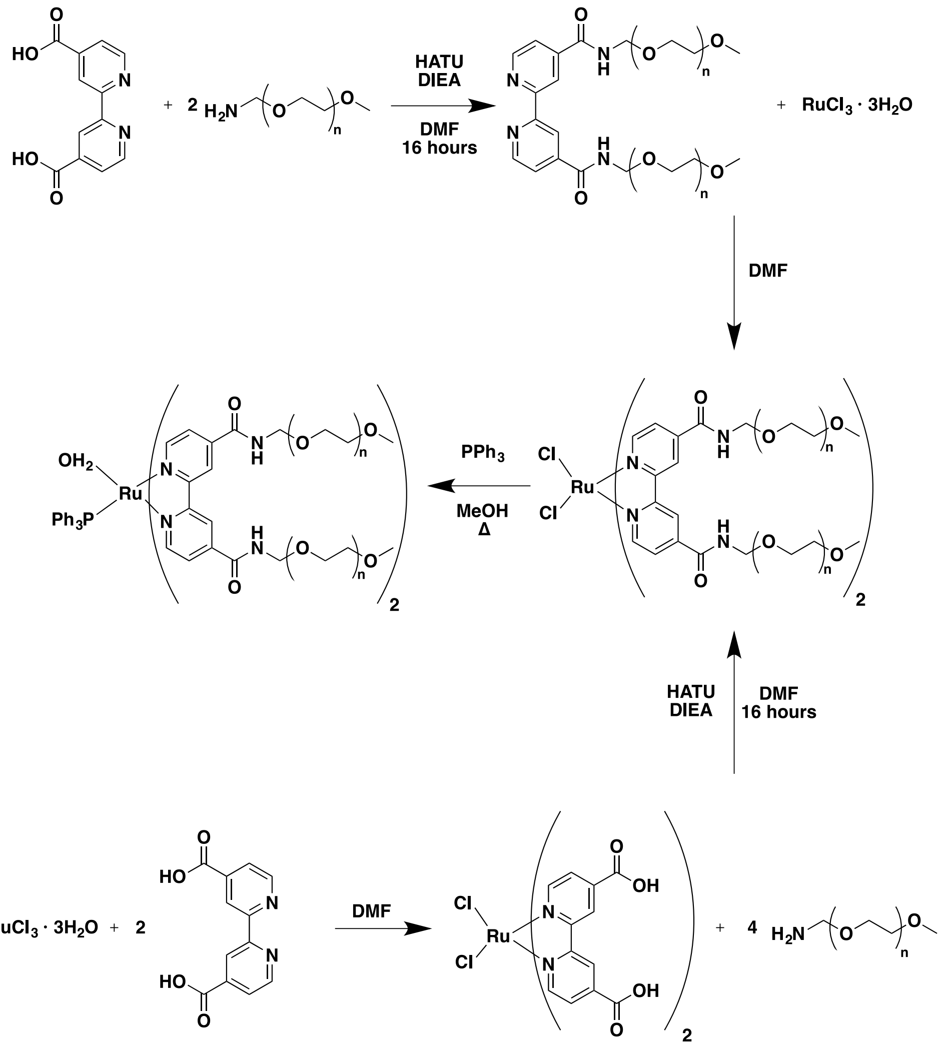

Figure 3.11: The synthesis of the PEGylated ruthenium photocages occurred by two different synthetic routes. Synthesis of the bpy-PEG ligand first (bottom), followed by metalation with ruthenium to afford Ru(bpy-PEG)2Cl$_2$. Alternatively, amide coupling of the Ru(4,4'-dicarboxy-bpy)2Cl$_2$ complex, with PEG afforded the same Ru(bpy-PEG)2Cl$_2$ molecule. The PPh3 lignad was then added to the complex, and the resulting Ru(bpy-PEG)2(PPh$_3$)(H$_2$O) was used.

In a effort to remove the deleterious interactions between the ruthenium complex and the ion channels other synthetic modifications were used. PEGylation of the dicarboxy-bipyridine, through amide bond formation chemistry, afforded a bipyridine ligand with two PEG-1K moieties. The complex was either synthesized by synthesis of the bpy-PEG ligand, then metalation, or by taking the Ru(4,4'(COO$^-$)-bpy)$_2$Cl$_2$ and performing the amide-coupling reaction with PEG (Figure 3.11). Purification by PD-10 size-exclusion chromatography separated the large Ru(bpy-PEG)$_2$Cl$_2$ product, from any byproducts. Any compounds smaller than 3000 Da are separated from the heavier Ru(bpy-PEG)$_2$(Cl)2, providing clean isolation from the bpy-PEG ligand, and other side products. $Ru(bpy\text{-}PEG)2(PPh_3)(H_2O)$ was then synthesized and the Ru-PEG interactions with ELIC and $5HT_{3A}$ examined.

ELIC receptors were exposed to 200 μM Ru-PEG complex and the response was examined in the presence of propylamine. Preincubation of ELIC with Ru-PEG, followed by application of Ru-PEG with propylamine resulted in an attenuated ELIC response (Figure 3.12a). To examine if the effect was due to the pre-incubation, ELIC was first exposed to propylamine, followed by co-application of propylamine with Ru-PEG. Upon co-application, the ELIC response is lost (Figure 3.12b). After exposure to Ru-PEG attenuation in ELIC response to propylamine was observed. The attenuation in the presence of Ru-PEG is similar to the interaction observed for the parent $Ru(bpy)_2(PPh_3)(H_2O)^{2+}$ complex. Less attenuation of ELIC by Ru-PEG is observed, but the existence of any attenuation suggests that Ru-PEG is not suitable to for the use in the photoactivation of ELIC.

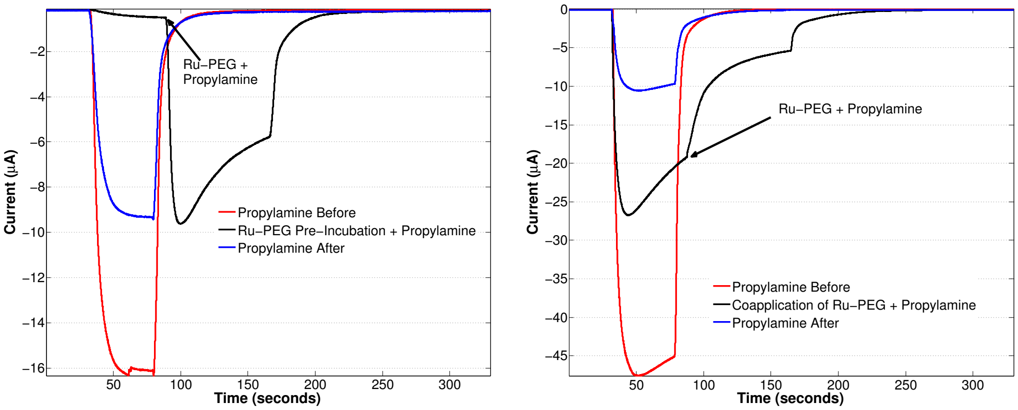

(a) **(b)**

Figure 3.12: (a) The preincubation of ELIC with $Ru(bpy\text{-}PEG)_2(PPh_3)(H_2O)$, followed by activation with propylamine in the presence of Ru-PEG results in attenuation of the ELIC signal (black line). Removal of the Ru-PEG, followed by application of propylamine resulted in a diminished ELIC response in the absence of ruthenium (blue line). (b) Exposure of activated ELIC to $Ru(bpy\text{-}PEG)_2(PPh_3)(H_2O)$ results in a decrease in the signal (black line). The inhibition of ELIC response to propylamine remains after removal of ruthenium (blue line). Pre-incubation (a), and co-application (b), of $Ru(bpy\text{-}PEG)_2(PPh_3)(H_2O)$ suggests the order of application is not responsible for the observed effects.

The serotonin receptor response to Ru-PEG was much different than to the parent $Ru(bpy)_2(PPh_3)(H_2O)^{2+}$ complex. Exposure of $5HT_{3A}$ receptors to Ru-PEG, in either addition order, results in positive modulation of the serotonin receptor response to agonist (Figure 3.13). The response of $5HT_{3A}$ receptors to serotonin after Ru-PEG exposure is robust. The concentration of Ru-PEG used in these experiments was 200 μM , a value 100 times the IC_{50} of the parent complex (Figure 3.9b). This dramatic increase in tolerance of the Ru-PEG complex appears to suggest that PEGylation of the molecule does remove the inhibition interactions. However, positive modulations of the channel are now observed. Any interaction with the channel is undesired, thus also ruling out this complex in the activation of serotonin receptors.

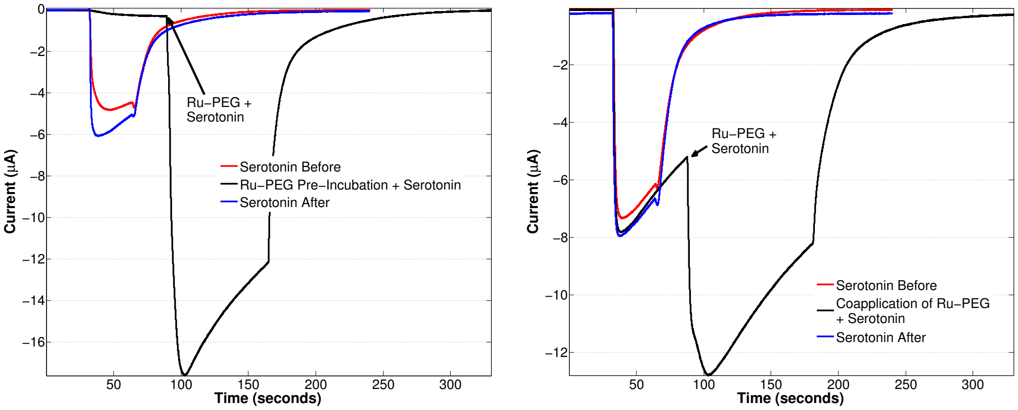

(a) **(b)**

Figure 3.13: The preincubation (a), or co-application (b), of $Ru(bpy\text{-}PEG)_2Cl_2$ with serotonin results in a large positive modulation of the serotonin receptors response to application of saturating serotonin concentrations (black line) when compared to serotonin alone (red line). After removal of the Ru-PEG complex from solution the $5HT_{3A}$ receptor response to serotonin alone (blue line) is similar to the response observed before ruthenium exposure (red line).

The non-selective inhibition that was observed between $Ru(bpy)_2(PPh_3)(H_2O)^{2+}$ complexes, and ion channels, motivated some investigation into the mode of inhibition. To determine the origins of the interactions of the ruthenium photocage with the ion channels studied $Ru(bpy)_2(PPh_3)(H_2O)^{2+}$ was dissected. ELIC exposed to bpy-PEG with propylamine after preincubation displayed inhibition of the propylamine response, that persisted after the removal of the bpy-PEG compound (Figure 3.14a). Exposure of activated ELIC to bpy-PEG resulted in slight positive modulation of the signal (Figure 3.14b), with no inhibition of the propylamine signal observed after removal of bpy-PEG. Application of just the bpy-PEG ligand to serotonin receptors does not result in substantial change of response to agonist (Figure 3.14c and d). This suggests that the interaction is not exclusively due to the bpy-PEG ligand.

ELIC and serotonin receptors were then exposed to $Ru(bpy)_2(H_2O)_2{}^{2+}$. The Ru(II)-polypyridyl system allows for efficient photosubstitution; removal of the phosphine ligand will determine if the base $Ru(bpy)_2$ complex can be used for the photoacti-

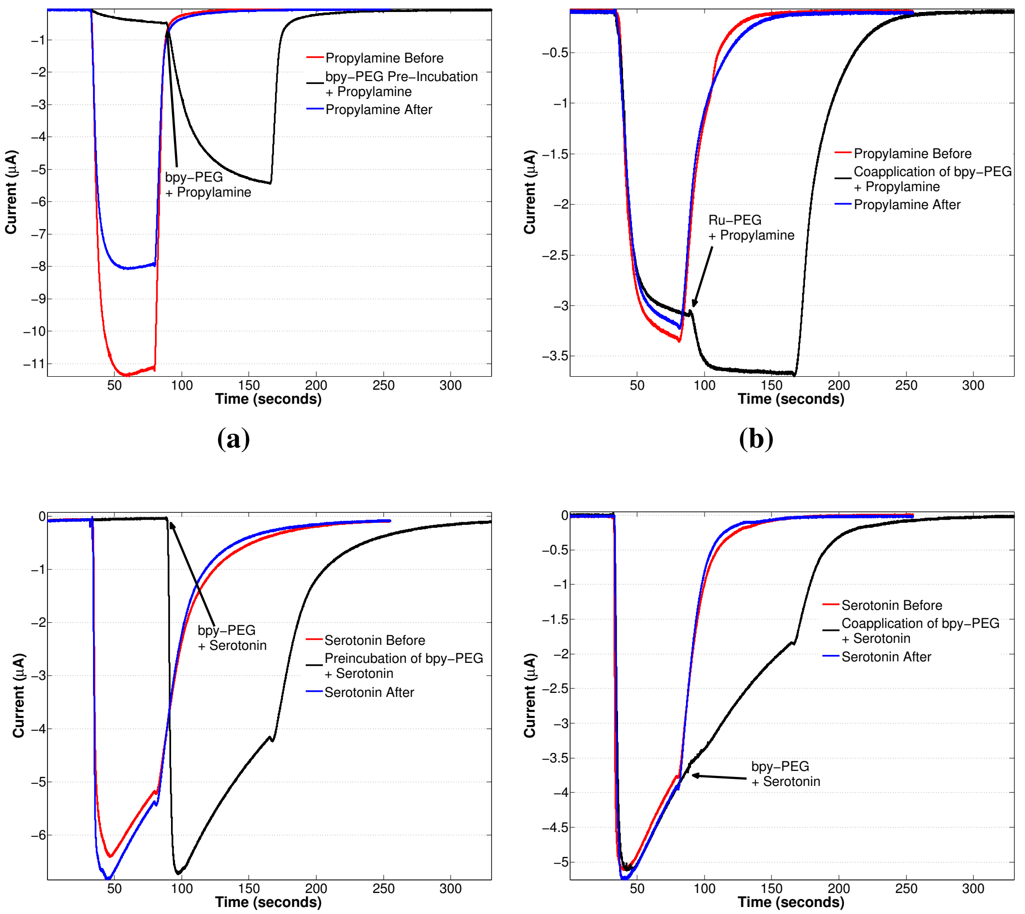

(a) **(b)**

(c) **(d)**

Figure 3.14: The preincubation (a) of bpy-PEG with propylamine results in inhibition of the response to propylamine by ELIC (black line). This inhibition lasted after removal of the bpy-PEG compound (blue line). (b) Co-application of the bpy-PEG with propylamine to activated ELIC ion channels results in a slight positive modulation of the signal (black line). In the co-application example, the propylamine response of ELIC after removal of bpy-PEG (blue line) is similar as before exposure to bpy-PEG (red line). The $5HT_{3A}$ receptor response to serotonin are not affected by addition of bpy-PEG in either order of addition (c) and (d). The concentrations of bpy-PEG in these experiments is 150 μM .

vation of ion channels. Removal of the phosphine ligand resulted in the elimination of the inhibition properties observed for both ELIC and serotonin receptors (Figure 3.15). This result suggests that the inhibition is likely due to the phosphine ligand on the ruthenium photocage. The effect of the phosphine moiety was mentioned briefly previously [32]. However, only effects of millimolar phosphine concentrations were discussed. The high-concentration requirement previously observed is not in agreement with my observations. Preparation of phosphine-free ruthenium photocages with similar electronic structures was then examined.

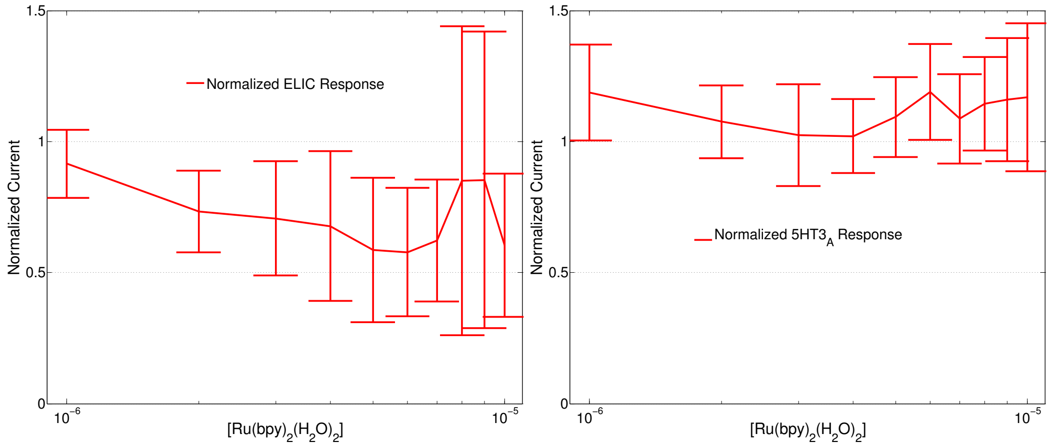

(a) **(b)**

Figure 3.15: (a) The inhibition of propylamine signal observed upon co-application of $Ru(bpy)_2(H_2O)_2$ and propylamine to ELIC receptors. Little inhibition is observed across the 10 μM range, however these concentrations are much lower than needed to ELIC activation. (b) $5HT_{3A}$ receptor response to co-application of $Ru(bpy)_2(H_2O)_2$ and serotonin. There is little inhibition observed at any of the concentrations tested. This is in contrast to the inhibition interactions observed between $5HT_{3A}$ and $Ru(bpy)_2(PPh_3)(H_2O)^{2+}$ (Figure 3.9).

3.3.3 Synthesis and Characterization of Phosphine-Free Ruthenium Photocages

The addition of a phosphine ligand to Ru complexes lowers the energy difference between the MLCT and LF states, allowing for more thermal population of the dissosiative LF state at room temperature (Figure 1.5). Removal of the PPh_3 ligand from the Ru photocage results in a significant decrease in quantum yield for ligand release [18]. $Ru(bpy)_2(PrNH_2)_2$ was synthesized (Figure 3.1b) and irradiated to examine the photochemistry. Free propylamine appears in the NMR over five hours, and the expected red-shift in the UV-visible spectrum also occurs (Figure 3.16a and b). In comparison, the release of agonist from $Ru(bpy)_2(PPh_3)(Agonist)^{n+}$ was complete in minutes (Figure 3.2). The prolonged irradiation time of ${Ru(bpy)_2(PrNH_2)_2}^{2+}$ required for propylamine release renders this complex useless for photoactivation studies.

${Ru(tpy)(PrNH_2)_3}^{2+}$ was also synthesized (Figure 3.1c) as a phosphine-free derivative. The known photophysical properties of ${Ru(tpy)_2}^{2+}$ motivated the synthesis of ${Ru(tpy)(PrNH_2)_3}^{2+}$. ${Ru(tpy)_2}^{2+}$ has a short excited-state lifetime, suggesting efficient non-radiative decay. Population of the LF states, and subsequent dissociation of a ligand, is a mechanism of non-radiative decay that could lead to a shorter excited-state lifetime. No release of propylamine was observed from the ${Ru(tpy)(PrNH_2)_3}^{2+}$

complex following 5 hours of irradiation. The NMR and the UV-visible spectrum are almost identical before and after irradiation (Figure 3.16c and d). However, given the photostability, it does not appear that the Ru(tpy)$(PrNH_2)_3{}^{2+}$ complex decays via the LF states.

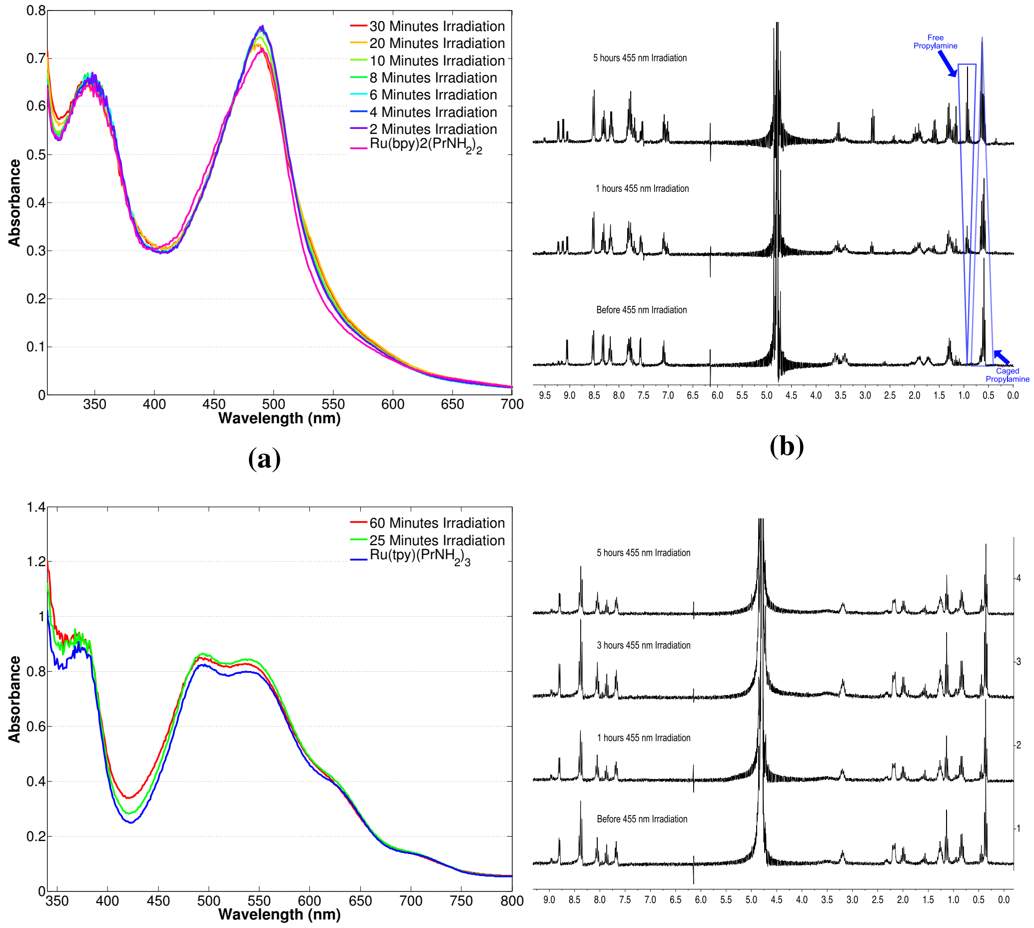

(a) **(b)**

(c) **(d)**

Figure 3.16: The irradiation of $Ru(bpy)_2(PrNH_2)_2{}^{2+}$ followed by UV-visible (a) and NMR spectroscopy (b). There is little change in the UV-visible spectra over the course of an hour irradiation. Release of propylamine is observed in the NMR after 5 hours of irradiation. The methyl peaks of propylamine are highlighted in the blue triangles for clarity. Caged propylamine resonance is present at *ca.* 0.5 ppm, and the free propylamine resonance is at *ca.* 1.0 ppm. Irradiation of Ru(tpy)$(PrNH_2)_3{}^{2+}$ does not result in a change in the UV-visible spectrum (c) after an hour of irradiation. There is no free propylamine observed in the NMR (d) after 5 hours of irradiation. In the case of Ru(tpy)$(PrNH_2)_3{}^{2+}$, there is no change observed in the NMR.

The photostability of $Ru(bpy)_2(PrNH_2)_2{}^{2+}$ and Ru(tpy)$(PrNH_2)_3{}^{2+}$ led to further modifications of the Ru(II) platform. I was able to synthesize $Ru(dmb)_2(PrNH_2)_2{}^{2+}$ and Ru(tpy)(dmb)$(PrNH_2)^{2+}$; these derivatives used 6,6'-dimethyl-bipyridine (dmb) in place of the unsubstituted bipyridine ligand. The methyl groups on the bpy ligand point toward the metal center of the complex. The resulting steric crowding creates distortion of the symmetry. It was recently shown that the distorted octahedral results in a large increase in photodissociation of amine ligands in aqueous environments [15, 26, 33].

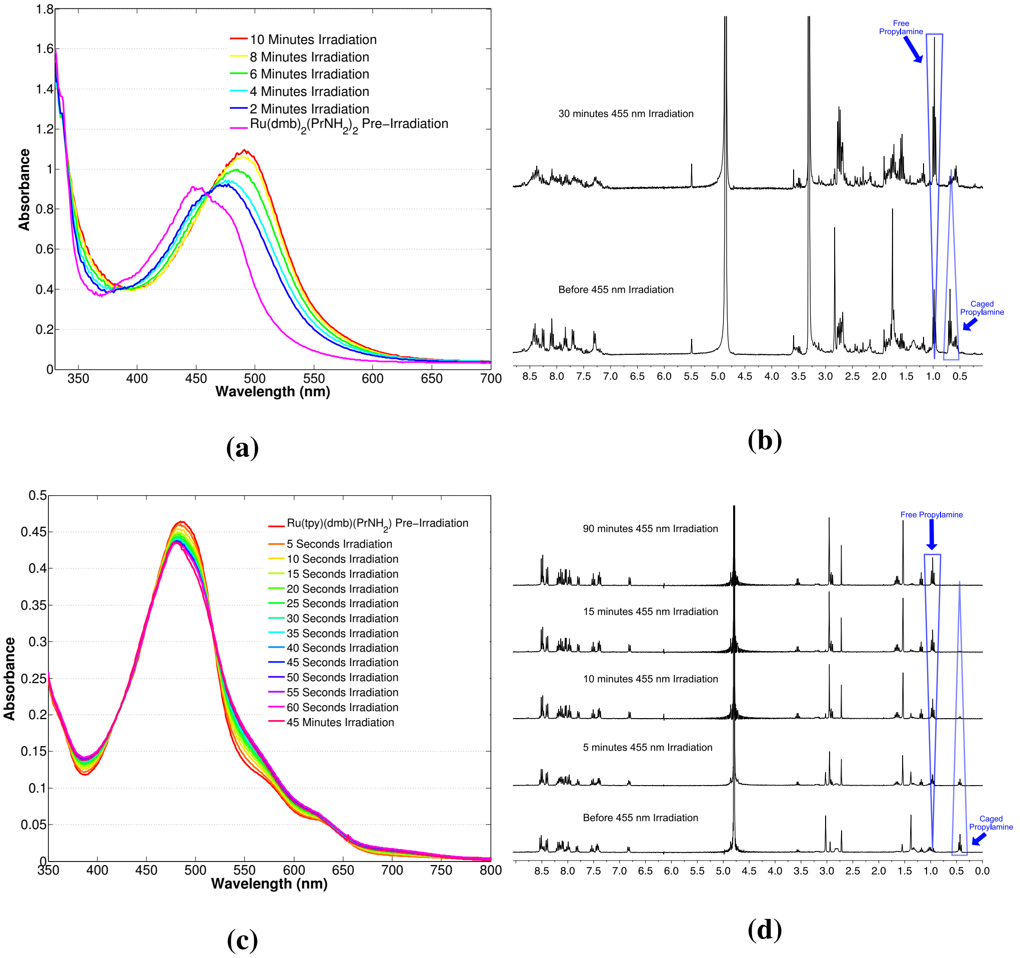

(a) **(b)**

(c) **(d)**

Figure 3.17: Monitoring the phosphine-free Ru complexes by UV-visible (a and c) and ^{1}H NMR spectroscopy (b and d). In the NMR spectra the propylamine methyl peaks are highlighted in the blue triangles; the methyl peaks are the easiest to track. The caged propylamine is observed at *ca.* 0.5 ppm, and free propylamine is observed at *ca.* 1.0 ppm. The irradiation of $\mathrm{Ru(dmb)_2(PrNH_2)_2}^{2+}$ by 455 nm light, monitored by UV-visible (a) and NMR spectroscopy (b). Rapid change in the UV-visible spectrum is observed even after 1 minute, and appears to be complete after 10 minutes of irradiation. After 30 minutes of 455 nm irradiation, release of propylamine is observed in the NMR as well. The release of propylamine occurs much faster than the analogous $\mathrm{Ru(bpy)_2(PrNH_2)_2}^{2+}$ complex. Irradiation of $\mathrm{Ru(tpy)(dmb)(PrNH_2)}^{2+}$ results in complete conversion in 60 seconds as monitored by UV-visible spectroscopy (c). Free propylamine is observed in the NMR after five minutes of irradiation, and complete conversion is observed by 15 minutes of irradiation (d).

The $\mathrm{Ru(dmb)_2(PrNH_2)_2}^{2+}$, and $\mathrm{Ru(tpy)(dmb)(PrNH_2)}^{2+}$ complexes were examined for use as a photocaged for propylamine. Irradiation of $\mathrm{Ru(dmb)_2(PrNH_2)_2}^{2+}$ resulted in the rapid release of propylamine. Complete conversion of the UV-visible spectrum is observed after 10 minutes of 455 nm irradiation (Figure 3.17a). Monitoring the photoreaction by NMR shows the rapid appearance of free propylamine (Figure 3.17b). $Ru(dmb)_2(PrNH_2)_2{}^{2+}$ can release two equivalents of propylamine. Quantification of the release could be achieved using a NMR standard. Also, under irradiation the NMR peaks corresponding to the dimethyl groups disappear. No free dmb is present in the NMR, and it is unclear what is occurring and further investigation is needed.

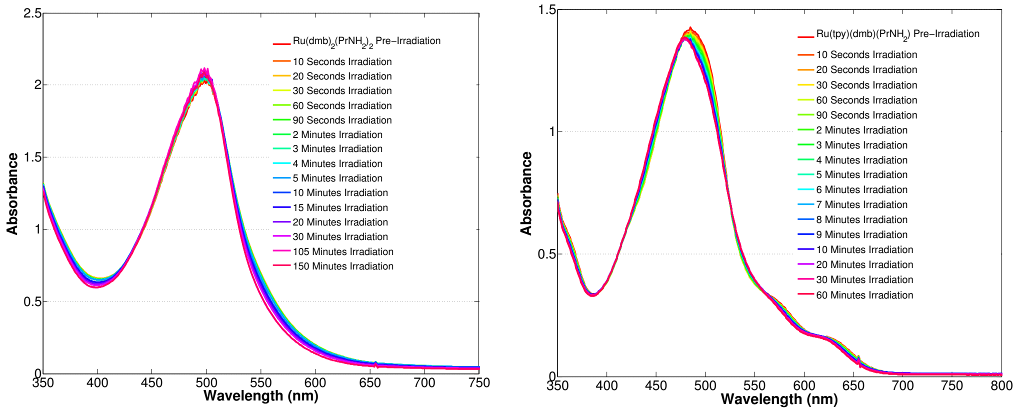

(a) **(b)**

Figure 3.18: Irradiation of $Ru(dmb)_2(PrNH_2)_2{}^{2+}$ (a), and $Ru(tpy)(dmb)(PrNH_2)^{2+}$ by a 10 mW HeNe laser resulted in release of propylamine after 60 minutes. This timescale for release is longer than with 455 nm irradiation; however, this demonstrates that $Ru(dmb)_2(PrNH_2)_2{}^{2+}$ and $Ru(tpy)(dmb)(PrNH_2)^{2+}$ can release ligands under red light irradiation.

$Ru(tpy)(dmb)(PrNH_2)^{2+}$ also displayed favourable release kinetics. Irradiation with a 455 nm light resulted in complete conversion of the UV-visible spectrum in 60 seconds (Figure 3.17c), with propylamine release complete in 15 minutes as observed by NMR (Figure 3.17d). The difference in irradiation time required is due to differences in experimental setup. UV-visible experiments were done on an optically dilute sample, while the NMR experiments require much higher concentrations; the light source is the same, and the intensity of the irradiation limits the conversion rate in the NMR experiments. The release of propylamine from the 6,6'-dimethyl-bpy derivatives is much more rapid than the bpy complexes, highlighting the importance of the geometric distortion. Another exciting feature of these complexes is the red-shifted MLCT transition in the absorption spectrum. Irradiation using a HeNe laser (632.8) resulted in release of propylamine from both complexes (Figure 3.18). Decaging of molecules using red-light is of interest for use in a photodynamic therapies. The release of propylamine using 632.8 nm light showcases the potential application of Ru(dmb)$_2$(L)$_2$$^{2+}$ and Ru(tpy)(dmb)(L)$^{2+}$ as a generic photocage for biological applications.

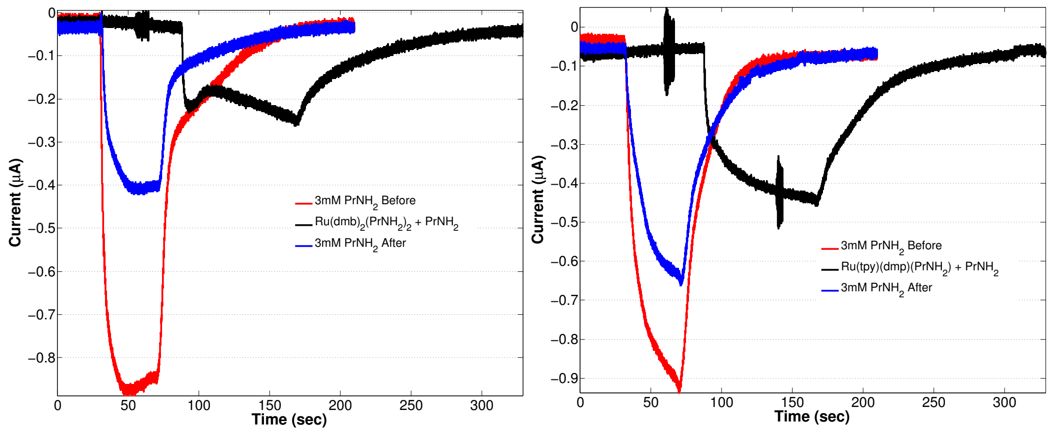

(a) **(b)**

Figure 3.19: (a) Application of Ru(dmb)$_2$(PrNH$_2$)$_2$$^{2+}$ to ELIC in the presence of propylamine results in an attenuated response to propylamine (black line). After removal of Ru(dmb)$_2$(PrNH$_2$)$_2$$^{2+}$, the ELIC response to propylamine is not the same as the propylamine response before ruthenium exposure (blue line). (b) The ELIC response to propylamine with Ru(tpy)(dmb)(PrNH$_2$)$^{2+}$ is attenuated (black line) compared with the propylamine response before ruthenium exposure (red line). After removal of Ru(tpy)(dmb)(PrNH$_2$)$^{2+}$ the ELIC response to propylamine is diminished (blue line). This suggests that phosphine-free ruthenium complexes also interact in a deleterious manner.

Ru(dmb)$_2$(PrNH$_2$)$_2$$^{2+}$ and Ru(tpy)(dmb)(PrNH$_2$)$^{2+}$ were then tested for interactions with ELIC. Application of 100 μM Ru(tpy)(dmb)(PrNH$_2$)$^{2+}$ did not result in any ELIC activation upon application in the dark. Co-application of Ru(tpy)(dmb)(PrNH$_2$)$^{2+}$ with propylamine resulted in significantly attenuated ELIC response to propylamine (Figure 3.19b, black line). The buffer was exchanged, and ELIC response to propylamine after exposure to Ru(tpy)(dmb)(PrNH$_2$) was significantly attenuated compared to before ruthenium application (Figure 3.19b, blue line). This suggests that some deleterious interactions still exists even with the removal of the phosphine ligand. Ru(dmb)$_2$(PrNH$_2$)$_2$$^{2+}$ was also tested, and similar attenuation of ELIC activation was observed (Figure 3.19a). The phosphine-free ruthenium complexes display favourable photosubstitution properties *in vitro*, though interactions between the complexes and ELIC still exist. ELIC is significantly perturbed, which prohibits the use of these complexes as molecules for use in the photoactivation of ELIC. ELIC is a very agonist-insensitive ion channel and requires high concentration of propylamine. As a result, 100 μM ruthenium was used, at a concentration much higher than was used in the Ru(bpy)$_2$(H$_2$O)$_2$$^{2+}$ response curves previously. This inhibition suggests at high concentrations, even the phosphine-free ruthenium complexes complex still inhibit ion channels.

3.3.4 Inhibitions by Ruthenium Complexes in Mammalian Cells

Inhibition has been observed with a variety of Ru(II) photocages and ion channels. All of these studies used *Xenopus laeviss* oocyte cells to express the ion channel under study. To examine if the effect observed is an oocyte phenomenon inhibition studies with mammalian cells were conducted. Serotonin receptors were expressed in HEK293T cells, and activation assayed by monitoring the fluorescence of a membrane-potential sensitive fluorescent dye. The membrane-potential sensing dye incorporates into the membrane bilayer, and the resting potential of the membrane results in dye localizing on the extracellular side of the membrane. An external quencher is applied resulting in fluorescence quenching of the dye. Upon activation of receptors, the dye moves across the membrane toward the cytoplasm, and away from the quencher, resulting in an increase in fluorescence observed.

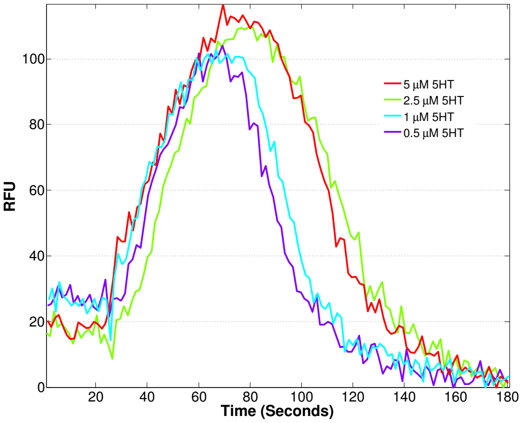

Figure 3.20: The application of varying concentrations of serotonin to HEK293T cells expressing the $5HT_{3A}$ receptor. A fluorescence increase is observed for all concentrations of serotonin added. This fluorescence increase is indicative of receptor activation.

To test for $5HT_{3A}$ expression in HEK293T cells, serotonin was applied and an increase in fluorescence of the dye was observed (Figure 3.20). The increase in fluorescence indicates activation of ion channels. Following verification of expression, the cells were exposed to either 10 μM or 100 μM $Ru(dmb)_2(PrNH_2)_2{}^{2+}$, with or without 5 μM serotonin present. No activation of serotonin receptors was observed upon application of $Ru(dmb)_2(PrNH_2)_2{}^{2+}$ alone (Figure 3.21a and b, red lines). Co-application of serotonin with $Ru(dmb)_2(PrNH_2)_2{}^{2+}$ does not result an increase in fluorescence as observed with just 5 μM serotonin alone (Figure 3.21a and b, blue lines). $Ru(tpy)(dmb)(PrNH_2)^{2+}$ was tested in the same way, to similar ends (Figure 3.21c and d). No activation of serotonin receptors was observed with just Ru(tpy)(dmb)($PrNH_2$)$^{2+}$ alone. No activation of the serotonin receptor upon co-application of Ru(tpy)(dmb)($PrNH_2$)$^{2+}$ and serotonin at either concentration used was observed. The inhibition of $5HT_{3A}$ receptors in mammalian cells with Ru(tpy)(dmb)($PrNH_2$)$^{2+}$ and $Ru(dmb)_2(PrNH_2)_2{}^{2+}$ suggests that these compounds are not a viable for use in the photoactivation of ion channels. The activation assay method does not provide information to distinguish between inhibition or cell death. Both cell death, or inhibition, are undesired perturbations of the system. The HEK293T experiments indicate that the inhibition that was observed for a variety of ruthenium photocage complexes is most likely not an oocyte-specific phenomenon.

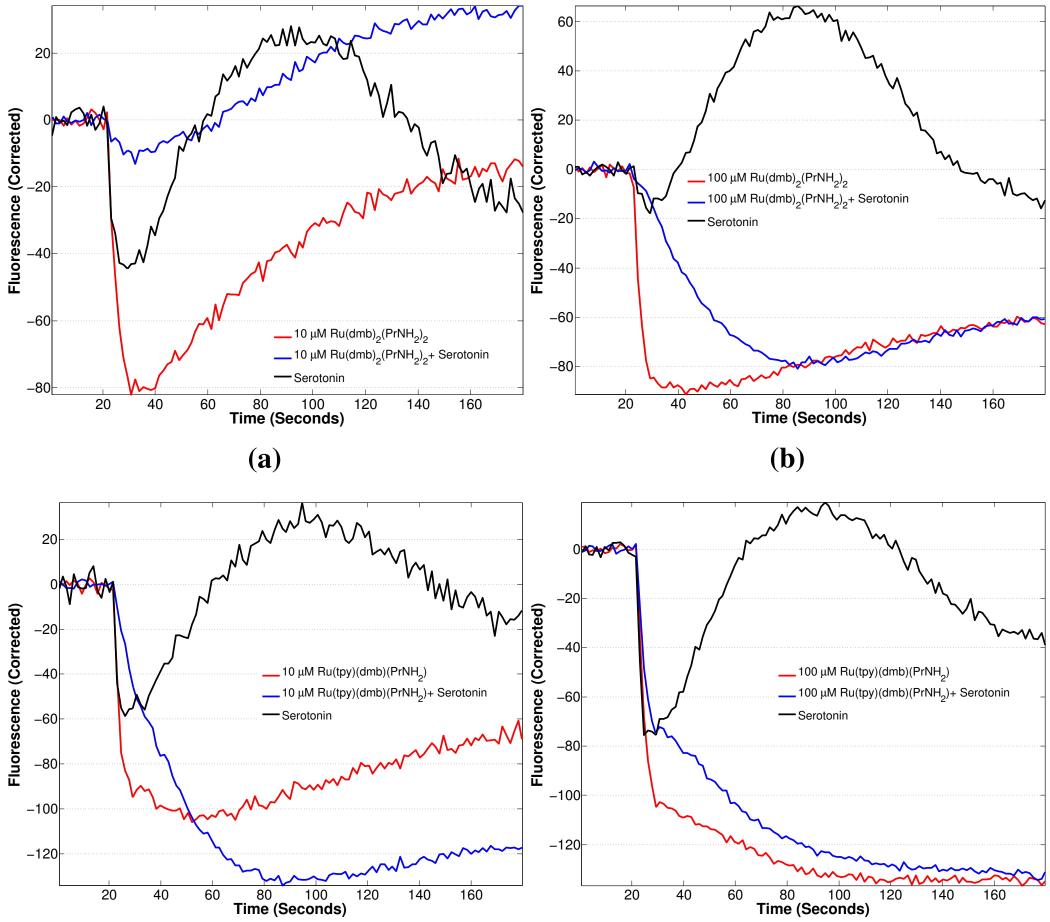

(a) **(b)**

(c) **(d)**

Figure 3.21: Application of 10 μM (a) and 100 μM (b) $Ru(dmb)_2(PrNH_2)_2{}^{2+}$ without serotonin (red lines) does not activate $5HT_{3A}$ receptors. Co-application of $Ru(dmb)_2(PrNH_2)_2{}^{2+}$ with serotonin (blue lines) does not result in activation of the $5HT_{3A}$ receptors. (c) and (d) Application of Ru(tpy)(dmb)($PrNH_2$)$^{2+}$ alone (red line), and with serotonin (blue lines) does not result in the activation of the serotonin receptors expressed in HEK cells. Inhibition of the serotonin receptor is observed by both $Ru(dmb)_2(PrNH_2)_2{}^{2+}$ and Ru(tpy)(dmb)($PrNH_2$)$^{2+}$ in HEK293T cells.

3.3.5 Potential Applications for Ruthenium Photocages

In an effort to find a use for $Ru(dmb)_2(L)_2^{n+}$ and $Ru(tpy)(dmb)(L)^{n+}$ photocages the AMPA receptors were investigated. Previous studies with $Ru(bpy)_2(PPh_3)(H_2O)^{2+}$ showed no interaction between the AMPA receptors and the Ru photoproduct (Figure 3.7a). This assay was then repeated with $Ru(tpy)(dmb)(H_2O)^{2+}$ to see if the previous result holds for the phosphine-free derivatives. Application of 50 μM $Ru(tpy)(dmb)(H_2O)^{2+}$ with glutamate present did not result in the significant inhibition of the AMPA receptors (Figure 3.22). There is about 20 % decrease in signal observed upon co-application, however it is unclear if this decrease is due to the presence of Ru. Rundown behaviour like this has been observed before with repeated I_{max} doses of agonist. Multiple application of I_{max} doses of just glutamate will determine if the behaviour observed is just rundown. The use of 50 μM ruthenium is still higher than would be needed with the AMPA receptor. The potentially low ruthenium concentration requirement, and the very mild inhibition of the APMA receptor, suggest that the Ru(tpy)(dmb)(Glutamate) complex might be viable for photoactivation.

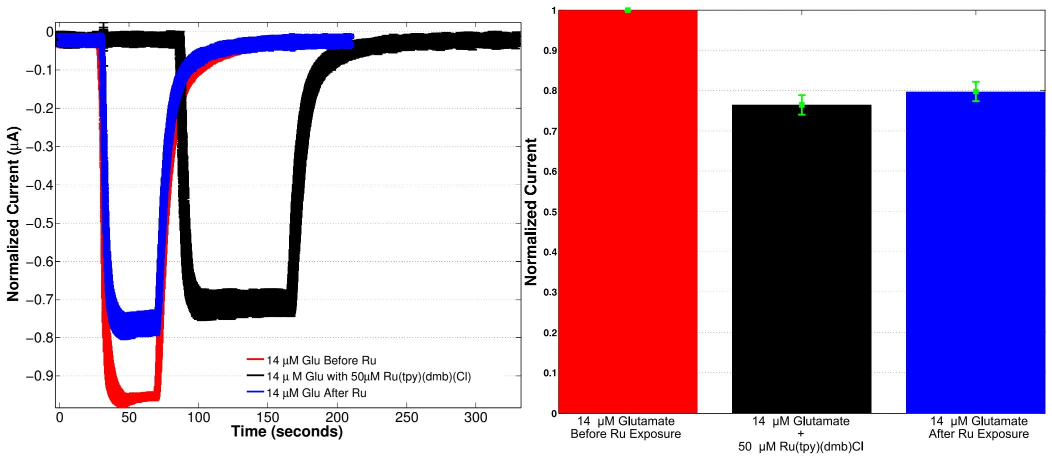

(a)

(b)

Figure 3.22: (a) An electrophysiology trace of the average response of AMPA receptors to the application of 14 μM glutamic acid (Glu). The currents are normalized to the Glu response before exposure to ruthenium (red line). Application of $Ru(tpy)(dmb)(H_2O)^{2+}$ with Glu (black line) results in very modest inhibition of the AMPA receptors. Exposure of the AMPA receptors to Glu after ruthenium (blue line) results in the same response as observed in the presence of $Ru(tpy)(dmb)(H_2O)^{2+}$. (b) A bar-graph representation of the same experiment as in (a).

3.3.6 Luminescence Properties of Ruthenium Photocages

The effective photodissociation of a ligand from the ruthenium complexes results from efficient crossing to the LF states, from the excited MLCT state. Efficient radiative decay indicates relaxation of the excited state in a non-productive manner for photodissociation. Thermal population of the LF states results in an increase in non-radiative decay pathways, a decrease in room-temperature luminescence, and an increase in photodissociation. The room-temperature and 77K luminescence spectra were examined for a series of ruthenium photocage complexes: $Ru(bpy)_2(PPh_3)(PrNH_2)^{2+}$, $Ru(bpy)_2(PrNH_2)_2{}^{2+}$, $Ru(tpy)(PrNH_2)_3{}^{2+}$, $Ru(dmb)_2(PrNH_2)_2{}^{2+}$, and $Ru(tpy)(dmb)(PrNH_2)^{2+}$. These complexes display varying levels of photodissociation. Luminescence of all the complexes is only present at 77K in a MeOH:EtOH glass (Figure 3.23, solid lines). No room temperature luminescence is visible (Figure 3.23, dashed lines). The luminescence spectra of all the complexes are similar to $Ru(bpy)_3{}^{2+}$ emission. This observation is consistent with the thermal enhancement of non-radiative decay pathways. Thermal activation of the LF states is likely a dominant decay pathway for the complexes with efficient photosubstitution: ($Ru(bpy)_2(PPh_3)(PrNH_2)^{2+}$, $Ru(dmb)_2(PrNH_2)_2{}^{2+}$, and $Ru(tpy)(dmb)(PrNH_2)^{2+}$). However, it is interesting in the case of the $Ru(tpy)(PrNH_2)_3{}^{2+}$ complex, where photostability is the greatest, that no room temperature luminescence is observed. The lack of luminescence suggests non-radiative decay from the excited state is the predominant form of relaxation, but not through the population of a dissociative LF state. Further investigation into the photophysics of these compounds might yield insight into the excited state energy surfaces. This could help in the further design of highly efficient ruthenium photocages.

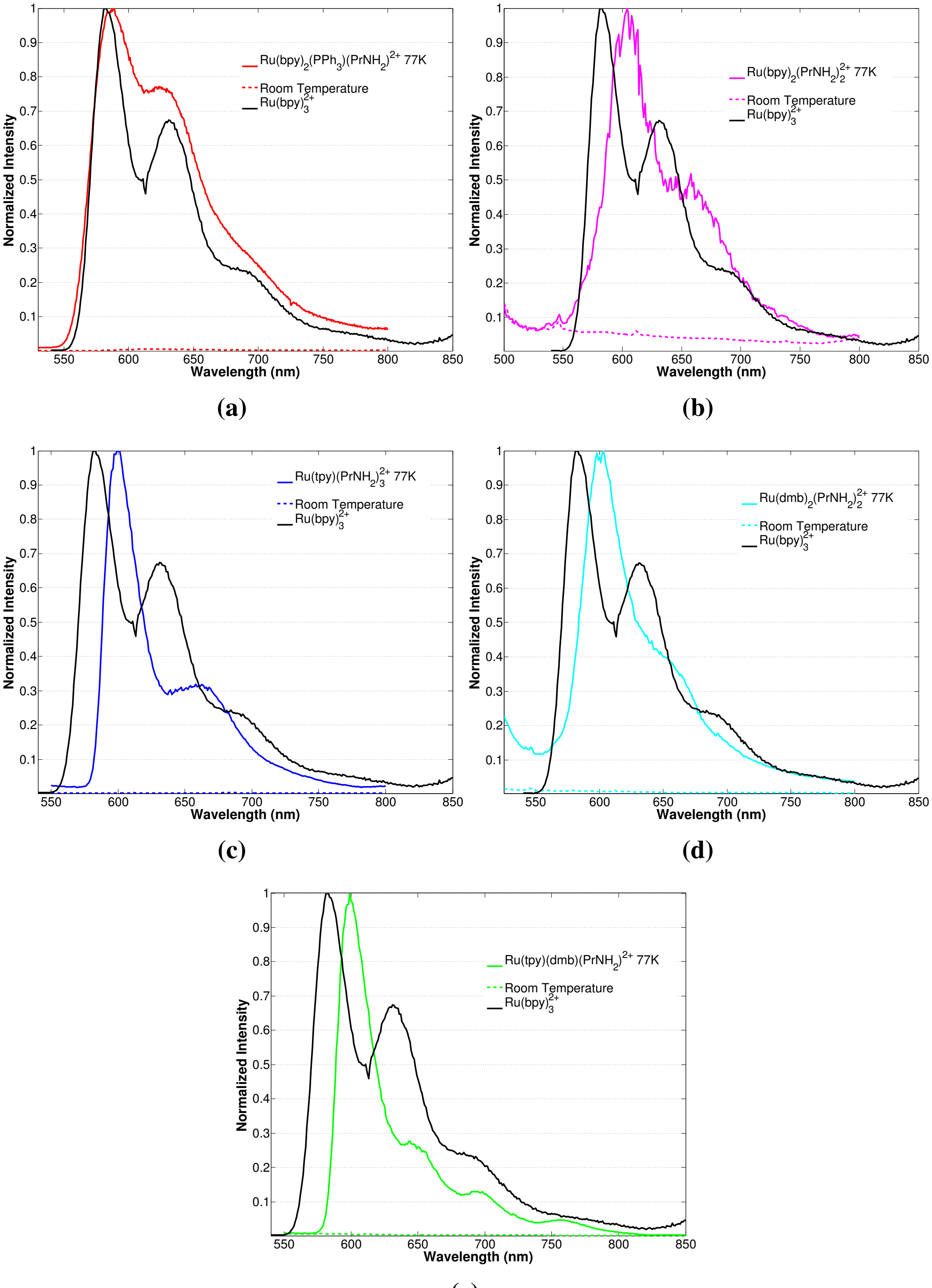

(a) **(b)** **(c)** **(d)** **(e)**

Figure 3.23: The steady-state luminescence measurements of $Ru(bpy)_2(PPh_3)(PrNH_2)^{2+}$ (a), $Ru(bpy)_2(PrNH_2)_2{}^{2+}$ (b), $Ru(tpy)(PrNH_2)_3{}^{2+}$ (c), $Ru(dmb)_2(PrNH_2)_2{}^{2+}$ (d), and $Ru(tpy)(dmb)(PrNH_2)^{2+}$ (e), in a 1:1 methanol:ethanol solvent mixture at 77K (solid lines), compared with the room temperature spectrum (dashed lines). All figures contain the same $Ru(bpy)_3{}^{2+}$ luminescence spectrum (black line) obtained at 77K. No room temperature luminescence is observed for any of the ruthenium complexes.

3.4 Conclusions and Future Outlooks

I investigated Ru(II) complexes for use in the photoactivation of ion channels. $Ru(bpy)_2(PPh_3)(L)^{n+}$ had previously been used for the photoactivation of ion channels, and I sought to use established systems for activation of ELIC. The propylamine derivative was synthesized, and displayed the reported *in vitro* properties. Unfortunately ELIC is a very insensitive channel, and oocytes did not survive the high concentrations (1 mM) of ruthenium required. Lower concentrations of ruthenium were able to photoactivate ELIC. However it was shown that photoproduct ($Ru(bpy)_2(PPh_3)(H_2O)^{2+}$) significantly inhibits activated ELIC. This inhibition was present even after extensive washing to remove the ruthenium. $Ru(bpy)_2(PPh_3)(H_2O)^{2+}$ was then tested across a panel of ligand-gated ion channels. Inhibition of all ion channels tested, except for two, occurred. A dose-dependent inhibition was observed for the serotonin receptor, with an IC_{50} value of 2.6 μM. This inhibition affinity is weak, but in a concentration range that competes with the activation of the receptors. Competitive inhibition and activation limits the functionality of these complexes as phototriggers.

Synthetic modifications such as PEGylation of the complexes did not eliminate the deleterious interactions observed between the ion channels and the ruthenium photoproduct. Little inhibition was observed with $Ru(bpy)_2(H_2O)_2{}^{2+}$, a difference of just a single phosphine ligand. The addition of the phosphine ligand to the $Ru(bpy)_2$-platform substantially enhances the efficiency of photodissocation. Derivatives of phosphine-free ruthenium photocages were then synthesized; complexes with a bulky 6,6'-dimethyl-bipyridine were able to efficiently release amine ligands under red light irradiation, which is a notable result. Inhibition was still observed between the phosphine-free ruthenium photocages, and ELIC. This is likely due to the high concentrations needed for ELIC activation. Inhibition was also observed between serotonin receptors expressed in mammalian cells, demonstrating that the inhibition is not oocyte cell specific. The conclusions from this work show that these compounds are useful for the photodeprotection of amine-based ligands. However, significant perturbation is observed across a large variety of channels. This limits the use of these compounds when studying ion channels.

The use of Ru(II) as photolabile protecting group is an attractive platform for the delivery of biologically active molecules. The ruthenium complexes are strongly absorbing in the visible region of the spectrum, and can display very efficient photodissociation. This system is also modular, and one can envision many different amines being protected using this method. However, I have shown in this chapter that significant interactions exist between the Ru(II) class of photocages and many different ion channels. I think examination of the specific interactions that exist between the ion channels and the $Ru(bpy)_2(PPh_3)(H_2O)^{2+}$ is warranted. If an interaction is identified, new Ru(II) complexes could be synthesized that would eliminate this interaction. I would also be interested in obtaining the dose-dependent inhibition for all the channels tested. The dose-dependent behaviour might provide insight as to the specificity of ion channel inhibition. One of the few remaining experiments that I think are worth trying is to examine the photoactivation of the AMPA receptor and the glycine receptor. These are the only two receptors that were not inhibited by the $Ru(bpy)_2(PPh_3)(H_2O)^{2+}$ photoproduct. I think that making the analogous glycine and glutamate protected Ru(tpy)(dmb)(L) is worth pursuit. These complexes are triggered by red light irradiation, providing potentially interesting biological photoactivation. I would recommend focusing on the glutamate receptor, as it is a common receptor found in the brain, and responsible for the excitatory signals.

From the work above I conclude that these Ru(II) protecting groups are not generally applicable for use in the study of ion channels. I would also caution the use of these complexes in systems that also have ion channels present. Side interactions are likely to occur. These complexes are an interesting platform for the generic photoprotection of amine ligands, and a good study of inorganic photochemistry.

References

(1) Crosby, G. A.; Perkins, W. G.; Klassen, D. M. *The Journal of Chemical Physics* **1965**, *43*, 1498–1503.

(2) Gafney, H. D.; Adamson, A. W. *Journal of the American Chemical Society* **1972**, *94*, 8238–8239.

(3) Durham, B.; Caspar, J. V.; Nagle, J. K.; Meyer, T. J. *Journal of the American Chemical Society* **1982**, *104*, 4803–4810.

(4) Creutz, C.; Chou, M.; Netzel, T. L.; Okumura, M.; Sutin, N. *Journal of the American Chemical Society* **1980**, *102*, 1309–1319.

(5) Sato, T.; Nozawa, S.; Tomita, A.; Hoshino, M.; Koshihara, S.-y.; Fujii, H.; Adachi, S.-i. *The Journal of Physical Chemistry C* **2012**, *116*, 14232–14236.

(6) Gawelda, W.; Johnson, M.; de Groot, F. M. F.; Abela, R.; Bressler, C.; Chergui, M. *Journal of the American Chemical Society* **2006**, *128*, 5001–5009.

(7) Gray, H. B.; Maverick, A. W. *Science* **1981**, *214*, 1201–1205.

(8) Wang, P.; Zakeeruddin, S. M.; Moser, J. E.; Nazeeruddin, M. K.; Sekiguchi, T.; Grätzel, M. *Nature Materials* **2003**, *2*, 402–407.

(9) Prier, C. K.; Rankic, D. A.; MacMillan, D. W. C. *Chemical Reviews* **2013**, *113*, 5322–5363.

(10) Winkler, J. R.; Gray, H. B. *Journal of the American Chemical Society* **2014**, *136*, 2930–2939.

(11) Knoll, J. D.; Albani, B. A.; Turro, C. *Accounts of Chemical Research* **2015**, *48*, 2280–2287.

(12) Sgambellone, M. A.; David, A.; Garner, R. N.; Dunbar, K. R.; Turro, C. *Journal of the American Chemical Society* **2013**, *135*, 11274–11282.

(13) Miskowski, V. M.; Gray, H. B.; Wilson, R. B.; Solomon, E. I. *Inorganic Chemistry* **1979**, *18*, 1410–1412.

(14) Pinnick, D. V.; Durham, B. *Inorganic Chemistry* **1984**, *23*, 1440–1445.

(15) Knoll, J. D.; Albani, B. A.; Durr, C. B.; Turro, C. *The Journal of Physical Chemistry A* **2014**, *118*, 10603–10610.

(16) Albani, B. A.; Durr, C. B.; Turro, C. *The Journal of Physical Chemistry A* **2013**, *117*, 13885–13892.

(17) Zayat, L.; Salierno, M.; Etchenique, R. *Inorganic Chemistry* **2006**, *45*, 1728–1731.

(18) Zayat, L.; Noval, M. G.; Campi, J.; Calero, C. I.; Calvo, D. J.; Etchenique, R. *ChemBioChem* **2007**, *8*, 2035–2038.

(19) Zayat, L.; Calero, C.; Alborés, P.; Baraldo, L.; Etchenique, R. *Journal of the American Chemical Society* **2003**, *125*, 882–883.

(20) Filevich, O.; Salierno, M.; Etchenique, R. *Journal of Inorganic Biochemistry* **2010**, *104*, 1248–1251.

(21) Filevich, O.; Carrone, G.; Andino Pavlovsky, V.; Etchenique, R. *Analytical Chemistry* **2012**, *84*, 5618–5624.

(22) Salierno, M.; Marceca, E.; Peterka, D. S.; Yuste, R.; Etchenique, R. *Journal of Inorganic Biochemistry* **2010**, *104*, 418–422.

(23) Sullivan, B. P.; Salmon, D. J.; Meyer, T. J. *Inorganic Chemistry* **1978**, *17*, 3334–3341.

(24) Sullivan, B. P.; Calvert, J. M.; Meyer, T. J. *Inorganic Chemistry* **1980**, *19*, 1404–1407.

(25) Collin, J. P.; Sauvage, J. P. *Inorganic Chemistry* **1986**, *25*, 135–141.

(26) Bahreman, A.; Limburg, B.; Siegler, M. A.; Bouwman, E.; Bonnet, S. *Inorganic Chemistry* **2013**, *52*, 9456–9469.

(27) Rienzo, M.; Lummis, S. C. R.; Dougherty, D. A. *Chemistry & Biology* **2014**, *21*, 1700–1706.

(28) Zimmermann, I.; Dutzler, R. *PLoS biology* **2011**, *9*, e1001101.

(29) Duffy, N. H.; Lester, H. A.; Dougherty, D. A. *ACS Chemical Biology* **2012**, *7*, 1738–1745.

(30) Daeffler, K. N. M. Functional evaluation of noncovalent interactions in neuroreceptors and progress toward the expansion of unnatural amino acid methodology., Ph.D. Thesis, Caltech: Caltech, 2014.

(31) Zimmermann, I.; Marabelli, A.; Bertozzi, C.; Sivilotti, L. G.; Dutzler, R. *PLOS Biol* **2012**, *10*, e1001429.

(32) Rial Verde, E.; Zayat, L.; Etchenique, R.; Yuste, R.; Verde, E. M. R.; Zayat, L.; Etchenique, R.; Yuste, R. *Frontiers in Neural Circuits* **2008**, *2*, 2.

(33) Jakubikova, E.; Chen, W.; Dattelbaum, D. M.; Rein, F. N.; Rocha, R. C.; Martin, R. L.; Batista, E. R. *Inorganic Chemistry* **2009**, *48*, 10720–10725.

Chapter 4

THE *IN VITRO* ACTIVATION OF FUNCTIONALLY RECONSTITUTED ELIC

4.1 Introduction

The ultimate goal of this project is to monitor the conformational changes associated with ion channel activation. The technique that was ultimately to achieve this is time-resolved fluorescence energy transfer (TR-FET). The use of the TR-FET technique requires the study be conducted in an *in vitro* setting. Any *in vitro* study must retain the *in vivo* function of the system being studied. The *in vitro* study of ion channels requires functional reconstitution of the desired ion channel into a membrane environment.

Functional reconstitution of ion channels requires: the ion channel isolable in large enough quantities to perform the experiments; an artificial membrane environment; and an assay to probe the function of the reconstituted ion channel. A number of ion channels have been successfully reconstituted previously in many membrane environments and used with various different assays to determine the functional state of the ion channel [1]. I want to reconstitute ion channels into lipid bilayer vesicles. Vesicles are amenable to characterization in cuvettes, a requirement for the future laser experiments. Previous ion channel reconstitutions into vesicles have used a variety of functional assays including: radioactive ion flux measurements [2], fluorescence measurements [3, 4], and injection into oocytes for electrophysiological measurements [5]. Radioactive measurements and fluorescence measurements directly assay the ion channel in the artificial environment, and I will use these to probe the function of reconstituted ion channels. In this chapter I discuss the heterologous expression and purification of ELIC. I examine various methods, and conditions used to reconstitute ELIC. I finally discuss the methods that succeeded in the functional reconstitution of ELIC into liposomes.

4.2 Methods and Materials

4.2.1 General Procedures

Purification of ELIC and GLIC occurred as previously published [6]. Standard biochemical techniques were used for the amplification of DNA in XL1-Blue *E. coli* cells (EMD Millipore). Protein expression took place in the BL21(DE3) strain of *E. coli*, also obtained from EMD Millipore. Protein gel electrophoresis occured using the PhastSystem (GE Healthcare), using SDS-PAGE (8-25%) gradient gels. The precision blue protein ladder was used as reference (Bio-rad). All chemicals were obtained from Sigma-Aldrich or Thermo Scientific and used without further purification. Lipids were obtained from Avanti Polar Lipids, and used without further purification. n-Dodecyl β-D-maltoside (DDM) detergent was obtained from Anatrace. UV-Visible spectra were obtained using a 1 cm quartz cuvette and a HP-8453 spectrometer. Steady-state luminescence experiments were conducted using a Jobin Yvon Spex Fluorolog-3-11 spectrometer. Samples were excited by a 450 W xenon arc lamp through a monochromator for excitation wavelength selection. Emission was collected upon scanning a monochromator, with detection achieved by a Hamamatsu R928P photomultiplier tube in photon counting mode. FlexStation (Molecular Devices) experiments used a standard glass-bottom 96-well plate for a sample holder. Excitation occurred with a xenon arc-lamp, and wavelength was selected using a monochromator. Emission was monitored over a single wavelength using a photomultiplier tube in photon counting mode. A minimum of 50 μl of solution was used for FlexStation experiments, which afforded complete coverage of a single well. Addition of solutions occurred using the FlexMode setting of the FlexStation, with addition of equi-volume of the below described manipulation solution as the sample volume. The FlexStation PMT sensitivity was set to 8, with sampling occurring as fast as possible. Stopped-flow measurements were conducted on a Kintek SF-2004 stopped-flow. Excitation was from a xenon arc-lamp, wavelength selected using a monochromator. Emission was collected through band-pass filters onto a photomultiplier tube in photon counting mode at the maximum acquisition rate of 1000 Hz. All data work up was done in MATLAB R2013b (Mathworks, Inc.).

4.2.2 Purification of ELIC

ELIC was purified as described elsewhere [6], and is discussed briefly here. ELIC with an N-terminal maltose-binding protein (MBP) tag, in pERCH6 vector was transformed into BL21(DE3) cells, and streaked onto an LB/agar petri dish. Overnight growth at 37°C afforded individual colonies. Single colonies were then picked, and allowed to grow overnight at 28°C in 25 mL of TB broth containing ampicillin. 5 mL of starter culture was used to innoculate 1 L of growth, which was shaken at 37°C until $OD_{600} = 3$. The cultures were cooled to 21°C for 1 hour. Expression was induced upon addition of 1 mM ICPP, and the cells were incubated at 21°C overnight. Cells were then harvested upon centrifugation at 10,000 g. Each 1 L of cells was resuspended in 10 mL of 50 mM Tris pH 7.5, 150 mM NaCl (Buffer A), with the addition of 4 tablets of cOmplete protease inhibitor (Roche). Resuspension occurred using a dounce homogenizer, and the resuspension passed through a microfluidizer for lysis. The lysate was then centrifuged at 12,000 g for 1 hour at 4°C. Resuspension of the solid fraction in buffer A occurred, followed by centrifugation at 110,000 g, 4°C for 2 hours to isolate the membrane fraction. The membrane fraction was then homogenized in 1 mL of buffer per 1 g of dry weight in buffer A with the addition of 2% DDM by weight. The resusupension was gently stirred at 4°C overnight. The next day the mixture was then centrifuged at 30,000 g to remove any non-solublized components, and the supernatent was loaded onto an amylose resin gravity column at 4°C. This column was washed with excess buffer A in the presence of 0.1% DDM. After the elutant desplayed no A_{280} signal, the protein was eluted with buffer A supplemented with 0.1% DDM and 20 mM maltose. The MBP-ELIC protein was then exposed to 100 equiv. of HRV 3C protease and incubated overnight at 4°C. Separation of the ELIC from MBP occured using a Superdex 200 10/300 size exclusion column equilibrated with buffer A and 0.1% DDM. A flow rate set to 0.1 mL/min yielded the best seperation. The second fraction tended to be ELIC, which was verified using SDS-PAGE. ELIC was then concentrated to no more than 10 mg/ml and either used fresh or flash frozen and stored at -80°C.

4.2.3 Formation of LUVs

The formation of large unilamellar vesicles (LUVs) was done using standard extrusion techniques available on the Avanti website, and briefly described below. Lipids dissolved in chloroform were dried under argon, then overnight under vacuum, in a glass vial. Resuspension of the lipids was achieved by addition of the desired solution (buffer, fluorescent dye, salts, etc) to the dried lipids, and vigorously shaken for 10 minutes. The samples were then subjected to five cycles of freeze-thaw in a dry-ice/ethanol bath to induce formation of unilamellar vesicles. Following the freeze-thaw cycles the lipids were extruded through a polycarbonate filter of desired diameter an odd number of times, generally 27. If the buffer needed to be exchanged these extruded liposomes were then subjected to standard PD-10 gel filtration conditions. The lipid vesicles were used as rapidly as possible.

4.2.4 Reconstitution without Detergent Destabilization

Purified ELIC or GLIC was mixed with preformed vesicles (with the desired encapsulated dye) to a desired w/w ratio. After incubation for 1 hour at room temperature, activated bio-beads were added (50 mg). Incubation with Bio-Beads SM2 (Bio-Rad) for an hour followed, after which the solution was transferred to clean container with new bio-beads. This process occurred for hours to days, depending on the sample. After incubation with at least 3 rounds of bio-beads, the samples were either used or stored at 4°C

4.2.5 Detergent-Destabilization Reconstitution

The procedure for detergent destabilization is generalized below [7]. Vesicles were preformed as above. After extrusion, vesicles were mixed with either CHAPS (5 mM) or DDM (0.5%) and incubated for 1 hour. After incubation, purified ELIC was added and incubated for 1 hour at room temperature. The addition of 5 rounds of 100 mg bio-beads occured, with each round incubating for 30 minutes at room temperature. After detergent extraction, the vesicles were either used immediately, or stored overnight at 12.5°C. The protocol that resulted in the most successful reconstitution of ELIC is as follows. 11.3 mg of DOPC and 3.7 mg of POPG were mixed together to form a 3:1 DOPC:POPG (mol/mol) ratio and were dried overnight. The lipids were rehydrated in 1114 μl of 10 mM HEPES, 10 mM succinate, 100 mM KNO_3 pH 7.0 (hydration buffer), and 557 μl hydration buffer supplimented with 75 mM ANTS. Vortexing for three minutes afforded a cloudy green solution. This solution was then subjected to 5 rounds of freeze-thaw. 5 mM CHAPS was added and sonicated for 1 minute. Purified ELIC was then added (the higher concentration the better), and incubated with the lipid solution for 1 hour at room temperature. 5 rounds of 100 mg addition of bio-beads occured over two and one half hours. The solution was then desalted on a PD-10 column to remove excess ANTS from solution. The samples were stored overnight at 12.5°C and used the next day.

4.3 Results and Discussion

4.3.1 Expression and Purification of ELIC

The plasmid for ELIC and the expression and purification protocols used were provided by Dr. Raimund Dutzler from the University of Zurich. I would like to make several comments about the expression and purification of ELIC. Use of a microfluidizer for cell lysis is crucial; sonication was used to lyse cells and no purified ELIC was isolated. Isolation of the membrane fraction, and proper resuspension before solubilization is crucial. Use of an ultra-centrifuge for membrane isolation is required. A regular floor centrifuge did not isolate the cell membrane fractions effectively. A dounce homogenizer effectively resuspended the membrane for solubilization. If large chunks of membrane remained after resuspension it is likely complete exposure to detergent molecules did not occur, and ELIC was less effectively solubilized. This sample also resulted in lower ELIC yields. All purification should be done at 4°C. A 100% yield of cleavage of the maltose-binding protein (MBP), with HRV3c protease, was never achieved. In the presence of huge excesses of HRV3C protease, complete cleavage did not occur. Figure 4.1a shows a typical chromatograph of the final sized exclusion column, with the large peak arising from the uncleaved ELIC-MBP pentamers. The expression and purification of HRV3c protease in house (it is very expensive to purchase) would allow for optimization of ELIC-MBP cleavage, or the use of enough to result in full cleavage. Replacing the HRV3C protease site with another common protease site is another potential option. The uncleaved MBP-ELIC was purified from the cleavage reaction, but due to limitations in protease supply I never subjected these fraction to repeated cleavage conditions.

After isolation of purified, detergent-solublized, ELIC, gel electrophoresis was performed to verify the protein purity (Figure 4.1b); the ELIC-MBP fusion protein, ELIC monomer, and MBP monomer were observed. ELIC is purified as a pentamer and elutes before MBP on the column (Figure 4.1a, not shown), but the denaturing conditions of the gel result in the protein running as a monomer. Mass spectrometry on the purified samples was unsuccessful; however, with the advances in membrane protein mass spectrometry, use of mass spectrometry might prove useful [8]. Purified ELIC was either used fresh or flash frozen stored at -80°C until further use. The concentration of ELIC was determined using the BCA assay (Figure 4.1c) [9]. Comparison of the BCA derived ELIC concentration with that of the ϵ_{280} (63495 M^{-1} cm^{-1} per monomer, 317475 M^{-1} cm^{-1} per pentamer) calculated from the amino acid sequence using the ExPASy toolbox, yielded similar concentrations. Future calculations of ELIC concentration used the absorbance measurements.

4.3.2 Reconstitution of GLIC and use of Sodium Green and SBFI as Functional Reporters

I briefly mention efforts into the reconstitution of GLIC, using sodium green as a reporter of functional channels. GLIC was purified in the same way as ELIC. Lipid (3:1 POPC:POPG) vesicles were formed in the presence of 12 μM NaGreen,

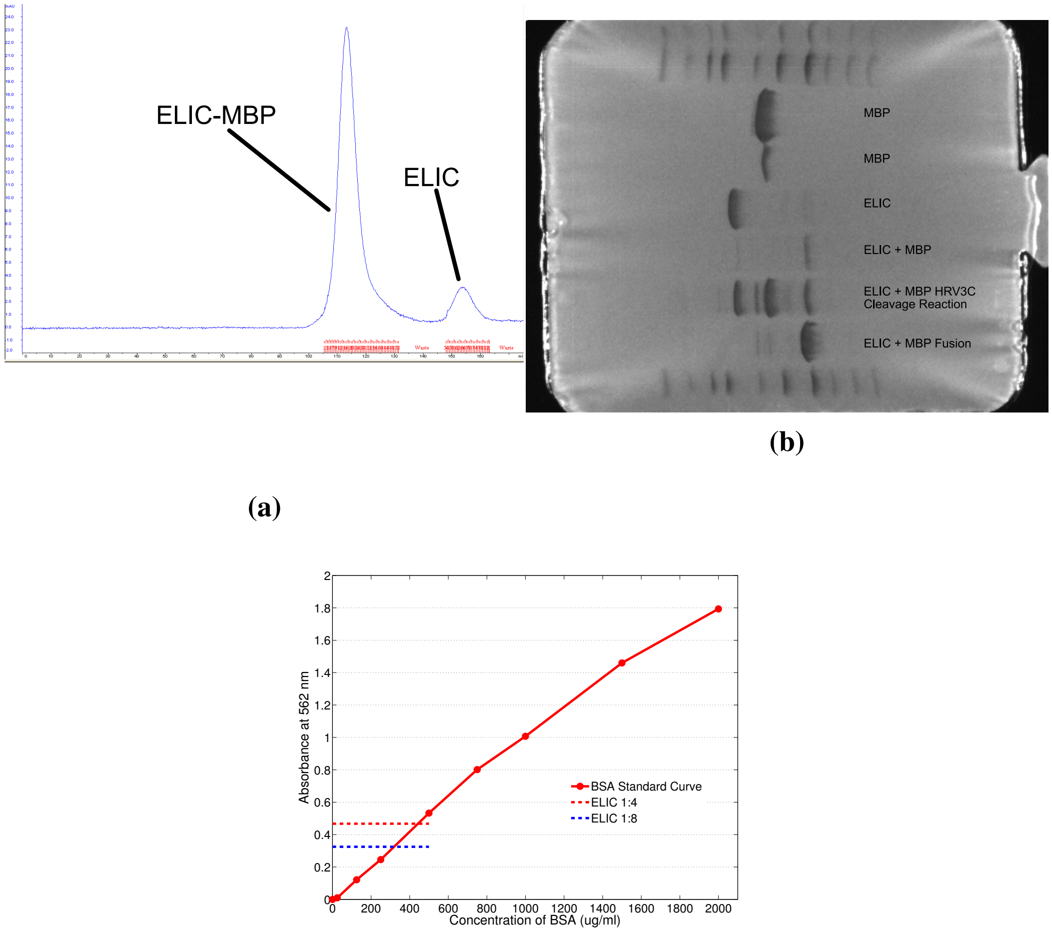

(b)

(a)

(c)

Figure 4.1: (a) The final size exclusion chromatograph of ELIC purification. The first peak is that of the MBP-ELIC pentamer, followed by just the purified ELIC. Not shown is the peak associated with the cleaved MBP. (b) All of the peaks were isolated and subjected to SDS-PAGE analysis. The denaturing conditions of SDS-PAGE resulted in the isolated pentamers running as monomers. Purified ELIC is observed around 37 kDa. (c) A BCA protein concentration calibration curve with ELIC concentrations referenced. The ELIC concentration from the BCA assay was then compared with the theoretical ϵ_{280} value and found to be in good agreement.

and excess dye removed using size exclusion chromatography (PD-10 column). Vesicles and detergent solubilized GLIC were mixed and incubated in the presence of polystyrene beads (Bio-Beads). Bio-Beads selectively remove detergent from solution [10]; removal of detergent will cause GLIC to enter the only membrane envrionment remaining in solution, the vesicles. The proteoliposomes were then subjected to size exclusion chromatography to remove all Na^+ present in solution. GLIC proteoliposomes were placed in a 96 well plate and each well was subjected to different conditions. GLIC is an acid sensitive ion channel. Proteoliposomes were exposed to low pH buffers in the presence and absence of NaCl. Exposure to low pH buffers resulted in the decrease of NaGreen fluorescence (Figure 4.2a). NaGreen is a fluorescein-derived dye attached to a Na^+ chelating moiety; fluorescein luminescence is well known to have a pH dependence [11]. Functional GLIC would have activated and allowed Na^+ ions to flow through the channel, binding to NaGreen and increasing fluorescence. An opposite trend is observed in the NaGreen fluorescence. To examine the fluorescence of NaGreen as a function of pH, addition of NaCl buffer at various pHs to a solution of just NaGreen (Figure 4.2b). A decrease in fluorescence was observed for solution pH < 6.0, while an increase in fluorescence was observed for pH > 6.0. The pH dependence of NaGreen fluorescence eliminates the use of NaGreen as a reporter for the reconstituiton of acid sensitive ion channels.

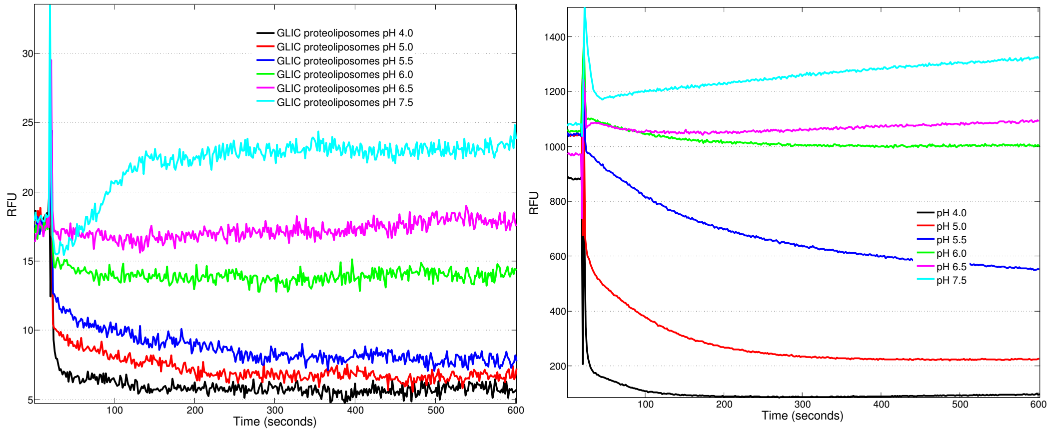

(a) **(b)**

Figure 4.2: (a) GLIC proteoliposomes exposed to various low pH buffers, monitoring of NaGreen fluorescence as a function of pH and time. A NaGreen fluorescence decrease is observed for low pH buffers in the presence of Na^+. (b) The NaGreen fluorescence monitored in the presence of various pH buffers displays similar behaviours as what is observed in the proteoliposomes. This shows that a obvious pH dependence in fluorescence is observed, and NaGreen is not a suitable indicator for GLIC activation.

The use of sodium sensor SBFI was also examined (Figure 4.3). No SBFI fluorescence changed is observed in the presence of low pH and Na^+ for GLIC proteoliposomes (Figure 4.3a). SBFI fluorescence was then monitored as a function of pH. A SBFI fluorescence decrease was observed for solution pH < 6.0, while an increase was observed for pH > 6.0 (Figure 4.3b). SBFI and NaGreen are two commercially available sodium sensors that are described in the literature. The pH dependent fluorescence observed suggests these two dyes are not viable fluorescence indicators for functional reconstitution of acid-sensitive ion channels. Focus shifted to the reconstitution of ELIC, an amine-activated ion channel where pH is controlled.

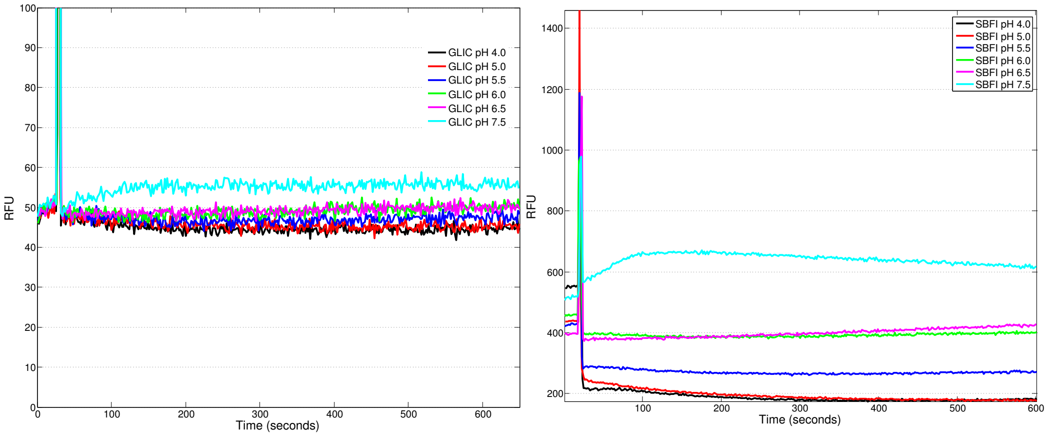

(a) **(b)**

Figure 4.3: (a) GLIC proteoliposomes exposed to various low pH buffers, monitoring of SBFI fluorescence as a function of pH and time. There is little fluorescence change observed in any of the SBFI proteoliposome samples. This is likely due to the efficient removal of extravesicular SBFI.(b) The SBFI fluorescence monitored in the presence of various pH buffers. Again, SBFI displays a clear pH dependence of fluorescence in the range needed for GLIC activation. SBFI is not a useful Na^+ indicator for GLIC activation due to the pH-dependent fluorescence.

4.3.3 Reconstitution of ELIC and use of a Sodium Dependent Functional Reporter

ELIC had previously been reconstituted into artificial membranes made of POPC:POPG lipids [12]. I focused on the reconstitution of ELIC into LUVs. LUVs have a diameter on the order of 100 nm, and have been used previously to reconstitute ligand-gated ion channels [3–5, 13]. As with GLIC, measurements of ion flux will be used to monitor the functional state of the reconstituted ion channels. Sodium selective dyes are encapsulated within the LUVs; the fluorescence of the Na^+ dye is monitored under ELIC activation conditions. A fluorescence turn-on should only occur in the presence of agonist and functional ELIC. Activation of ELIC will allow sodium ions from the solution to flux into the lumen of the vesicles, bind to the sodium sensitive dye, and increase fluorescence. Increase in fluorescence after addition of agonist will indicate successful functional reconstitution. To further examine the reconstituted state of the channels, a fluorescence dose-response curve can be obtained and compared to the electrophysiology response of ELIC. This comparison provides a measurement to the perturbation of channels as a result of reconstitution. A dose-response similar to what is observed using electrophysiology will suggest that the ion channels are functionally reconstituted.

ELIC is activated by many small molecule amine agonists [14]; propylamine will be used because of the high ELIC sensitivity and ease of manipulation. The fluorescence of NaGreen was monitored when exposed to propylamine. An increase in NaGreen fluorescence was observed upon addition of Na^+ regardless of the presence of propylamine (Figure 4.4b, black and green lines). Unlike the effect of pH on the fluorescence of NaGreen propylamine does not alter the fluorescent properties of the dye, suggesting NaGreen can be used as a functional Na^+ flux indicator in ELIC reconstitution experiments. ELIC was purified, and reconstitution undertaken in a similar manner as with GLIC above. The fluorescence of NaGreen was monitored upon addition of NaCl ± propylamine to ELIC proteoliposomes to test for function. Upon addition of the NaCl + propylamine buffer the fluorescence increased (Figure 4.4a, red lines). However, fluorescence increase of a similar magnitude is also observed with just the NaCl buffer (Figure 4.4a, blue lines). The nonselective fluorescence increase shows only Na^+ is needed for the observed effect, not propylamine + Na^+. Functionally reconstituted ELIC would result in a differental response in the presence of propylamine. Sodium ion flux through activated ELIC would increase Na^+ concentration within the vesicles increasing the NaGreen fluorescence over the non-specific fluorescence. The anticipated propylamine-specific increase in fluorescence is not observed. The fluorescence increase observed is due to extravesicular NaGreen. The reconstitution protocol was repeated, and modified, in an attempt to functionally reconstitute ELIC. ELIC amount, incubation time, and fluorescent dye concentration were altered. None of the variations in reconstitution protocol resulted in the selective increased fluorescence turn-on of NaGreen in the presence of propylamine (Figure 4.5a), indicating that ELIC was not functionally reconstituted.

To determine if the FlexStation is able to detect the fluorescence of NaGreen inside the LUVs, Triton X-100 was used to lyse the vesicles. Addition of triton will solublize the lipid vesicles and release the contents of the LUVs into the solution. Upon addition of triton, a fluorescence increase is observed for the buffers containing NaCl ± propylamine. The lysed fluorescence increase is larger than the non-specific increase observed without triton (Figure 4.5b). The increase of fluorescence upon lysis indicates that the detection method is sensitive enough to measure a theoretical 100% turn-on of the NaGreen inside the LUVs. Given that a fluorescence increase can be observed upon intravesicular NaGreen binding sodium, it does not appear that the reconstitution protocol used yields functional ion channels.

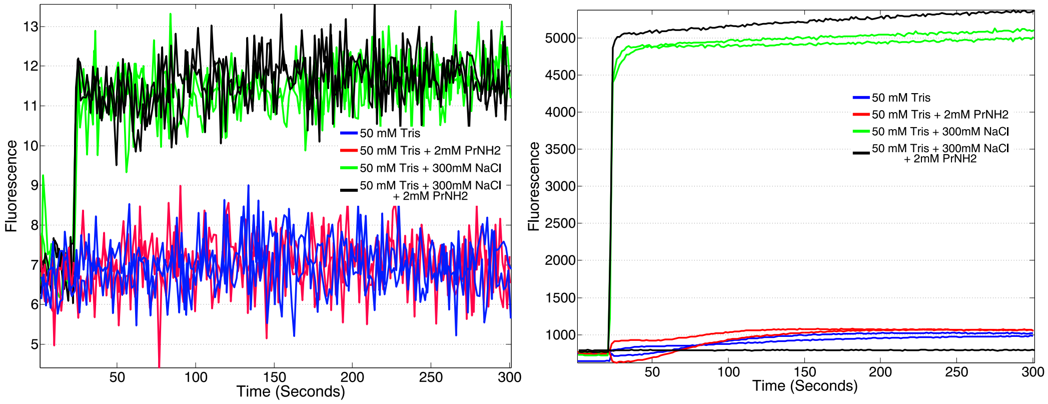

(a) **(b)**

Figure 4.4: (a) ELIC proteoliposomes exposed to buffers containing 2 mM propylamine for activation, monitoring of NaGreen fluorescence as a function of time. An increase in NaGreen fluorescence is observed for buffers containing Na^+ ions. No selective NaGreen fluorescence is observed upon addition of proteoliposomes, suggesting that the ion channels are not functionally reconstituted (b) NaGreen fluorescence monitored in the presence of propylamine displays an increase upon addition of Na^+ ions. No difference is observed in the fluorescence in the presence of propylamine suggesting that the NaGreen dye can be used to monitor the activation of ELIC.

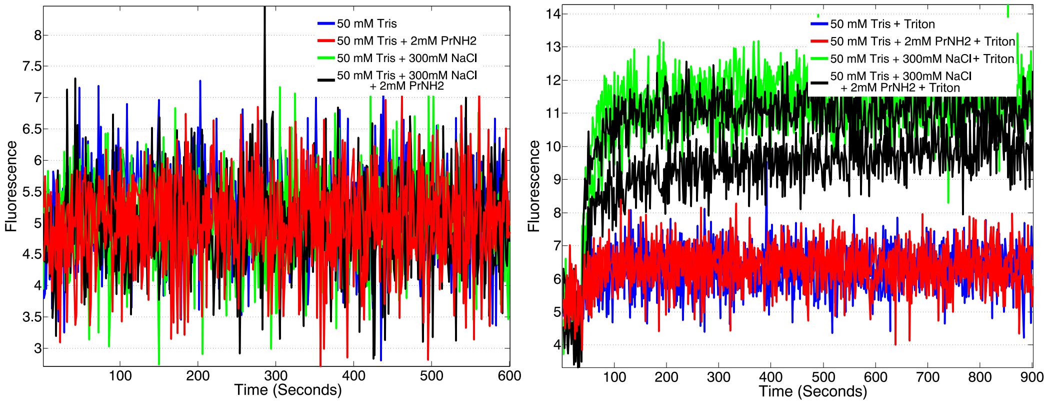

(a) **(b)**

Figure 4.5: (a) ELIC proteoliposomes exposed to buffers containing 2 mM propylaime for activation, monitoring of NaGreen fluorescence as a function of time. No increase in fluorescence is observed for the addition of Na^+ ions. This shows that the ELIC ion channels are not functionally reconstituted, and that the previously observed increase in fluorescence (Figure 4.4 is due to incomplete removal of extravesicular NaGreen. (b) NaGreen fluorescence monitored upon lysis of proteoliposomes with Triton X-100. A measurable fluorescence increase is observed in the presence of triton, showing that the detection method is sensitive to the theoretical fluorescence increase from NaGreen binding Na^+.

4.3.4 Reconstitution of ELIC Through Partial Destabilization of Lipid Vesicles

A new method for reconstitution of ELIC into LUVs was used. Vesicles were formed with the desired dye trapped in the lumen, and moderately destabilized with detergent. Formation of vesicles, then addition of DDM detergent (0.05% w/w) will generate lipid vesicles with saturating amounts of detergent in the lipid bilayers (Figure 4.6a). Addition of more DDM will result in the formation of lipid-detergent micelles, while less detergent results in less destabilization of the bilayers. Following destabilization of the vesicle, purified protein is added, and the detergent is removed with biobeads. The assay to determine function is the same NaGreen fluorescence assay used above.

ELIC was added to the destabilized vesicles, and incubated at room temperature for 2 hours. Biobeads were then added to remove the detergent. Replacement of the biobeads every 90 minutes occurred, finally the vesicle/ELIC mixture was incubated overnight at 4°C in the presence of biobeads. Long incubation periods require ELIC to be stable for extended periods. However, the stability of ELIC is not known; a functional assay (once developed) can be used to test *in vitro* stability of ELIC. After incubation overnight, the vesicle solution was isolated by ultracentrifugation. Isolation, followed by resuspension of the proteoliposomes in protein-free, dye-free, salt-free buffer occurred at least three times in an effort completely remove any non-vesicle components. Following the final ultracentrifugation, the lipids were resuspended to 20 mg/mL and either used immediately or flash frozen and stored at -80°C.

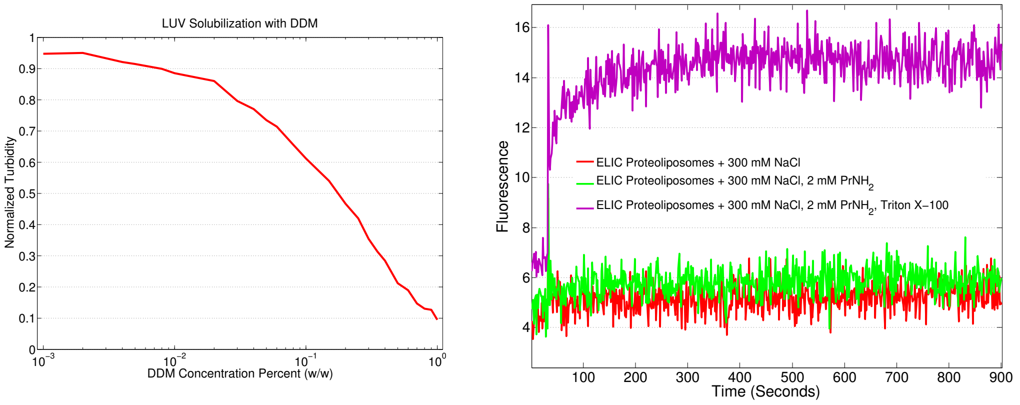

(a)

(b)

Figure 4.6: (a) Turbidity of liposomes, as measured by A_{560}, in the presence of increasing amounts of DDM detergent. As the detergent concentration increases the turbidity of the vesicle solution decreases. This is a result of the formation of detergent-lipid micelles, which do not scatter light. Minimal micellular formation is observed for DDM concentrations less than .01%. (b) NaGreen fluorescence of reconstituted ELIC upon addition of NaCl ± propylamine ± Triton X-100. No fluorescence increases observed in the presence of propylamine suggesting that ELIC is not functionally reconstituted. A large fluorescence increase is observed for lysed vesicles.

To determine if ELIC was present in the isolated vesicles SDS-PAGE analysis was performed on the vesicles. Protein staining (Coomassie Blue) showed the presence of protein consistent with the ELIC molecular weight suggesting that ELIC is incorporated into the vesicles (Figure 4.7a) [15, 16]. Ultracentrifugation of the lipid vesicles removes the soluble components of the reconstitution mixture (excess dye, non-incorporated ion channel, etc). Protein analysis of the isolated lipid vesicles provides a direct measurement as to the presence of the desired protein in the lipid vesicles. The same FlexStation fluorescence assays unfortunately did not yield evidence for functional ELIC (Figure 4.6b). Similar results were obtained using SBFI as the fluorescence indicator, but are not shown. Application of high NaCl buffers in the presence or absence of propylamine resulted in very minimal increases in NaGreen fluorescence (Figure 4.6b, red and green lines). Lysis of the vesicles exposed intravessicular NaGreen to the bulk, and resulted in a large increase in fluorescence (Figure 4.6b, purple line), suggesting that NaGreen fluorescence can detected if Na$^+$ entered the vesicles through ELIC. The FlexStation results show that no functional ELIC has been incorporated into the vesicles (Figure 4.6b, red and green lines). Gel electrophoresis of the reconstituted lipid vesicles shows the presence of ELIC protein in lipid vesicles isolated with ultracentrifugation. The combined FlexStation and SDS-PAGE results indicate that whatever ELIC present with the vesicles is not functional.

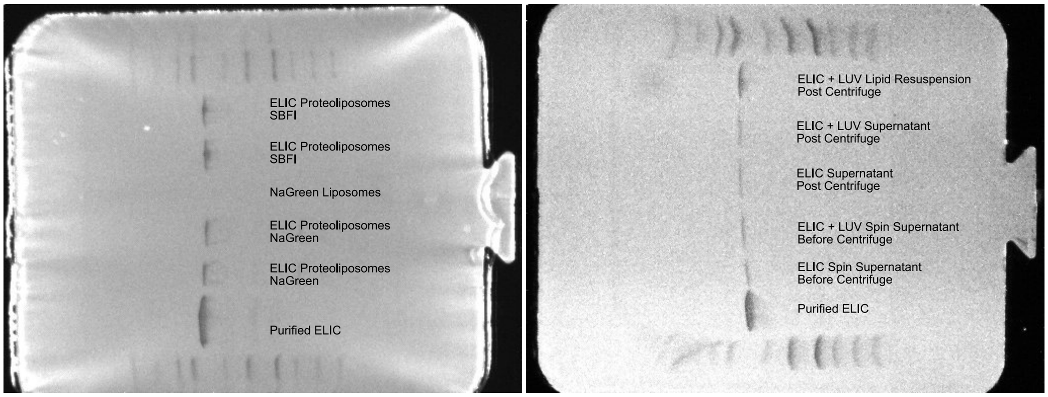

(a) **(b)**

Figure 4.7: (a) A coomassie-stained SDS-PAGE gel of the ultracentrifuge-isolated proteoliposomes after reconstitution. The ELIC proteoliposomes display a clear band corresponding to ELIC, showing evidence for successful ELIC reconstitution. This band is absent if no ELIC is added to the liposomes. (b) SDS-PAGE coomassie-stained protein analysis of the various fractions of ELIC mixed with liposomes, followed by immediate ultracentrifugation. The evidence of ELIC present in the top band shows that the ELIC association with the liposomes is not specific to the reconstitution protocol used.

To determine if the ELIC observed in the vesicle isolate is specific to the reconstitution protocol purified ELIC was added to a solution of vesicles, and instead of subjecting the ELIC to the reconstitution protocol (vessicle destabilization, incubation, detergent removal), this sample was immediately spun down in the ultracentrifuge. The isolated lipids were resuspended, and along with the supernatent of the centrifugation assayed for ELIC by gel electrophoresis. Surprisingly, after three washes, and no reconstitution protocol, evidence for ELIC in the isolated vesicles was present (Figure 4.7b). The presence of ELIC suggests that protein-gel analysis is not a valid indication of the successful incorporation of ELIC into vesicles (Figure 4.7a). It appears that a non-specific interaction between ELIC and the vesicles exists. This interaction is strong enough to survive multiple ultracentrifugation and washing steps. Following this result, a new method for reconstitution is needed.

4.3.5 Test of NaGreen and SBFI for use in Monitoring Na$^+$ Flux into Vesicles

I then determined if NaGreen or SBFI fluorescence is a valid method to monitor functionally reconstituted systems. I sought to use a robust ion channel with well established reconstitution protocols to test NaGreen and SBFI. Gramicidin is a 15 amino-acid peptide that self assembles to form ion channels in membranes, has been studied extensively [17], can be purchased commercially, and many protocols exist for the reconstitution of Gramicidin.

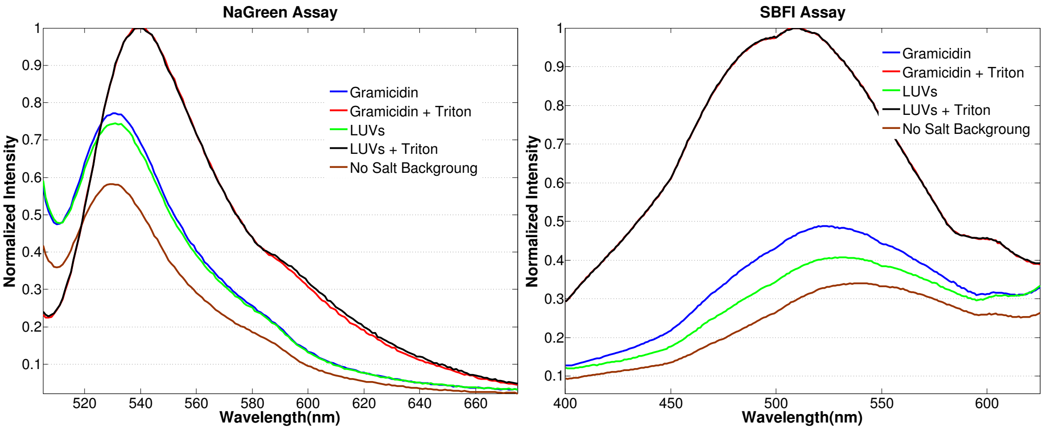

(a) **(b)**

Figure 4.8: (a) Steady-state fluorescence spectra of NaGreen with Gramicidin proteoliposomes in the presence or absence of NaCl (blue and brown lines respectively). The NaGreen fluorescence of pure liposomes is shown in the green line. There is little difference in fluorescence of the Gramicidin vesicles. (b) The same measurements but with SBFI as the fluorescent dye. The small increase of fluorescence in the presence of Gramicidin indicates that the NaGreen or SBFI dyes are not robust measurements for Na$^+$ flux measurements into vesicles. All the fluorescence intensities are normalized to the intensity observed upon vessicle lysis of the sample (red and black lines).

Gramicidin was reconstituted by addition, and overnight incubation, with vesicles enclosing NaGreen or SBFI [18]. The fluorescence of NaGreen and SBFI was monitored upon addition of NaCl solutions to the gramicidin proteoliposomes. Fluorescence measurements display a peak at *ca.*540 nm and *ca.*520 nm for NaGreen and SBFI, respectively. Vesicle samples (±gramicidin) exhibited an increased fluorescence upon addition of Na^+ ions (Figure 4.8, blue and green lines compared to brown). Unfortunately, a large difference in fluorescence of gramicidin vesicles compared with the control vesicles was not observed. A 5% change in fluorescence in the presence of gramicidin is observed for NaGreen, while a 10% increase in fluorescence of SBFI. Gramicidin reconstitution is basically idiot-proof, and gramicidin channels are known to conduct ions effectively. If the NaGreen or SBFI indicators were efficient reportors of Na^+ flux, a large increase in fluorescence should have been observed with Gramicidin vesicles. The very small difference of NaGreen or SBFI fluorescence with gramicidin limits the use of NaGreen or SBFI in the reconstitution of ELIC. As a result, further efforts into the reconstitution will use a different indicator for testing of reconstitution ion channels.

4.3.6 Reconstitution of ELIC and use of a Thallium Quenching Assay

A new assay for monitoring the functional state of reconstituted ion channels was needed. Common assays for ion channel reconstitution are radioactive ion flux [2], and thallium fluorescence quenching [4, 19]. Neither option is ideal due to the hazards of working with either material, and in the end I chose to use the Tl^+ quenching assay. Nicotinic acetylcholine receptors, ion channels in the same family as ELIC, have been functionally reconstituted and assayed using Tl^+ flux [19]. In Tl^+ flux assays, the fluorescence of 8-aminonaphthalene-1,3,6-trisulfonic acid, disodium salt (ANTS) is monitored upon addition of agonist to a proteoliposome sample. Thallium(I) is a similar size to K^+, allowing thallium flux through the cation-selective ion channels and into the vesicle. Inside the vesicle collisional quenching of Tl^+ with ANTS results in a decrease in ANTS fluorescence. The activated ion channels provide a pathway for thallium to enter the vesicles, resulting in increased ANTS quenching in the presence of functionally reconstituted ion channels.

ELIC was reconstituted using the partially destabilizing protocol as above, incorporating ANTS inside the vesicles. ANTS quenching was monitored upon addition of Tl^+ containing buffers using the FlexStation. All thallium samples resulted in quenching of ANTS fluorescence, and no difference in quenching was observed be-

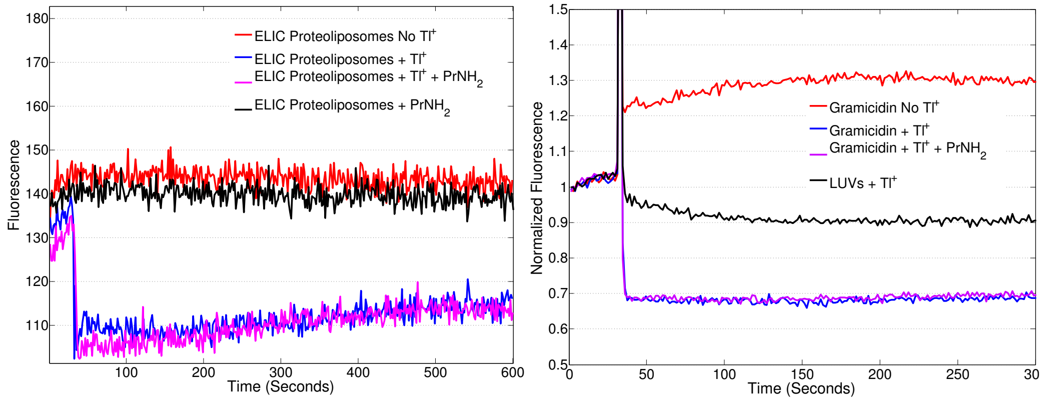

(a) **(b)**

Figure 4.9: (a) The fluorescence of ANTS as ELIC proteoliposomes are exposed to Tl^+ ± propylamine. Quenching of fluorescence is observed for all samples that contain Tl^+. (b) The ANTS quenching by Tl^+ with gramicidin proteoliposomes. A large quenching of ANTS is observed for the gramicidin vesicles mixed with Tl^+ buffers ± propylamine (blue and magenta lines). This shows that propylamine does not effect the assay. Less fluorescence quenching is observed for LUVs alone (black line), however quenching is still observed.

tween samples exposed to thallium in the presence or absence of propylamine (Figure 4.9a). To verify the assay gramicidin was reconstituted into liposomes and ANTS quenching monitored using the FlexStation (Figure 4.9b). Addition of thallium buffers resulted in a step-like quenching of ANTS fluorescence for vesicles ± gramicidin. Tl^+ ions non-selectively cross membranes, and this gramicidin-independent quenching suggests the FlexStation sampling rate is not fast enough to resolve selective thallium flux through channels. A stopped-flow is required to separate the rapid flux of Tl^+ ions through the ion channel from non-selective flux across the membrane. Gramicidin was reconstituted [18] and mixed with thallium buffers in a stopped-flow. Rapid quenching of the ANTS fluorescence is observed only in in the presence of gramicidin proteoliposomes (Figure 4.10b, green line). Thallium quenching of ANTS fluorescence was much slower in the absence of gramicidin (Figure 4.10b, blue line), consistent with literature observations [18, 19].

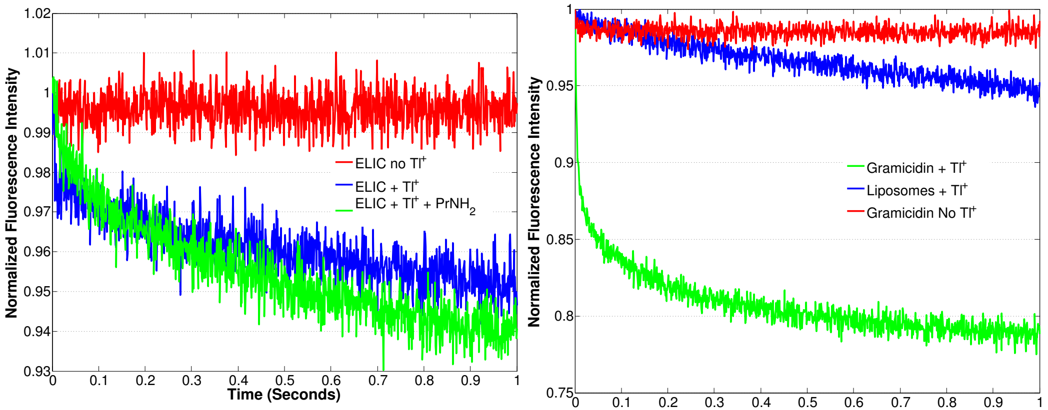

(a)

(b)

Figure 4.10: (a) The fluorescence of ANTS as ELIC proteoliposomes are exposed to Tl^+ ± propylamine. ANTS quenching is observed upon exposure to Tl^+ alone (blue line), with the slow quenching of ANTS consistent with non-selective ion flux across the membrane. Addition of propylamine and Tl^+ to ELIC proteoliposomes resulted in an increase in quenching (green line), suggesting that functional ELIC is present (in small quantities). (b) The fluorescence quenching of ANTS when gramicidin proteoliposomes are exposed to Tl^+ containing buffers. Slow ANTS quenching is observed for LUVs without gramicidin (blue line), highlighting the non-specific flux across the membrane. Rapid ANTS quenching is observed with gramicidin vesicles (green line). Gramicidin vesicles form ion channels and allow for thallium to enter the vesicles through the ion channel, which occurs much more rapidly then the flux across the membrane.

Reconstitution of ELIC was repeated, using the Tl^+ quenching assay to monitor function, using the reconstitution protocol of Russinova and coworkers [4]. POPC:POPG lipids were resuspended in an ANTS solution and CHAPS detergent was added. The lipids were then sonicated; however, a clear lipid solution was not achieved as in the published protocol [4]. The formation of a clear solution indicates the formation of degergent/lipid micelles, and vesicles are then formed by removal of the detergent in the presence of the ion channel. Regardless of the inability to produce a clear solution, ELIC was added to this solution and incubated for 30 minutes. Detergent removal with biobeads formed LUVs, which were then extruded through a 100 nm pore. Excess ANTS dye was removed through size exclusion chromatography. Mixing of ELIC proteoliposomes with thallium buffer in the presence of propylamine resulted in an increased quenching of ANTS compared with just thallium buffer alone (Figure 4.10a, green vs blue lines). This is the first example where reconstituted ELIC exhibited a different behaviour in the presence of propylamine suggesting some (albeit, minimal) functional reconstitution. Repeated attempts to reconstitute ELIC in a similar manner resulted in limited improvements of signal. Discussion with Russinova at Cornell Medical College highlighted the importance of complete formation of lipid/detergent micelles in the protocol, an outcome that I was unable to achieve.

To optimize ELIC reconstitution I spent two weeks working with Russinova in the Andersen lab. The protocol developed is outlined in the methods section above. The optimized protocol uses a higher concentration of purified ELIC (9 mg/ml vs. 1 mg/ml) during the reconstitution protocol. Higher concentration results in less dilution of the reconstitution mixture. Another difference in the developed protocol was the use of DOPC lipids in place of POPC lipids, with the vesicles consisting of 3:1 DOPC:POPG. Working in the Andersen lab, I was able to successfully reconstitute ELIC using two different methods.

One method of reconstitution used the protocol of complete solubilization of lipids [4], which I was previously not able to achieve due to the low-powered sonicator. Reconstitution following complete solubilization resulted in increased thallium-induced ANTS quenching with propylamine present in the solution (Figure 4.11a, magenta line). Rapid quenching in the presence of propylamine suggests that ELIC is functionally reconstituted. A large burst-phase in quenching was observed with this reconstitution sample. The initial fluorescence with any thallium buffer was about 15% lower than the fluorescence in the absence of thallium (Figure 4.11a, magenta and green lines). This burst-phase is attributed the quenching of free ANTS in solution, an event that occurs faster than the dead-time of the stopped-flow. ELIC proteoliposomes were prepared at a 1:15 (w/w) ratio of ELIC:lipids resulting in *ca.* 30 ELIC pentamers per vesicle. High concentration of protein in the vesicle can lead to the destabilization of the vesicles, and subsequent leakage of ANTS. Excess ANTS in the bulk solution would result in the large burst-phase quenching. The goal of high protein concentration was to observe any signal possible, but it appears that too much protein can be deleterious.

ELIC was also reconstituted with the partial destabilization protocol using lower ELIC concentrations. ANTS quenching analysis revealed successful reconstitution of ELIC. The samples all display similar burst-phase quenching of ANTS, with about 5% quenching observed. This is much lower than the 15% observed above. This is likely due to the lower concentration of ELIC in the vesicles, resulting in less leakage of ANTS into solution. Stopped-flow mixing of ELIC proteoliposomes with thallium resulted in slow nonselective ANTS quenching (Figure 4.11b, orange line). Addition of propylamine activated reconstituted ELIC, and results in a rapid increase in ANTS quenching (Figure 4.11b). Higher concentration of propylamine

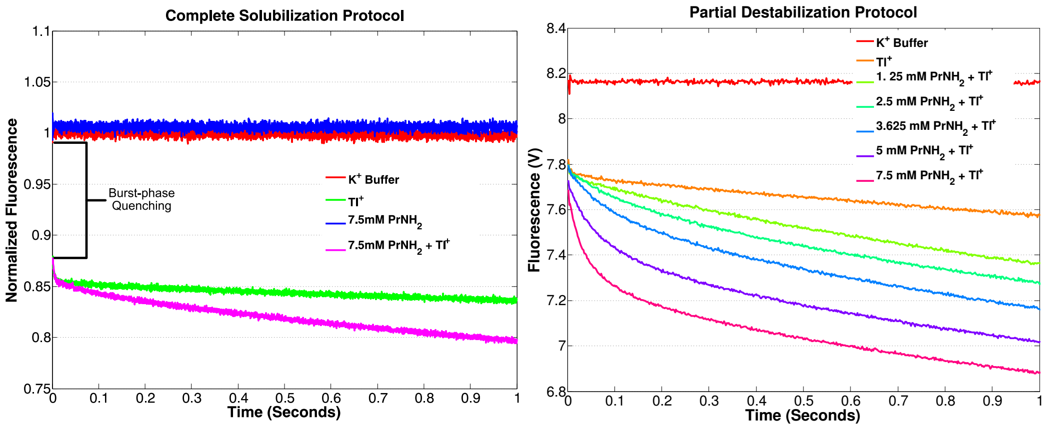

(a) **(b)**

Figure 4.11: (a) ELIC, reconstituted using the complete solubilization protocol, assayed for function using Tl^+ quenching of ANTS. In the presence of thallium buffer (green and magenta lines) a 15% decrease in ANTS fluorescence is observed at the initial timepoint. This is due to excess ANTS in solution, the quenching of which occurs faster than the dead-time of the stopped-flow. The slow ANTS quenching observed for mixing of ELIC proteoliposomes with Tl^+ buffer alone (green line) is due to non-selective Tl^+ flux into the vesicle. Addition of propylamine to the solution results in a rapid quenching of ANTS (magenta line). The increased quenching in the presence of propylamine suggests some functional reconstitution of ELIC. (b) ELIC reconstitution using partial destabilization, assayed using Tl^+ flux quenching of ANTS at various concentrations of propylamine. Increased ANTS quenching is observed upon an increase in the propylamine concentration. The dose-response in quenching shows that with more agonist in solution, Tl^+ is able to enter the vesicle quicker. This occurs through the activation of ELIC ion channels, with more ELIC ion channels being activated at higher agonist concentrations. The concentration-dependent quenching shows that functional reconstitution of ELIC has occurred.

displayed an increase in quenching rate and magnitude. The agonist dose-response in quenching has previously be observed with reconstituted ion channels KcsA and nAChR [4, 19]. An increased concentration of agonist in solution allows for activation of more ELIC channels present resulting in a more rapid quenching of ANTS. ANTS quenching rate, and magnitude, increase are analogous to the dose-response, observed as current, in electrophysiology experiments. The propylamine-specific quenching of ANTS shows that ELIC has been functionally reconstituted.

ELIC is known to enter a ligand-bound nonconducting (desensitized) state upon prolonged exposure to propylamine [14]. To further confirm that ANTS quenching is due to ELIC activation, desensitization experiments were conducted. ELIC proteoliposomes were pre-incubated with propylamine buffer lacking thallium. After 1 minute of pre-incubation, the proteoliposomes were mixed with thallium buffer containing the same concentration of propylamine. Upon mixing with the thallium buffer, the same burst-phase quenching is observed (Figure 4.12a). This suggests

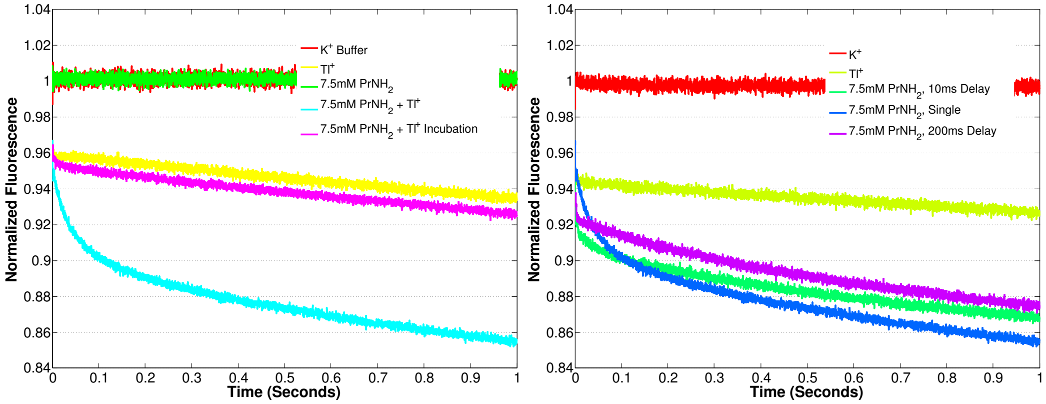

(a) **(b)**

Figure 4.12: (a) ELIC desensitization observed upon 1 minute pre-incubation with propylmaine. One minute incubation with propylamine results in ELIC entering a propylamine-bound non-conducting state (magenta line). In this state, thallium flux through ELIC is not possible. The only remaining ANTS quenching pathway is the non-specific flux across the membrane. The quenching observed with desensitized ELIC (magenta line), and just Tl^+ (yellow line) is similar. (b) Desensitization of ELIC as a function of pre-incubation time with propylamine. Desensitization is observed after incubating ELIC for 200 ms with propylamine (magenta line). Incubation for 10 ms (green line) results in a quenching profile that is similar to the no incubation mixing (blue line).

that the origin of the burst-phase is independent of ELIC. The subsequent quenching of ANTS was significantly attenuated (Figure 4.12a, magenta vs. cyan lines). The quenching rate and magnitude were similar to the thallium alone quenching rate (Figure 4.12a, yellow line). The pre-incubation of ELIC proteoliposomes eliminated any rapid ANTS quenching by Tl^+. This ANTS quenching profile is further evidence that the quenching observed without pre-incubation results from functionally reconstituted ELIC. The incubation with propylamine activates ELIC, followed by ELIC entering a desensitized state. The desensitized state is non-conducting, and when mixed with thallium the only ANTS quenching pathway is the non-selective membrane flux pathway. Further desensitization experiments utilized a delay mechanism in the stopped-flow that allows for the precise control of the incubation time. Incubation periods > 10 ms resulted in similar desensitization behaviour as observed with the one minute incubation (Figure 4.12b). Desensitization in electrophysiology experiments was observed over the course of seconds, not milliseconds. The discrepancy in desensitization rates suggests that the ELIC is reconstituted in a different functional state. Reconstituted ELIC is activated at 7.5 mM, compared to 100% activation by 2 mM propylamine in electrophysiology experiments, showing a decreased sensitivity of reconstituted ELIC to propylamine. The differences in activation profiles of reconstituted ELIC from electrophysiology show ELIC has been perturbed out of the so-called native state.

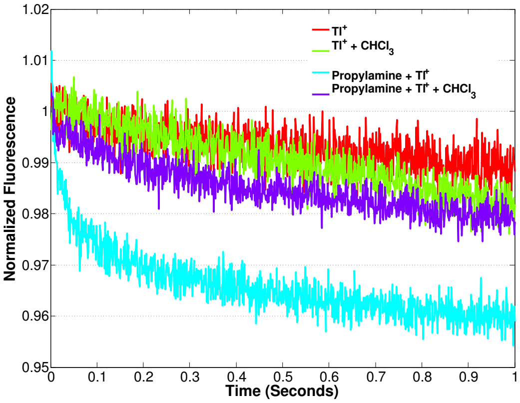

Figure 4.13: ELIC proteoliposomes functional assay the presence of propylamine (cyan line) and known ELIC blocker, chloroform (purple line). The rapid quenching of ANTS is eliminated in the presence of chloroform. Chloroform blocks ELIC ion channel activation, preventing any ion flux through the pore. The elimination of rapid quenching with chloroform provides further support for the successful reconstitution of ELIC.

ELIC Blocking studies further confirmed the ANTS quenching results from Tl^+ flux through activated ELIC. ELIC is blocked by common anesthetic molecules such as chloroform [20]. Chloroform was added to the thallium and propylamine buffers, and mixed with ELIC proteoliposomes in the stopped-flow. A significant attenuation of the ANTS quenching rate was observed with chloroform present (Figure 4.13). Chloroform blocks ion flux through ELIC. The observed ANTS quenching with chloroform is due to the non-selective Tl^+ flux across the membrane. The elimination of rapid ANTS quenching in the presence of a ELIC-specific blocker further confirms that ELIC has been functionally reconstituted

4.4 Conclusions and Future Directions

In this chapter I outlined efforts towards the functional reconstitution of ELIC and GLIC ion channels. I was able to purify both receptors using a heterologous expression system. Any measurement made on a biological system *in vitro* requires that the function of the system has not been altered from the observed *in vivo* properties. ELIC is a membrane protein activated by propylamine. ELIC was reconstituted using LUVs as the *in vitro* membrane environment. LUVs were chosen because a defined inside and outside of the vesicles exist, akin to the inside and outside of a cell. Many different protocols for reconstitution of ELIC were attempted. All of the functional assays used monitored the flux of ions through an activated ELIC receptor. The use of sodium sensitive dyes did not prove a viable method for the detection of Na^+ flux through an activated ion channel. The Na^+ sensitive dyes were not sensitive enough to report the small fluorescence changes needed. Thallium quenching of a fluorescent dye (ANTS) encapsulated inside vesicles was then used to monitor ion flux through the activated ion channels. These measurements required the use of a stopped-flow, as non-selective thallium flux across the membrane occurs on the order of seconds. After many attempts, and variations on the reconstitution protocols, ELIC was functionally reconstituted. Rapid ANTS quenching upon mixing with propylamine, and elimination of quenching in the presence of a specific ELIC blocker, suggests that ELIC has been successfully reconstituted.

However, the functional state of reconstituted ELIC is different, as evident from the shifted dose-response to propylamine. Further optimization is needed to bring the reconstituted ELIC dose-response to levels observed in electrophysiology experiments. The ELIC expression and purification is not a high-yielding process, which limits the use of brute force optimization. Optimization should focus on shifting the sensitivity to propylamine of reconstituted ELIC to values observed in electrophysiology experiments. The functional properties of reconstituted ELIC need to be the same as *in vivo* ELIC for use in an *in vitro* system. Also, maximum activation of the reconstituted ELIC will achieve higher signals of ANTS quenching and provide a larger change in fluorescence for the mixer experiments. Alteration of the lipid bilayer properties by changing the lipid head groups, or acyl chain length can serve as a starting point for optimization. Examination of the lipid composition of the native organism, *Erwinia chrysanthemi*, could provide valuable insight.

Reconstitution yields a statistical distribution of the orientation of ion channels. Half the ion channels are oriented correctly, with the extracellular domain residing in the bulk buffer, and half the opposite incorrect orientation. Activation of ELIC requires agonist binding to the extracellular domain preventing half of the reconstituted ELIC from being activated. There has been some success in the orientation of reconstituted ion channels [21], but without specialized protocols I assume that half of the ion channels will be oriented in the incorrect manner. The orientation and insensitivity of reconstituted ELIC results in low signals (5 - 10% of max quenching). Increased agonist sensitivity will activate more of ELIC channels present allowing for more quenching of ANTS. More ELIC channels will also result in large quenching of ANTS. The reconstitution of *ca.* 30 pentamers resulted in destabilization of the proteoliposomes. A 100 nm LUV has a surface area of roughly 125,000 nm^2, and the transmembrane area of ELIC is roughly 2000 nm^2. From resulting sizes, 30 ELIC pentamers will occupy almost half of the surface area of a 100 nm LUV; it does not come as a surprise that the high concentration proteoliposomes could cause leakage across the membrane. A detailed study investigating the signal vs. ELIC concentration would allow for maximum signal to be obtained. Many protocols were used in the reconstitution of ELIC. There was very little difference between the unsuccessful attempts, and the successful protocol conducted in the Andersen lab. The differences are as follows: 1 - detergent-solubilized ELIC concentration was 10 times higher, and 2 - the lipids used were DOPC:POPG (3:1) as opposed to POPC:POPG (3:1). It seems remarkable that such little difference in protocols can make all the difference. Regardless, the use of these modifications resulted in the functional incorporation of ELIC into liposomes.

References

(1) Miller, C., *Ion Channel Reconstitution*; Springer Science & Business Media: 1986.

(2) Maduke, M.; Pheasant, D. J.; Miller, C. *The Journal of General Physiology* **1999**, *114*, 713–722.

(3) Moore, H.-P. H.; Hartig, P. R.; Wu, W. C. .-.-S.; Raftery, M. A. *Biochemical and Biophysical Research Communications* **1979**, *88*, 735–743.

(4) Rusinova, R.; Kim, D. M.; Nimigean, C. M.; Andersen, O. S. *Biophysical Journal* **2014**, *106*, 1070–1078.

(5) Dellisanti, C. D.; Ghosh, B.; Hanson, S. M.; Raspanti, J. M.; Grant, V. A.; Diarra, G. M.; Schuh, A. M.; Satyshur, K.; Klug, C. S.; Czajkowski, C. *PLOS Biol* **2013**, *11*, e1001714.

(6) Hilf, R. J. C.; Dutzler, R. *Nature* **2008**, *452*, 375–379.

(7) Geertsma, E. R.; Nik Mahmood, N. A. B.; Schuurman-Wolters, G. K.; Poolman, B. *Nature Protocols* **2008**, *3*, 256–266.

(8) Mehmood, S.; Allison, T. M.; Robinson, C. V. *Annual Review of Physical Chemistry* **2015**, *66*, 453–474.

(9) Smith, P. K.; Krohn, R. I.; Hermanson, G. T.; Mallia, A. K.; Gartner, F. H.; Provenzano, M. D.; Fujimoto, E. K.; Goeke, N. M.; Olson, B. J.; Klenk, D. C. *Analytical Biochemistry* **1985**, *150*, 76–85.

(10) Rigaud, J.-L.; Levy, D.; Mosser, G.; Lambert, O. *European Biophysics Journal* **1998**, *27*, 305–319.

(11) Martin, M. M.; Lindqvist, L. *Journal of Luminescence* **1975**, *10*, 381–390.

(12) Hilf, R. J. C.; Dutzler, R. *Nature* **2008**, *457*, 115–118.

(13) Ingólfsson, H. I.; Andersen, O. S. *ASSAY and Drug Development Technologies* **2010**, *8*, 427–436.

(14) Zimmermann, I.; Dutzler, R. *PLoS biology* **2011**, *9*, e1001101.

(15) Meyer, T. S.; Lamberts, B. L. *Biochimica et Biophysica Acta (BBA) - General Subjects* **1965**, *107*, 144–145.

(16) Fazekas de St Groth, S.; Webster, R. G.; Datyner, A. *Biochimica Et Biophysica Acta* **1963**, *71*, 377–391.

(17) Kelkar, D. A.; Chattopadhyay, A. *Biochimica et Biophysica Acta (BBA) - Biomembranes* **2007**, *1768*, 2011–2025.

(18) Ingólfsson, H. I.; Sanford, R. L.; Kapoor, R.; Andersen, O. S. **2010**, e2131.

(19) Moore, H. P.; Raftery, M. A. *Proceedings of the National Academy of Sciences* **1980**, *77*, 4509–4513.

(20) Spurny, R.; Billen, B.; Howard, R. J.; Brams, M.; Debaveye, S.; Price, K. L.; Weston, D. A.; Strelkov, S. V.; Tytgat, J.; Bertrand, S.; Bertrand, D.; Lummis, S. C. R.; Ulens, C. *Journal of Biological Chemistry* **2013**, *288*, 8355–8364.

(21) Yanagisawa, M.; Iwamoto, M.; Kato, A.; Yoshikawa, K.; Oiki, S. *Journal of the American Chemical Society* **2011**, *133*, 11774–11779.

Chapter 5

USE OF ULTRA-FAST CONTINUOUS-FLOW MIXING FOR RAPID ACTIVATION OF ELIC

5.1 Introduction

As the thesis title might suggest, I have developed methods to rapidly and precisely control the activation of ligand-gated ion channels. A lot of work (see Chapter 2 and 3) has focused on the development of photochemical triggers. The idea of rapid mixing of ion channels with agonist was always pushed aside, despite the fact that rapid mixing had been used previously to study biological events such as protein folding [1–3]. Rapid mixing is able to achieve mixing times in the 10's of μs regime [4]. Outlined in Figure 5.1 is a schematic of the ultra-fast mixer used in these studies. The mixing on the 10^{-5} s timescale provides a substantial gain in temporal resolution for the monitoring of ion channel activation.

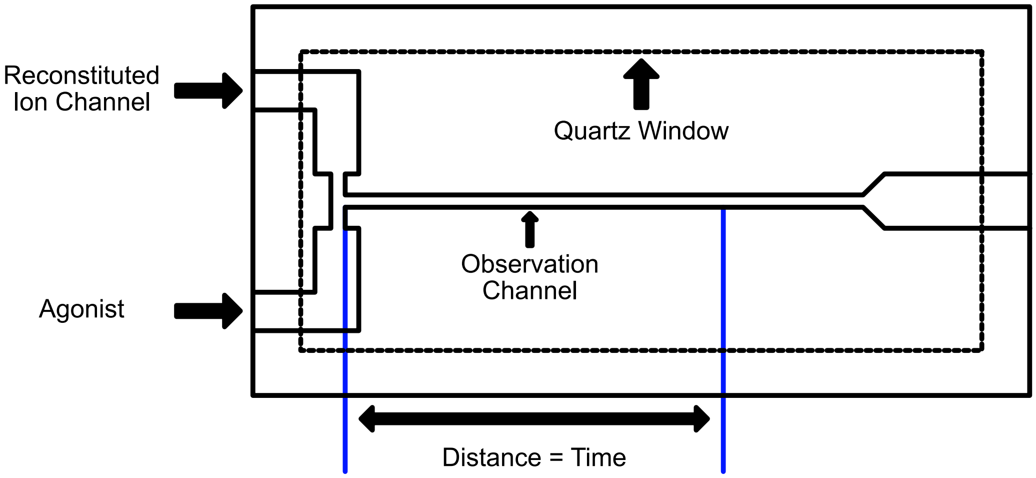

Figure 5.1: A schematic of the ultra-fast continuous-flow mixer used in these experiments. Two solutions (reconstituted ion channel and agonist in this schematic) are held in separate syringes and a syringe pump is used to drive the solutions through the mixer. The mixing speed is determined by the rate of volume flow, and is controlled by the syringe pump. The mixed solutions travels down an observation channel; the distance from the point of mixing can be converted into time after mixing and allows for monitoring reactions during the process (blue lines). The sample then gets collected in the trash (far right of the figure). The mixing channel is made out of 200 μm thick stainless steel plate that is sandwiched in between two quartz pieces (dotted box) which allow for optical measurements to be made.

ELIC is much larger than the proteins used previously [2, 5], and also must exist in a lipid vesicle environment. Mixing on the 10 μs timescale requires extremely high velocities (12 m/s) and might result in the perturbation of the vesicles or proteoliposomes in solution. ELIC has successfully been reconstituted into liposomes (see Chapter 4 for details), and the proteoliposomes will be subjected to ultra-fast continuous-flow mixing. Mixing of ELIC proteoliposomes with propylamine will allow for activation of ELIC on the microsecond timescale. In this chapter I examine the effects of ultra-fast mixing on liposomes and proteoliposomes. I then design and calibrate an intensity-based detection system for use in the ultra-fast mixing experiments. Finally I will discuss the work done to monitor the activation of ELIC at early time points.

5.2 Methods and Materials

5.2.1 General Considerations

ELIC was expressed and reconstituted as above (Chapter 4). All chemicals were obtained from Sigma-Aldrich and used without further purification. $Os(bpy)_3{}^{2+}$ was synthesized by stirring $Os(bpy)_2Cl_2$ with 5 equiv. of 2,2'-bipyridine in methanol at reflux overnight. The solution was then filtered over celite, and the solvent evaporated. The solid was then dissolved in acetonitrile, loaded onto a alumna column, washed with excess acetonitrile, and eluted as a green band with 100% methanol. The UV-visible spectrum agreed well with the published values [6, 7]. $Ru(bpy)_3{}^{3+}$ was formed by oxidation of a solution of $Ru(bpy)_3{}^{2+}$ with PbO_2, and filtering to remove excess PbO_2 yielding a green solution, the spectrum of which agreed with the published spectrum [7, 8]. The concentration of Fe^{2+} in solution was determined using the 1,10-phenanthroline titration assay described previously [9]. Stopped-flow and steady-state luminescence measurements were performed as described above (Chapter 4). Dynamic light scattering measurements were made on Wyatt Technology NanoStar, using 659 nm laser for measurements. Cryo-electron microscopy used a FEI Tecnai 120 keV tranmission electron microscope. Images were collected on a Gatan Ultrascan 2 x 2K camera with 14 μm pixel size. Samples were frozen on a FEI vitrobot mkIII in ethane on quantifoil grids. The operating conditions were as follows: -170°C, 120 keV, magnification 22,000x, objective aperature size of 40 μm, and exposure times of 0.3s. The ultra-fast continuous-flow mixer used was home built as described in [1]. The detection system is described below, and the samples were mixed using a syringe pump (Harvard Apparatus) set to the desired mixing speed. Images were collected using a Thorlabs DCC1545M CMOS detector. Typically 100 frame movies were collected, at a sampling rate of 5 frames per second, a pixel clock speed of 10 MHz, and integration times that allowed for maximum intensity values without saturating the camera. Images were processed in ImageJ. The movie files were imported as grayscale videos, and z-stack averaged. The averaged image was then saved as a tiff file, and imported into MATLAB for further analysis. All data work up was done in MATLAB R2013b (Mathworks, Inc.).

5.3 Results and Discussion

5.3.1 Microfludic ultra-fast Continuous-Flow Mixing of Lipid Vesicles

Initial ultra-fast mixing experiments examined the mixing of liposomes alone. Liposome-only mixing will establish the stability of empty vesicles to the mixing conditions. If empty vesicles do not survive mixing, it is unlikely proteoliposomes would. The study of only LUVs also limits the use of ELIC, which is a very time consuming and costly protein to purify. Previous experiments using this mixer resulted in a dead-time of mixing was estimated to be *ca.* 150 μs [1]; a 150 μs dead-time is almost an order of magnitude faster than previous ion channel activation studies. Mixing of lipid vesicles occurred under similar conditions. Characterization of the vesicles before and after mixing allows for any perturbation of the vesicles to be monitored.

Vesicle were characterized prior to, and following, mixing in the ultra-fast continuous-flow mixer. The vesicles were characterized using dynamic light scattering (DLS), fluorescence leakage assays, and cryo-EM tomography ensuring that no change in the vesicles occurred upon mixing. Dynamic light scattering monitors the bulk particle size in solution [10]; use of DLS will determine the vesicle size distribution before and after mixing. DLS measurements of vesicles before and after mixing resulted in a similar observed size-distribution (Figure 5.2). The vesicle radius is centered around 60 nm, in good agreement with the expected size from use of a 100 nm polycarbonate filter during vesicle formation. No bulk size change in the vesicle solution suggests that there are no fusion or rupturing events that occur during the mixing process. This does not rule out the complete dissolution of the vesicles and the subsequent formation of lipid micelles smaller then the measurement limits of DLS.

Slight deformation of the vesicle bilayer, which could result in undesired exchange between the lumen solution and the bulk, could occur with out an observed change in the DLS signal. A fluorescence leakage assay was used to examine the possibility of this event from occurring. A quenched fluorescent dye is encapsulated inside

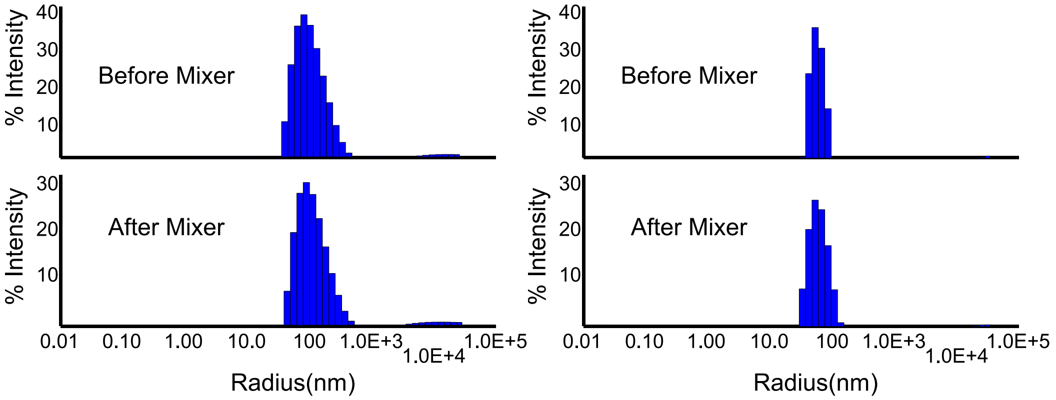

(a) **(b)**

Figure 5.2: DLS measurements of fluorescein-encapsulated LUVs (a) and ANTS/DPX-encapsulated LUVs (b) before and after mixing with a calculated mixing speed of 2000 mm/s. The vesicle size before and after mixing are the same. This suggests that the mixing conditions do not disrupt the bulk properties of the LUVs.

the LUVs, and with perturbation of the lipid bilayer the dye can escape the lumen and enter the bulk. Bulk dye is no longer quenched, resulting in a fluorescence increase. Two different dye and quenching methods were used. I will first mention the fluorescein quenching experiments. At high concentrations, fluorescein is self-quenched [11], and has been used previously to monitor vesicle leakage [12]. The complete removal of extra-vesicular fluorescein was very difficult and resulted in high background fluorescence signals (Figure 5.3a). Regardless, the fluorescein leakage experiments suggest that little disruption of the vesicles occurs. The mixed sample only had around 5% greater fluorescence (Figure 5.3a, Red vs. Black lines).

In a effort to have lower background fluorescence, ANTS (fluorophore) and DPX (quencher) were contained within vesicles [13, 14]. Background fluorescence signals of 25% of the theoretical maximum (Figure 5.3b, black line) were observed using ANTS/DPX. LUVs containing ANTS and DPX were mixed, and collected after mixing for fluorescence measurements. To control for inconsistencies arising from dilution errors, and the sample-to-sample variation in fluorescence, each sample was normalized to the 100% fluorescence intensity (Figure 5.3, blue line). The 100% fluorescence intensity was obtained by lysing each sample with Triton X-100 detergent (Figure 5.3, Blue lines). Lysis of the vesicles releases ANTS and DPX into the bulk, diluting the effective concentration of each, and at these dilute concentrations ANTS is not quenched by DPX. The fluorescence observed from the lysed samples then results in the fluorescence from a 0% quenched ANTS. Around a

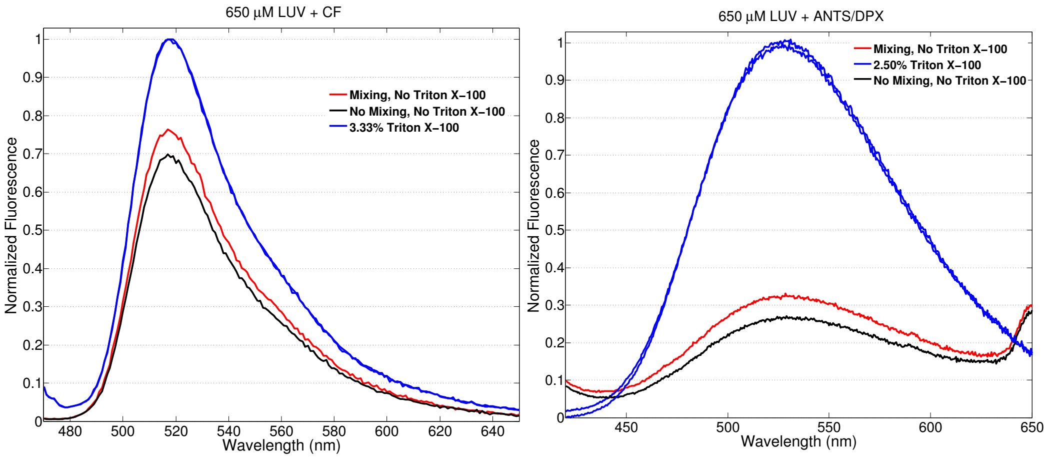

(a) **(b)**

Figure 5.3: (a) Steady-state luminescence spectrum of LUVs with self-quenching fluorescein encapsulated within the lumen before and after mixing. A background fluorescence of around 70% is observed for the quenched fluorescein samples (black line). A *ca.* 5% increase in fluorescein fluorescence is seem for the mixed LUVs (red line), when compared to the unmixed samples. (b) ANTS/DPX encapsulated vesicles steady-state luminescence spectrum before and after mixing. The background fluorescence of the ANTS/DPX assay 25% (black line); much lower background fluorescence is observed for ANTS/DPX than fluorescein. Mixing of the LUVs resulted in a 5% increase in ANTS fluorescence (red line). The minimal increase in fluorescence after mixing of the vesicles suggests that little perturbation of the lipid vesicles occurs.

5% difference in the fluorescence of ANTS between the mixed or unmixed vesicles (Figure 5.3b, Red and Black lines) was observed. This was true for a number of mixing speeds and liposome concentrations. Perturbation of the lipid membrane would release ANTS and DPX into the bulk solution and result in a increase of fluorescence. The similar ANTS fluorescence of the mixed and unmixed samples shows that little perturbation of the lipid bilayer occurs during the mixing process.

Cyro-EM tomography was the last characterization technique used to monitor vesicle stability. Vesicles were collected after mixing, and the mixed and unmixed vesicles were flash-frozen on separate EM grids. Cryo-EM allowed for direct imaging of the lipid vesicles. The morphologies and size distribution of the lipid vesicles did not change significantly as observed by cryo-EM (Figure 5.4). The mixing speeds of the above experiments were the same as previous experiments that yielded a 150 μs dead-time. The maximum linear velocity of solution in the flow channel, as determined by conversion of volume flow, is 2000 mm/sec. The vesicle stability and dead-time are both functions of this mixing speed; changing the mixing speed will require the reexamination of both the vesicle stability and dead-time. Under a velocity of 2000 mm/sec, DLS, fluorescence leakage, and cryo-EM indicate that

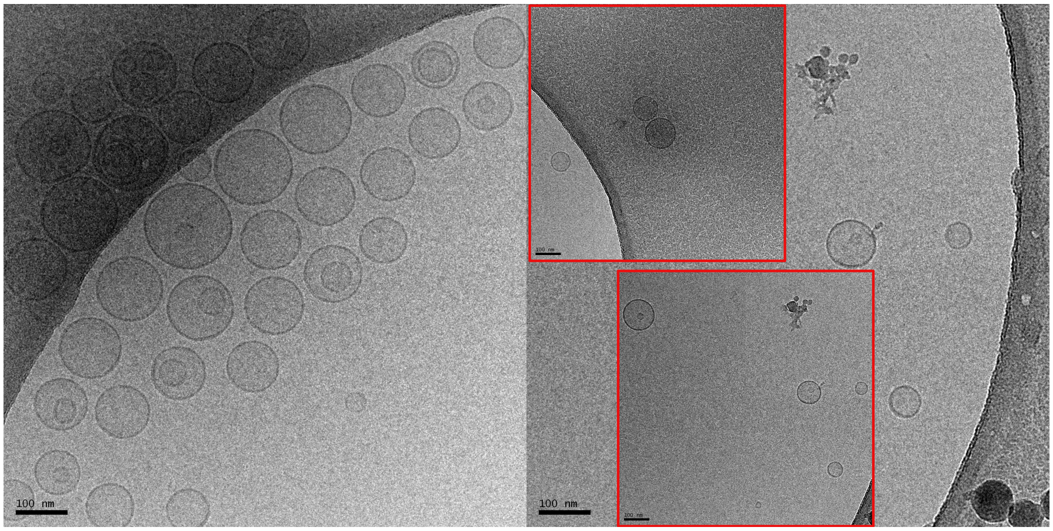

(a) (b)

Figure 5.4: Cryo-EM tomography images of ANTS/DPX filled vesicles before (a) and after (b) mixing through the ultra-fast continuous-flow mixer at 2000 mm/s. The scale bar for each figure is 100 nm. (b) The insets (boxed in red) which are separate images of the same mixed sample. The concentration of the mixed sample is lower than the pre-mixed sample, and the multiple images are used to display a number of vesicles that were observed. In all the images, the vesicles appeared circular, mostly unilamellar, and around 100 nm in diameter. No deformation of the vesicles confirms that there is no perturbation of LUVs upon mixing.

there is little perturbation of the liposomes under the ultra-fast continuous-flow mixing conditions.

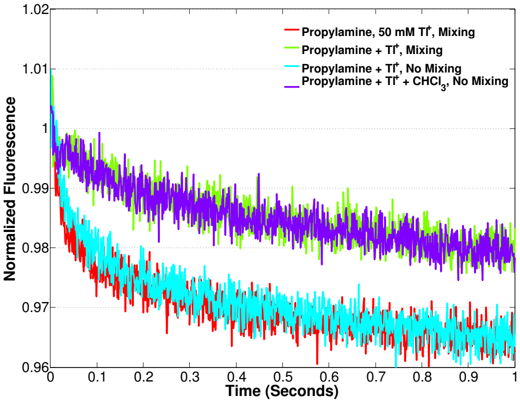

Figure 5.5: ELIC proteoliposomes functional assay using Tl^+ quenching before and after mixing in the ultra-fast continuous-flow mixer at 2000 mm/s. Rapid ANTS quenching is observed in upon mixing ELIC proteoliposomes with propylamine. This quenching is attenuated with the addition of chloroform, a known ELIC inhibitor. Mixing of ELIC proteoliposomes does not alter the ANTS quenching profiles, showing that ELIC proteoliposomes retain function after ultra-fast mixing.

I want to mix reconstituted ELIC with propylamine to monitor the activation of ELIC. Mixing of ELIC proteoliposomes requires that mixing does not perturb

ELIC proteoliposomes as well; it is not known the effect ELIC will have on the properties of the liposomes. To address this, ELIC was reconstituted into vesicles and function confirmed as above. Functional ELIC proteoliposomes were then mixed through the ultra-fast continuous-flow mixer and collected after mixing. The ELIC proteoliposome function was then tested. ELIC proteoliposomes after mixing displayed the same functional behaviour as unmixed samples; an increased quenching rate was observed in the presence of propylamine, which was inhibited by the addition of chloroform (Figure 5.5). This result shows ELIC function is retained after the rapid mixing. While the function of ELIC is retained it is unclear the extent to which function is retained; a portion of the sample could be rendered nonfunctional by the mixing. Use of the DLS, fluorescence leakage, and cyro-EM assays as above, could address this issue. The raw fluorescence intensity under activation could also be used. Lower intensity might suggest that fewer channels are activated, an indication that mixing perturbs some of the system. I am hesitant to use intensity measurements because of the fluctuation in this value. I have previously observed large fluctuations in raw measurements between different repeats of the same sample. Regardless, the thallium quenching assay would not work if there was complete proteoliposome destruction. Functionally reconstituted ELIC in liposomes is able to retain function after rapid mixing.

5.3.2 Fluorescence Intensity Detection Setup

I have established both lipid vesicles, and functionally reconstituted ELIC, can survive the rapid mixing. An assay that will measure ion channel activation at this timescale needs to be developed; initial efforts will focus on using the established ANTS quenching assay to monitor the first few milliseconds of the ion channel activation [3]. These measurements will examine the initial burst phase of quenching that is observed in the stopped-flow measurements. A flow velocity of 2000 mm/s will translate to an observable time of 6 ms in the mixing channel. On this timescale, thallium flux across the membrane in a non-selective manner is not a concern, which will simplify the analysis. The readout for the ultra-fast continuous-flow mixing will be ANTS fluorescence quenching by thallium, as was the case in the stopped-flow measurements. Because the lifetime of the ANTS is not needed for these measurements, a new detection system was designed that can measure the intensity of ANTS fluorescence in the mixer.

A fluorescence-intensity detection system was built (Figure 5.6). The ANTS optical absorption spectrum has a peak at 355 nm, with the emission peak at 520 nm. A 405

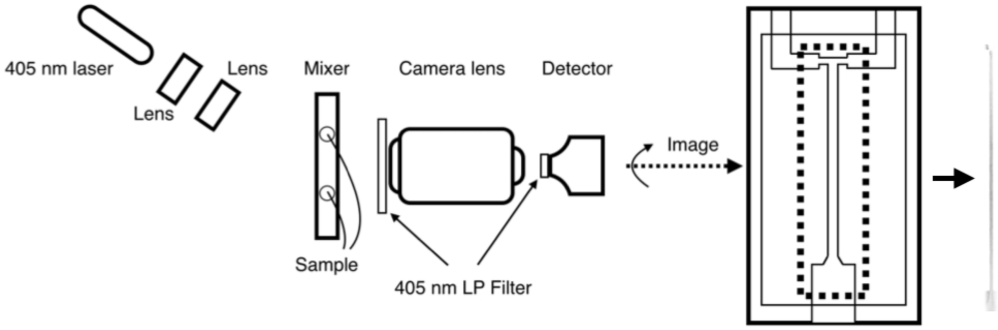

Figure 5.6: A schematic representation of the fluorescence detection system using a 405 nm diode laser for excitation, and a Thorlabs CMOS sensor for luminescence detection. The sample is mixed through the mixer with the desired buffer. The excitation from the 405 nm laser is shaped into a sheet and excites the mixing channel (highlighted in a dashed box). The fluorescence is then collected using a camera lens, and imaged on a detector. An image of the fluorescence observed from the mixing of ANTS-filled LUVs with water is found at the far right of the figure.

nm diode laser was used as an excitation source; the absorbance peak is broad and 405 nm will be able to excite ANTS. The laser is then defocused using a negative focal length lens, followed by a cylindrical lens. The cylindrical lens focuses the laser into a sheet that is used to excite the mixing channel. Emission was then focused using a camera lens, onto a commercially available monochromatic CMOS detector from Thorlabs. Excitation light was rejected using two highly refelective 405 nm dielectric mirrors, one placed before the collection lens, and the other placed in front of the CMOS detector. Use of just one mirror resulted in detection of the excitation source. The ultra-fast continuous-flow mixer image was then projected onto the entire CMOS detector sensor. A few dark pixels on either end of the mixing chamber were used to provide background measurements. Mixing speeds of 2000 mm/s resulted in 6 μs per pixel time resolution. Magnification of the mixing chamber would allow for faster time resolution; however, imaging the entire channel proved more useful. Lipid vesicles were prepared in the absence of ELIC to determine the fluorescence sensitivity of the detector setup. Imaging of these vesicles resulted in ANTS fluorescence observed in the mixing chamber (Figure 5.6, far right). The fluorescence was not present without excitation or without ANTS present. This result shows that the detection system developed is able to image 100% of the ANTS fluorescence that will be present in the ELIC proteoliposomes.

5.3.3 Determination of Mixing Dead-Time

The mixer dead-time needs to be determined in conjunction with use of the detector setup. Standard dead-time calibrations of stopped-flows and continuous-flow mixers [3, 15] use the fluorescence quenching of N-acetyl-L-tryptophanamide (NATA) by

N-bromosuccinimide (NBS). In this reaction NATA is excited with UV (254 nm) light, and the fluorescence is monitored at 330 nm. This assay will not work with the current detection system. The CMOS detector is not sensitive to UV light.

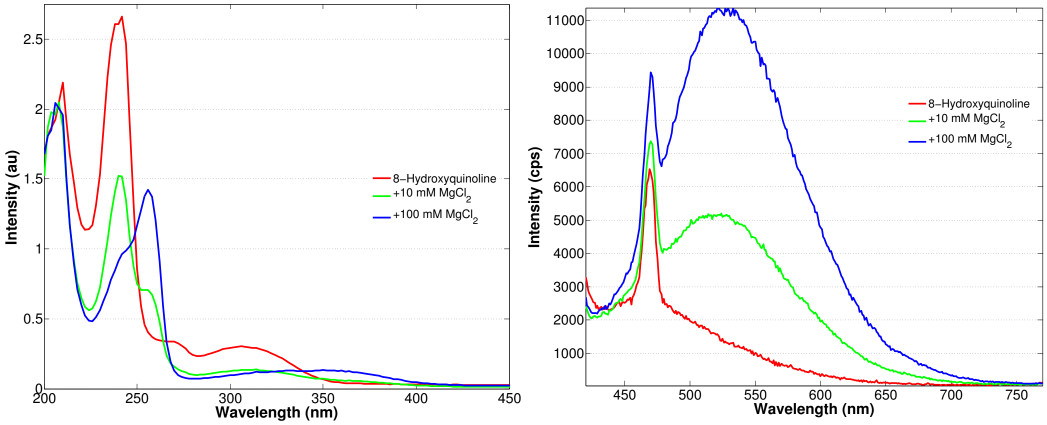

(a) **(b)**

Figure 5.7: (a) The UV-visible spectra of 8-hydroxyquinoline (8HQ, red line), 8HQ + 10 mM $MgCl_2$ (green line) and 8HQ + 100 mM $MgCl_2$ (blue line). Addition of Mg to a solution of 8HQ results in a the formation of a Mg-8HQ chelate, as is evident from the shift in the UV-visible spectrum. There is very low absorbance at 405 nm of the Mg-8HQ chelate. (b) Steady-state luminescence spectra of 8HQ upon excitation at 405 nm (red line), and with addition of 10 mM and 100 mM $MgCl_2$ (green and blue lines, respectively). No emission is observed without Mg present. A weak fluorescence peak is observed at *ca.* 530 nm. The water Raman stretch is also visible at 460 nm, which highlights how weak the fluorescence of the Mg-8HQ chelate is with 405 nm excitation.

Magnesium chelation of 8-hydroxyquinoline has been reported as a visible-wavelength fluorescence turn-on assay used to measure dead-times of mixing [16]. This assay was not successful. No fluorescence of the Mg-8HQ chelate was observed using the CMOS detector. This result is not shown because it is a black image. Little 405 nm absorbance was observed even at high Mg concentrations (Figure 5.7a). Using a steady-state fluorometer, weak fluorescence of the Mg-8HQ system is observed (Figure 5.7b). The luminescence (405 nm excitation) is so weak that the water Raman scattering (Figure 5.7b, peak at 460 nm) can be observed; the Raman scatter is typically washed out in the luminescence. The steady-state fluorometer uses a PMT for fluorescence detection, which is a method that results in amplification of the signal. This amplification of the signal allows for the weak fluorescence to be observed. The CMOS detector is a direct intensity measurement. The low fluorescence observed with the fluorometer suggests that this assay is not adaptable for the detection system utilizing the CMOS camera.

A new dead-time determination assay is needed that has the following requirements:

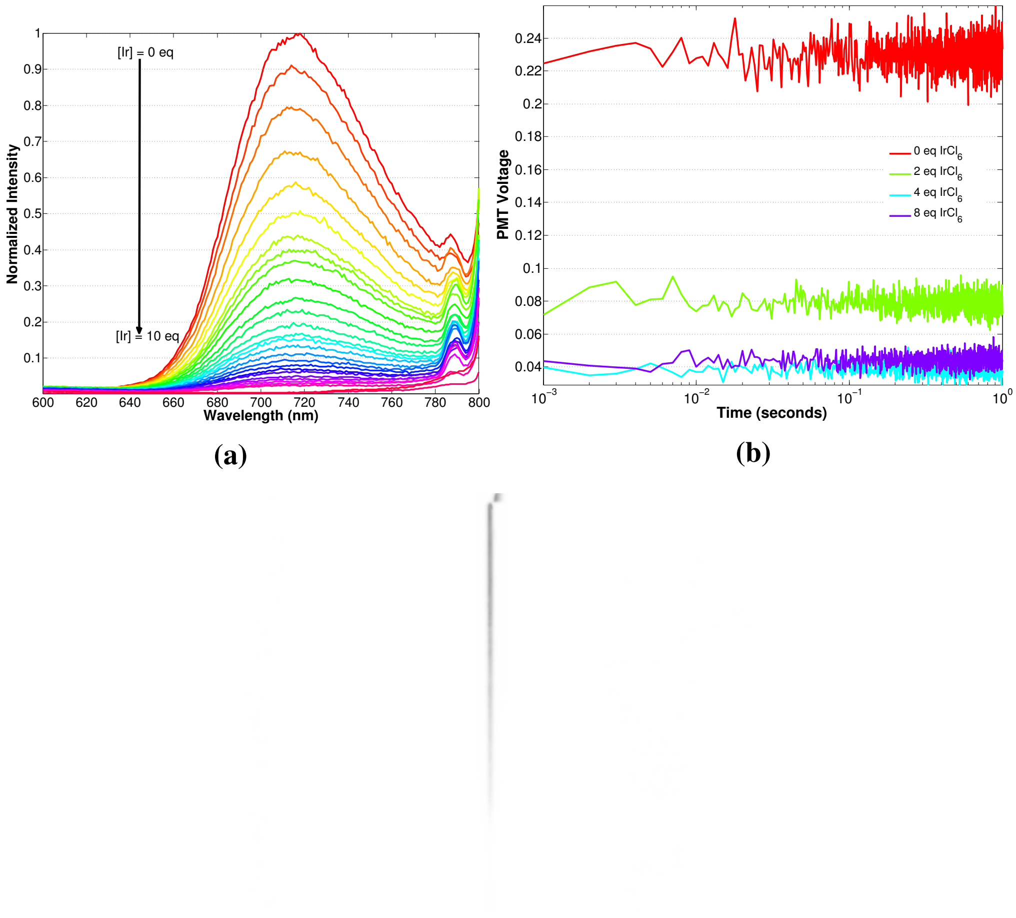

(a) **(b)**

(c)

Figure 5.8: (a) Luminescence quenching of $Os(bpy)_3{}^{2+}$ by hexachloroiridate as observed under steady-state conditions, λ_{ex} = 405 nm. The luminescence peak is observed at 720 nm, and is quenched upon addition of increasing equiv. of Ir^{4+}. This oxidation by Ir^{4+} results formation of Os^{3+} which is not luminescent. (b) Stopped-flow luminescence of $Os(bpy)_3{}^{2+}$ with increasing amounts of Ir^{4+} quencher. In the absence of Ir^{4+}, and at maximum detector voltage, there is very little Os^{2+} luminescence observed (red line). Addition of Ir^{4+} will quench the luminescence, and results in no signal detected (green, purple, and cyan lines). The quenching of Os^{2+} appears as a decrease in the intensity, this shows that the reaction with Ir^{4+} is complete under the mixing conditions. (c) Image of the luminescence of $Os(bpy)_3{}^{2+}$ within the ultra-fast continuous-flow mixer using the Thorlabs detector (Figure 5.6). The incomplete image in is due to misalignment of the detector system, and not quenching of the luminescence.

1 - visible light fluorescence, 2 - 405 nm excitation, and 3 - large quantum yield of emission. Two systems were designed that met these requirements. The first would examine the $Os(bpy)_3{}^{2+}$ luminescence quenching by oxidation of Os^{2+} to Os^{3+} with hexachloroiridate (Figure 5.8a). Os^{2+} luminescence was observed with 405 nm excitation in the ultra-fast mixer detection setup with the Thorlabs detector (Figure 5.8c). To verify the use of Os^{2+} oxidation to determine the dead-time, the mixing

of Os^{2+} with Ir^{4+} occurred in a stopped-flow (Figure 5.8b). Using a stopped-flow allows for referencing the Os^{2+} method with the established NATA/NBS protocol, and determination of the second-order rate constant for Ir^{4+} oxidation of Os^{2+}. Unfortunately, the Os^{2+} data did not yield useful information. $Os(bpy)_3{}^{2+}$ luminescence is weak and red-shifted; the emission peak is at 720 nm [7]. Stopped flow measurements of Os^{2+} fluorescence in the absence of Ir^{4+} yielded very little signal (Figure 5.8b, red line). This is likely due to the combination of weak luminescence, coupled with red emission. The sensitivity of the PMT detector is about ten-fold less sensitive at 720 nm than at the maximum sensitivity wavelength. Mixing Os^{2+} with Ir^{4+} yields a decrease in the luminescence signal that is not resolved in the stopped-flow (Figure 5.8b, green, purple and cyan line). This behaviour suggests that the reaction between Os^{2+} and Ir^{4+} occurs faster than the response time of the instrument. To observe this reaction the Os^{2+} concentration could be lowered; unfortunately, the small unquenched Os^{2+} luminescence does not allow the concentration to be lowered. As a result, the Os^{2+} system is not amenable for dead-time calculations.

A new method was developed for use in the determination of the dead-time of the mixer, which has higher luminescence quantum yields and a blue-shifted emission (limitations of the Os^{2+} assay). The oxidation of Fe^{2+} ions by mixing with $Ru(bpy)_3{}^{3+}$ was examined. The resulting solution will give Fe^{3+} and luminescent $Ru(bpy)_3{}^{2+}$. At neutral pH, Ru^{3+} is not stable requiring the experiments to be conducted in 1 M perchloric acid. Working with such highly acidic solutions is likely to increase the viscosity of the solutions. A higher viscosity solution will alter the mixing properties, but would provide a lower-limit of mixing dead-time. Fortunately, 1 M perchloric acid has a similar viscosity (*ca.* 1 cPa) as water at 20°C [17, 18]. To confirm the CMOS detector can detect Ru^{2+} luminescence, $Ru(bpy)_3{}^{2+}$ was mixed and the luminescence detected (Figure 5.9d).

This assay had not been used previously for dead-time determination; the dead-time of a stopped-flow was determined. Oxidation of Fe^{2+} by Ru^{3+} resulted in a dead-time of *ca.* 2 ms (Figure 5.9b). The use of NATA/NBS assay resulted in a dead-time of around 1.5 ms (Figure 5.9a). The second-order rate constant observed for Fe^{2+} oxidation was similar to the published value [8]. The Ru^{3+} reaction is a turn-on fluorescence assay, as opposed to the quenching NATA/NBS reaction. For the determination of the dead-time using NATA/NBS, the pseudo-first order quenching rate is fit to a single exponenetial and extrapolated beyond observed t_0 to

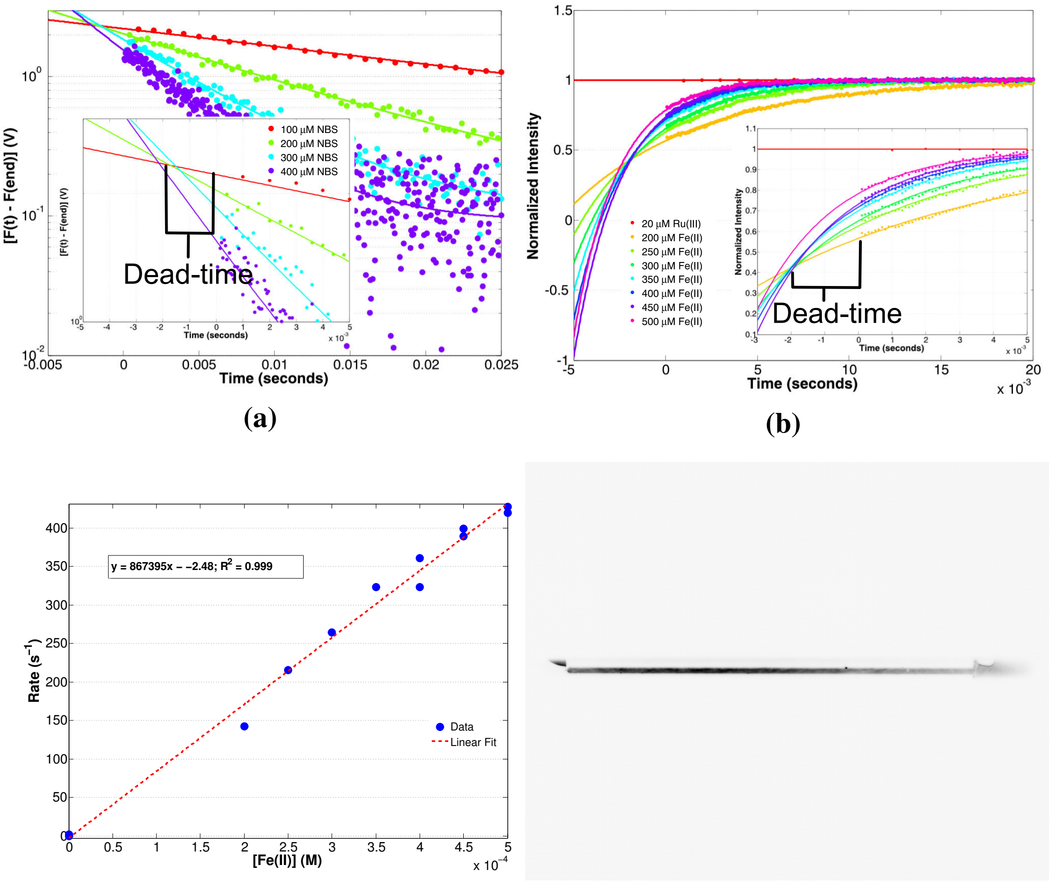

(a) **(b)**

(c) **(d)**

Figure 5.9: (a) Dead-time determination of the stopped-flow using a the standard NATA/NBS reaction [15]; inset is magnification around the observe zero time point. The dead-time of the stopped-flow is around 1.5 ms. For (a) and (b) the luminescence intensity values are shown as circles, with the single-exponential fits as solid lines. (b) Verification of Ru^{3+}/Fe^{2+} assay for dead-time determination; inset is magnification around time zero. The fluorescence intensity of $Ru(bpy)_3{}^{2+}$ is monitored as a function of time. Increasing time results in formation of more luminescent $Ru(bpy)_3{}^{2+}$ and an increase in signal. The luminescence intensity is normalized to the last points. Extrapolation of the exponential fit results in a dead-time of 2 ms, close to the value obtained in (a). (c) Second-order quenching reaction of Ru^{3+} with Fe^{2+} under pseudo-first order conditions; slope is the second-order rate constant, in good agreement with the published value [8]. (d) Image of $RuRu(bpy)_3{}^{2+}$ luminescence in the ultra-fast continuous-flow mixer, the difference in intensity across the mixer is due to the vignetting of the image.

a point where the fits intersect. The difference in time between observed t_0 and point of intersection is the dead-time of the reaction. The Fe^{2+} oxidation reaction was normalized to the t_∞ luminescence value, fit to a single exponential, and extrapolated past observed t_0 to a point of crossing. Extrapolation of the fit before t_0 provides values of either 100% fluorescence (NATA/NBS) or 0% fluorescence (Ru^{3+}/Fe^{2+}), a point in which there has been no mixing of the two components. The difference between this time point and the observed t_0 is the dead-time of the instrument.

The Ru^{3+}/Fe^{2+} assay was then used to determine the dead-time of the ultra-fast continuous flow mixer. Mixing at speeds used previously (2000 mm/s), the Ru^{2+} fluorescence was monitored over the length of the channel. The complete reduction of Ru^{3+} occurred by the end of the mixing channel. The data obtained from the mixer fluorescence detection system needs to be corrected for the reduction of the image intensity at the edge of the image (vignetting) observed. To correct for image distortion, a 100% luminescence sample (Ru^{2+} of the same concentration was mixed in the absence of Fe^{2+}) and used as a correction curve. The luminescence intensity should be the constant across the entire mixing channel, and any difference in intensity is due to vignetting of the image. The Ru^{2+} image was normalized, and all of the other images were multiplied by the reciprocal of the normalized pixel value. In the case of the Ru^{2+} sample, the correct image results in completely flat line across the mixing chamber. All of the pixel rows that consisted of the Ru^{2+} luminescence signal were combined and averaged. The final adjustment converts the pixel number to a timepoint. This was achieved by using the known mixer channel distance (13.5 mm) and converting the pixel to mm using ImageJ64 measurement tools.

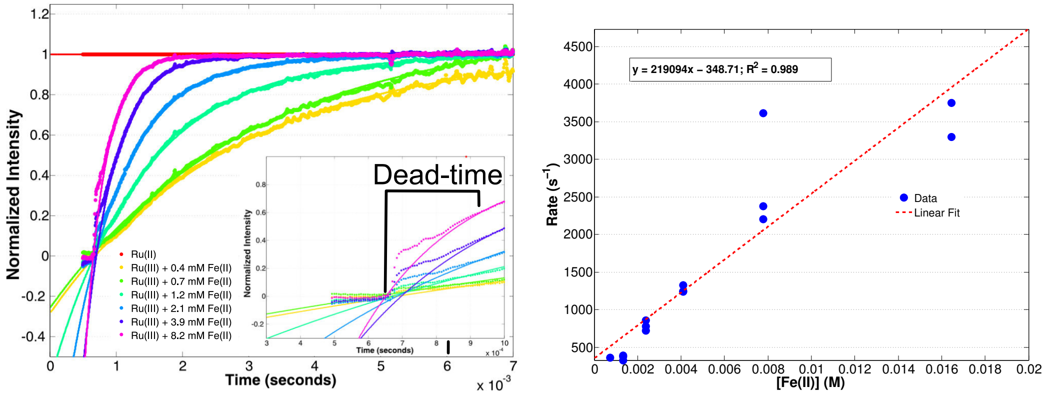

(a) **(b)**

Figure 5.10: (a) Dead-time determination of the mixer using a the oxidation of Fe^{2+} by Ru^{3+}; inset is magnification around the observe zero time point. Corrected luminescence intensity is shown as circles, with the single-exponential fits as solid lines. The intensity values are normalized to the last pixel in the mixer. A increase in Ru^{2+} formation is observed under higher Fe ion concentrations. Extrapolation of the exponential fits of the reaction results in a dead-time between 100 and 200 μs. (b) Second-order quenching reaction of Ru(III) with Fe(II) under pseudo-first order conditions; slope is the second-order rate constant, which is different than what is observed using stopped-flow measurements.

Using the above image correction method, luminescence traces were obtained (Figure 5.10a) for the oxidation of Fe^{2+} by Ru^{3+}. A concentration-dependent increase in luminescence was observed for these mixing conditions (Figure 5.10a). Fitting the turn-on luminescence curves resulted in a second-order rate constant for the reaction of 2.2 $\times 10^5 M^{-1} s^{-1}$ (Figure 5.10b), about three fold lower than the published value. The second-order rate constant is consistently low across multiple samples. One source of error could come from the sensitivity of this measurement towards the alignment of the detection system. Misalignment results in uneven illumination of the mixing chamber and skewing the image collected on the detector. Misalignment causes in unequal weight placed on pixels during the correction process. Because these measurements are raw intensity measurements, it is critical to collect the reference (Ru^{2+}) image in the exact same manner as the experimental data. If the alignment changes slightly throughout sample collection, error in the correction of the samples will occur.

One additional complication, and potential source of error, is that Ru^{3+} is a 1.23 V oxidant [7]. Ru^{3+} was reduced by the mixer in the absence of any aqueous Fe^{2+} ions. One source of reduction of Ru^{3+} was exposure to the stainless-steel filter. Removal of these filters from the lines resulted in less Ru^{3+} reduction observed in the absence of Fe^{2+}. Stainless-steel oxidation by Ru^{3+} is not too surprising, 1.23 V is very oxidizing, and stainless-steel has a lot of additives which could serve as reductants. Flow through a high-surface area frit provides much more exposure to the steel. The removal of all the stainless steel in the mixer could not occur. The mixer housing and the mixing channel are both made of stainless steel, and neither of these pieces can be removed from the mixer. Ru^{3+} reduction did not occur if the mixing speed remained at 2000 mm/s in the absence of the frits. Slower mixing speeds, or static Ru^{3+} in the mixing chamber resulted in the formation of Ru^{2+} in the absence of aqueous Fe^{2+} ions. The non-specific reaction between Ru^{3+} and the mixer can complicate dead-time determination. Unfortunately, the removal of the filters caused the channel to become clogged with dust particles. Removing these particles required dismantling of the detection setup; this dismantling alters the imaging position and causing errors during the vignetting correction procedure. Despite all of these issues with the assay, the dead-time was determined using this assay. The extrapolated fits intersect at a value between 100 μs and 200 μs (Figure 5.10a, inset), a number that will be used conservatively as the dead-time of the mixer with this detection setup.

5.3.4 Measurement of ELIC Activation using the Continuous-Flow Mixer

The fluorescence detection system above was used to monitor the ANTS fluorescence-quenching by Tl^+ with reconstituted ELIC. ELIC was reconstituted as above, and function verified by stopped-flow (Figure 5.11a). ELIC proteoliposomes were then mixed in the ultra-fast continuous-flow mixer with blank buffer (no thallium or propylamine), Tl^+ buffer, Tl^+ buffer with propylamine, and finally Tl^+, propylamine, and chloroform buffer. ANTS fluorescence is not quenched in the absence of thallium and the blank buffer was the image used for correction of the observed vignetting.

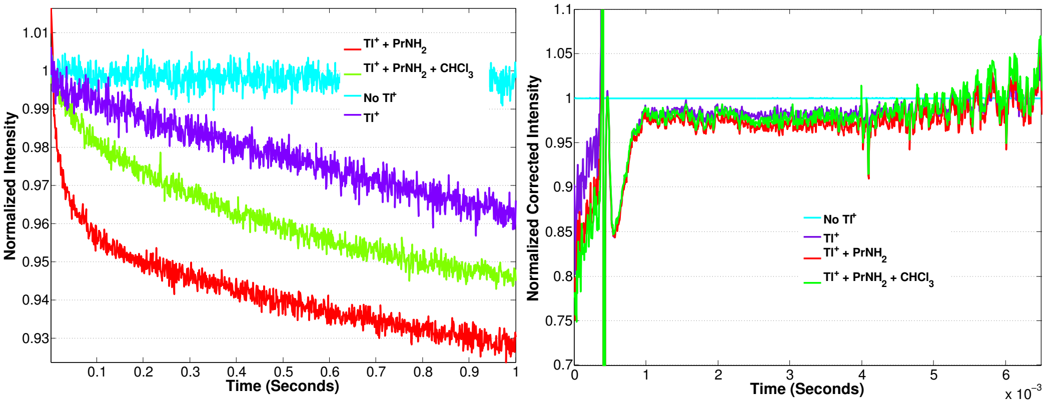

(a) **(b)**

Figure 5.11: (a) Stopped-flow ANTS fluorescence intensity of ELIC proteoliposomes in the presence of thallium (Purple line) with activating proplyamine (Red line), and ELIC blocker (Green line). A rapid quenching of ANTS fluorescence is observed in the presence of propylamine, which is attenuated by chloroform. This shows that the ELIC is functionally reconstituted into these proteoliposomes (b) Monitoring of ANTS fluorescence from ELIC proteoliposomes exposed to thallium (Purple line) with activating proplyamine (Red line), and ELIC blocker (Green line) in the ultra-fast continuous-flow mixer using the Thorlabs detection system. The mixing channel starts around 400 μs. There is no difference in ANTS fluorescence observed for any Tl^+ sample. The lack of propylamine-specific quenching demonstrates that the activation of ELIC is not observed using this setup.

No difference in ANTS fluorescence quenching was observed for all the samples exposed to thallium (Figure 5.11b). All of the Tl^+ buffers resulted in quenched ANTS fluorescence. The non-specific quenching is likely due to the quenching of free ANTS in solution, the burst-phase quenching observed in the stopped-flow measurements. Examination of the stopped-flow experiments show a 4% decrease in ANTS fluorescence (in the first 100 ms), and a much smaller decrease in the first 6 ms, for activated ELIC proteoliposomes. ELIC proteoliposomes in the absence of propylamine recorded a change of about 1% in ANTS fluorescence over this timescale. These are very small fluorescence changes, especially when attempting to distinguish between the two. The scatter in the mixer data appears to be around ±2%. The sensitivity of the mixing experiments is not high enough to distinguish a difference in the ANTS quenching of ELIC proteoliposomes as a result. At longer timepoints, there is around 10% change in fluorescence; however, a stopped-flow is a perfect tool for measurement at these longer time points. Use of a different detector, such as a cooled CCD or CMOS detector, might provide higher dynamic range, and lower the noise. One issue I would like to mention is that continuous-flow measurements use an absurd amount of sample. This presents a problem when conducting experiments with sample limitations such as the ELIC experiments. The ELIC continuous-flow mixing results suggest the fluorescence detection system, as designed, is not suitable to monitor ELIC activation on these timescales.

5.4 Conclusions and Future Outlooks

Despite the altered *in vitro* functional state of ELIC, the above (Chapter 4) reconstitution protocol was used to monitor the first 6 ms of ANTS quenching using a continuous-flow mixer. I was able to show that lipid vesicles were able to survive rapid mixing that affords a 150 μs mixing dead-time. I was also able to show that the functionality of ELIC was preserved upon mixing. A fluorescence detection system was then designed, using a CMOS detector, which would allow for direct intensity measurements to be made of the rapid mixing events. A new dead-time determination assay was developed utilizing the oxidation of Fe^{2+} by $Ru(bpy)_3{}^{3+}$. Using this assay, with the fluorescence detection system, resulted in the determination of dead-time of mixing (*ca.* 200 μs) of the continuous-flow mixer. The mixer was then used, in combination with the ANTS quenching assay, to monitor the early stage activation of ELIC. Unfortunately, with the functionally reconstituted samples available, monitoring of ELIC activation was not possible with this new system.

What I have established in this chapter are a few initial results that can serve as starting points for further optimization of the system. Optimization of the dead-time calibration is necessary; the second-order rate constant should agree with the literature value (as was observed in the using stopped-flow, shown in 5.9c). This discrepancy could be due to the reaction of Ru^{3+} with other species besides Fe^{2+} ions in the mixer, or an error in the Fe^{2+} concentration. A fluorescence quenching assay monitoring the oxidation of tris(tetramethyl-dipyridyl)Ru^{2+} by Ir^{4+} could be used as an alternative assay. The reduction potential of this substituted Ru^{2+} complex is similar to the $Os(bpy)_3{}^{2+}$ allowing for oxidation by Ir^{4+}. Verification the mixer detection setup can monitor the ANTS quenching is also necessary. Collection of more frames to limit the noise is not the most practical approach; S/N goes as the square of the sample number and is not possible for sample-limited experiments. Gramicidin vesicles could be used to verify the detector setup. Gramicidin vesicles result in a 10 - 15% change in ANTS fluorescence in the first few ms (Figure 4.10b) which might provide a signal large enough to be observed. Gramicidin is commercially available so the sample would not be limited. A different detector also could provide greater sensitivity, but detectors are expensive and unless the system will be used extensively I do not recommend this. Time-resolved measurements is another potential avenue that could be explored; dynamic quenching of ANTS would result in a decrease in ANTS fluorescence lifetime dependent on thallium concentration. ANTS/thallium quenching rates could be determined *in vitro* and compared with those obtained in the mixing experiments. This method, however, depends on dynamic quenching of ANTS by thallium which needs to be confirmed first. Also, time-resolved measurements, using a streak-camera for detection, would require even more sample. This limits the practicality of these experiments. While I do not advocate pursuing this system further, I have outlined above potential places for improvement. In all I believe that this work presents initial attempts at the monitoring of ion channel activation gaining about one order of magnitude on previous measurements.

References

(1) Kimura, T.; Lee, J. C.; Gray, H. B.; Winkler, J. R. *Proceedings of the National Academy of Sciences* **2007**, *104*, 117–122.

(2) Kimura, T.; Lee, J. C.; Gray, H. B.; Winkler, J. R. *Proceedings of the National Academy of Sciences* **2009**, *106*, 7834–7839.

(3) Shastry, M. C. R.; Luck, S. D.; Roder, H. *Biophysical Journal* **1998**, *74*, 2714–2721.

(4) Gambin, Y.; Simonnet, C.; VanDelinder, V.; Deniz, A.; Groisman, A. *Lab on a Chip* **2010**, *10*, 598–609.

(5) Yamada, S.; Ford, N. D. B.; Keller, G. E.; Ford, W. C.; Gray, H. B.; Winkler, J. R. *Proceedings of the National Academy of Sciences* **2013**, *110*, 1606–1610.

(6) Burstall, F. H.; Dwyer, F. P.; Gyarfas, E. C. *Journal of the Chemical Society* **1950**, 953–955.

(7) Creutz, C.; Chou, M.; Netzel, T. L.; Okumura, M.; Sutin, N. *Journal of the American Chemical Society* **1980**, *102*, 1309–1319.

(8) Braddock, J. N.; Meyer, T. J. *Journal of the American Chemical Society* **1973**, *95*, 3158–3162.

(9) Fortune, W. B.; Mellon, M. G. *Industrial & Engineering Chemistry Analytical Edition* **1938**, *10*, 60–64.

(10) Hallett, F. R.; Watton, J.; Krygsman, P. *Biophysical Journal* **1991**, *59*, 357–362.

(11) Chen, R. F.; Knutson, J. R. *Analytical biochemistry* **1988**, *172*, 61–77.

(12) Weinstein, J. N.; Blumenthal, R.; Klausner, R. D. In *Methods in Enzymology*, Jere P. Segrest, J. J. A., Ed.; Plasma Lipoproteins Part A: Preparation, Structure, and Molecular Biology, Vol. Volume 128; Academic Press: 1986, pp 657–668.

(13) Ellens, H.; Bentz, J.; Szoka, F. C. *Biochemistry* **1985**, *24*, 3099–3106.

(14) Smolarsky, M.; Teitelbaum, D.; Sela, M.; Gitler, C. *Journal of Immunological Methods* **1977**, *15*, 255–265.

(15) Peterman, B. F. *Analytical Biochemistry* **1979**, *93*, 442–444.

(16) Brissette, P.; Ballou, D. P.; Massey, V. *Analytical Biochemistry* **1989**, *181*, 234–238.

(17) Clark, L. H.; Putnam, G. L. *Journal of the American Chemical Society* **1949**, *71*, 3445–3447.

(18) Kestin, J.; Sokolov, M.; Wakeham, W. A. *Journal of Physical and Chemical Reference Data* **1978**, *7*, 941–948.

Chapter 6

FUTURE DIRECTION TO OBSERVE ION CHANNEL GATING

6.1 Introduction

The goal that motivated this thesis in motion, to monitor ion channel activation, never actually came to fruition. However, I never lost sight of the ultimate goal and in the last few months I have been thinking about the big picture and how I might go about trying to achieve that goal. I want to use this chapter to lay out how I would now approach the project, and hopefully be able to monitor the conformational changes associated with ligand-gated ion channel activation.

6.2 Azobenzene Phototriggers for Ion Channel Activation

I still think that the hardest part in the entire project will be to activate ion channels with precise control. One photochemical method of ion channel activation that I did not explore is the use of azobenzene molecules. Azobenzene molecules are well-studied organic chromophores that, upon irradiation, undergo rapid cis-trans isomerization. The isomerization is accompanied by a structural change that results in a 5 Å contraction of the distance between the 4 and 4' carbons [1]. Azobenzene molecules have been used as molecular switches, to photoactivate peptides, and to induce hairpin formation in DNA [2]. Additionally, azobenzene molecules have been used to activate ion channels with light. In early ion channel studies, Lester and coworkers were able to induce activation and inhibition using azobenzene molecules covalently attached to the protein of interest [3, 4]. More recently Trauner synthesized a series of azobenzene molecules that enabled optical control of iGluR channels, pLGICs, and K^+ channels [5–7].

Azobenzene photoactivation of ion channels can occur by covalent linkage of one end of the azobenzene to the protein. The other end of the molecule has an appended ligand that can activate the desired ion channel. Upon irradiation the azobenzene will isomerize and the resulting structural changes will bring the agonist into ligand-binding site and activate the ion channel. To induce the opposite isomerization event the azobenzene can then be irradiated again which will allow for reversible activation of the ion channel. Azobenzene molecules are synthetically tuneable and many biologically important modulating ligands could be attached to potentiate different ion channels. The wavelength of *cis-trans* isomerization is also tunable.

For example red-shifted azobenzene molecules will allow for isomerization without the use of UV irradiation [8].

The photoisomerization properties of azobenzenes are amenable rapid activation of ion channels. The *trans* isomer of azobenzene is present at room temperature, and upon irradiation undergoes isomerization to the *cis*-form within a few picoseconds [9]. Thermal *cis*-to-*trans* back isomerization rates can vary widely (hours to ms); the *cis*-to-*trans* isomerization occurs within picoseconds if phototriggered [2]. The quantum yield for photoisomerization also varied depending on the specific azobenzene molecule, and can be as high as 0.20 [2, 9]. The relatively high quantum yield allows for efficient photochemical triggering of isomerization in both directions. This, coupled with the reversible nature of the azobenzene activation, provides a huge advantage in application to the study of ion channels.

Thermal or phototriggered *cis*-to-*trans* isomerization will allow for the precise control of the deactivation of ion channels, and potentially facilitate monitoring of ion channel activation and deactivation. The rapid rates at which azobenzene molecules isomerize are crucial for the precise and rapid control of ion channel activation/deactivation. Picosecond isomerization rates allows for the ligand to bind in advance of ion channel activation events (*vida supra*). It is crucial that the rapid isomerization occurs. Knowledge of the thermal *cis*-*trans* isomerization is also crucial; deactivation occurring during any measurements will present a problem. Nevertheless, the photophysical properties of azobenzeme molecules should allow for the rapid activation and deactivation of ligand-gated ion channels.

6.3 Using Lanthanide Energy Transfer to Monitor Ion Channel Activation

The use of time-resolved energy transfer provides a dynamic experimental method to monitor the activation of ion channels. Luminescence resonance energy transfer (LRET) measurements monitor the stimulated-emission lifetime of an acceptor fluorophore using a lanthanide-cheleate donor [10, 11]. The lifetime is proportional to the energy transfer efficiency of the donor-acceptor pair and it is a sensitive probe of the distance between the donor and acceptor [12, 13]. The distances obtained from the lifetime measurements are then used to map out conformational changes of the protein. As outlined above (Chapter 1), LRET was previously used to monitor the conformational changes of voltaged-gated ion channels under activation [14–16].

Lanthanide luminescence is not efficiently triggered with direct excitation of the metal center and requires sensitization [17]. Excitation of an organic dye appended to a lanthanide chelate allows for energy transfer from the excited dye to the metal-centered excited states [18, 19]. The metal-centered excited states can then undergo intersystem crossing and radiatively decay to ground state. The lanthanide emission contains many sharp peaks with large Stokes-shifts. An organic fluorphore with absorbance overlap with a lanthanide emission band is used as the acceptor. The lanthanide luminescence and the acceptor stimulated-emission can be spectrally separated because of multiple sharp emission features of the lanthanide luminescence. The spectral seperation of the donor and acceptor emission allows for concurrent measurements of the donor and acceptor lifetimes. The long lifetime of the acceptor stimulated-emission allows for the temporal separation of any direct fluorescence from the acceptor. Fluorescence lifetimes of common small-molecule organic fluorphores are on the order of nanoseconds. Gating of the fluorescence measurements, i.e. delaying the start of data acquisition, by tens of nanoseconds will allow for the rejection of any direct fluorescence measurement.

The long lifetimes of the LRET measurements also allow for the use of PMT detectors. The TR-FET measurements use photon counting to detect the fluorescence lifetime. The photon counting detection is a direct measurement, and requires longer acquisition times to get good signal. PMT detectors can be coupled with electronic amplifiers to measure the long-lifetimes of the LRET emissions. This could provide much quicker acquisition times, and use of less sample. LRET acceptor (and donor) lifetime measurements will provide information about the energy transfer efficiency, and as a consequence, the distance between donor and acceptor.

6.4 Labeling of Ion Channels

The reason I never incorporated azobenzene molecules into my research was the requirement for covalent attachment to the ion channel. The design of the experiment requires that the azobenzene, the donor, and the acceptor are covalently attached to the ion channels. These three orthogonal labeling reactions would result in a very low yield of fully labeled ion channels. This becomes a larger issue when heterologous expression and purification of the ion channel is needed. The function of the labeled ion channel needs to be verified, and I was never able to efficiently and functionally (without any perturbation) reconstitute ion channels *in vitro*.

I propose to use *Xenopus laevis* oocytes as the expression system, as well as the ultimate membrane environment with which the experiments are conducted [20].

The oocyte system is known to robustly express ion channels, and standard electrophysiological techniques can be used to monitor the function of the ion channels. Mutations can be made site-specifically to incorporate functional handles with which to label the ion channel. Every mutant permutation can be subjected to electrophysiology to confirm the presence of functional ion channel. Any shift in EC_{50} would provide an easy readout of perturbation to the system. Oocytes also allow for more "rapid" screening of different labeling sites; two-day incubation of injected oocytes is a lot shorter than the week (or more) that it takes to purify and reconstitute ion channels. The use of oocytes also allows for the extension of these studies to a larger subset of ion channels.

An issue with this proposal is orthogonality in the labeling. The initial efforts could focus on incorporating cysteine mutants at specific sites of interest. The background ion channel cysteines would have to be mutated, and the Cys-free ion channel would need to be fully functional. Cysteine labeling would not provide an orthogonal method of labeling, but the use of LRET coupled with an azobenzene phototrigger might not require completely orthogonal labeling. Ion channel activation will only occur if the azobenzene phototrigger is labeled at the correct site [5]. The use of LRET for monitoring conformational changes will only allow the ion channels labeled with a donor and acceptor pair to be monitored [10]. The stimulated-emission of the acceptor only occurs with the correct labeling. The direct acceptor emission lifetime is much shorter than the stimulated emission. The temporal difference in the acceptor emission allows for the identification of the correctly labeled systems. The use of non-specific labeling of the ion channel with the azobenzene phototrigger, donor, and acceptor would provide a means by which only correctly labeled ion channel activation could be monitored.

The true advantage to using the oocyte system is leveraging the unnatural amino acid (UAA) mutagenesis methods that have been developed in the Dougherty group [21]. These methods allow for multiple orthogonal labeling sites to be incorporated. For example the use of azide-substituted aminoacids would provide a handle for [3+2] cycloadditions conjugation reactions, and incorporation of many other bioorthogonal handles could be achieved with similar methods [22]. Direct incorporation of the donor, acceptor, and/or azobenzene required for the experiments, could also occur with UAA mutagenesis. The Dougherty group has demonstrated successful incorporation of multiple fluorescent amino acids [23]. The azobenzene phototrigger could be synthetically modified to be attached to an UAA, and placed very specifically within the protein framework near the ligand binding site. A combination of UAA mutagenesis and traditional labeling strategies could be pursued to optimize the conditions necessary for the experiments. The use of UAA mutagenesis provides a highly orthogonal labeling strategy that could greatly increase the yield of fully labeled ion channels.

6.5 The Final Experimental Design

The ion channel of interest (I recommend the muscle-type nAChR as a starting point) would be expressed in oocytes. Site-directed mutagenesis near the ligand-binding site can be used to label the azobenzene phototrigger [4, 5]. The azobenzene can either be attached through bioconjugation chemistry (Cys-labeling, or "click," for example), or incorporated directly as an UAA. The donor chelate ligand, and the acceptor fluorophore can be incorporated by similar means. Terbium (or any other lanthanide of choice) will then be added to solution to allow for formation of the lanthanide-chelate donor complex. After complete labeling of the ion channel with the azobenzene phototrigger, donor, and acceptor, the triply-labeled ion channel function can be probed by electrophysiology. Any shift in the dose-response from wild-type would indicate perturbation of the ion channel function. The locations of the three labels could be moved accordingly to afford a minimally-perturbed system. Photoactivation by the azobenzene should also be confirmed by irradiating labeled oocytes and monitoring ion channel activation by electrophysiology. It is crucial that activation only occurs under irradiation, and the thermal relaxation (or phototriggered back isomerization) results in a closed ion channel. Cycling of the photoactivation/photo-deactivation will determine the robustness of the sample. For any mutant that is made it would be necessary to reconfirm the properties listed above. After confirmation of functionally labeled ion channel is obtained the system can then be used in the LRET measurements.

There will be some technical challenges associated with this project. The azobenzene isomerization needs to be triggered, and could be achieved using a pulsed laser of the necessary wavelength. The lanthanide will also need to be excited. It would be best if the lanthanide excitation wavelength is different from the azobenzene. The timing of the lanthanide excitation with relation to the azobenzene photoisomerization is critical. The photoisomerization will activate the ion channel and we want to measure the conformational changes during activation. This requires that the LRET measurements occur at various timepoints after ligand binding. Lanthanide excitation before the azobenzene should provide measurements corresponding to the resting state. Likewise, excitation at time points seconds after azobenzene irradiation will provide information about the open or desensitized states. Changing the delay time between the azobenzene isomerization trigger, and the LRET trigger will allow for the mapping of conformational changes during the entire activation process. The direct fluorescence of the acceptor, and any auto-fluorescence from the oocytes will need to be rejected. Previous LRET meaurements used electronic gating to turn off the detector around the excitation pulse. The exact timing of the gating will need to be optimized; the maximum amount of data with the lowest non-specific fluorescence should be achieved. If photoisomerization to the resting state is desired, a third light source will need to be used. This could be a LED that can be shuttered independently of the lasers. The timing of the excitation and collection systems is crucial, and I imagine will prove non-trivial.

6.6 Conclusion

After the laser system is built, and the ion channel is functional with three labels, the experiments could proceed. The crystal structures provide a good starting point for the geometric analysis of any distance changes that are observed. Initial measurement on the resting and open (or desensitized) state would serve as a proof of principle. I think that the most challenging parts of the experiments will be the successful labeling of three sites with the correct molecules. UAA and oocytes will help, but expression of an UAA can alter the function of the ion channel dramatically. The lanthanide chelate and fluorescent acceptor could be chosen to accommodate the necessary properties required. Rejection of any autofluorescence of the oocyte, and the fluorescent acceptor emission will also be critical to gaining a clear picture of gating. The long stimulated-emission of the acceptor should help with this. I am still very interested in figuring out a way to monitor the conformational changes associated with ion channel gating. If I were to start this project now I would approach it in the above fashion. The exercise is left to the reader. Godspeed.

References

(1) Rabek, J. F.; Scott, G. W., *Photochemistry and Photophysics*; CRC Press: 1989.

(2) Beharry, A. A.; Woolley, G. A. *Chemical Society Reviews* **2011**, *40*, 4422–4437.

(3) Lester, H. A.; Krouse, M. E.; Nass, M. M.; Wassermann, N. H.; Erlanger, B. F. *Nature* **1979**, *280*, 509–510.

(4) Lester, H.; Krouse, M.; Nass, M.; Wassermann, N.; Erlanger, B. *The Journal of General Physiology* **1980**, *75*, 207–232.

(5) Tochitsky, I.; Banghart, M. R.; Mourot, A.; Yao, J. Z.; Gaub, B.; Kramer, R. H.; Trauner, D. *Nature Chemistry* **2012**, *4*, 105–111.

(6) Polosukhina, A.; Litt, J.; Tochitsky, I.; Nemargut, J.; Sychev, Y.; De Kouchkovsky, I.; Huang, T.; Borges, K.; Trauner, D.; Van Gelder, R. N.; Kramer, R. H. *Neuron* **2012**, *75*, 271–282.

(7) Berlin, S.; Szobota, S.; Reiner, A.; Carroll, E. C.; Kienzler, M. A.; Guyon, A.; Xiao, T.; Tauner, D.; Isacoff, E. Y. *eLife* **2016**, *5*, e12040.

(8) Konrad, D. B.; Frank, J. A.; Trauner, D. *Chemistry – A European Journal* **2016**, *22*, 4364–4368.

(9) Bandara, H. M. D.; Burdette, S. C. *Chemical Society Reviews* **2012**, *41*, 1809–1825.

(10) Selvin, P. R.; Rana, T. M.; Hearst, J. E. *Journal of the American Chemical Society* **1994**, *116*, 6029–6030.

(11) Selvin, P. R. In; Methods in Enzymology, Vol. 246, 1995, pp 300–334.

(12) Heyduk, T. *Current Opinion in Biotechnology* **2002**, *13*, 292–296.

(13) Heyduk, T.; Heyduk, E. *Analytical Biochemistry* **2001**, *289*, 60–67.

(14) Posson, D. J.; Selvin, P. R. *Neuron* **2008**, *59*, 98–109.

(15) Posson, D. J.; Ge, P.; Miller, C.; Bezanilla, F.; Selvin, P. R. *Nature* **2005**, *436*, 848–851.

(16) Cha, A.; Snyder, G. E.; Selvin, P. R.; Bezanilla, F. *Nature* **1999**, *402*, 809–813.

(17) Bünzli, J.-C. G. *Chemical Reviews* **2010**, *110*, 2729–2755.

(18) Chen, J.; Selvin, P. R. *Bioconjugate Chemistry* **1999**, *10*, 311–315.

(19) Selvin, P. R.; Jancarik, J.; Li, M.; Hung, L.-W. *Inorganic Chemistry* **1996**, *35*, 700–705.

(20) Lester, H. *Science* **1988**, *241*, 1057–1063.

(21) Dougherty, D. A.; Van Arnam, E. B. *ChemBioChem* **2014**, *15*, 1710–1720.

(22) Sletten, E. M.; Bertozzi, C. R. *Angewandte Chemie International Edition* **2009**, *48*, 6974–6998.

(23) Pantoja, R.; Rodriguez, E. A.; Dibas, M. I.; Dougherty, D. A.; Lester, H. A. *Biophysical Journal* **2009**, *96*, 226–237.

Appendix A

MECHANISTIC STUDY OF QUINONE PHOTOREDUCTION

A.1 Introduction

I participated in a collaborative study with the Dougherty group investigating the mechanism of a new photocage. A series of organic molecules that undergo photodissociation of a protected amide or ester were synthesized. The compound of interest consists of a 1,4-benzoquinone building block, with addition of a thioether, and a trimethyl-lock (TML) moiety to the 1 and 5 positions (Figure A.1). Photoreduction of quinones is known and can occur via intramolecular and intermolecular reductive quenching [1, 2]. The TML is a well studied decaging strategy; the nucelophilic phenol of the reduced quinone can react with the sterically crowded TML [3–5]. Lactonization of the TML moiety occurs rapidly and results in the release of the protected ester or amide. Lactone formation occurs more rapidly for esters than amides [5]. The moieties necessary for intramolecular photoreduction and TML lactonization were combined into a series of generic photolabile protecting groups (Figure A.1). Irradiation of the thioether-quinone-TML compound (S-R PRTL) results in two-electron reduction of the quinone followed by lactonization of the TML group. Lactone formation releases the protected ester or amide molecule (Figure A.1) [6]. The system is synthetically modular; the substitution on the thioether and the trimethyl-lock can afford many different variants of the molecule. I have investigated a series of S-R PRTL compounds and examined the transient absorption spectra, as well as the electrochemical and spectroelectrochemical (SpecEChem) properties. I will discuss below the results of those experiments and their implications towards the mechanism of photorelease. This compound is designed as a generic photolabile protecting group for use in the treatment of traumatic brain injury (TBI). For use in TBI, near-infrared (NIR) irradiation is needed for any significant light penetration of the skull to occur. Mechanistic understanding of how these molecules undergo photodissociation provides insights allowing for the synthetic modifications of the base building block to achieve a NIR photocage.

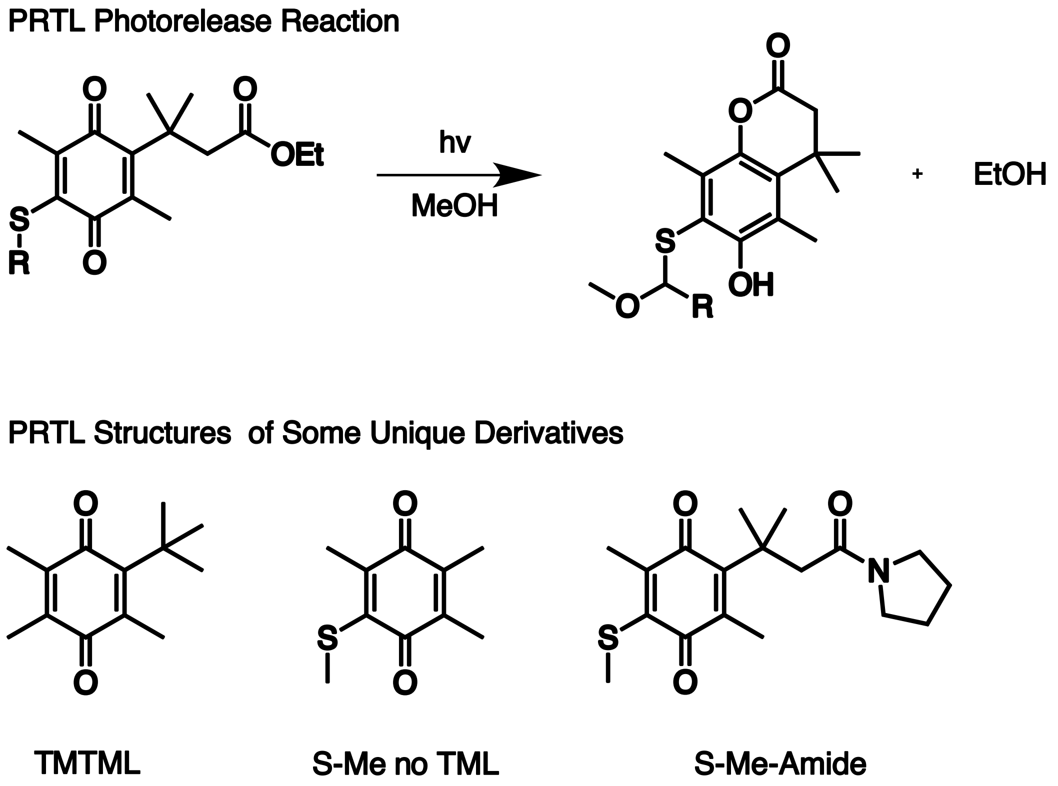

Figure A.1: The general structure of the PRTL compounds contains a thioether attached to a 1,4-benzoquinone, containing a TML group. Under irradiation in MeOH, lactone formation occurs and releases the protected ester, EtOH in this example. The wavelength of light used to trigger the photochemical reaction, and the efficiency of release, depend on the thioether substitution. Some unusual PRTL derivatives are shown on the bottom. These were used to investigate the mechanism by transient absorption spectroscopy and electrochemistry.

A.2 Methods and Materials

A.2.1 General Considerations

All of the PRTL compounds were obtained from D. Paul Walton in the Dougherty group, and the synthetic route should be published shortly. These complexes were stored in the dark, and samples were prepared fresh for each experiment. All of the samples contained a protected ethanol on the ester of the TML group unless otherwise noted. Analysis of the samples before and after experimentation confirmed that laser photolysis resulted in the same photochemistry as bulk photolysis.

A.2.2 Laser Sample Preparation

S-R PRTL was dissolved in the indicated solvent, and the concentration was diluted such that $A_{355} < 0.4$. The sample was placed in a four sided quartz cuvette (Starna Cells) with a small stir bar. This cuvette was open to air for the oxygen-saturated samples. Air-free samples underwent three freeze-pump-thaw cycles to remove any oxygen, and after the final thaw were backfilled with argon. A custom cuvette that could connect to a Schlenk line, and be sealed using a high-vacuum Teflon valve (Kontes), was used for samples void of oxygen.

A.2.3 Transient Absorption Spectroscopy

Excitation using the third harmonic from a Q-switched Nd:YAG laser (Spectra-Physics, Quanta-Ray PRO Series) provided 355 nm pulses, 8 ns, at 10 Hz. For single-wavelength transient absorption experiments, a 75 W Xe arc-lamp operated in continuous or pulsed mode, was passed through the sample colinearly with the excitation pulse. Probe wavelengths were selected using a double monochromator, with appropriate short-pass and long-pass filters to remove stray light, as well as a neutral density filter to regulate intensity. Light was detected by a photomultiplier tube (Hamamatsu R928), and amplified using a 200 MHz wideband voltage amplifier (FEMTO, DHPVA-200). Around 150 shots were collected for each wavelength, and the data were log-compressed and then fit in MATLAB. For full-spectrum transient absorption, data were collected using the same laser system, but using a nanosecond flash lamp and diode detector as described elsewhere [7].

A.2.4 Electrochemistry

Electrochemical experiments were carried out under an inert atmosphere inside a glovebox, using a Gamry Reference 600 potentiostat/galvanostat using a standard three electrode configuration. In all experiments acetonitrile was used as the solvent, and the supporting electrolyte was 0.1 M tetrabutlyammonium hexafluorophosphate (Fluka, electrochemical grade). Typical cyclic votammetry experiments used a basel-plane graphite working electrode, with a platinum wire counter electrode, and a silver wire quasi-reference electrode. The quasi-reference electrode was immersed in a 0.1 M solution of $TBAPF_6$, and separated from the main solution using a vycor frit. The ferricenium/ferrocene couple was used as an external reference. Typical concentrations of compound used were 10^{-3} M.

A.2.5 UV-Visible Spectroelectrochemistry

Spectroelectrochemical measurements were carried out under similar conditions to the electrochemical measurements. The sample was placed in a quartz cuvette, with a 1 mm optical pathlength. The above three-electrode configuration was used with a modification to the working electrode; a platinum-wire mesh working electrode was used which provides optical transparency for UV-visible data collection. After equilibration with an applied potential in chronoamperommerty mode, spectra were collected using an Ocean Optics USB2000+ spectrometer.

A.3 Results and Discussion

A.3.1 Transient Absorption Spectroscopy of PRTL Compounds

All of the PRTL compounds tested have similar absorbance features. There are strong features in the UV region of the spectrum, and a weaker ($\epsilon = 1000\ \mathrm{M}^{-1}\mathrm{cm}^{-1}$) feature in the visible with a peak at 411 nm for the S-Me derivative, resulting in a yellow colour. Irradiation at 410 nm and 365 nm (in bulk) results in lactone formation (Figure A.1a, top), and formation of a colourless solution. Use of 355 nm excitation in the laser experiments occurred for ease of experimentation.

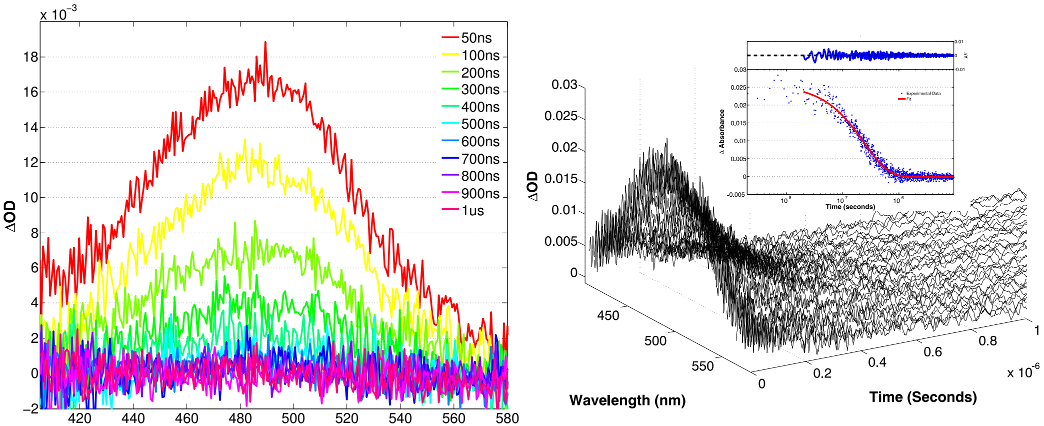

(a)

(b)

Figure A.2: (a) Full-spectrum transient absorption trace for S-Me in air-equilibrated acetonitrile. The transient species has a peak at 480 nm, and decays to baseline by 1 μs. (b) The single-wavelength kinetics traces from 405 nm to 575 nm with 5 nm steps between wavelengths shows the same apparent transient species. The inset shows the 480 nm trace fit to a single exponential yielding a lifetime of 238 ns.

Excitation of the SMe-PRTL compound induces a large increase in absorbance from 410 nm to 580 nm, with a peak at 480 nm (Figure A.2). The species decayed to baseline by 1 μs for an air-equilibrated solution, with a lifetime of 191 ns (in MeOH). No other transient species were observed on longer timescales. No clear solvent dependence on the transient lifetime of S-Me PRTL was observed; hexanes, acetonitrile, and MeOH samples all decayed to baseline by 1 μs (Figure A.3a, solid lines). Formation of only the lactone product occurs in MeOH, with irradiation in MeCN and hexanes forming an intractable mixture of products. It is interesting that there is no clear solvent dependency of the transient.

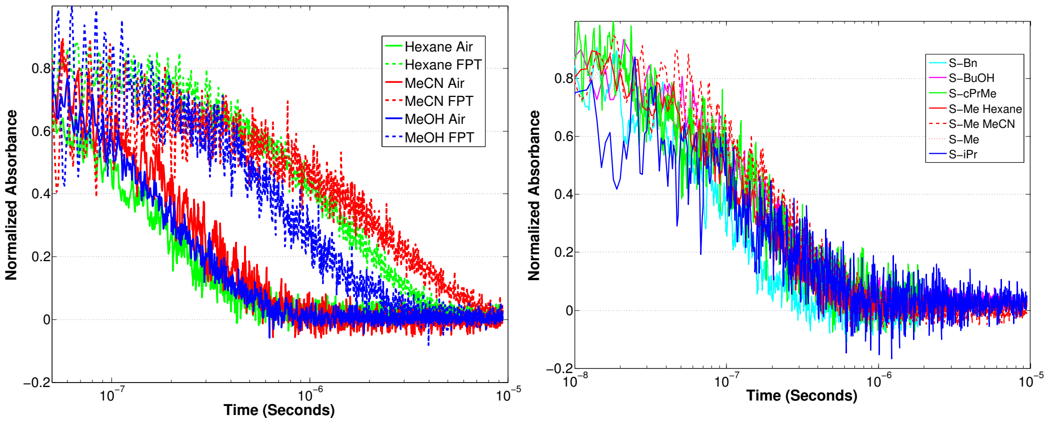

(a) **(b)**

Figure A.3: (a) The transient absorption decay at 480 nm of S-Me in MeOH (blue), Hexanes (green), and MeCN (red) in air-equilibrated solvents (solid lines) and under an atmosphere of Ar (dotted lines). The air-equilibrated lifetimes are independent of the solvent. Removal of oxygen results in a solvent-dependent lifetime being observed. (b) The transient species (480 nm) in the presence of oxygen has a derivative-independent lifetime.

The transient absorption spectra were also collected for a variety of S-R derivatives (S-Bn, S-BuOH, S-cPrMe, S-iPr) in MeOH. A strong absorbance increase in the visible centered at 480 nm was observed for all the derivatives. The transient lifetimes for all of the samples are between 100 ns and 200 ns, in air-equilibrated solutions (Figure A.3b). The bulk quantum yields for lactonization differ depending on the derivative; the lactonization yield of S-Bn is five times larger than S-Me, with all other derivatives falling in between. The observed transient lifetimes vary by a factor of 2, while the quantum yield for photodissociation varies by 5 fold. This suggests that the transient decay does not proceed to 100% product.

To examine the effect of oxygen on the system, the samples were degassed as described above. A five-fold increase in lifetime of the transient decay (930 ns) was observed in the absence of oxygen (Figure A.3a, blue lines). For the S-Me PRTL solvent-dependent lifetimes were observed (Figure A.3a, dotted lines) in the absence of oxygen (τ_{MeCN} = 2600 ns, $\tau_{Hexanes}$ = 1400 ns,τ_{MeOH} = 930 ns). The photochemistry only occurs in good yield in MeOH and the cause of the solvent dependence is not obvious. Transient absorption studies on other PRTL derivatives were only conducted in MeOH.

The transient lifetimes of various S-R derivatives (for an entire list see Table A.1) were examined in the absence of oxygen and were found to vary depending on the thioether substitutation. Transient lifetimes of the PRTL compounds increased in the absence of oxygen. The transient species observed in the air-equilibrated samples likely decays due to oxygen quenching, as well as the other decay mechanisms. The solubility of oxygen in methanol is *ca.* 10 mM [8]; if a diffusion controlled reaction between the transient species and O_2 is assumed (10^9 $M^{-1}s^{-1}$) a reaction would be observed in *ca.* 100 ns. For oxygen to quench the transient species, the decay pathways of the transient species must be slower than oxygen quenching rate. The lifetime of S-Bn PRTL is roughly the same with and without the presence of oxygen, suggesting that the transient decay pathways of S-Bn PRTL competes with oxygen quenching. S-Bn PRTL is the most efficient compound for photoinduced lactone formation, and correspondingly has the shortest lifetime. The S-cPrMe PRTL compound contains a well known radical clock. The transient lifetime of the S-cPrMe PRTL compound is the same as the analogous S-iPr PRTL compound. Radical-induced rearrangement occurs more rapidly than the transient decay ("The rates are in The Book, what page Dennis?" - OSS, "p479" - DAD). This suggests that the transient observed decay does not proceed through a radical. The transient lifetimes correlate well with the quantum yield for TML lactone formation, and shorter lifetimes have higher quantum yields of lactonization, supporting the notion that the transient is on path.

S-R	Solvent	Atm	Rate (sec^{-1})	Lifetime (ns)
S-Ph	MeOH	FPT	1.79 x 10^{7}	56
S-Bn			6.99 x 10^{6}	143
S-Bn-pCl			5.38 x 10^{6}	186
TMTML			5.03 x 10^{6}	199
S-CH$_2$-C(O)OMe			4.85 x 10^{6}	206
S-Me no TML			3.45 x 10^{6}	290
S-Me + 10mM TEA			2.70 x 10^{6}	370
S-iPr			1.84 x 10^{6}	543
S-cPrMe			1.84 x 10^{6}	544
S-CH$_2$-CH$_2$-TMS			1.80 x 10^{6}	555
S-Bn-pOMe			1.79 x 10^{6}	560
S-Bn-D$_2$			1.73 x 10^{6}	577
S-CH$_2$-CH$_2$-tBu			1.61 x 10^{6}	620
S-neopentyl			1.58 x 10^{6}	633
S-C$_6$F$_5$			1.54 x 10^{6}	650
S-fluorenyl			1.47 x 10^{6}	680
S-Et			1.33 x 10^{6}	750
S-Me-Amide			1.30 x 10^{6}	770
S-Me			1.08 x 10^{6}	930
S-CD$_3$			9.35 x 10^{5}	1070
S-CH$_2$-CF$_2$			9.17 x 10^{5}	1091
S-tBu			$\emptyset$	$\emptyset$
S-CH$_2$-TMS			$\emptyset$	$\emptyset$
S-Me	Hexane		7.1 x 10^{5}	1414
S-Me	MeCN		3.8 x 10^{5}	2647
S-Bn	MeOH	Air	1.0 x 10^{7}	96
S-Me	Hexane		6.9 x 10^{6}	146
S-cPrMe	MeOH		6.0 x 10^{6}	166
S-iPr			5.4 x 10^{6}	186
S-Me			5.2 x 10^{6}	191
S-BuOH			4.9 x 10^{6}	202
S-Me	MeCN		4.2 x 10^{6}	238
S-tBu	MeCN		$\emptyset$	$\emptyset$

Table A.1: Table of rates and lifetimes of the transient species observed at 480 nm. Not all of the derivatives result in productive photochemistry. Experimental data fit to a single exponential $f(x) = A * e^{-kt} + C$. All of the PRTL compounds were excited at 355 nm with a pulse energy of 5 mJ/pulse. If a value is missing from the table, the value is the same as the previous entries value.

To examine the quenching of the transient, a well established quencher, and electron donor, triethylamine (TEA) was used [9]. The transient lifetime of the S-Me PRTL complex was quenched in the presence of 10 mM TEA to *ca.* 300 ns in the absence of oxygen (Figure A.4a). Experiments with TEA resulted in a transient spectrum with a peak blue-shifted to 460 nm. A long-lived species (*ca.* 500 ms) was also observed (Figure A.4b). The quenching of the transient species with TEA supports that the observed species is a triplet. Quenching by TEA likely occurs via an electron transfer to the excited state quinone, analogous to species that have been studied previously [1]. More investigation into the transient with TEA present is needed, the full-spectrum of the transient should be obtained and compared with the spectrum obtained via spectroelectrochemistry (*vida infra*).

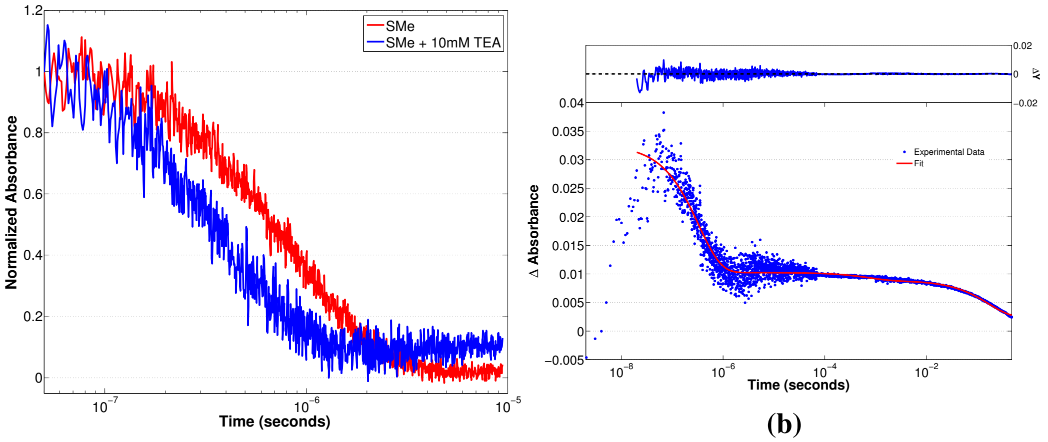

(a) **(b)**

Figure A.4: The transient lifetime at 480 nm observed upon excitation of S-Me is quenched with the addition of 10 mM TEA (blue line). The lifetime in the presence of TEA is 370 ns. The transient feature observed at 480 nm does not return to zero by 10 μs in the presence of TEA. The prolonged state is consistent with previous work on reductive quenching of duroquinone [1]. (b) The long-lived transient does not decay to baseline after 500 ms.

The photoreduction, and lactonization, requires proton transfer to balance the reaction. To examine the impact of proton transfer on the transient lifetime the deuterated S-Me PRTL and S-Bn PRTL compounds were studied (Figure A.5). A 10% increase in lifetime was observed for the S-Me PRTL complex (Figure A.5a); the S-Bn(D_2) PRTL complex displayed a four fold increase in lifetime (Figure A.5b). The quantum yield for bulk lactonization for the deuterated SMe-PRTL and SBn-PRTL are four fold and two fold lower, respectively. The differences in relative lifetime and quantum yield measurements shows that the transient species (if on path) is not 100% decaying via proton transfer mechanism.

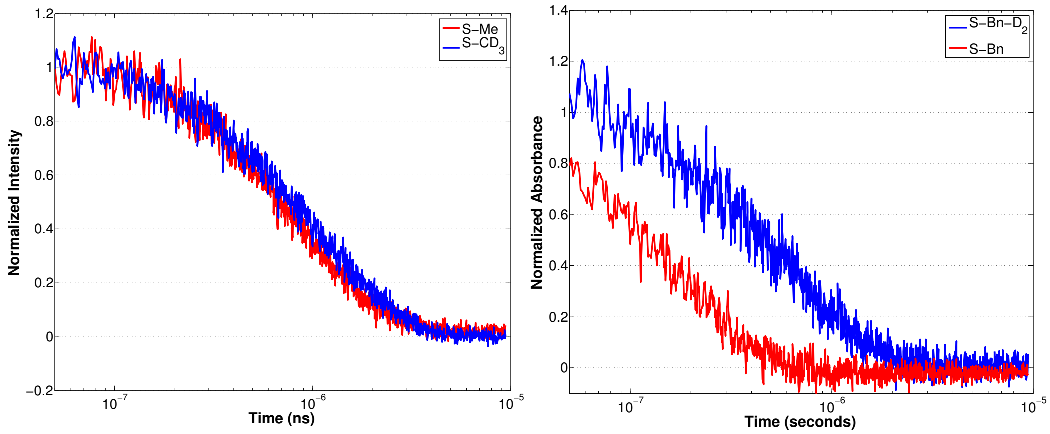

(a) **(b)**

Figure A.5: (a) The transient decay of S-Me (red line) and S-CD$_3$ (blue line) at 480 nm in MeOH under an atmosphere of Ar. The decay lifetime of the deuterated compound does not shift substantially from the proteo-derivative. (b) The S-Bn (red line) and S-Bn(D$_2$) 480 nm transient decay in MeOH. There is a four fold increase in lifetime for the transient in the deuterated complex. An isotope effect might have been expected to be observed if the transient decay pathway involves proton shift.

Two PRTL derivatives examined did not result in an observable transient species, S-tBu PRTL and S-CH$_2$TMS PRTL. The S-tBu PRTL cannot undergo lactone formation by the same mechanism because no proton is available to shift. The lack of transient with the S-tBu PRTL compound suggests that the transient that observed occurs after the initial proton transfer. The S-tBu PRTL compound has a shifted UV-visible absorbance spectrum, and is also predicted to have a distorted geometry compared with the other derivatives. For these reasons it might not be the best direct comparison.

Derivatives that provided PRTL core variations (Figure A.1, bottom) were also examined. Substitution of the protected ester for an amide resulted in a similar transient species. The lactone formation of the S-Me amide compound is much slower than the analogous ester [5]. The reduced S-Me amide lactonization has been observed by NMR, indicating that the lactone formation happens on a very slow timescale. The observed transient lifetime is 770 ns, suggesting that the transient decay is not due to lactone formation. S-Me PRTL without the TML (S-Me no TML) moiety was also studied. This compound has a lifetime of 290 ns, significantly shorter than the parent S-Me PRTL compound. Removing the thioether moiety produced a trimethyl-TML (TMTML) compound that had an observed lifetime of 200 ns. The TML appendage is sterically bulky and removing the TML might create a different chromophore. Likewise, without the thioether, intramolecular ET is unlikely to occur. It would be good to collect the transient full-spectrum of these compounds to confirm that the transient species is the same as the S-Me PRTL derivative.

A.3.2 Electrochemistry and Spectroelectrochemistry of PRTL Compounds

Chemical reduction of the PRTL compounds results in lacotonization so the electrochemical and UV-visible spectroelectrochemical properties of the PRTL compounds were also examined. The electrochemistry of the following PRTL derivatives were investigated: S-Me, S-tBu, S-cPrMe, S-Me amide, and S-Me no TML (Figure A.6). In all cases two reductive peaks are observed. The first occurs around -1.0 V vs. Fc^+/Fc, and is a quasi-reversible one-electron reduction (Figure A.6a, red line). At -1.8V vs. Fc^+/Fc a second reductive peak is observed. This peak is not reversible, and scanning past this peak results in a chemical reaction (Figure A.6a, black line). The first reduction becomes less reversible, and an oxidative feature is observed at -0.1 V vs. Fc^+/Fc (Figure A.6c). This oxidation peak is only present after scanning past the second reduction, indicative of electrochemical-chemical-electrochemical behaviour. Lactone formation requires two-electron reduction. It is then likely that after the second reduction lactone formation occurs. The observed oxidative peak could be due to the newly formed lactone compound.

To investigate if the oxidative feature is due to lactone formation, the amide-protected S-Me PRTL compound was investigated (Figure A.6b). Cyclic voltammatry of the amide compound shows the same reversible first reduction, with the second reduction becoming more reversible. Notably, no oxidation is observed, consistent with lactone formation occurring much slower in the amide derivatives. The S-Me no TML compound was also investigated; this compound cannot form a lactone under reduction. Reversible reductions occur at the same potentials as observed in the other derivatives, and no oxidation is observed. The reversible nature of the second reduction event, and no observed oxidation, in the PRTL derivatives that do not form lactones suggests the oxidation at -0.1 V is likely due to the lactone product. The PRTL compounds display electrochemistry consistent with the observed chemical and photochemical reduction requiring two electrons to undergo lactone formation.

The UV-visible spectroelectrochemistry of the PRTL compounds was also investigated (Figure A.7). The SpecEChem measurements are able to provide the UV-visible absorption spectrum under a defined potential. This allows for the UV-visible spectrum to be obtained under one-electron and two-electron conditions. The one-

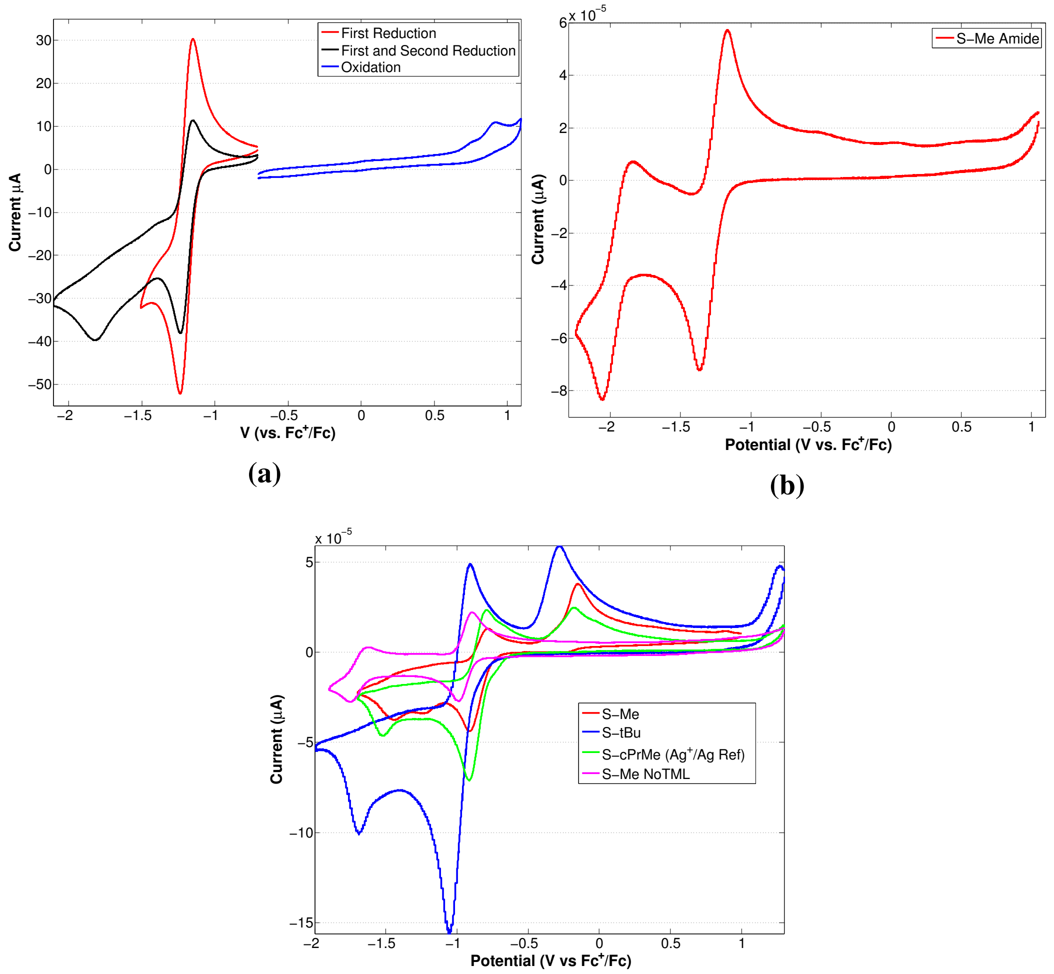

(a)

(b)

(c)

Figure A.6: (a) The cyclic voltammetry of S-Me PRTL performed under an inert atmosphere in MeCN with 0.1 M TBAPF$_6$, at a scan rate of 100 mV/s. The first reduction is at *ca.* -1.0 V (red line) and the second reduction is found at -1.8 V (black line). The first reduction is quasi-reversible and scanning just to the first wave results in a clean return oxidation peak. The second reduction appears irreversible. There are no oxidative features observed if scanned to positive potential initially (blue line). The irreversible nature of the second reduction is consistent with lactone formation occuring after two-electron reduction of the system. Lactone formation results in a new molecule that does not have the same electrochemistry, resulting in the irreversible nature of the second reductive peak. (b) The S-Me amide compound was investigated to examine the effect of lactone formation on the second reduction feature. The amide derivative undergoes the same lactone formation but at a much slower rate. The second reduction of the amide derivative is quasi-reversible suggesting that the oxidation of the two-electron reduced species is able to occur before lactone formation. (c) The full sweep of the remaining PRTL derivatives tested. The reductive peaks appear in relatively the same place for all the derivatives. If the compound doubly-reduced, an oxidation peak is visible around -0.1 V due to the lactone species. The electrochemistry of the S-Me no TML derivative shows a reversible second reduction peak and no oxidation, much like the S-Me amide. This shows that the oxidation is likely the occurring on the lactonized compound, an ECE mechanism.

electron and two-electron reduced spectra are then used to determine if the transient spectrum is of the reduced species.

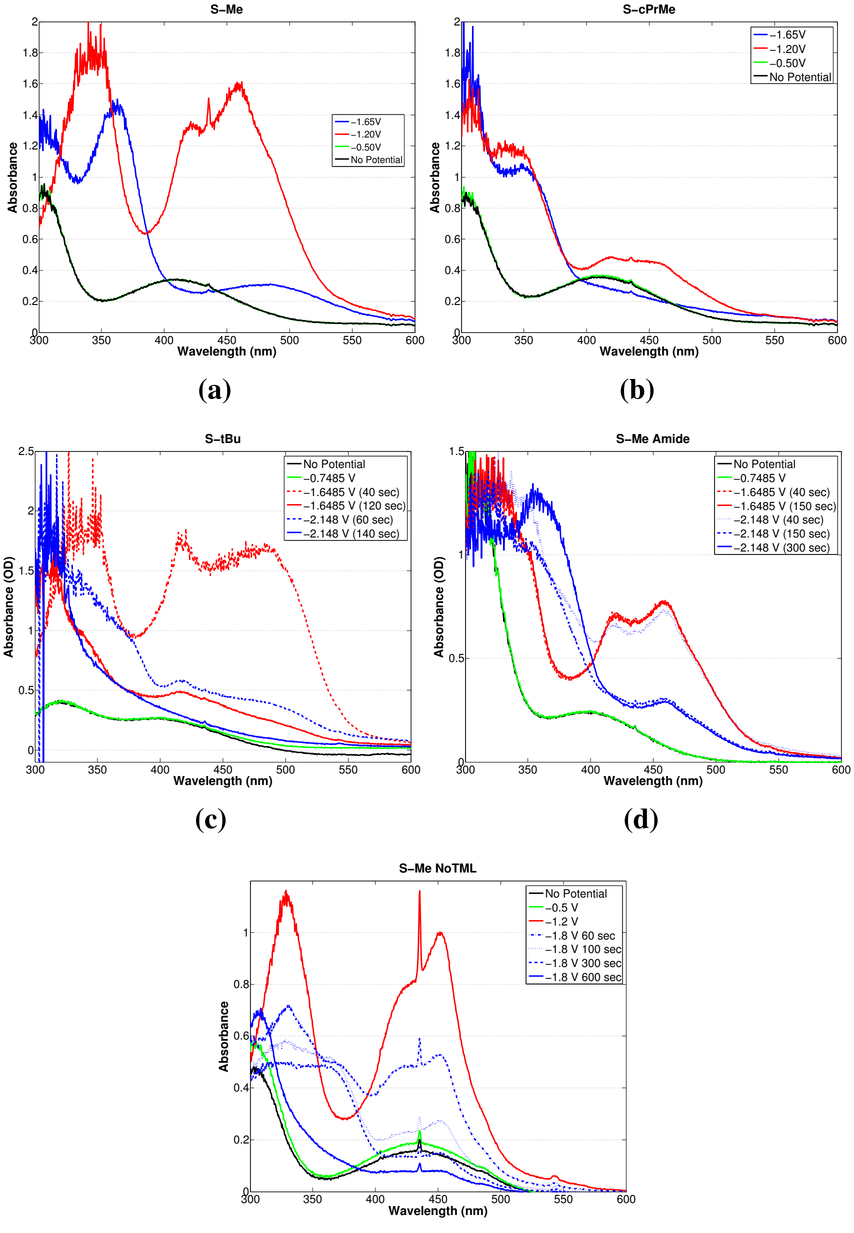

(a) **(b)** **(c)** **(d)** **(e)**

Figure A.7: UV-visible spectroelectrochemistry of a variety of PRTL derivatives performed under an inert atmosphere, in MeCN with 0.1 M TBAPF$_6$. Without polarization of the solution the spectrum appears like the ground state spectrum (black line). Spectra were acquired after polarization of the cell to the indicated voltage. For all samples there is no change in the spectrum upon polarization to -0.5 V (green line), a value at which no reduction occurs (Figure A.6). Polarization more negative than the first reduction peak results in a large visible band with a peak around 460 nm (red line). Prolonged polarization at the one-electron reduced potential results in a change in the optical spectrum, likely due to disproportionation. Polarization beyond the second reduction results in growth of a band at 375 nm, followed by disappearance of the visible band over continued polarization. The optical spectra observed under electrochemical reduction are different that what is observed in the transient absorption experiments (Figure A.2). This suggests that the transient species is not a simple one- or two-electron reduced PRTL compound.

The UV-visible spectra under no external polarization, and > -1.0 V polarization look the same (Figure A.7, black and green lines, respectively). This is consistent with the electrochemistry observed. No polarization provides the ground state spectrum, and polarization to a value less negative than the first reduction peak does not change the spectrum because no reduction occurs. The spectra of all the PRTL derivatives are similar upon one-electron reduction (Figure A.7, red line). A large increase in the visible from 400 nm to 500 nm is observed; two clear peaks in the spectra, one at 425 nm and the other at 460 nm, are seen. The one-electron reduced UV-visible spectrum is independent of the substitutions on the PRTL compound suggesting the spectrum observed is primarily of a reduced quinone. The similarity of S-Me no TML further confirms this (Figure A.7e). The one-electron reduced spectra are different from the spectra obtained in transient absorption studies. The transient spectra have a red-shifted peak (480 nm), and absorption extends into the red. Significant absorbance at 400 nm is observed in the singly-reduced species, whereas little absorption by the transient species (Figure A.2) is observed in this region. Prolonged polarization at the one-electron potential results in degradation of the spectrum, which could be due to disproportionation of the molecule. Polarization of the solution beyond the second reduction potential results in a new spectrum (Figure A.7, blue line). There are not any prominent features in the visible region for any of the compounds, which suggests that the transient spectra observed are distinct from the two-electron reduced quinone. Two-electron reduction results in lactone formation and an entirely different chemical species is then present in solution. The spectrum of the two-electron reduced species should appear similar to the photolysis product, though these experiments were never done. The starting UV-visible spectrum is observed after polarization is stopped.

The S-Me no TML derivative cannot undergo lactone formation, and the UV-visible spectrum of the one-electron reduced species is remarkably similar to the parent S-Me PRTL. This suggests that single-electron reduction of the PRLT compounds is quinone centered. The second reduction of the No-TML derivative displays a slightly different spectrum, and is more persistent that any of the TML derivatives. Lactone formation can occur with all the other derivatives, which will alter the spectrum. This is not possible for the no-TML derivative. The spectroelectrochemistry of the S-tBu PRTL is slightly different from the other derivatives. The S-tBu PRTL compound cannot undergo photoreduction, but under the two-electron reducing conditions that are present in electrochemistry lactone formation can occur. The difference in the spectra likely reflects difference in geometry, and is represented by the altered ground-state UV-visible spectrum. The similarity between all of the PRTL derivative's observed spectra suggests that the spectra are largely quinone based. It also shows that the spectra obtained in the transient absorption experiments correspond to different species.

A.4 Conclusions and Future Outlooks

A set of new photocages was developed in the Dougherty group by D. Paul Walton. This system is very modular, and in collaboration with the members of the Dougherty group, we set out to gain mechanistic understanding of the photorelease. I was able to contribute by providing nanosecond transient absorption studies and electrochemical studies. The results above outline the transient absorption and electrochemical experiments performed on the a variety of PRTL compounds. The transient spectra obtained were very similar for all of the derivatives examined, with a peak at 480 nm. The lifetime of the transient was 930 ns for the S-Me PRTL parent complex. The lifetime of the transient was shorter in the presence of oxygen, and independent of the derivative. The oxygen sensitivity suggests that triplet quenching occurs; the transient lifetime is also quenched by the well established triplet quencher TEA. The lifetime in the absence of oxygen correlates well with the quantum yield for bulk photolysis product formation. Product formation is a result of lactonization; the transient species observed does not decay via lactone formation because derivatives that are much slower to form lactones decay at similar rates. It was also established that the decay mechanism isn't due to the formation of a radical. Experiments with derivatives that undergo rearrangement upon radical formation decay at the same rate as the analogous compounds. In combination with the other mechanistic work done in the Dougherty group, it would appear that the transient is a triplet the species, might be on path, and is not decaying through lactone formation.

The electrochemistry of the PRTL compounds was all similar regardless of the derivative. A reversible one-electron reduction occurred around -1.0 V (vs Fc^+/Fc), with a second one-electron reduction occurring at < 1.8 V (vs Fc^+/Fc). The second reduction is irreversible, consistent with the known chemical reaction; two-electron reduction of the PRLT compound results in lactone formation. No oxidation was observed for any of the PRTL compounds. After two-electron reduction of the PRLT compounds an oxidation peak became apparent (*ca.* -0.1 V (vs Fc^+/Fc)). The oxidation is only present if the solution had been polarized at potentials more negative than the second reduction peak, suggesting oxidation of a different chemical species is occurring. Lactone formation occurs after two-electron reduction and is likely the species being oxidized. Study of a PRTL compound that undergoes slow (S-Me amide PRTL), or no (S-Me no TML), lactone formation resulted in a reversible second reduction peak, and no oxidation event.

The spectroelectrochemistry of the derivatives looks similar. The singly-reduced species exhibited a visible absorbance from 400 nm to 500 nm; the second reduction resulted in formation of a broad shoulder in the visible. Prolonged polarization at any reducing potential likely resulted in disproportionation of the species. The steady-state spectra are not similar to the transient spectra, suggesting that the transient species that is observed is not the purely one- or two-electron reduced quinone.

Clint Regan has shown that the photochemistry can be sensitized by thioxanthone in bulk and it might be useful to reproduce these experiments using the transient absorption system. It would be interesting to see if the same transient species is observed in the sensitization experiments. Likewise, more extensive triplet quenching experiments could be performed. Transient full-spectrum traces of the pared down PRTL derivatives (Figure A.1, bottom) would also be useful. This will allow for more accurate comparison of the various derivatives. Ultrafast transient absorption experiments might provide some insight into the early photochemical events as well. The experiments that I believe would be interesting are nanosecond-IR experiments. The photolysis of the PRTL compounds converts a quinone to a hydroquinone. The necessary controls need to be run first to determine if the starting material and product need to have sufficient spectroscopic handles for TR-IR to be a viable experiment. These experiments would consume large quantities of sample due to the irreversible photochemistry that occurs so a flow-cell is needed. Regardless, I think that the IR experiments would serve as a nice compliment to the time-resolved visible spectra already obtained. Monitoring the reaction by time-resolved IR experiments might further help us understand the mechanism, allowing us to design new compounds with the desired properties.

References

(1) Scheerer, R.; Graetzel, M. *Journal of the American Chemical Society* **1977**, *99*, 865–871.

(2) Darwent, J. R.; Kalyanasundaram, K. *Journal of the Chemical Society, Faraday Transactions 2: Molecular and Chemical Physics* **1981**, *77*, 373–382.

(3) Milstien, S.; Cohen, L. A. *Journal of the American Chemical Society* **1972**, *94*, 9158–9165.

(4) Levine, M. N.; Raines, R. T. *Chemical Science* **2012**, *3*, 2412–2420.

(5) Carpino, L. A.; Triolo, S. A.; Berglund, R. A. *The Journal of Organic Chemistry* **1989**, *54*, 3303–3310.

(6) Iwamoto, H. *Bulletin of the Chemical Society of Japan* **1989**, *62*, 3479–3487.

(7) Dempsey, J. L.; Winkler, J. R.; Gray, H. B. *Journal of the American Chemical Society* **2010**, *132*, 1060–1065.

(8) Battino, R.; Rettich, T. R.; Tominaga, T. *Journal of Physical and Chemical Reference Data* **1983**, *12*, 163–178.

(9) Bhattacharyya, K.; Das, P. K. *The Journal of Physical Chemistry* **1986**, *90*, 3987–3993.

Appendix B

USE OF COBALT AS A PROTECTING GROUP FOR RELEASE OF AMINES

B.1 Introduction

The aim of this work was to use Co^{3+}-amine complexes as photocages for the release of propylamine to activate ELIC. Reduction of Co^{3+} will form Co^{2+}, and rapid ligand exchange will occur. Co^{2+} complexes are substitutionally labile, whereas Co^{3+} are substitutionally inert. This ligand exchange releases any amine ligands, and forms $Co(H_2O)_6{}^{2+}$. The release of amines occurs rapidly upon reduction of Co^{3+} complexes; release of 6 NH_3 ligands occurs by 700 μs [1, 2]. Release of cheleated amines such as ethylenediamine is slower, but still occurs. Photochemical reduction of the Co^{3+} center was done by intramolecular reduction from an oxalate ligand [3]. Irradiation of an oxalato-cobalt^{3+} complex undergoes intramolecular reduction with irradiation into the ligand-to-metal charge transfer (LMCT) band. This resuts in the formation of a Co^{2+} center, and release of CO_2 as well as CO_2 radical [3]. The radical is then able to reduce another Co^{3+} molecule in solution. Theoretically, with one photon, up to eight ligands can be released from an oxalato-tetra(amine)-Co^{3+} complex. We sought to use oxalato-tetrakis(n-propylamino)cobalt^{3+} (Co-propylamine) as a photocage for the release of propylamine for the activation of ELIC.

B.2 Methods and Materials

B.2.1 General Considerations

All the chemicals were purchased from Sigma-Aldrich. Procedures for synthesis of cobalt compounds are have been previously published and were adapted with minimal modification [4–6]. The synthesis of oxalato-tetrakis(n-propylamino)cobalt(III) occurred by dissolving $Co(NH_3)_4(C_2O_4)$ in neat propylamine and stirring for 5 days [7]. The solution was filtered to remove any excess starting material, and the filtrate was purple. The solvent was then removed with a rotovap, and a purple solid was obtained and dried *in vaccuo*. This solid was used without further purification. The NMR and UV-visible spectra suggested that the compound was made; crystal growth did not yield crystals amenable to XRD studies. ELIC was expressed, and electrophysiology was performed, as above (Chapter 3). A 365 nm LED (Thorlabs, M365L1) was used for irradiation of the Co-propylamine complex.

B.3 Results and Discussion

The UV-visible spectrum of Co-propylamine has two clear peaks, one centered at 355 nm, and the second at 511 nm (Figure B.1a). The ^{1}H NMR of the Co-complex shows only the propylamine peaks, which are shifted from free propylamine resonances (Figure B.1b). The down-field shift observed is likely due to the ligation of the propylamine onto the cobalt metal. The amine protons are not visible in the NMR due to proton exchange with the solvent. Irradiation of this complex in water with 365 nm light results in an increase in the pH of the solution. For some reason I never irradiated an NMR sample to watch the release of propylamine. The only issue with this is upon irradiation, formation of a Co^{2+} paramagnetic species occurs. To confirm propylamine release, irradiation of the Co-propylamine complex in the presence of an acyl chloride would result in the acyl chloride reacting with the free propylamine. Isolation of the newly formed amide compound might provide evidence for propylamine release. Regardless, this compound was then used for the activation of ELIC.

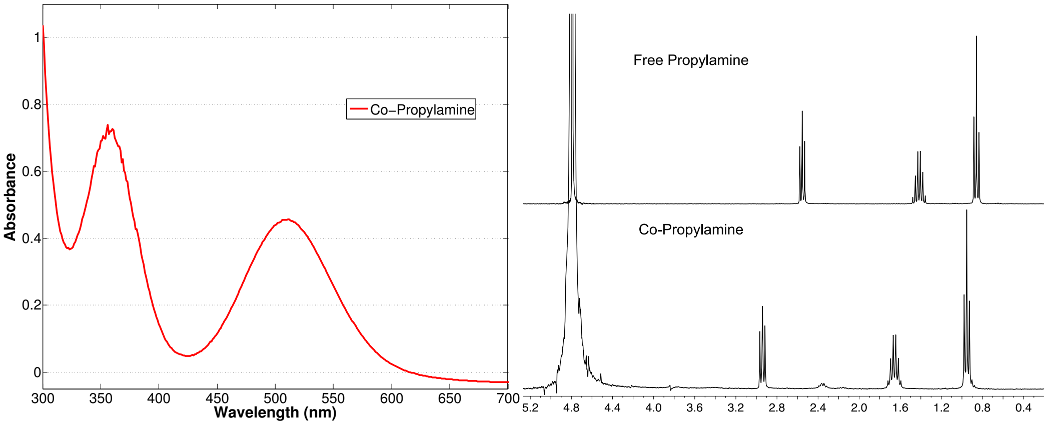

(a) **(b)**

Figure B.1: (a) The UV-visible spectrum of Co-propylamine, with a peak at 355 nm and another peak at 511 nm. This results in a nice purple colour. (b) The ^{1}H NMR spectra of free propylamine and Co-propylamine in D_2O. The propylamine peaks are shifted down-field from the free propylamine peaks.

Application of Co-propylamine to ELIC-expressing oocytes resulted in an immediate increase in current observed indicative of activation of ELIC (Figure B.2a). Activation of ELIC occurred before irradiation, suggesting that the Co-propylamine is an agonist of ELIC, and not suitable for use as a photocage. To examine the agonist behaviour of Co-propylamine further, a dose-response curve for the activation of

ELIC by Co-propylamine was obtained (Figure B.2b). The effective concentration of half-maximal activation (EC_{50} of ELIC obtained for Co-propylamine was 480 μM. This value is among the most potent agonists of ELIC [8]. It was surprising that the Co-propylamine compound was an agonist of ELIC. In an effort to understand the ELIC-Co interactions, crystals of ELIC were soaked with Co-propylamine. Unfortunately, these crystals did not diffract to a quality amenable for high-resolution structural characterization. No activation should be observed in the dark and the agonist behaviour of Co-propylamine eliminates the use of this compound as a photocage of ELIC.

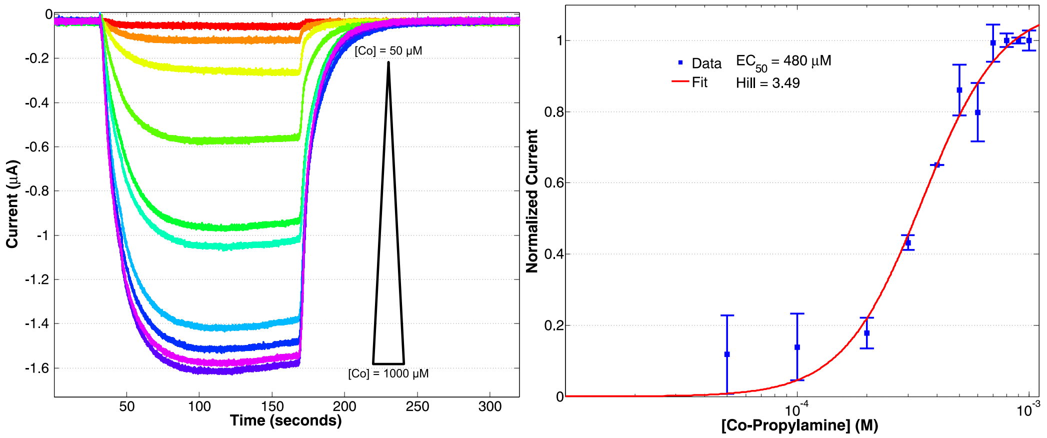

(a) **(b)**

Figure B.2: (a) Whole-cell voltage-clamp electrophysiology trace (see Figure 1.3 for background) of ELIC-expressing oocytes with increasing concentrations of Co-propylamine. Application of Co-propylamine results in the activation of ELIC, and demonstrates the agonist behaviour of Co-propylamine towards ELIC. (b) The normalized current response of ELIC to various concentrations of Co-propylamine. The data is fit to the hill equation, with an EC_{50} = 480 μM and a hill coefficient of 3.5. ELIC is a very insensitive ligand-gated ion channel and Co-propylamine is among the most potent agonists that have been reported [8]. The agonist behaviour that is observed suggests that Co-propylamine is not a useful photocage because activation occurs prior to irradiation.

The efficacy of Co-propylamine was also examined. In these experiments, a maximum activation concentration of propylamine was applied to ELIC. The maximum activation concentration of Co-propylamine was then applied to the same oocyte. The current response of propylamine activation was then compared with the current response of Co-propylamine activation. The current response for maximum activation of ELIC by Co-propylamine is *ca.* 25% of the current elicited from propylamine activation, showing that Co-propylamine is a partial agonist of ELIC (Figure B.3). One explanation for the observed agonist behaviour of Co-propylamine was that exposure to adventitious light could trigger the photochemical reaction and release propylamine into solution. The resulting free propylamine in solution would then be the true agonist in solution. This is unlikely because irradiation of a solution of Co-propylamine (*in vitro*) with visible light does not result in an increase in the pH. The solutions that were applied to ELIC were prepared fresh and kept in an opaque plastic container that would absorb any UV photons present. Also the markedly different EC_{50} value and the partial agonist activity suggests that Co-propylamine is acting as a distinct agonist.

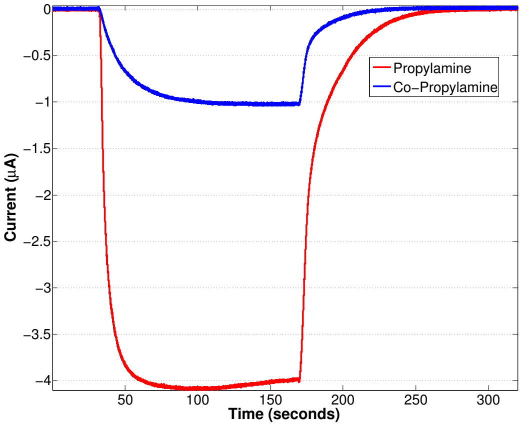

Figure B.3: The application of a maximum-activation dose of Co-propylamine elicits a current response (blue line) that is 25% of the maximum current observed using propylamine (red line) as the agonist. Co-propylamine is a partial agonist of ELIC.

Irradiation of Co-propylamine should cause the release of (at least) four propylamine molecules. Activation of ELIC might still be possible at low concentrations of Co-propylamine because of the four-fold increase in propylamine concentration upon irradiation. ELIC exposed to Co-propylamine was irradiated with 365 nm light (Figure B.4a). Before irradiation ELIC was already activated (*vida supra*). Irradiation of the Co-propylamine solution results in a decrease in the ELIC-activation currents. The decrease of current suggests that the photoproduct of the reaction interacts with ELIC in an inhibitory manner. The photoproducts of the reaction are CO_2, Co^{2+}, and propylamine. Propylamine is known to activate ELIC, and CO_2 was assumed to mind its own business. To investigate the effect of Co^{2+} on ELIC, ELIC was activated by propylamine, and addition of Co^{2+} in solution resulted in a decrease in current of ELIC (Figure B.4b, blue line). This is not surprising as ELIC is blocked by divalent cations. Co^{2+} is about the same size as Zn^{2+} and it has been shown that Zn^{2+} plugs the bottom of the pore of a related ion channel. The block of ELIC by Co^{2+} eliminates the use of the Co-propylamine complex (and any other Co^{3+} complex that will ultimately form Co^{2+}) as a photocage for ELIC.

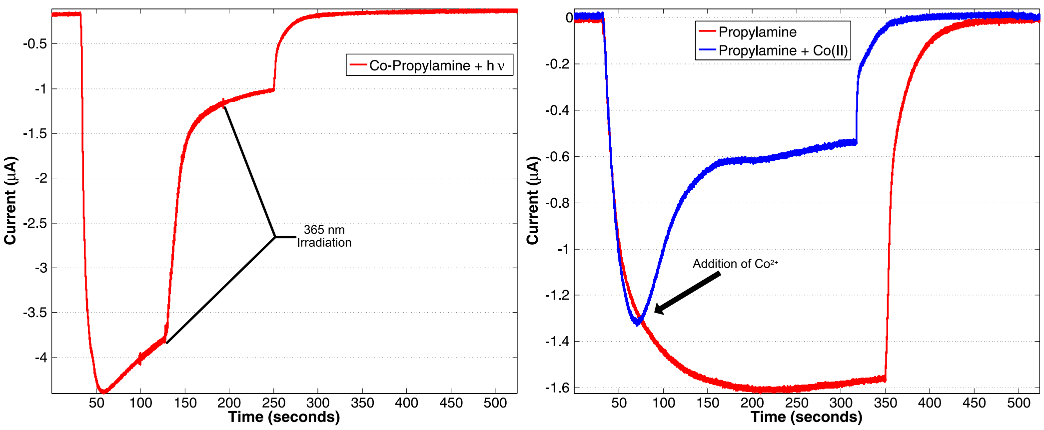

(a) **(b)**

Figure B.4: (a) The application of Co-propylamine results in the activation of ELIC (*vida supra*). Irradiation of Co-propylamine in the presence of activated ELIC results in a substantial decrease in the ELIC signal. Co-propylamine is a partial agonist, and irradiation releases four equivalents of propylamine suggesting that the current decrease observed under irradiation is due to some interaction of the photoproduct with activated ELIC. (b) Application of Co^{2+} in solution with propylamine results in significant attenuation of ELIC signals. The photoproduct in (a) is Co^{2+}, which has now been shown to inhibit ELIC signals. The inhibition observed eliminates the reduction of Co^{3+} for use as protecting groups for the activation of ELIC.

B.4 Conclusions

The reduction of a substitutionally-inert Co^{3+}-amine complex will form a labile Co^{2+} species and eject the ligated amines. Attachment of propylamine to a Co^{3+} system allowed for the caging of an ELIC agonist. The Co-propylamine complex was made, under 365 nm irradiation appears to release propylamine. Co-propylamine was then applied to ELIC and activation was observed; Co-propylamine was found to be a partial agonist with *ca.* 25% efficacy, and have an EC_{50} of 480 μM. Irradiation of the Co-propylamine solution in the presence of activated ELIC resulted in a decrease in signal. Irradiation of Co-propylamine will release propylamine, but also Co^{2+}. Co^{2+} was found to inhibit activated ELIC alone. The activation of ELIC in the dark by Co-propylamine and the inhibition by the photoproduct eliminate the use of Co-propylamine as photocage for ELIC.

The reason that I am putting this work in the thesis is because I want to make sure that people are aware of the hazards involved with Co protecting groups. Different cobalt complexes were synthesized that contained chelating ELIC agonists. The chelated Co^{3+} complexes were not agonists of ELIC. Other reductive mechanisms were also implemented using $Ru(bpy)_3^{2+}$ as an electron donor. This was all before any of the other ruthenium work was conducted (Chapter 3), so the deleterious interactions between Ru and ELIC were not known. Regardless, any use of Co^{3+} as a protecting group will ultimately form Co^{2+} that will then go and block ELIC, and potentially other monovalent cation-selective ion channels. Activation of anion-selective channels might be able to be accomplished using this strategy. Also formation of a Co^{2+} complex that is not $Co(H_2O)_6{}^{2+}$ is another approach [1]. Using a high-affinity bulky ligand such as nitrilotriacetic acid (NTA) might result in the formation of a Co^{2+}-NTA complex that is unable to block the channel. The Co^{3+}-NTA complex would need to be reduced somehow. Attaching a Co^{3+} system to a $Ru(bpy)_3{}^{2+}$ complex has been used previously to achieve ligand substitution of a Co^{3+} system in a biological setting [9]. It might be interesting to use this dinuclear complex to activate ion channels. In all, one has to be careful anytime hexaaquo-Co^{2+} is formed in solution with an ion channel, and it might not be a generically applicable photocage.

References

(1) Lilie, J.; Shinohara, N.; Simic, M. G. *Journal of the American Chemical Society* **1976**, *98*, 6516–6520.

(2) Endicott, J. F.; Hoffman, M. Z. *Journal of the American Chemical Society* **1965**, *87*, 3348–3357.

(3) Cordemans, L.; Olieslager, J.; Hendrix, J.; De Jaegere, S. *The Journal of Physical Chemistry* **1974**, *78*, 1361–1367.

(4) Dwyer, F. P.; Reid, I. K.; Garvan, F. L. *Journal of the American Chemical Society* **1961**, *83*, 1285–1287.

(5) Bailar, J. C.; Rollinson, C. L. In *Inorganic Syntheses, Volume 2*, Fernelius, W. C., Ed.; John Wiley & Sons, Inc.: 2007, pp 222–225.

(6) Mori, M.; Shibata, M.; Kyuno, E.; Adachi, T. *Bulletin of the Chemical Society of Japan* **1956**, *29*, 883–886.

(7) Palmer, W. G., *Experimental Inorganic Chemistry*; Cambridge University Press: Cambridge England; New York, 1954.

(8) Zimmermann, I.; Dutzler, R. *PLoS biology* **2011**, *9*, e1001101.

(9) Holbrook, R. J.; Weinberg, D. J.; Peterson, M. D.; Weiss, E. A.; Meade, T. J. *Journal of the American Chemical Society* **2015**, *137*, 3379–3385.